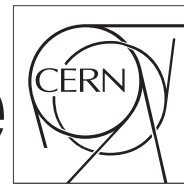




The Compact Muon Solenoid Experiment

CMS Draft Note

Mailing address: CMS CERN, CH-1211 GENEVA 23, Switzerland



2019/12/20

Archive Hash: 3cd013f

Archive Date: 2019/12/20

Study of Higgs boson production in association with top quarks in final states with electrons, muons and taus using the full Run 2 dataset

The ttH multi-lepton and tau-tau working group

Abstract

The production of Higgs (H) bosons in association with either one (tH) or two ($t\bar{t}H$) top quarks is studied in final states with electrons, muons and taus, using proton-proton collision data recorded at $\sqrt{s} = 13$ TeV center-of-mass energy during the period 2016 to 2018, corresponding to an integrated luminosity of 137.2 fb^{-1} . The sensitivity of the analysis is improved by using matrix element and machine learning methods to separate the signal from backgrounds. The measured signal rates for tH and $t\bar{t}H$ production amount to $X.XX^{+X.XX}_{-X.XX}$ and $X.XX^{+X.XX}_{-X.XX}$ times the production rate expected in the Standard Model. The measured production rates are used to determine constraints on the coupling of the H boson to the top quark.

This box is only visible in draft mode. Please make sure the values below make sense.

PDFAuthor:

TBD

PDFTitle:

Study of Higgs boson production in association with top quarks in final states with electrons, muons, and taus using the full Run 2 dataset

PDFSubject:

CMS

PDFKeywords:

CMS, physics, Higgs

Please also verify that the abstract does not use any user defined symbols

1 Contents

2	1	Introduction	3
3	2	Data samples and Monte Carlo simulation	6
4	3	Particle reconstruction and identification	8
5	3.1	Electrons and muons	8
6	3.2	Hadronic τ decays	28
7	3.3	Jets	30
8	4	Reconstruction of event level quantities	31
9	5	Event selection	32
10	5.1	Triggers	32
11	5.2	E_T^{miss} filters	33
12	5.3	Event channels	33
13	6	Data-to-MC corrections	39
14	6.1	Pileup reweighting	42
15	6.2	Trigger efficiency	42
16	6.3	Identification and isolation efficiency for e and μ	43
17	6.4	Identification efficiency for τ	43
18	6.5	Energy scale of τ_h	44
19	6.6	b-tag efficiency and mistag rate	45
20	6.7	E_T^{miss} resolution and response	46
21	6.8	Prefiring probability of L1 ECAL trigger	46
22	6.9	Drell-Yan reweighting	48
23	6.10	t <bar>t} reweighting</bar>	50
24	7	Background estimation	50
25	7.1	“Fake” background	52
26	7.2	Charge “flip” background	54
27	8	Systematic uncertainties	54
28	9	Signal extraction	60
29	9.1	Signal regions with DNNs	62
30	9.2	Signal regions with BDTs	69
31	9.3	Control regions	71
32	10	Theory elements to BSM interpretation	76
33	11	Results	79
34	11.1	Standard Model interpretation	79
35	11.2	Beyond the Standard Model interpretation	79
36	12	Summary	90
37	A	Background control regions	91
38	A.1	t <bar>t}W</bar>	91
39	A.2	t <bar>t}Z</bar>	91
40	A.3	WZ+jets	91
41	A.4	“Fake” background control plots	91
42	A.5	1 ℓ + 2ss τ_h	91
43	A.6	ttbar background	91

44	B	Deep Neural Networks	102
45	C	Boosted Decision Trees	104
46	D	Higgs Jet Tagger	111
47	E	Hadronic Top Tagger	113
48	F	Matrix Element Method	117
49	G	Single variable analysis	120
50	H	Differential cross-section measurements	124
51	H.1	Available final states	124
52	H.2	Reconstructing the Higgs boson p_T in the $2\ell ss + 0\tau_h$ final state	126
53	H.3	Regressing the Higgs transverse momentum with a Deep Artificial Neu- ral Network	132
54	I	Measurement of lepton misidentification rates	135
55	I.1	Closure test	143
56	J	Measurement of τ_h misidentification rate	148
57	K	Measurement of the lepton charge misidentification rate	152
58	K.1	Electrons	152
59	K.2	Muons	154
60	L	Measurement of the phase space extrapolation uncertainty	157
61	L.1	Introduction	157
62	L.2	Phase space extrapolation uncertainty	157
63	L.3	Application to $t\bar{t}$ -enriched analyses	158
64	L.4	Conclusions	161
65	M	Prefiring	162
66	N	Tables with event yields, prefit/postfitplots, ML fit diagnostics, etc	165
67	O	Results separated by year	166

69 1 Introduction

70 The discovery of the Higgs (H) boson by the CMS and ATLAS experiments in 2012 [1, 2] opened
71 a new field for exploration in the realm of particle physics. It is important to study the prop-
72 erties of this newly discovered resonance in order to ascertain if it is indeed the scalar particle
73 predicted by the Standard Model (SM). Given the mass of H , the SM accurately predicts all its
74 properties, e.g., the branching fractions and couplings to other SM particles, etc. Currently the
75 mass of the discovered particle is measured with $< 2\%$ accuracy ($m_H = 125.09 \pm 0.24$ GeV [3])
76 by a combined analysis of data recorded by the CMS and ATLAS experiments during LHC Run
77 1. Results from Run 1 also indicate that the couplings of the H boson to the W and Z bosons
78 are SM-like [4]. However, H to fermion couplings have only been constrained with large un-
79 certainty. In the SM, the Yukawa coupling y_f of the H boson to fermions is proportional to
80 the mass m_f of the fermion, namely $y_f = \sqrt{2m_f/v}$, where $v \approx 246$ GeV denotes the vacuum
81 expectation value of the Higgs field. With a mass of $m_t = 173.34 \pm 0.76$ GeV [5], the top quark
82 is by far the heaviest fermion known till date, and its Yukawa coupling y_t is of the order one.
83 The large mass of the top quark may indicate that it plays a special role in the mechanism of
84 electroweak symmetry breaking [6–8]. Deviations of y_t from the SM prediction would unam-
85 biguously indicate the presence of new physics beyond the SM, and thus the determination of
86 y_t is of special interest in the study of the Higgs boson.

87 The production of the Higgs in association with a top quark pair ($t\bar{t}H$) provides direct access to
88 the magnitude of y_t . The SM cross section for $t\bar{t}H$ production in proton-proton (pp) collisions at
89 center-of-mass energy $\sqrt{s} = 13$ TeV amounts to 506.5 fb [9], computed at next-to-leading (NLO)
90 accuracy in quantum chromodynamics (QCD), along with electroweak corrections computed
91 at the same order in perturbation theory. The cross section for the associated production of a H
92 boson with a single top quark (tH production) is significantly smaller, amounting to 74.3 fb [9]
93 in the SM, computed at NLO accuracy in QCD with the so-called five-flavour scheme (5 FS). In
94 the 5 FS, bottom quarks are modelled by parton distribution functions (PDFs) of the proton and
95 may appear in the initial state of scattering processes, as opposed to the four-flavour scheme
96 (4 FS), where bottom quarks are produced by gluon splitting at the matrix element level and
97 occur only in the final state [10].

98 The leading order (LO) Feynman diagrams for H boson production in association with a pair
99 top quarks ($t\bar{t}H$) is shown in Fig. 1. The tH production occurs through three different channels,
100 namely the t-channel (tHq), tW -associated (tHW) and s-channel. The Feynman diagrams for
101 these three production modes in the 5 FS can be found in Figs. 2, 3 and 4. The contribution
102 of the s-channel is negligible at LHC energies. The rates of the tHq and tHW production pro-
103 cesses are small in the SM, due to the destructive interference between diagrams where the H
104 boson couples either to the top quark (left side diagrams of Figs. 2 and 3) or to the W boson
105 (right side diagrams of Figs. 2 and 3). In the case where y_t differs from the value predicted by
106 the SM, the cross section for tH production may be modified significantly. The largest enhance-
107 ment of the tH production rate is attained when y_t is negative, referred to as the inverted top
108 coupling (ITC) scenario. In this case the destructive interference between diagrams turns into
109 a constructive interference, and the cross section amounts to 848.0 fb [9]. The measurement
110 of the tH production rate thus allows not only for a model independent determination of the
111 magnitude of y_t , but also of its relative sign with respect to the W - H coupling, which makes
112 the study of this process particularly interesting.

113 The decay rate of the H boson to photon pairs also provides sensitivity to the relative sign of
114 y_t [11], as does the rate of the associated production of a H boson with a Z boson [12]. The
115 measured rates of these processes suggest that the H boson coupling to top quarks is SM-like.

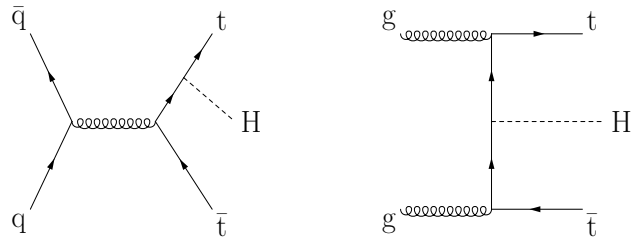


Figure 1: Representative Feynman diagrams for the $t\bar{t}H$ production processes.

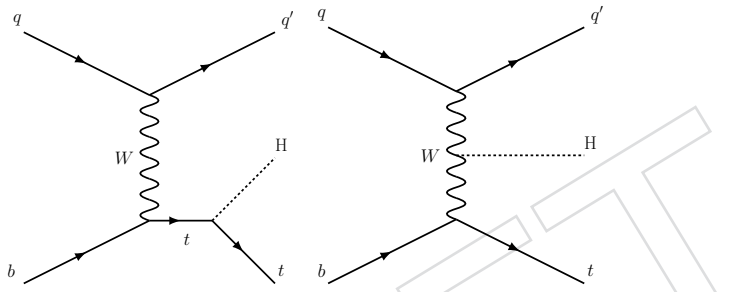


Figure 2: Representative Feynman diagrams for the t -channel tH production processes.

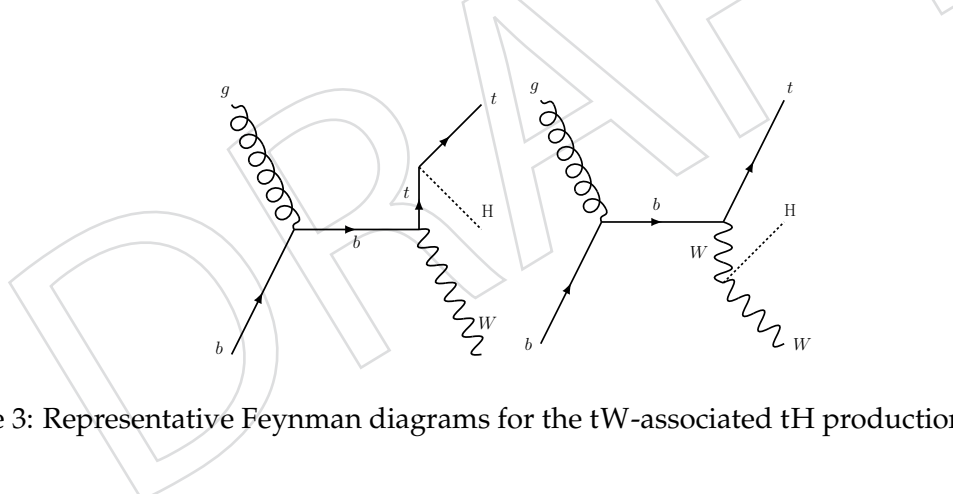


Figure 3: Representative Feynman diagrams for the tW -associated tH production processes.

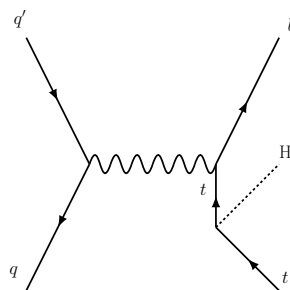


Figure 4: Representative Feynman diagram for the s -channel tH production processes.

116 However, contributions of non-SM particles to these loops may compensate, and thus mask,
117 deviations of y_t from its SM value. A model independent direct measurement of the top quark
118 Yukawa coupling in $t\bar{t}H$ and tH productions is thus well motivated. The comparison of the
119 magnitude and sign of y_t obtained from the measurement of the $t\bar{t}H$ and tH production rates,
120 where y_t enters at tree level, with the value of y_t obtained from processes where y_t enters via
121 loop contributions will provide complimentary evidence either for or against such new physics
122 phenomena.

123 In this paper we report on the measurement of the $t\bar{t}H$ and tH production rates in final states
124 with multiple electrons, muons and hadronically decaying τ leptons. The measurement is
125 based on data recorded by the CMS experiment in pp collisions at $\sqrt{s} = 13$ TeV center-of-mass
126 energy during LHC Run 2, corresponding to an integrated luminosity of 137.2 fb^{-1} .

127 The associated production of H bosons with top quark pairs has previously been studied by
128 ATLAS and CMS with up to 24.8 fb^{-1} of data recorded at $\sqrt{s} = 7$ and 8 TeV during LHC Run
129 1 [13–17] and with up to 79.8 fb^{-1} of data recorded at $\sqrt{s} = 13$ TeV during LHC Run 2 [18–24].
130 The combined analysis of data recorded at $\sqrt{s} = 7, 8$ and 13 TeV allowed for the observation
131 of $t\bar{t}H$ production with significances of 5.2 and 6.3 standard deviations by CMS and ATLAS,
132 respectively [25, 26]. The production of H bosons in association with a single top quark has
133 been studied by ATLAS and CMS with data recorded during LHC Run 1 [27] and during LHC
134 Run 2 [28]. These analyses covered the H boson decay modes to bottom quark-antiquark pairs,
135 photon pairs, pairs of τ leptons and combinations of quarks and leptons originating from the
136 decay of intermediate on- or off-shell W and Z bosons.

137 The measurement of the $t\bar{t}H$ and tH production rates presented in this paper constitutes the
138 first CMS analysis in which both the $t\bar{t}H$ and the tH processes are studied together. This joint
139 search is motivated by the high degree of overlap in the experimental signatures of the two
140 processes, while their production rates vary differently as function of y_t . Compared to previous
141 studies, the sensitivity of the analysis presented here is enhanced through the optimization of
142 the object and event selections. First, the identification of bottom quark jets and of hadronic
143 τ decays has been improved. Moreover, the analysis has been extended to cover a total of ten
144 different experimental signatures, which target the H boson decay modes $H \rightarrow WW$, $H \rightarrow \tau\tau$
145 and $H \rightarrow ZZ$. The final states $1\ell + 2\tau_h$, $2\ell ss + 0\tau_h$, $2\ell ss + 1\tau_h$, $2\ell os + 1\tau_h$, $2\ell + 2\tau_h$, $3\ell + 0\tau_h$,
146 $3\ell + 1\tau_h$ and $4\ell + 0\tau_h$ target events in which at least one top quark decays leptonically, while
147 the final states $0\ell + 2\tau_h$ and $1\ell + 1\tau_h$ target events in which all top quark decays hadronically.
148 The symbol ℓ denotes light leptons (e, μ), where “ss” and “os” mean “same sign” and “opposite
149 sign”, respectively. The symbol τ_h denotes hadronically decaying τ ’s. As in previous analysis,
150 the separation of the $t\bar{t}H$ and tH signals from backgrounds is improved with machine learning
151 techniques, mainly boosted decision trees (BDTs) and artifical neural networks (ANNs) [29–31],
152 as well as with matrix element methods (MEM) [32, 33]. Moreover, machine learning methods
153 are also employed to improve the separation between the $t\bar{t}H$ and tH signals. The measured
154 $t\bar{t}H$ and tH production rates are used to set limits on y_t .

155 This document is structured as follows. The data and simulation samples are presented in Sec-
156 tion 2. The procedures used for the reconstruction of particles and event-level quantities are
157 described in Section 3 and Section 4, respectively. The triggers and the basic event selection
158 are explained in Section 5. The description of the data-to-simulation corrections applied can be
159 found in Section 6. In Section 7 we explain the background estimation techniques, while Sec-
160 tion 8 describes the systematic uncertainties associated to this analysis. The analysis strategy
161 and the MVA methods are presented in Section 9. In Section 10 we outline basic theoretical
162 elements for the BSM interpretation of the results, which are presented in Section 11.

163 2 Data samples and Monte Carlo simulation

164 The analyzed data has been collected in pp collisions at $\sqrt{s} = 13$ TeV center-of-mass energy
 165 and 25 ns bunch crossing period. The events have been recorded using a combination of single,
 166 double and triple lepton triggers and by triggers based on the presence of two τ_h or a lepton
 167 and a τ_h . Only data-taking periods where all detector systems were fully operational are in-
 168 cluded in the analysis. The integrated luminosity of the analyzed dataset amounts to 35.9 fb^{-1}
 169 in 2016, 41.5 fb^{-1} in 2017 and 59.7 fb^{-1} in 2018, totaling 137.2 fb^{-1} in the full LHC Run 2. Ap-
 170 proximately 30 inelastic pp interactions (pileup) occurred per bunch crossing on average. The
 171 datasets analyzed by different channels are given in Tables 1-3. The data collected in 2016 and
 172 2017 have been reconstructed using CMSSW_9_4_x, while the data collected in 2018 has been
 173 reconstructed using CMSSW_10_2_x. All data is analyzed in CMSSW_10_2_x.

174 Samples of $t\bar{t}H$, tHq and tHW signals and of background events, produced by Monte Carlo
 175 simulation, are used for the purpose of estimating signal and background yields in the analy-
 176 sis and to train machine learning algorithms. The following processes are simulated: Z+jets,
 177 W+jets, single top and top quark pairs, diboson (WW, WZ, ZZ, $W\gamma$ and $Z\gamma$) and triboson
 178 (WWW, WWZ, WZZ, ZZZ and $WZ\gamma$) production, the production of a single H boson by
 179 gluon-gluon fusion (ggF) and by vector-boson fusion (VBF), the associated production of a H
 180 boson with vector bosons (WH and ZH), as well as a few selected “exotic” processes. The exotic
 181 processes, such as $t\bar{t}\bar{t}$ and the production of same-sign WW boson pairs, typically have very
 182 small cross sections, but may nevertheless yield non-negligible background contributions in
 183 some event categories. The simulated events assume a H boson mass of $m_H = 125$ GeV.

184 The samples that are produced from leading-order (LO) matrix elements are generated with
 185 program MADGRAPH5_AMCATHNLO [35]. The implementation of next-to-leading-order (NLO)
 186 matrix elements in the simulation is with MADGRAPH5_AMCATHNLO and POWHEG v2 [36–
 187 38]. Parton shower, hadronization processes and decays of τ leptons, including polarization
 188 effects, are modeled using the generator PYTHIA with the tunes CUETP8M1, CUETP8M2 or
 189 CUETP8M2T4 [39, 40] in 2016 MC samples, and with tune CP5 [41] in 2017 and 2018 MC sam-
 190 ples. The event generator tunes are based on the Monash tune [42]. The samples produced
 191 by PYTHIA with CUETP8M1 tune use the NNPDF2.3LO set of parton distribution functions.
 192 The samples produced by MADGRAPH and POWHEG, or by PYTHIA with CUETP8M2* tune,
 193 use the NNPDF3.0 set. Finally, the samples produced by PYTHIA with CP5 tune use the
 194 NNPDF3.1 set [43–45].

195 In the case of the $t\bar{t}H$, tHq and tHW signal processes, each sample is generated with a set
 196 of event weights corresponding to different values of the Higgs-top and Higgs-W coupling
 197 modifiers. Similarly, there exist event weights which correspond to different values of the CP
 198 phase of the top Yukawa coupling.

199 The Z+jets, W+jets and $t\bar{t}$ +jets events are normalized to cross sections computed at next-to-
 200 next-to-leading-order (NNLO) accuracy [46–49]. The cross sections of single top quark [50–52],
 201 $t\bar{t}W$ and $t\bar{t}Z$ backgrounds, as well as $t\bar{t}H$, tHq and tHW signal processes [9], are computed at
 202 NLO accuracy.

203 The complete list of signal and background samples used in estimating the event yields are
 204 given in Tables 4–12. The list of datasets used in data-driven methods and in the derivation of
 205 associated systematic uncertainties are given in Tables 13–15 and in Tables 49–51. The samples
 206 that are used to train machine learning algorithms are listed in Tables 16–18.

207 Minimum bias events generated with PYTHIA are overlaid on all simulated events, according
 208 to the luminosity profile of the analyzed data and for a pp inelastic cross section of 69.2 mb.

Dataset name	Run-range	Int. luminosity (fb ⁻¹)
/SingleElectron/Run2016B-17Jul2018_ver2-v1/MINIAOD ¹	273150–275376	5.75
/SingleElectron/Run2016C-17Jul2018-v1/MINIAOD ¹	275656–276283	2.57
/SingleElectron/Run2016D-17Jul2018-v1/MINIAOD ¹	276315–276811	4.24
/SingleElectron/Run2016E-17Jul2018-v1/MINIAOD ¹	276831–277420	4.02
/SingleElectron/Run2016F-17Jul2018-v1/MINIAOD ¹	277932–278808	3.10
/SingleElectron/Run2016G-17Jul2018-v1/MINIAOD ¹	278820–280385	7.58
/SingleElectron/Run2016H-17Jul2018-v1/MINIAOD ¹	281613–284044	8.65
/SingleMuon/Run2016B-17Jul2018_ver2-v1/MINIAOD ¹	273150–275376	5.75
/SingleMuon/Run2016C-17Jul2018-v1/MINIAOD ¹	275656–276283	2.57
/SingleMuon/Run2016D-17Jul2018-v1/MINIAOD ¹	276315–276811	4.24
/SingleMuon/Run2016E-17Jul2018-v1/MINIAOD ¹	276831–277420	4.02
/SingleMuon/Run2016F-17Jul2018-v1/MINIAOD ¹	277932–278808	3.10
/SingleMuon/Run2016G-17Jul2018-v1/MINIAOD ¹	278820–280385	7.58
/SingleMuon/Run2016H-17Jul2018-v1/MINIAOD ¹	281613–284044	8.65
/DoubleEG/Run2016B-17Jul2018_ver2-v1/MINIAOD ¹	273150–275376	5.75
/DoubleEG/Run2016C-17Jul2018-v1/MINIAOD ¹	275656–276283	2.57
/DoubleEG/Run2016D-17Jul2018-v1/MINIAOD ¹	276315–276811	4.24
/DoubleEG/Run2016E-17Jul2018-v1/MINIAOD ¹	276831–277420	4.02
/DoubleEG/Run2016F-17Jul2018-v1/MINIAOD ¹	277932–278808	3.10
/DoubleEG/Run2016G-17Jul2018-v1/MINIAOD ¹	278820–280385	7.58
/DoubleEG/Run2016H-17Jul2018-v1/MINIAOD ¹	281613–284044	8.65
/DoubleMuon/Run2016B-17Jul2018_ver2-v1/MINIAOD ¹	273150–275376	5.75
/DoubleMuon/Run2016C-17Jul2018-v1/MINIAOD ¹	275656–276283	2.57
/DoubleMuon/Run2016D-17Jul2018-v1/MINIAOD ¹	276315–276811	4.24
/DoubleMuon/Run2016E-17Jul2018-v1/MINIAOD ¹	276831–277420	4.02
/DoubleMuon/Run2016F-17Jul2018-v1/MINIAOD ¹	277932–278808	3.10
/DoubleMuon/Run2016G-17Jul2018-v1/MINIAOD ¹	278820–280385	7.58
/DoubleMuon/Run2016H-17Jul2018-v1/MINIAOD ¹	281613–284044	8.65
/MuonEG/Run2016B-17Jul2018_ver2-v1/MINIAOD ¹	273150–275376	5.75
/MuonEG/Run2016C-17Jul2018-v1/MINIAOD ¹	275656–276283	2.57
/MuonEG/Run2016D-17Jul2018-v1/MINIAOD ¹	276315–276811	4.24
/MuonEG/Run2016E-17Jul2018-v2/MINIAOD ¹	276831–277420	4.02
/MuonEG/Run2016F-17Jul2018-v1/MINIAOD ¹	277932–278808	3.10
/MuonEG/Run2016G-17Jul2018-v1/MINIAOD ¹	278820–280385	7.57
/MuonEG/Run2016H-17Jul2018-v1/MINIAOD ¹	281613–284044	8.65
/Tau/Run2016B-17Jul2018_ver2-v1/MINIAOD ¹	273150–275376	5.75
/Tau/Run2016C-17Jul2018-v1/MINIAOD ¹	275656–276283	2.57
/Tau/Run2016D-17Jul2018-v1/MINIAOD ¹	276315–276811	4.24
/Tau/Run2016E-17Jul2018-v1/MINIAOD ¹	276831–277420	4.02
/Tau/Run2016F-17Jul2018-v1/MINIAOD ¹	277932–278808	3.10
/Tau/Run2016G-17Jul2018-v1/MINIAOD ¹	278820–280385	7.58
/Tau/Run2016H-17Jul2018-v1/MINIAOD ¹	281613–284044	8.65

¹ Cert_271036-284044_13TeV_23Sep2016ReReco_Collisions16_JSON.txt

Table 1: List of 2016 datasets analyzed by different channels. The JSON file [34] used to apply a good-run selection is indicated with superscripts.

209 All generated events are passed through a detailed simulation of the CMS apparatus, based on
 210 GEANT4 [63], and are reconstructed using the same version of the CMS event reconstruction
 211 software as used for data.

Dataset name	Run-range	Int. luminosity (fb ⁻¹)
/SingleElectron/Run2017B-31Mar2018-v1/MINIAOD ¹	297047-299329	4.79
/SingleElectron/Run2017C-31Mar2018-v1/MINIAOD ¹	299368-302029	9.63
/SingleElectron/Run2017D-31Mar2018-v1/MINIAOD ¹	302030-302663	4.25
/SingleElectron/Run2017E-31Mar2018-v1/MINIAOD ¹	303818-304797	9.31
/SingleElectron/Run2017F-31Mar2018-v1/MINIAOD ¹	305040-306460	13.54
/SingleMuon/Run2017B-31Mar2018-v1/MINIAOD ¹	297047-299329	4.79
/SingleMuon/Run2017C-31Mar2018-v1/MINIAOD ¹	299368-302029	9.63
/SingleMuon/Run2017D-31Mar2018-v1/MINIAOD ¹	302031-302663	4.25
/SingleMuon/Run2017E-31Mar2018-v1/MINIAOD ¹	303824-304797	9.31
/SingleMuon/Run2017F-31Mar2018-v1/MINIAOD ¹	305040-306462	13.54
/DoubleEG/Run2017B-31Mar2018-v1/MINIAOD ¹	297047-299329	4.79
/DoubleEG/Run2017C-31Mar2018-v1/MINIAOD ¹	299368-302029	9.63
/DoubleEG/Run2017D-31Mar2018-v1/MINIAOD ¹	302030-302663	4.25
/DoubleEG/Run2017E-31Mar2018-v1/MINIAOD ¹	303818-304797	9.31
/DoubleEG/Run2017F-31Mar2018-v1/MINIAOD ¹	305040-306460	13.54
/DoubleMuon/Run2017B-31Mar2018-v1/MINIAOD ¹	297047-299329	4.79
/DoubleMuon/Run2017C-31Mar2018-v1/MINIAOD ¹	299368-302029	9.63
/DoubleMuon/Run2017D-31Mar2018-v1/MINIAOD ¹	302031-302663	4.25
/DoubleMuon/Run2017E-31Mar2018-v1/MINIAOD ¹	303824-304797	9.31
/DoubleMuon/Run2017F-31Mar2018-v1/MINIAOD ¹	305040-306462	13.54
/MuonEG/Run2017B-31Mar2018-v1/MINIAOD ¹	297047-299329	4.79
/MuonEG/Run2017C-31Mar2018-v1/MINIAOD ¹	299368-302029	9.63
/MuonEG/Run2017D-31Mar2018-v1/MINIAOD ¹	302031-302663	4.25
/MuonEG/Run2017E-31Mar2018-v1/MINIAOD ¹	303824-304797	9.31
/MuonEG/Run2017F-31Mar2018-v1/MINIAOD ¹	305040-306460	13.54
/Tau/Run2017B-31Mar2018-v1/MINIAOD ¹	297047-299329	4.79
/Tau/Run2017C-31Mar2018-v1/MINIAOD ¹	299368-302029	9.63
/Tau/Run2017D-31Mar2018-v1/MINIAOD ¹	302031-302663	4.25
/Tau/Run2017E-31Mar2018-v1/MINIAOD ¹	303824-304797	9.31
/Tau/Run2017F-31Mar2018-v1/MINIAOD ¹	305040-306460	13.53

¹ Cert_294927-306462_13TeV_EOY2017ReReco_Collisions17_JSON_v1.txt

Table 2: List of 2017 datasets analyzed by different channels. The JSON file [34] used to apply a good-run selection is indicated with superscripts.

3 Particle reconstruction and identification

The information provided by all CMS subdetectors is employed by a particle-flow (PF) algorithm [64–68] to identify and reconstruct individual particles in the event, namely muons, electrons, photons, and charged and neutral hadrons. These particles are then used to reconstruct jets, τ_h candidates and the missing transverse momentum vector, as well as to quantify the isolation of leptons.

Some of the criteria used for particle identification, in particular the isolation of electrons and muons, depend on the choice of a primary collision vertex (PV). In this analysis, the chosen vertex is the one that has the highest sum of the squared transverse momenta of the associated tracks.

3.1 Electrons and muons

The identification of electrons and muons is performed in two stages. In the first stage, basic electron (muon) identification and isolation criteria developed by the EGamma (Muon) POG are applied to separate genuine leptons from jet backgrounds. In the second stage, the leptons originating from decays of W , Z or τ leptons are separated from leptons produced in the

Dataset name	Run-range	Int. luminosity (fb ⁻¹)
/SingleMuon/Run2018A-17Sep2018-v2/MINIAOD ¹	315257-316995	14.03
/SingleMuon/Run2018B-17Sep2018-v1/MINIAOD ¹	317080-319310	7.06
/SingleMuon/Run2018C-17Sep2018-v1/MINIAOD ¹	319337-320065	6.90
/SingleMuon/Run2018D-22Jan2019-v2/MINIAOD ¹	320500-325175	31.74
/EGamma/Run2018A-17Sep2018-v2/MINIAOD ¹	315257-316995	14.03
/EGamma/Run2018B-17Sep2018-v1/MINIAOD ¹	317080-319310	7.06
/EGamma/Run2018C-17Sep2018-v1/MINIAOD ¹	319337-320065	6.90
/EGamma/Run2018D-22Jan2019-v2/MINIAOD ¹	320413-325175	31.74
/DoubleMuon/Run2018A-17Sep2018-v2/MINIAOD ¹	315257-316995	14.03
/DoubleMuon/Run2018B-17Sep2018-v1/MINIAOD ¹	317080-319310	7.06
/DoubleMuon/Run2018C-17Sep2018-v1/MINIAOD ¹	319337-320065	6.90
/DoubleMuon/Run2018D-PromptReco-v2/MINIAOD ¹	320500-325175	31.74
/MuonEG/Run2018A-17Sep2018-v1/MINIAOD ¹	315257-316995	14.03
/MuonEG/Run2018B-17Sep2018-v1/MINIAOD ¹	317080-319310	7.06
/MuonEG/Run2018C-17Sep2018-v1/MINIAOD ¹	319337-320065	6.90
/MuonEG/Run2018D-PromptReco-v2/MINIAOD ¹	320500-325175	31.74
/Tau/Run2018A-17Sep2018-v1/MINIAOD ¹	315257-316995	14.01
/Tau/Run2018B-17Sep2018-v1/MINIAOD ¹	317080-319310	7.06
/Tau/Run2018C-17Sep2018-v1/MINIAOD ¹	319337-320065	6.90
/Tau/Run2018D-PromptReco-v2/MINIAOD ¹	320497-325175	31.74

¹ Cert_314472-325175_13TeV_17SeptEarlyReReco2018ABC_PromptEraD_Collisions18_JSON.txt

Table 3: List of 2018 datasets analyzed by different channels. The JSON file [34] used to apply a good-run selection is indicated with superscripts.

227 decays of charm (c) and bottom (b) quarks, making use of MVA techniques which have been
 228 developed specifically for this analysis. We refer to the former as “prompt” or signal leptons
 229 and to the latter as “non-prompt” or background leptons. Details on both identification steps
 230 are described in the following.

231 3.1.1 Basic electron identification

232 The first step of the electron identification is performed by a multivariate algorithm [69, 70]
 233 based on a BDT [29] which has been trained to discriminate electrons against jets. The training
 234 is performed by the EGamma POG in DY+Jets MC samples with the `xgboost` algorithm, and
 235 is done in separate bins of p_T (5-10 GeV and >10 GeV) and η (inner barrel, outer barrel and
 236 endcap). Two independent discriminants have been trained: one with the three PF isolation
 237 components (tracker, ECAL, HCAL) as input, and the other without. In this analysis we use the
 238 latter one, which is tagged as Fall17noIsoV2. Three working-points (WP) have been defined
 239 based on the BDT output score: WP-loose, WP-90 and WP-80, corresponding to 98%, 90% and
 240 80% signal efficiency respectively. We require the electrons to pass the WP-loose, which has the
 241 highest overall selection efficiency. The BDT cuts associated to this WP, applied in different p_T
 242 and η bins, are given in Ref. [70].

243 In order to remove electron candidates that are due to photon conversions, we require that the
 244 electron track is associated to a hit in each layer of the pixel detector that is crossed by the track,
 245 allowing missing hits in at most one layer.

246 3.1.2 Basic muon identification

247 The first step of the muon identification consists on linking track segments reconstructed in the
 248 silicon tracking detector with those in the muon system [71]. The matching is done outside-in,

Table 4: List of 2016 MC samples used to model the $t\bar{t}H$ and tH signal and different irreducible background processes. The table lists the samples of the processes for which the simulation is used to extract the final yields and shapes. Datasets marked with (#) are used exclusively in $0\ell + 2\tau_h$ and $1\ell + 1\tau_h$ event categories.

Process	Sample name	Cross section [pb]
$t\bar{t}H$	/ttHJetToNonbb_M12.5_13TeV_amcatnlo_FXFX_madspin_pythia8_mWCut_fix/1	2.12×10^{-1} [53, 54]
tHq	/tH_Af_ct_cvcvcp_Hincl_M12.5_TuneCP5_13TeV_madgraph_pythia8/2	5.07×10^{-1} [53, 54]
tHW	/THQ_ct_cvcvcp_Hincl_M12.5_TuneCP5_13TeV_madgraph_pythia8/2	2.31×10^{-2} [55]
$t\bar{t}W$	/THW_ct_cvcvcp_Hincl_M12.5_TuneCP5_13TeV_madgraph_pythia8/2	5.09×10^{-3} [55]
$t\bar{t}Z$	/TTWJetsToLNu_TuneCUETP8M1_13TeV-amcatnlo_FXFX_madspin_pythia8/3	1.96×10^{-1} [9, 56]
$t\bar{t}WW$	/TTW_W_TuneCUETP8M2_T4_13TeV-madgraph_pythia8/4	6.98×10^{-3} [57]
$t\bar{t}Z$	/TTZToLL_M-1to1_0_TuneCUETP8M1_13TeV-madgraphMLM_pythia8/5	4.54×10^{-2} [9, 58]
$t\bar{t} + \gamma + \text{jets}$	/TTZToLLNuNu_M-10_TuneCUETP8M1_13TeV-madgraph_pythia8/3_6	2.07×10^{-1} [9, 58]
WW	/TGGJets_TuneCUETP8M1_13TeV-amcatnlo_FXFX_madspin_pythia8/1_7	4.22 [57]
WW	/WWTo2L2Nu_13TeV-powheg/7	1.02 [57]
WZ	/WWTo2L2Nu_DoubleScattering-13TeV-pythia8/7	1.22×10^1 [55]
WZ	/WpWp_JJ_EMK-QCD_TuneCUETP8M1_13TeV-madgraph_pythia8/2	2.23×10^{-1} [57]
ZZ	/WZTo3LNu_TuneCUETP8M1_13TeV-madgraph_pythia8/7	4.93×-2 [57]
ZZ	/WZTo2L2Q_13TeV_amcatnlo_FXFX_madspin_pythia8/2	4.43 [55]
WW	/ZZTo4L_13TeV_powheg_pythia8/2	5.60 [59]
WW	/ZZTo2L2Q_13TeV_amcatnlo_FXFX_madspin_pythia8/7 (#)	1.26 [55]
WW	/WGToLNuG_TuneCUETP8M1_13TeV-amcatnlo_FXFX_pythia8/3_4_6	5.52 [59]
WW	/ZGTo2LG_TuneCUETP8M1_13TeV-amcatnlo_FXFX_pythia8/4	4.65×10^2 [57]
WW	/WWW_4F_TuneCUETP8M1_13TeV-amcatnlo_FXFX_pythia8/7	1.24×10^2 [57]
WW	/WWZ_TuneCUETP8M1_13TeV-amcatnlo_FXFX_pythia8/7	2.09×10^{-1} [57]
WW	/WZ_Z_TuneCUETP8M1_13TeV-amcatnlo_FXFX_pythia8/7	1.68×10^{-1} [57]
WW	/WZ_Z_TuneCUETP8M1_13TeV-amcatnlo_FXFX_pythia8/7	5.70×10^{-2} [57]
ZZZ	/ZZZ_TuneCUETP8M1_13TeV-amcatnlo_FXFX_pythia8/7	1.47×10^{-2} [57]
$WZ\gamma$	/WZG_TuneCUETP8M1_13TeV-amcatnlo_FXFX_pythia8/2	4.35×10^{-2} [57]
$WZ\gamma$	/tZq_11_4f_13TeV_amcatnlo_FXFX_pythia8/4	7.36×10^{-2} [57]
Single top quark +Z	/tZq_11_4f_PSWeights_13TeV_amcatnlo_FXFX_pythia8/2	8.21×10^{-3} [57]
$t\bar{t}\bar{t}$	/TTT-TuneCUETP8M1_13TeV_amcatnlo_FXFX_pythia8/7	

1 RunIIISummer16MiniAODv3-PUMoriond17_94X_mcRun2-asymptotic_v3_ext1-v2/MINIAODSIM

2 RunIIISummer16MiniAODv3-PUMoriond17_94X_mcRun2-asymptotic_v3-v1/MINIAODSIM

3 RunIIISummer16MiniAODv3-PUMoriond17_94X_mcRun2-asymptotic_v3_ext2-v1/MINIAODSIM

4 RunIIISummer16MiniAODv3-PUMoriond17_94X_mcRun2-asymptotic_v3_ext1-v1/MINIAODSIM

5 RunIIISummer16MiniAODv3-94X_mcRun2-asymptotic_v3-v1/MINIAODSIM

6 RunIIISummer16MiniAODv3-PUMoriond17_94X_mcRun2-asymptotic_v3_ext3-v1/MINIAODSIM

7 RunIIISummer16MiniAODv3-PUMoriond17_94X_mcRun2-asymptotic_v3-v2/MINIAODSIM

Table 5: List of 2017 MC samples used to model the $t\bar{t}H$ and tH signal and different irreducible background processes. The table lists the samples of the processes for which the simulation is used to extract the final yields and shapes. Datasets marked with (\dagger) are used exclusively in $0\ell + 2\tau_h$ and $1\ell + 1\tau_h$ event categories.

Process	Sample name	Cross section [pb]
tH	/ttHJetToNonbb_M1.25.TuneCP5_1.3TeV-madspin-pythia8/1 /TH4f-ctcvcp-TuneCP5_1.3TeVmadgraph-pythia8/2 /THQ-ctcvcp-4f_Hincl_1.3TeVmadgraph-pythia8/2 /THW_ctcvcp_5f_Hincl_1.3TeV madgraph-pythia8/2 /TTWJetsToLNu_TuneCP5_1.3TeV-amcatnloFXFX-madspin-pythia8/3 /TTWJetsToLNu_TuneCP5_PSweights_1.3TeV-amcatnloFXFX-madspin-pythia8/1 /TTWW_TuneCP5_1.3TeV-madgraph-pythia8/4 /TTZToLL_M-1to10.TuneCP5_1.3TeV-amcatnlo-pythia8/3 /TTZToLLNuNu_M-10.TuneCP5_1.3TeV-amcatnlo-pythia8/3 /TTZToLLNuNu_M-10.TuneCP5_PSweights_1.3TeV-amcatnlo-pythia8/2 /TTGJets_TuneCP5_1.3TeV-amcatnloFXFX-madspin-pythia8/15 /TGGJets_leptonDecays_TuneCP5_PSweights_1.3TeV-amcatnlo-pythia8/2 /WWTo2L2Nu_NNPDF31.TuneCP5_1.3TeV-powheg-pythia8/2 /WWTo2L2Nu_NNPDF31.TuneCP5_PSweights_1.3TeV-powheg-pythia8/6 /WWTo2L2Nu_DoubleScattering_1.3TeV-pythia8/3 /WWp_WpJJ_EWK-QCD_TuneCP5_1.3TeV-madgraph-pythia8/2 /WZTo3LNu_TuneCP5_1.3TeV-amcatnloFXFX-pythia8/1 /WZTo2L2Q_1.3TeV_amcatnloFXFX_madspin-pythia8/2 (\dagger) /ZZTo4L_1.3TeV_powheg-pythia8/167 /ZZTo2L2Q_1.3TeV_amcatnloFXFX_madspin-pythia8/2 (\dagger) /WGToLNuG_TuneCP5_1.3TeV-madgraphMLM-pythia8/2 /ZGToLLG_01J_5f_TuneCP5_1.3TeV-amcatnloFXFX-pythia8/8 /WW_4F_TuneCP5_1.3TeV-amcatnlo-pythia8/3 /WWZ_4F_TuneCP5_1.3TeV-amcatnlo-pythia8/3 /WZZ_TuneCP5_1.3TeV-amcatnlo-pythia8/2 /ZZZ_TuneCP5_1.3TeV-amcatnlo-pythia8/3 /WZG_TuneCP5_1.3TeV-amcatnlo-pythia8/2 /tZq_ll_4f_ckm_NLO_TuneCP5_PSweights_1.3TeV-amcatnlo-pythia8/9 /TTTT_TuneCP5_1.3TeV-amcatnlo-pythia8/3 /TTTT_TuneCP5_PSweights_1.3TeV-amcatnlo-pythia8/2	2.12 $\times 10^{-1}$ [53, 54] 5.07 $\times 10^{-1}$ [53, 54] 2.31 $\times 10^{-2}$ [55] 5.09 $\times 10^{-3}$ [55] 1.96 $\times 10^{-1}$ [9, 56] 6.98 $\times 10^{-3}$ [57] 4.54 $\times 10^{-2}$ [9, 58] 2.07 $\times 10^{-1}$ [9, 58] 4.22 [57] 1.02 [57] 1.22 $\times 10^1$ [55] 2.23 $\times 10^{-1}$ [57] 4.93 $\times 10^{-2}$ [57] 4.43 [55] 5.60 [59] 1.26 [55] 5.52 [59] 4.65 $\times 10^2$ [57] 5.56 $\times 10^1$ [57] 2.09 $\times 10^{-1}$ [57] 1.68 $\times 10^{-1}$ [57] 5.70 $\times 10^{-2}$ [57] 1.47 $\times 10^{-2}$ [57] 4.35 $\times 10^{-2}$ [57] 7.36 $\times 10^{-2}$ [57] 8.21 $\times 10^{-3}$ [57]
tHq		
tHW		
tFW		
$t\bar{t}WW$		
$t\bar{t}Z$		
$t\bar{t} + \gamma + \text{jets}$		
WW		
ZZ		
$W\gamma$		
$Z\gamma$		
WWW		
WWZ		
WZZ		
ZZZ		
$WZ\gamma$		
Single top quark + Z		
$t\bar{t}t\bar{t}$		

¹ RunIIIFall17MiniaODv2-PU2017-12Apr2018_new_pmx_94X_mc2017_realistic_v14-v1/MINIAODSIM

² RunIIIFall17MiniaODv2-PU2017-12Apr2018_94X_mc2017_realistic_v14-v1/MINIAODSIM

³ RunIIIFall17MiniaODv2-PU2017-12Apr2018_94X_mc2017_realistic_v14-v2/MINIAODSIM

⁴ RunIIIFall17MiniaODv2-PU2017-12Apr2018_new_pmx_94X_mc2017_realistic_v14_ext1-v1/MINIAODSIM

⁵ RunIIIFall17MiniaODv2-PU2017-12Apr2018_94X_mc2017_realistic_v14_ext1-v2/MINIAODSIM

⁶ RunIIIFall17MiniaODv2-PU2017-12Apr2018_94X_mc2017_realistic_v14_ext1-v1/MINIAODSIM

⁷ RunIIIFall17MiniaODv2-PU2017-12Apr2018_94X_mc2017_realistic_v14_ext2-v1/MINIAODSIM

⁸ RunIIIFall17MiniaODv2-PU2017-12Apr2018_94X_mc2017_realistic_v14-v3/MINIAODSIM

⁹ RunIIIFall17MiniaODv2-PU2017-12Apr2018_new_pmx_94X_mc2017_realistic_v14-v2/MINIAODSIM

Table 6: List of 2018 MC samples used to model the $t\bar{t}H$ and tH signal and different irreducible background processes. The table lists the samples of the processes for which the simulation is used to extract the final yields and shapes. Datasets marked with (\ddagger) are used exclusively in $1\ell + 2\tau_h$ and $1\ell + 1\tau_h$ event categories. Datasets marked with (*) are also used in the training of signal extraction algorithms, where the events are selected based on the divisibility of the event numbers.

Process	Sample name	Cross section [pb]
$t\bar{t}H$	$/t\bar{t}HJetToNonbb_M125_TuneCP5_13TeV-amcatnloFXFX-madspin-pythia8/1$	2.12×10^{-1} [53, 54]
tHq	$/TTH_4f_ctccvcp_TuneCP5_13TeV_madgraph-pythia8/1$	5.07×10^{-1} [53, 54]
tHW	$/THQ_ctccvcp_4f_Hincl_1.3TeV_madgraph-pythia8/1$ (*)	2.31×10^{-2} [55]
$t\bar{t}W$	$/TTWJetsToLNu_TuneCP5_13TeV_amcatnloFXFX-madspin-pythia8/2$	5.09×10^{-3} [55]
$t\bar{t}WW$	$/TTWW_TuneCP5_13TeV-madgraph-pythia8/2$	1.96×10^{-1} [9, 56]
$t\bar{t}Z$	$/TTZToLL_M-1to10_TuneCP5_13TeV-amcatnlo-pythia8/2$	6.98×10^{-3} [57]
$t\bar{t} + \gamma + \text{jets}$	$/TTZToLLNuNu_M-10_TuneCP5_13TeV-amcatnlo-pythia8/2$	4.54×10^{-2} [9, 58]
$\text{Single top quark} + \gamma + \text{jets}$	$/TTGJets_TuneCP5_13TeV-amcatnloFXFX-madspin-pythia8/2$	2.07×10^{-1} [9, 58]
WW	$/WWTo2L2Nu_NNPDF31_TuneCP5_13TeV-powheg-pythia8/1$	4.22 [57]
WZ	$/WWTo2L2Nu_DoubleScattering_TuneCP5_13TeV-pythia8/1$	1.02 [57]
ZZ	$/WpWpJJ_EWK-QCD_TuneCP5_13TeV-madgraph-pythia8/1$	1.22×10^1 [55]
$W\gamma$	$/WZTo3LNu_TuneCP5_13TeV-amcatnloFXFX-pythia8/2$	2.23×10^{-1} [57]
$Z\gamma$	$/WZTo2L2Q_1.3TeV-amcatnloFXFX-madspin-pythia8/1$ (\ddagger)	4.93×-2 [57]
WWW	$/ZZTo4L_TuneCP5_13TeV-powheg_pythia8/2$	4.43 [55]
WWZ	$/ZZTo2L2Q_1.3TeV-amcatnloFXFX-madspin-pythia8/1$ (\ddagger)	5.60 [59]
$WZ\gamma$	$/WGT0LNUG_TuneCP5_13TeV-madgraphMIM-pythia8/1$	1.26 [55]
WZZ	$/ZGToLLG_01J_5f_TuneCP5_13TeV-amcatnloFXFX-pythia8/2$	5.52 [59]
ZZZ	$/WWW_4F_TuneCP5_13TeV-amcatnlo-pythia8/2$	4.65×10^2 [57]
$WZ\gamma$	$/WWZ_TuneCP5_1.3TeV-amcatnlo-pythia8/2$	5.56×10^1 [57]
WZZ	$/WZZ_TuneCP5_1.3TeV-amcatnlo-pythia8/2$	2.09×10^{-1} [57]
ZZZ	$/ZZZ_TuneCP5_1.3TeV-amcatnlo-pythia8/2$	1.68×10^{-1} [57]
$Single top quark + Z$	$/WZG_TuneCP5_1.3TeV-amcatnlo-pythia8/1$	5.70×10^{-2} [57]
$t\bar{t}\bar{t}$	$/tZq_1.1.4f_ckm_NLO_TuneCP5_13TeV-madgraph-pythia8/2$	1.47×10^{-2} [57]
	$/TTT_TuneCP5_1.3TeV-amcatnlo-pythia8/2$	4.35×10^{-2} [57]
		7.36×10^{-2} [57]
		8.21×10^{-3} [57]

¹ Run II Aut umn18MiniAOD-102Xupgrade2018-realistic-v15-v1/MINIAODSIM

² Run II Autumn18MiniAOD-102Xupgrade2018-realistic-v15-ext1-v2/MINIAODSIM

³ Run II Aut umn18MiniAOD-102Xupgrade2018-realistic-v15-ext2-v1/MINIAODSIM

⁴ Run II Aut umn18MiniAOD-102Xupgrade2018-realistic-v15-ext2-v2/MINIAODSIM

Table 7: List of 2016 MC samples used to model irreducible background processes involving Higgs boson.

Process	Sample name	Cross section [pb]
W/Z + H	/VHToNonbb_M125_13TeV_amcatnloFXFX_madspin_pythia8/ ¹ /ZH_HToBB_ZToLL_M125_13TeV_powheg_pythia8/ ² /ZHToTauTau_M125_13TeV_powheg_pythia8/ ¹	9.42×10^{-1} [53, 54] 5.2×10^{-2} [53, 54] 5.54×10^{-2} [53, 54]
ggF H	/GluGluHToTauTau_M125_13TeV_powheg_pythia8/ ³ /GluGluHToZZTo4L_M125_13TeV_powheg2_JHUGenV6_pythia8/ ⁴ /GluGluHToWWToLNuQQ_M125_13TeV_powheg_JHUGenV628_pythia8/ ² /GluGluHToWWTo2L2Nu_M125_13TeV_powheg_JHUGen_pythia8/ ¹ /GluGluHToMuMu_M-125_TuneCP5_PSweights_13TeV_powheg_pythia8/ ⁴ /GluGluHToBB_M125_13TeV_amcatnloFXFX_pythia8/ ^{1,2} /GluGluHToGG_M125_13TeV_amcatnloFXFX_pythia8/ ⁵	3.05 [53, 54] 1.30×10^{-2} [53, 54, 58] 4.56 [53, 54, 56] 1.10 [53, 54, 56] 1.06×10^{-2} [53, 54] 2.83×10^1 [53, 54] 1.10×10^{-1} [53, 54]
VBF H	/VBFHToTauTau_M125_13TeV_powheg_pythia8/ ¹ /VBF_HToZZTo4L_M125_13TeV_powheg2_JHUGenV6_pythia8/ ¹ /VBFHToWWToLNuQQ_M125_13TeV_powheg_JHUGenV628_pythia8/ ² /VBFHToWWTo2L2Nu_M125_13TeV_powheg_JHUGenV628_pythia8/ ¹ /VBFHToMuMu_M-125_TuneCP5_PSweights_13TeV_powheg_pythia8/ ⁴ /VBFHToBB_M-125_13TeV_powheg_pythia8_weightfix/ ^{2,4} /VBFHToGG_M125_13TeV_amcatnlo_pythia8/ ^{5,6}	2.37×10^{-1} [53, 54] 1.01×10^{-3} [53, 54, 58] 3.55×10^{-1} [53, 54, 56] 8.59×10^{-2} [53, 54, 56] 8.23×10^{-4} [53, 54] 2.20 [53, 54] 8.58×10^{-3} [53, 54]
t̄tWH	/TTWH_TuneCUETP8M2T4_13TeV-madgraph-pythia8/ ²	1.58×10^{-3} [9]
t̄tZH	/TTZH_TuneCUETP8M2T4_13TeV-madgraph-pythia8/ ²	1.54×10^{-3} [9]

¹ RunIIISummer16MiniAODv3-PUMoriond17_94X_mcRun2_asymptotic_v3-v2/MINIAODSIM

² RunIIISummer16MiniAODv3-PUMoriond17_94X_mcRun2_asymptotic_v3_ext1-v1/MINIAODSIM

³ RunIIISummer16MiniAODv3-PUMoriond17_94X_mcRun2_asymptotic_v3-v3

⁴ RunIIISummer16MiniAODv3-PUMoriond17_94X_mcRun2_asymptotic_v3-v1/MINIAODSIM

⁵ RunIIISummer16MiniAODv3-PUMoriond17_94X_mcRun2_asymptotic_v3_ext2-v2/MINIAODSIM

⁶ RunIIISummer16MiniAODv3-PUMoriond17_94X_mcRun2_asymptotic_v3_ext1-v2/MINIAODSIM

Table 8: List of 2017 MC samples used to model irreducible background processes involving Higgs boson.

Process	Sample name	Cross section [pb]
W/Z + H	/VHToNonbb_M125.13TeV-amcatnloFXFX_madspin-pythia8/1 /ZH_HToBB_ZToLL_M125.13TeV-powheg-pythia8/2 /ZHToTauTau_M125.13TeV-powheg-pythia8/2	9.42×10^{-1} [53, 54] 5.2×10^{-2} [53, 54] 5.54×10^{-2} [53, 54]
ggF H	/GluGluHToTauTau_M125.13TeV-powheg-pythia8/3 ⁴ /GluGluHToZZTo4L_M125.13TeV-powheg2_JHUGenV7011_pythia8/4 ^{5,6} /GluGluHToZZTo2L2Q_M125.13TeV-powheg2_JHUGenV7011_pythia8/1 /GluGluHToWWToLNuQQ_M125_NNPDF31_TuneCP5_PSwieghts_13TeV-powheg_JHUGen710_pythia8/1 /GluGluHToWWTo2L2Nu_M125.13TeV-powheg2_JHUGenV714_pythia8/2 /GluGluHToMuMu_M-125_TuneCP5_PSwieghts_13TeV-powheg_pythia8/2 ⁴ /GluGluHToBB_M125.13TeV-amcatnloFXFX_pythia8/1 /GluGluHToGG_M125.13TeV-amcatnloFXFX_pythia8/1	3.05 [53, 54] 1.30×10^{-2} [53, 54, 58] 1.80×10^{-1} [53, 54, 58] 4.56 [53, 54, 56] 1.10 [53, 54, 56] 1.06×10^{-2} [53, 54] 2.83×10^1 [53, 54] 1.10×10^{-1} [53, 54]
VBF H	/VBFHToTauTau_M125.13TeV-powheg-pythia8/7 /VBFHToZZTo4L_M125.13TeV-powheg2_JHUGenV7011_pythia8/2 ^{4,8} /VBFHToWWToLNuQQ_M125_NNPDF31_TuneCP5_PSwieghts_13TeV-powheg_JHUGen710_pythia8/2 /VBFHToWWTo2L2Nu_M125.13TeV-powheg2_JHUGenV714_pythia8/2 /VBFHToMuMu_M-125_TuneCP5_PSwieghts_13TeV-powheg_pythia8/2 /VBFHToBB_M-125.13TeV-powheg_pythia8_weightfix/2 /VBFHToGG_M125.13TeV_amcatnlo_pythia8/2 ⁴	2.37×10^{-1} [53, 54] 1.01×10^{-3} [53, 54, 58] 3.55×10^{-1} [53, 54, 56] 8.59×10^{-2} [53, 54, 56] 8.23×10^{-4} [53, 54] 2.20 [53, 54] 8.58×10^{-3} [53, 54]
t̄WH	/TTWH_TuneCP5_13TeV-madgraph-pythia8/7 /TTZH_TuneCP5_13TeV-madgraph-pythia8/7	1.58×10^{-3} [9] 1.54×10^{-3} [9]

- ¹ RunIIIFall17MiniaODv2–PU2017_12Apr2018_94X_mc2017_realistic_v14-v2/MINIAODSIM
² RunIIIFall17MiniaODv2–PU2017_12Apr2018_94X_mc2017_realistic_v14-v1/MINIAODSIM
³ RunIIIFall17MiniaODv2–PU2017_12Apr2018_new_pmx_94X_mc2017_realistic_v14-v2/MINIAODSIM
⁴ RunIIIFall17MiniaODv2–PU2017_12Apr2018_94X_mc2017_realistic_v14_ext1-v1/MINIAODSIM
⁵ RunIIIFall17MiniaODv2–PU2017_12Apr2018_94X_mc2017_realistic_v14_ext3-v1/MINIAODSIM
⁶ RunIIIFall17MiniaODv2–PU2017_12Apr2018_94X_mc2017_realistic_v14_ext4-v1/MINIAODSIM
⁷ RunIIIFall17MiniaODv2–PU2017_12Apr2018_new_pmx_94X_mc2017_realistic_v14-v1/MINIAODSIM
⁸ RunIIIFall17MiniaODv2–PU2017_12Apr2018_94X_mc2017_realistic_v14_ext2-v2/MINIAODSIM

Table 9: List of 2018 MC samples used to model irreducible background processes involving Higgs boson.

Process	Sample name	Cross section [pb]
W/Z + H	/VHToNonbb_M125_13TeV_amcatnloFXFX_madspin_pythia8/ ¹ /ZH_HToBB_ZToLL_M125_13TeV_powheg_pythia8/ ^{1,2} /ZHToTauTau_M125_13TeV_powheg_pythia8/ ¹	9.42×10^{-1} [53, 54] 5.2×10^{-2} [53, 54] 5.54×10^{-2} [53, 54]
ggF H	/GluGluHToTauTau_M125_13TeV_powheg_pythia8/ ¹ /GluGluHToZZTo4L_M125_13TeV_powheg2_JHUGenV7011_pythia8/ ¹ /GluGluHToZZTo2L2Q_M125_13TeV_powheg2_JHUGenV7011_pythia8/ ³ /GluGluHToWWToLNuQQ_M125_13TeV_powheg2_JHUGenV714_pythia8/ ³ /GluGluHToWWTo2L2Nu_M125_13TeV_powheg2_JHUGenV714_pythia8/ ³ /GluGluHToMuMu_M-125_TuneCP5_PSweights_13TeV_powheg_pythia8/ ^{1,2} /GluGluHToBB_M125_13TeV_amcatnloFXFX_pythia8/ ³ /GluGluHToGG_M125_TuneCP5_13TeV_amcatnloFXFX_pythia8/ ³	3.05 [53, 54] 1.30×10^{-2} [53, 54, 58] 1.80×10^{-1} [53, 54, 58] 4.56 [53, 54, 56] 1.10 [53, 54, 56] 1.06×10^{-2} [53, 54] 2.83×10^1 [53, 54] 1.10×10^{-1} [53, 54]
VBF H	/VBFHToTauTau_M125_13TeV_powheg_pythia8/ ² /VBF_HToZZTo4L_M125_13TeV_powheg2_JHUGenV7011_pythia8/ ¹ /VBFHToWWToLNuQQ_M125_13TeV_powheg_JHUGen_pythia8/ ³ /VBFHToWWTo2L2Nu_M125_13TeV_powheg2_JHUGenV714_pythia8/ ³ /VBFHToMuMu_M-125_TuneCP5_PSweights_13TeV_powheg_pythia8/ ³ /VBFHToBB_M-125_13TeV_powheg_pythia8_weightfix/ ³ /VBFHToGG_M125_13TeV_amcatnlo_pythia8/ ³	2.37×10^{-1} [53, 54] 1.01×10^{-3} [53, 54, 58] 3.55×10^{-1} [53, 54, 56] 8.59×10^{-2} [53, 54, 56] 8.23×10^{-4} [53, 54] 2.20 [53, 54] 8.58×10^{-3} [53, 54]
t̄tWH t̄tZH	/TTWH_TuneCP5_13TeV-madgraph_pythia8/ ⁴ /TTZH_TuneCP5_13TeV-madgraph_pythia8/ ⁴	1.58×10^{-3} [9] 1.54×10^{-3} [9]

¹ RunIIAutumn18MiniAOD-102X_upgrade2018_realistic_v15-v2/MINIAODSIM

² RunIIAutumn18MiniAOD-102X_upgrade2018_realistic_v15_ext1-v1/MINIAODSIM

³ RunIIAutumn18MiniAOD-102X_upgrade2018_realistic_v15-v1/MINIAODSIM

⁴ RunIIAutumn18MiniAOD-102X_upgrade2018_realistic_v15_ext1-v2/MINIAODSIM

Table 10: List of 2016 MC samples used to model irreducible background by HH processes.

Process	Sample name	Cross section [pb]
$\text{HH} \rightarrow b\bar{b}\text{WW}$, $\text{WW} \rightarrow \ell\nu\ell\nu$	/GluGluToHHTo2B2VTo2L2Nu_node_SM_13TeV-madgraph-v2/ ¹ /GluGluToHHTo2B2VTo2L2Nu_node_box_13TeV-madgraph-v2/ ¹ /GluGluToHHTo2B2VTo2L2Nu_node_1_13TeV-madgraph-v2/ ¹ /GluGluToHHTo2B2VTo2L2Nu_node_2_13TeV-madgraph-v2/ ² /GluGluToHHTo2B2VTo2L2Nu_node_3_13TeV-madgraph-v2/ ¹ /GluGluToHHTo2B2VTo2L2Nu_node_4_13TeV-madgraph-v2/ ¹ /GluGluToHHTo2B2VTo2L2Nu_node_5_13TeV-madgraph-v2/ ¹ /GluGluToHHTo2B2VTo2L2Nu_node_6_13TeV-madgraph-v2/ ¹ /GluGluToHHTo2B2VTo2L2Nu_node_7_13TeV-madgraph-v2/ ¹ /GluGluToHHTo2B2VTo2L2Nu_node_8_13TeV-madgraph-v2/ ¹ /GluGluToHHTo2B2VTo2L2Nu_node_9_13TeV-madgraph-v2/ ¹ /GluGluToHHTo2B2VTo2L2Nu_node_10_13TeV-madgraph-v2/ ¹ /GluGluToHHTo2B2VTo2L2Nu_node_11_13TeV-madgraph-v2/ ¹ /GluGluToHHTo2B2VTo2L2Nu_node_12_13TeV-madgraph-v2/ ¹	8.20×10^{-4} [53, 58, 60]
$H \rightarrow b\bar{b}\tau\tau$	/GluGluToHHTo2B2Tau_node_SM_13TeV-madgraph/ ¹ /GluGluToHHTo2B2Tau_node_box_13TeV-madgraph/ ¹ /GluGluToHHTo2B2Tau_node_2_13TeV-madgraph/ ¹ /GluGluToHHTo2B2Tau_node_9_13TeV-madgraph/ ¹ /GluGluToHHTo2B2Tau_node_10_13TeV-madgraph/ ¹ /GluGluToHHTo2B2Tau_node_11_13TeV-madgraph/ ¹ /GluGluToHHTo2B2Tau_node_12_13TeV-madgraph/ ¹ /GluGluToHHTo2B2Tau_node_13_13TeV-madgraph/ ³	2.27×10^{-3} [53, 60]
$\text{HH} \rightarrow \tau\tau\tau\tau$	/GluGluToHHTo4Tau_node_SM_13TeV-madgraph/ ¹ /GluGluToHHTo4Tau_node_box_13TeV-madgraph/ ¹ /GluGluToHHTo4Tau_node_2_13TeV-madgraph/ ¹ /GluGluToHHTo4Tau_node_3_13TeV-madgraph/ ¹ /GluGluToHHTo4Tau_node_4_13TeV-madgraph/ ¹ /GluGluToHHTo4Tau_node_5_13TeV-madgraph/ ¹ /GluGluToHHTo4Tau_node_6_13TeV-madgraph/ ¹ /GluGluToHHTo4Tau_node_7_13TeV-madgraph/ ¹ /GluGluToHHTo4Tau_node_8_13TeV-madgraph/ ¹ /GluGluToHHTo4Tau_node_9_13TeV-madgraph/ ¹ /GluGluToHHTo4Tau_node_10_13TeV-madgraph/ ¹ /GluGluToHHTo4Tau_node_11_13TeV-madgraph/ ¹ /GluGluToHHTo4Tau_node_12_13TeV-madgraph/ ¹	1.22×10^{-4} [53, 60]

¹ RunIIISummer16MiniAODv3-PUMoriond17_94X_mcRun2_asymptotic_v3-v2/MINIAODSIM² RunIIISummer16MiniAODv3-PUMoriond17_94X_mcRun2_asymptotic_v3-v3/MINIAODSIM³ RunIIISummer16MiniAODv3-PUMoriond17_94X_mcRun2_asymptotic_v3-v1/MINIAODSIM

Table 11: List of 2017 MC samples used to model irreducible background by HH processes. Here V refers to either W or Z boson.

Process	Sample name	Cross section [pb]
$\text{HH} \rightarrow b\bar{b}WW$, $WW \rightarrow \ell\nu\ell\nu$	/GluGluToHHTo2B2VTo2L2Nu_node_SM_13TeV-madgraph_correctedcfg/¹ /GluGluToHHTo2B2VTo2L2Nu_node_2_13TeV-madgraph_correctedcfg/¹ /GluGluToHHTo2B2VTo2L2Nu_node_3_13TeV-madgraph_correctedcfg/¹ /GluGluToHHTo2B2VTo2L2Nu_node_7_13TeV-madgraph_correctedcfg/¹ /GluGluToHHTo2B2VTo2L2Nu_node_9_13TeV-madgraph_correctedcfg/¹ /GluGluToHHTo2B2VTo2L2Nu_node_12_13TeV-madgraph_correctedcfg/¹	8.20×10^{-4} [53, 58, 60]
$H \rightarrow b\bar{b}\tau\tau$	/GluGluToHHTo2B2Tau_node_SM_13TeV-madgraph_correctedcfg/¹ /GluGluToHHTo2B2Tau_node_2_13TeV-madgraph_correctedcfg/¹ /GluGluToHHTo2B2Tau_node_3_13TeV-madgraph_correctedcfg/¹ /GluGluToHHTo2B2Tau_node_4_13TeV-madgraph_correctedcfg/¹ /GluGluToHHTo2B2Tau_node_7_13TeV-madgraph_correctedcfg/¹ /GluGluToHHTo2B2Tau_node_9_13TeV-madgraph_correctedcfg/¹ /GluGluToHHTo2B2Tau_node_12_13TeV-madgraph_correctedcfg/¹	2.27×10^{-3} [53, 60]
$\text{HH} \rightarrow \tau\tau\tau\tau$	/GluGluToHHTo4Tau_node_SM_13TeV-madgraph_correctedcfg/¹ /GluGluToHHTo4Tau_node_2_13TeV-madgraph_correctedcfg/¹ /GluGluToHHTo4Tau_node_3_13TeV-madgraph_correctedcfg/¹ /GluGluToHHTo4Tau_node_7_13TeV-madgraph_correctedcfg/¹ /GluGluToHHTo4Tau_node_9_13TeV-madgraph_correctedcfg/¹ /GluGluToHHTo4Tau_node_12_13TeV-madgraph_correctedcfg/¹	1.22×10^4 [53, 60]
$\text{HH} \rightarrow \tau\tau VV$	/GluGluToHHTo2V2Tau_node_SM_13TeV-madgraph_correctedcfg/¹ /GluGluToHHTo2V2Tau_node_2_13TeV-madgraph_correctedcfg/¹ /GluGluToHHTo2V2Tau_node_3_13TeV-madgraph_correctedcfg/¹ /GluGluToHHTo2V2Tau_node_4_13TeV-madgraph_correctedcfg/¹ /GluGluToHHTo2V2Tau_node_5_13TeV-madgraph_correctedcfg/¹ /GluGluToHHTo2V2Tau_node_6_13TeV-madgraph_correctedcfg/¹ /GluGluToHHTo2V2Tau_node_7_13TeV-madgraph_correctedcfg/¹ /GluGluToHHTo2V2Tau_node_8_13TeV-madgraph_correctedcfg/¹ /GluGluToHHTo2V2Tau_node_9_13TeV-madgraph_correctedcfg/¹ /GluGluToHHTo2V2Tau_node_10_13TeV-madgraph_correctedcfg/¹ /GluGluToHHTo2V2Tau_node_11_13TeV-madgraph_correctedcfg/¹ /GluGluToHHTo2V2Tau_node_12_13TeV-madgraph_correctedcfg/¹	9.34×10^{-4} [53, 60]
$\text{HH} \rightarrow VVVV$	/GluGluToHHTo4V_node_SM_13TeV-madgraph_correctedcfg/¹ /GluGluToHHTo4V_node_2_13TeV-madgraph_correctedcfg/¹ /GluGluToHHTo4V_node_3_13TeV-madgraph_correctedcfg/¹ /GluGluToHHTo4V_node_4_13TeV-madgraph_correctedcfg/¹ /GluGluToHHTo4V_node_5_13TeV-madgraph_correctedcfg/¹ /GluGluToHHTo4V_node_6_13TeV-madgraph_correctedcfg/¹ /GluGluToHHTo4V_node_7_13TeV-madgraph_correctedcfg/¹ /GluGluToHHTo4V_node_8_13TeV-madgraph_correctedcfg/¹ /GluGluToHHTo4V_node_9_13TeV-madgraph_correctedcfg/¹ /GluGluToHHTo4V_node_10_13TeV-madgraph_correctedcfg/¹ /GluGluToHHTo4V_node_11_13TeV-madgraph_correctedcfg/¹ /GluGluToHHTo4V_node_12_13TeV-madgraph_correctedcfg/¹	1.79×10^{-3} [53, 60]

¹ RunIIFall17MiniAODv2-PU2017_12Apr2018_94X_mc2017_realistic_v14-v1/MINIAODSIM

Table 12: List of 2018 MC samples used to model irreducible background by HH processes.

Process	Sample name	Cross section [pb]
$\text{HH} \rightarrow \tau\tau\tau\tau$	/GluGluToHHTo2B2Tau_node_SM_TuneCP5_PSWeights_13TeV ¹ /GluGluToHHTo2B2Tau_node_2_TuneCP5_PSWeights_13TeV ¹ /GluGluToHHTo2B2Tau_node_3_TuneCP5_PSWeights_13TeV ¹ /GluGluToHHTo2B2Tau_node_4_TuneCP5_PSWeights_13TeV ¹ /GluGluToHHTo2B2Tau_node_5_TuneCP5_PSWeights_13TeV ¹ /GluGluToHHTo2B2Tau_node_6_TuneCP5_PSWeights_13TeV ¹ /GluGluToHHTo2B2Tau_node_7_TuneCP5_PSWeights_13TeV ¹ /GluGluToHHTo2B2Tau_node_8_TuneCP5_PSWeights_13TeV ¹ /GluGluToHHTo2B2Tau_node_9_TuneCP5_PSWeights_13TeV ¹ /GluGluToHHTo2B2Tau_node_10_TuneCP5_PSWeights_13TeV ¹ /GluGluToHHTo2B2Tau_node_11_TuneCP5_PSWeights_13TeV ¹ /GluGluToHHTo2B2Tau_node_12_TuneCP5_PSWeights_13TeV ¹	1.22×10^{-4} [53, 60]

¹ `_madgraph-pythia8/RunIIAutumn18MiniAOD-102X_upgrade2018_realistic_v15-v1/MINIAODSIM`

249 starting from a track in the muon system, as well as inside-out, starting from a track recon-
 250 structed in the inner detector. In the case where a link can be established, the track parameters
 251 are refitted using the combination of hits in the inner and outer detectors and the track is re-
 252 ferred to as global muon track. Quality cuts are applied on the multiplicity of hits, on the
 253 number of matched segments and on the quality of the global muon track fit, quantified by χ^2 .
 254 The muon candidates used in the analysis are required to pass the loose PF muon identification
 255 criteria [72] provided by the Muon POG, which is designed to be highly efficient for prompt
 256 muons.

257 3.1.3 Electron and muon isolation

258 Electrons and muons in signal events are expected to be isolated, while leptons from c and
 259 b quark decays, as well as from in-flight decays of pions and kaons, are often reconstructed
 260 within jets. Isolated leptons are distinguished from leptons in jets by means of the sum of scalar
 261 p_T values of charged particles, neutral hadrons and photons that are reconstructed within a
 262 narrow cone centered on the lepton direction. The size R of the cone shrinks inversely propor-
 263 tional with the p_T of the lepton in order to increase the efficiency for leptons reconstructed in
 264 events with “boosted” topologies and/or high hadronic activity to pass the isolation criteria.
 265 The narrow cone size, referred to as “mini isolation”, has the added advantage that it reduces
 266 the effect of pileup (PU). Efficiency loss due to PU is further suppressed by considering only
 267 charged particles originating from the lepton production vertex in the isolation sum. Resid-
 268 ual contributions of PU to the neutral component of the isolation of the lepton are taken into
 269 account by means of so-called effective area corrections:

$$I_\ell = \sum_{\text{charged}} p_T + \max \left(0, \sum_{\text{neutrals}} p_T - \rho \mathcal{A} \left(\frac{R}{0.3} \right)^2 \right), \quad (1)$$

270 where ρ represents the energy density of neutral particles reconstructed within the geometric
 271 acceptance of the tracking detectors (`fixedGridRhoFastjetAll`), computed as described in
 272 Refs. [73, 74]. The size of the cone is given by:

Table 13: List of 2016 MC samples used to design the data driven methods and derive the associated systematics. The samples listed in the table are also used to estimate irreducible contribution to the signal region of $0\ell + 2\tau_h$ and $1\ell + 1\tau_h$ event categories.

Process	Sample name	Cross section [pb]
$t\bar{t}$ -jets	/TTJets_DiLept_TuneCUETP8M1_13TeV-madgraphMLM-pythia8/12	8.84×10^1 [56, 61]
	/TTJets_SingleLeptFromT_TuneCUETP8M1_13TeV-madgraphMLM-pythia8/12	1.83×10^2 [56, 61]
$Z/\gamma^* \rightarrow \ell\ell$	/DYJetsToLL_M-10to50_TuneCUETP8M1_13TeV-madgraphMLM-pythia8/2	1.86×10^4 [48]
	/DYJetsToLL_M-50_TuneCUETP8M1_13TeV-amcatnloFXFX-pythia8/3	6.08×10^3 [62]
W+jets	/WJetsToLNu_TuneCUETP8M1_13TeV-madgraphMLM-pythia8/24	6.15×10^4 [48]
Single top quark	/ST_s-channel_1_4f_leptonDecays_13TeV_PSwights-amcatnlo-pythia8/5	3.36 [56]
	/ST_s-channel_1_4f_leptonDecays_13TeV_PSwights-amcatnlo-pythia8/5	
	/ST_t-channel_1_top_4f_inclusiveDecays_13TeV_powhegV2-madspin-pythia8-TuneCUETP8M1/5	1.36×10^2 [56]
	/ST_t-channel_1_antitop_4f_inclusiveDecays_13TeV_powhegV2-madspin-pythia8-TuneCUETP8M1/5	8.10×10^1 [56]
	/ST_t-channel_1_antitop_4f_inclusiveDecays_13TeV_PSwights-powhegV2-madspin/5	
	/ST_tW_top_5f_inclusiveDecays_13TeV_powheg-pythia8-TuneCUETP8M1/6	3.58×10^1 [56]
	/ST_tW_antitop_5f_inclusiveDecays_13TeV_powheg-pythia8-TuneCUETP8M1/6	3.58×10^1 [56]
	/ST_tW11_5f_LO_13TeV_MadGraph-pythia8/5	1.10×10^{-2} [57]

¹ RunIIISummer16MiniAODv3-PUMoriond17_94X_mcRun2_asymptotic_v3_ext1-v2/MINIAODSIM

² RunIIISummer16MiniAODv3-PUMoriond17_94X_mcRun2_asymptotic_v3-v2/MINIAODSIM

³ RunIIISummer16MiniAODv3-PUMoriond17_94X_mcRun2_asymptotic_v3_ext2-v1/MINIAODSIM

⁴ RunIIISummer16MiniAODv3-PUMoriond17_94X_mcRun2_asymptotic_v3_ext2-v2/MINIAODSIM

⁵ RunIIISummer16MiniAODv3-PUMoriond17_94X_mcRun2_asymptotic_v3-v1/MINIAODSIM

⁶ RunIIISummer16MiniAODv3-PUMoriond17_94X_mcRun2_asymptotic_v3_ext1-v1/MINIAODSIM

Table 14: List of 2017 MC samples used to design the data driven methods and derive the associated systematics. The samples listed in the table are also used to estimate irreducible contribution to the signal region of $0\ell + 2\tau_h$ and $1\ell + 1\tau_h$ event categories.

Process	Sample name	Cross section [pb]
$t\bar{t}$ +jets	/TTJets.Dilept.TuneCP5_13TeV-madgraphMLM-pythia8/ ¹	8.84×10^1 [56, 61]
	/TTJets.SingleLeptFromT.TuneCP5_13TeV-madgraphMLM-pythia8/ ¹	1.83×10^2 [56, 61]
$Z/\gamma^* \rightarrow \ell\ell$	/DYJetsToLL_M-10to50.TuneCP5_13TeV-madgraphMLM-pythia8/ ^{1,2}	1.86×10^4 [48]
	/DYJetsToLL_M-50.TuneCP5_13TeV-amcatnloFXFX-pythia8/ ^{3,4}	6.08×10^3 [62]
W+jets	/WJetsToLNu.TuneCP5_13TeV-madgraphMLM-pythia8/ ^{2,5}	6.15×10^4 [48]
Single top quark	/ST-s-channel-4f_leptonDecays-TuneCP5_13TeV-amcatnlo-pythia8/ ⁶	3.36 [56]
	/ST-s-channel-4f_leptonDecays-TuneCP5_PSweights-13TeV-amcatnlo-pythia8/ ³	
	/ST-t-channel-top-4f_inclusiveDecays.TuneCP5_13TeV-powhegV2-madspin-pythia8/ ³	
	/ST-t-channel-top-4f_inclusiveDecays.TuneCP5_PSweights_13TeV-powheg-pythia8/ ¹	
	/ST-t-channelAntitop-4f_inclusiveDecays.TuneCP5_13TeV-powhegV2-madspin-pythia8/ ⁶	
	/ST-t-channelAntitop-4f_InclusiveDecays.TuneCP5_PSweights_13TeV-powheg-pythia8/ ¹	
	/ST-tW_top-5f_inclusiveDecays.TuneCP5_13TeV-powheg-pythia8/ ⁶	1.36×10^2 [56]
	/ST-tW_top-5f_inclusiveDecays.TuneCP5_PSweights_13TeV-powheg-pythia8/ ³	
	/ST-tw_Wantitop-5f_inclusiveDecays.TuneCP5_13TeV-powheg-pythia8/ ⁶	8.10×10^1 [56]
	/ST-tw_Wantitop-5f_inclusiveDecays.TuneCP5_PSweights_13TeV-powheg-pythia8/ ⁶	3.58×10^1 [56]
	/ST_tw_ll_5f_LO_TuneCP5_PSweights_13TeV-madgraph-pythia8/ ⁷	3.58×10^1 [56]
		1.10×10^{-2} [57]

¹ RunIIFall17MiniaODv2–PU2017_12Apr2018_94X_mc2017_realistic_v14-v1/MINIAODSIM

² RunIIFall17MiniaODv2–PU2017_12Apr2018_94X_mc2017_realistic_v14-ext1-v2/MINIAODSIM

³ RunIIFall17MiniaODv2–PU2017_12Apr2018_new-pmx_94X_mc2017_realistic_v14-v1/MINIAODSIM

⁴ RunIIFall17MiniaODv2–PU2017_12Apr2018_new-pmx_94X_mc2017_realistic_v14-ext1-v1/MINIAODSIM

⁵ RunIIFall17MiniaODv2–PU2017_12Apr2018_94X_mc2017_realistic_v14-v3/MINIAODSIM

⁶ RunIIFall17MiniaODv2–PU2017_12Apr2018_94X_mc2017_realistic_v14-v2/MINIAODSIM

⁷ RunIIFall17MiniaODv2–PU2017_12Apr2018_94X_mc2017_realistic_v14_ext1-v1/MINIAODSIM

Table 15: List of 2018 MC samples used to design the data driven methods and derive the associated systematics. The samples listed in the table are also used to estimate irreducible contribution to the signal region of $0\ell + 2\tau_h$ and $1\ell + 1\tau_h$ event categories.

Process	Sample name	Cross section [pb]
$t\bar{t}$ +jets	/TTJets.Dilept_TuneCP5_13TeV-madgraphMLM-pythia8/ ¹ /TTJets.SingleLeptFromT_TuneCP5_13TeV-madgraphMLM-pythia8/ /TTJets.SingleLeptFromBar_TuneCP5_13TeV-madgraphMLM-pythia8/ /DYJetsToLL_M-10to50_TuneCP5_13TeV-madgraphMLM-pythia8/ /DYJetsToLL_M-50_TuneCP5_13TeV-madgraphMLM-pythia8/ /WJetsToLNu_TuneCP5_13TeV-madgraphMLM-pythia8/ /ST_s-channel_4f_leptonDecays_TuneCP5_13TeV-madgraph-pythia8/ /ST_t-channel_top_4f_InclusiveDecays_TuneCP5_13TeV-powheg-madspin-pythia8/ /ST_t-channel_antitop_4f_InclusiveDecays_TuneCP5_13TeV-powheg-madspin-pythia8/ /ST_tW_top_5f_InclusiveDecays_TuneCP5_13TeV-powheg-pythia8/ /ST_tW_antitop_5f_InclusiveDecays_TuneCP5_13TeV-powheg-pythia8/ /ST_tw11_5f_ILO_TuneCP5_PSweights_13TeV-madgraph-pythia8/ ⁵	8.84×10^{-1} [56, 61] 1.83×10^2 [56, 61] 1.86×10^4 [48] 6.08×10^3 [62] 6.15×10^4 [48] 3.36 [56] 1.36×10^2 [56] 8.10×10^1 [56] 3.58×10^1 [56] 3.58×10^1 [56] 1.10×10^{-2} [57]

¹ RunIIIAutumn18MiniAOD-102X_upgrade2018_realistic_v15-v1/MINIAODSIM

² RunIIIAutumn18MiniAOD-102X_upgrade2018_realistic_v15-v2/MINIAODSIM

³ RunIIIAutumn18MiniAOD-102X_upgrade2018_realistic_v15-ext2-v1/MINIAODSIM

⁴ RunIIIAutumn18MiniAOD-102X_upgrade2018_realistic_v15_ext1-v4/MINIAODSIM

⁵ RunIIIAutumn18MiniAOD-102X_upgrade2018_realistic_v15_ext1-v1/MINIAODSIM

Table 16: List of 2016 MC samples used to train signal extraction methods. The samples listed in the first section are used to train the signal extraction methods in all event categories, while the samples listed in the second section are used to train these methods only in $0\ell + 2\tau_h$ and $1\ell + 1\tau_h$ event categories. Samples marked with (\ddagger) are used to estimate irreducible contribution to the signal regions of $0\ell + 2\tau_h$ and $1\ell + 1\tau_h$ event categories.

Process	Sample name	Cross section [pb]
tH	/ttHToNonbb_M125_TuneCUETP8M2_ttHrechne3_13TeV-powheg-pythia8/ ¹	2.12×10^{-1} [53, 54]
tHq	/THQ_Hincl_13TeV-madgraph-pythia8_TuneCUETP8M1/ ¹	2.31×10^{-2} [55]
	/THQ_ctcvcp_Hincl_13TeV-madgraph-pythia8_TuneCUETP8M1/ ¹	
tHW	/THW_Hincl_13TeV-madgraph-pythia8_TuneCUETP8M1/ ¹	5.09×10^{-3} [55]
	/THW_ctcvcp_Hincl_13TeV-madgraph-pythia8_TuneCUETP8M1/ ¹	
tW	/ttWJets_13TeV_madgraphMLM/ ²	6.01×10^{-1} [9]
tZ	/ttZJets_13TeV_madgraphMLM-pythia8/ ³	8.39×10^{-1} [9]
t+jets	/TTTo2L2Nu_TuneCP5_PSweights_13TeV-powheg-pythia8/ ³ (\ddagger)	8.84×10^1 [58, 61]
	/TTToSemiLeptonic_TuneCP5_PSweights_13TeV-powheg-pythia8/ ³ (\ddagger)	3.66×10^2 [58, 61]
	/TTToHadronic_TuneCP5_PSweights_13TeV-powheg-pythia8/ ³ (\ddagger)	3.78×10^2 [58, 61]
Z/ γ^* + jets	/DYJetsToLL_M-50 [†] / ^{4,5}	6.08×10^3 [62]
	/DYJetsToLL_M-10to50 [†] / ¹	1.86×10^4 [48]
	/DY1JetsToLL_M-10to50 [†] / ¹	8.60×10^2 [48, 57]
	/DY2JetsToLL_M-10to50 [†] / ¹	4.55×10^2 [48, 57]
	/DY3JetsToLL_M-10to50 [†] / ¹	1.12×10^2 [48, 57]
	/DY4JetsToLL_M-10to50 [†] / ¹	4.31×10^1 [48, 57]
	/DYJetsToLL_M-5to50_HT-100to200 [†] / ^{1,4}	2.63×10^2 [48, 57]
	/DYJetsToLL_M-5to50_HT-200to400 [†] / ^{1,4}	4.45×10^1 [48, 57]
	/DYJetsToLL_M-5to50_HT-400to600 [†] / ^{1,4}	4.28 [48, 57]
	/DYJetsToLL_M-5to50_HT-600toInf [†] / ^{1,4}	1.29 [48, 57]
	/DY1JetsToLL_M-50 [†] / ³	9.99×10^2 [57, 62]
	/DY2JetsToLL_M-50 [†] / ¹	3.49×10^2 [57, 62]
	/DY3JetsToLL_M-50 [†] / ¹	1.28×10^2 [57, 62]
	/DY4JetsToLL_M-50 [†] / ¹	5.04×10^1 [57, 62]
	/DYJetsToLL_M-50_HT-100to200 [†] / ^{1,4}	1.84×10^2 [57, 62]
	/DYJetsToLL_M-50_HT-200to400 [†] / ^{1,4}	5.54×10^1 [57, 62]
	/DYJetsToLL_M-50_HT-400to600 [†] / ^{1,4}	7.96 [57, 62]
	/DYJetsToLL_M-50_HT-600to800 [†] / ¹	2.09 [57, 62]
	/DYJetsToLL_M-50_HT-800to1200 [†] / ³	9.24×10^{-1} [57, 62]
	/DYJetsToLL_M-50_HT-1200to2500 [†] / ³	2.21×10^{-1} [57, 62]
	/DYJetsToLL_M-50_HT-2500toInf [†] / ³	4.01×10^{-3} [57, 62]

[†] _TuneCUETP8M1_13TeV-madgraphMLM-pythia8

¹ RunIIISummer16MiniAODv3-PUMoriond17_94X_mcRun2_asymptotic_v3-v2/MINIAODSIM

² RunIIISummer16MiniAODv3-94X_mcRun2_asymptotic_v3-v1/MINIAODSIM

³ RunIIISummer16MiniAODv3-PUMoriond17_94X_mcRun2_asymptotic_v3-v1/MINIAODSIM

⁴ RunIIISummer16MiniAODv3-PUMoriond17_94X_mcRun2_asymptotic_v3_ext1-v2/MINIAODSIM

⁵ RunIIISummer16MiniAODv3-PUMoriond17_94X_mcRun2_asymptotic_v3_ext2-v2/MINIAODSIM

Table 17: List of 2017 MC samples used to train signal extraction methods. The samples listed in the first section are used to train the signal extraction methods in all event categories, while the samples listed in the second section are used to train these methods only in $0\ell + 2\tau_h$ and $1\ell + 1\tau_h$ event categories. Samples marked with (‡) are used to estimate irreducible contribution to the signal regions of $0\ell + 2\tau_h$ and $1\ell + 1\tau_h$ event categories.

Process	Sample name	Cross section [pb]
tH	/ttHToNonbb_M125_TuneCP5_13TeV-powheg-pythia8/ ^{1,2}	2.12×10^{-1} [53, 54]
tW	/ttWJets_TuneCP5_13TeV_madgraphMLM_pythia8/ ^{2,3}	6.01×10^{-1} [9]
tZ	/ttZJets_TuneCP5_13TeV_madgraphMLM_pythia8/ ^{3,4}	8.39×10^{-1} [9]
t+jets	/TTTo2L2Nu_TuneCP5_13TeV-powheg-pythia8/ ¹ (‡) /TTTo2L2Nu_TuneCP5_PSweights_13TeV-powheg-pythia8/ ⁵ (‡) /TTToSemiLeptonic_TuneCP5_13TeV-powheg-pythia8/ ¹ (‡) /TTToSemiLeptonic_TuneCP5_PSweights_13TeV-powheg-pythia8/ ⁶ (‡) /TTToHadronic_TuneCP5_13TeV-powheg-pythia8/ ⁵ (‡) /TTToHadronic_TuneCP5_PSweights_13TeV-powheg-pythia8/ ¹ (‡)	8.84×10^1 [58, 61] 3.66×10^2 [58, 61] 3.78×10^2 [58, 61]
Z/ γ^* + jets	/DYJetsToLL_M-50/ ^{7,8} /DYJetsToLL_M-10to50/ ^{2,3} /DYJetsToLL_M-4to50_HT-100to200/ ^{5,9} /DYJetsToLL_M-4to50_HT-200to400/ ^{1,9} /DYJetsToLL_M-4to50_HT-400to600/ ^{3,9} /DYJetsToLL_M-4to50_HT-600toInf/ ^{3,9} /DY1JetsToLL_M-50/ ^{1,9} /DY2JetsToLL_M-50/ ^{3,10} /DY3JetsToLL_M-50/ ^{3,10} /DY4JetsToLL_M-50/ ¹¹ /DYJetsToLL_M-50_HT-70to100/ ³ /DYJetsToLL_M-50_HT-100to200/ ^{5,9} /DYJetsToLL_M-50_HT-200to400/ ^{6,9} /DYJetsToLL_M-50_HT-400to600/ ^{5,9} /DYJetsToLL_M-50_HT-600to800/ ⁵ /DYJetsToLL_M-50_HT-800to1200/ ⁵ /DYJetsToLL_M-50_HT-1200to2500/ ³ /DYJetsToLL_M-50_HT-2500toInf/ ⁵	6.08×10^3 [62] 1.86×10^4 [48] 2.39×10^2 [48, 57] 6.37×10^1 [48, 57] 6.73 [48, 57] 2.17×10^1 [48, 57] 9.99×10^2 [48, 57] 3.49×10^2 [48, 57] 1.28×10^2 [48, 57] 5.04×10^1 [48, 57] 1.67×10^2 [57, 62] 1.84×10^2 [57, 62] 5.54×10^1 [57, 62] 7.96 [57, 62] 2.00 [57, 62] 9.24×10^{-1} [57, 62] 2.20×10^{-1} [57, 62] 4.01×10^{-3} [57, 62]

[†] _TuneCP5_13TeV-madgraphMLM-pythia8

¹ RunIIFall17MiniAODv2-PU2017_12Apr2018_new_pmx_94X_mc2017_realistic_v14-v1/MINIAODSIM

² RunIIFall17MiniAODv2-PU2017_12Apr2018_94X_mc2017_realistic_v14_ext1-v2/MINIAODSIM

³ RunIIFall17MiniAODv2-PU2017_12Apr2018_94X_mc2017_realistic_v14-v1/MINIAODSIM

⁴ RunIIFall17MiniAODv2-PU2017_12Apr2018_94X_mc2017_realistic_v14_ext1-v3/MINIAODSIM

⁵ RunIIFall17MiniAODv2-PU2017_12Apr2018_new_pmx_94X_mc2017_realistic_v14-v2/MINIAODSIM

⁶ RunIIFall17MiniAODv2-PU2017_12Apr2018_94X_mc2017_realistic_v14-v2/MINIAODSIM

⁷ RunIIFall17MiniAODv2-PU2017RECOSIMstep_12Apr2018_94X_mc2017_realistic_v14-v1/MINIAODSIM

⁸ RunIIFall17MiniAODv2-PU2017RECOSIMstep_12Apr2018_94X_mc2017_realistic_v14_ext1-v1/MINIAODSIM

⁹ RunIIFall17MiniAODv2-PU2017_12Apr2018_94X_mc2017_realistic_v14_ext1-v1/MINIAODSIM

¹⁰ RunIIFall17MiniAODv2-PU2017_12Apr2018_new_pmx_94X_mc2017_realistic_v14_ext1-v2/MINIAODSIM

¹¹ RunIIFall17MiniAODv2-PU2017_12Apr2018_v2_94X_mc2017_realistic_v14-v2/MINIAODSIM

Table 18: List of 2018 MC samples used to train signal extraction methods. The samples listed in the first section are used to train the signal extraction methods in all event categories, while the samples listed in the second section are used to train these methods only in $0\ell + 2\tau_h$ and $1\ell + 1\tau_h$ event categories. Samples marked with (\ddagger) are used to estimate irreducible contribution to the signal regions of $0\ell + 2\tau_h$ and $1\ell + 1\tau_h$ event categories. Datasets marked with $(^*)$ are also used in the signal extraction, where the events are selected based on the divisibility of the event numbers.

Process	Sample name	Cross section [pb]
tH	/ttHToNonbb_M125_TuneCP5_13TeV-powheg-pythia8/ ¹	2.12×10^{-1} [53, 54]
tHQ	/THQ_ctcvcp_4f_Hincl_13TeV_madgraph_pythia8/ ² (*)	2.31×10^{-2} [55]
tHW	/THW_ctcvcp_5f_Hincl_13TeV_madgraph_pythia8/ ² (*)	5.09×10^{-3} [55]
tW	/ttWJets_TuneCP5_13TeV_madgraphMLM_pythia8/ ³	6.01×10^{-1} [9]
tZ	/ttZJets_TuneCP5_13TeV_madgraphMLM_pythia8/ ³	8.39×10^{-1} [9]
t+jets	/TTTo2L2Nu_TuneCP5_13TeV-powheg-pythia8/ ² (\ddagger)	8.84×10^1 [58, 61]
	/TTToSemiLeptonic_TuneCP5_13TeV-powheg-pythia8/ ² (\ddagger)	3.66×10^2 [58, 61]
	/TTToHadronic_TuneCP5_13TeV-powheg-pythia8/ ² (\ddagger)	3.78×10^2 [58, 61]
Z/ γ^* + jets	/DYJetsToLL_M-50 [†] / ² /DYJetsToLL_M-10to50 [†] / ¹ /DYJetsToLL_M-4to50_HT-70to100 [†] / ² /DYJetsToLL_M-4to50_HT-100to200 [†] / ² /DYJetsToLL_M-4to50_HT-200to400 [†] / ² /DYJetsToLL_M-4to50_HT-400to600 [†] / ² /DYJetsToLL_M-4to50_HT-600toInf [†] / ² /DY1JetsToLL_M-50 [†] / ¹ /DY2JetsToLL_M-50 [†] / ¹ /DY3JetsToLL_M-50 [†] / ¹ /DY4JetsToLL_M-50 [†] / ² /DYJetsToLL_M-50_HT-70to100 [†] / ² /DYJetsToLL_M-50_HT-100to200 [†] / ¹ /DYJetsToLL_M-50_HT-200to400 [†] / ¹ /DYJetsToLL_M-50_HT-400to600 [†] / ⁴⁵ /DYJetsToLL_M-50_HT-600to800 [†] / ¹ /DYJetsToLL_M-50_HT-800to1200 [†] / ¹ /DYJetsToLL_M-50_HT-1200to2500 [†] / ¹ /DYJetsToLL_M-50_HT-2500toInf [†] / ¹	6.08×10^3 [62] 1.86×10^4 [48] 1.72×10^2 [48, 57] 2.39×10^2 [48, 57] 6.37×10^1 [48, 57] 6.73 [48, 57] 2.17 [48, 57] 9.99×10^2 [57, 62] 3.49×10^2 [57, 62] 1.28×10^2 [57, 62] 5.04×10^1 [57, 62] 1.67×10^2 [57, 62] 1.84×10^2 [57, 62] 5.54×10^1 [57, 62] 7.96 [57, 62] 2.00 [57, 62] 9.24×10^{-1} [57, 62] 2.20×10^{-1} [57, 62] 4.01×10^{-3} [57, 62]

[†] _TuneCP5_13TeV-madgraphMLM-pythia8

[‡] _TuneCP5_ESweights_13TeV-madgraphMLM-pythia8

¹ RunIIAutumn18MiniAOD-102X_upgrade2018_realistic_v15-v2/MINIAODSIM

² RunIIAutumn18MiniAOD-102X_upgrade2018_realistic_v15-v1/MINIAODSIM

³ RunIIAutumn18MiniAOD-102X_upgrade2018_realistic_v15_ext1-v2/MINIAODSIM

⁴ RunIIAutumn18MiniAOD-102X_upgrade2018_realistic_v15-v7/MINIAODSIM

⁵ RunIIAutumn18MiniAOD-102X_upgrade2018_realistic_v15_ext2-v3/MINIAODSIM

$$R = \begin{cases} 0.05 & \text{if } p_T > 200 \text{ GeV} \\ 10 \text{ GeV}/p_T & \text{if } 50 < p_T < 200 \text{ GeV} \\ 0.20 & \text{if } p_T < 50 \text{ GeV} \end{cases}. \quad (2)$$

273 The effective area \mathcal{A} is obtained from the simulation by studying the correlation between I_ℓ and
 274 ρ , and is determined in bins of η separately for electrons and muons. The optimal values of the
 275 effective areas for the three years of data-taking are given in Table 19.

Electrons		
Pseudorapidity range	\mathcal{A}	
	2016	2017/2018
$0.0 \leq \eta < 1.0$	0.1752	0.1440
$1.0 \leq \eta < 1.479$	0.1862	0.1562
$1.479 \leq \eta < 2.0$	0.1411	0.1032
$2.0 \leq \eta < 2.2$	0.1534	0.0859
$2.2 \leq \eta < 2.3$	0.1903	0.1116
$2.3 \leq \eta < 2.4$	0.2243	0.1321
$2.4 \leq \eta \leq 2.5$	0.2687	0.1321

Muons		
Pseudorapidity range	\mathcal{A}	
	2016	2017/2018
$0.0 \leq \eta < 0.8$	0.0735	0.0566
$0.8 \leq \eta < 1.3$	0.0619	0.0562
$1.3 \leq \eta < 2.0$	0.0465	0.0363
$2.0 \leq \eta < 2.2$	0.0433	0.0119
$2.2 \leq \eta \leq 2.5$	0.0577	0.0064

Table 19: Effective areas \mathcal{A} used for the computation of electron (top) and muon (bottom) isolations.

276 3.1.4 Separation of prompt from non-prompt electrons and muons

277 The final separation of prompt leptons from non-prompt and fake leptons is performed with
 278 a BDT-based algorithm [75, 76] developed in this analysis. The algorithm has been improved
 279 with respect to previous iterations of the analysis, mainly introducing the latest improvements
 280 in object identification to the input variables, as well as implementing an enhanced training
 281 strategy making use of larger datasets.

282 The input variables considered for this discriminator concern the lepton kinematics, the lepton
 283 isolation, properties of the lepton’s nearest jet, the event impact parameters and basic lepton
 284 identification criteria. When computing the properties of the lepton’s nearest jet we consider
 285 the jets which are matched to the lepton, meaning that both objects share one of the PF candi-
 286 dates out of which they are composed. On top of that, a lower jet p_T threshold of 15 GeV is
 287 used for the matching.

288 The input variables used for the training are:

- 289 • Lepton p_T and $|\eta|$
- 290 • Lepton charged mini-isolation (`miniRelIsoCharged`): the isolation of the lepton
 291 with respect to charged particles, defined as $I_\ell^{\text{charged}} = \sum_{\text{charged}} p_T$.

- Lepton neutral mini-isolation (`miniRelIsoNeutral`): the isolation of the lepton with respect to neutral particles, corrected for PU effects, defined as:

$$I_\ell^{\text{neutrals}} = \max\left(0, \sum_{\text{neutrals}} p_T - \rho \mathcal{A} \left(\frac{R}{0.3}\right)^2\right).$$
- Lepton-to-jet p_T ratio (`jetPtRatio`): the ratio of the transverse momentum of the lepton to the transverse momentum of the nearest jet, p_T^ℓ / p_T^j .
- Lepton relative p_T (`jetPtRelv2`): the component of the lepton momentum in direction transverse to the jet, $p_T^{\text{rel}} = p_\ell \sin \theta$, where θ denotes the angle between the lepton and jet momentum vectors.
- Jet b-tagging score (`jetBTagDeepFlavB`): the discriminant value of the Deep Jet b-tagging algorithm of the matched jet (see Section 3.3).
- Jet charged constituents (`jetNDAuChargedMVASEl`): the number N_{charged} of charged particles within the matched jet.
- Impact parameters (`dxy`, `dz`): the transverse and longitudinal impact parameters of the lepton track with respect to the PV.
- Signed impact parameter (`sip3d`): the signed impact parameter, in three dimensions, of the lepton track with respect to the PV, divided by its uncertainty, which corresponds to its significance d/σ_d .
- Electron MVA ID discriminator (`mvaIdFall17noIsoV2`): the output of the BDT that separates electrons from jets, trained by the EGamma POG.
- Muon segment compatibility (`segmentCompatibility`): the compatibility of track segments in the muon system with the pattern expected for a minimum ionizing particle.

In case no jet is matched to the lepton, the value of the lepton-to-jet p_T ratio is set to $p_T^\ell / (p_T^\ell + I_\ell)$, whereas the values of the lepton relative p_T , the jet b-tagging score and the jet charged constituents are set to zero. We refer to the output of the BDT trained on electrons (muons) as prompt-e (prompt- μ) MVA.

The BDTs are trained separately for electrons and muons on simulated samples of prompt leptons and leptons produced in leptonic τ decays in $t\bar{t}H$ events (signal) and non-prompt leptons in semileptonic $t\bar{t}$ +jets events (background). Two trainings are performed for the electrons and the muons: one using Monte Carlo samples from 2016 and another one using Monte Carlo samples from 2017. The performance of the 2017 training evaluated in 2018 Monte Carlo samples is similar to the performance in 2017 Monte Carlo samples, as can be seen in Fig. 5, and hence the 2017 training is used for prompt-lepton identification in both 2017 and 2018 detector conditions.

The performance of the prompt lepton MVA has been compared to the previous iteration of the analysis (HIG-18-019). The latest training shows a significant improvement, as can be seen in Fig. 6. Additionally, the performance of multiclass neural networks has also been tested for this task, but has been seen to be comparable to that obtained with the BDTs.

3.1.5 Lepton selection

Based on the identification criteria mentioned above, this analysis makes use of three different levels of lepton selection for both the electrons and the muons: the "loose", "fakeable" and "tight" selections. The loose lepton collection is used for overlap cleaning amongst the objects and for the computation of invariant mass quantities used for background rejection. The fakeable leptons are used to estimate the fake lepton background from control regions in data, as

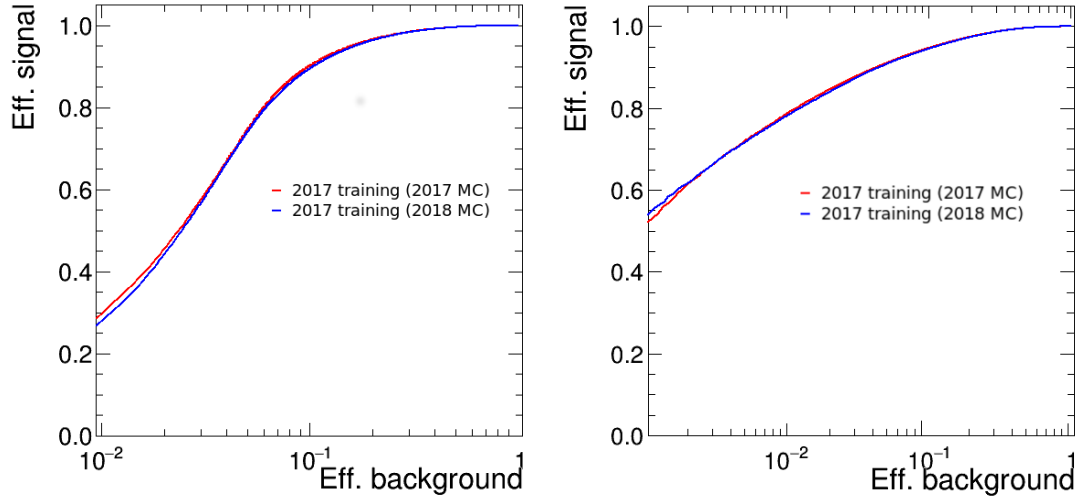


Figure 5: Performance of the prompt lepton for electrons (left) and muons (right) MVA trained in 2017 Monte Carlo samples and evaluated in 2017 and 2018 Monte Carlo samples.

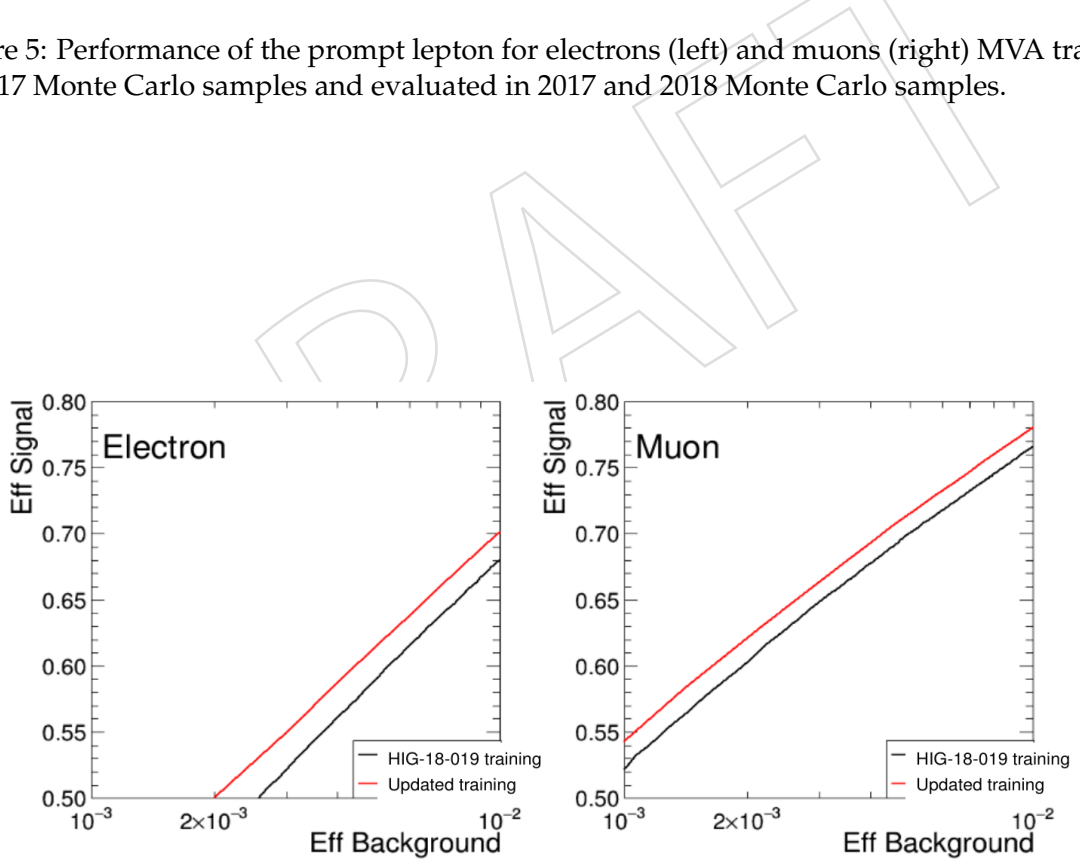


Figure 6: Performance of the updated prompt lepton MVA for electrons (left) and muons (right) compared to the previous iteration of the analysis (HIG-18-019).

336 well as to compute global kinematic properties of the events. The tight lepton selection is simi-
 337 lar to the fakeable one but with more stringent lepton MVA requirements, and is used for event
 338 selection in the signal regions.

339 In order to reduce potential biases of the background estimation procedure, the p_T of leptons
 340 that pass the fakeable but fail the tight lepton selection criteria is set to 0.90 times the p_T of
 341 the nearest jet in case the distance between lepton and nearest jet satisfies $\Delta R < 0.4$. In case
 342 $\Delta R > 0.4$ the p_T of fakeable leptons is set to $p_T^\ell / (p_T^\ell + I_\ell)$, where I_ℓ is the lepton isolation as
 343 defined before. We refer to the p_T of fakeable leptons computed this way as “cone- p_T ”. The
 344 cone- p_T in general exceeds the transverse momentum of the lepton that is determined by the
 345 electron and muon reconstruction algorithms. We refer to the latter as “reco- p_T ” to distinguish
 346 it from the cone- p_T in the cases where it could be ambiguous. Otherwise, we use the terms
 347 reco- p_T and p_T synonymously.

348 The different requirements for the loose, fakeable and tight electrons and muons are given in
 349 Tables 20 and 21. The properties used for such classifications include the kinematics of the
 350 lepton (cone- p_T , $|\eta|$), the impact parameters ($|d_{xy}|$, $|d_z|$, d/σ_d), the lepton isolation, properties
 351 of the nearest jet (Deep Jet b-tagging score, relative isolation), basic lepton identification criteria
 352 and the prompt-lepton MVA score. Additionally, fakeable and tight electrons are required to
 353 satisfy a set of conditions on the width of the electron cluster in η -direction ($\sigma_{i\eta i\eta}$), the ratio of
 354 energy in the HCAL to the energy in the ECAL that is associated to electron (H/E), and the
 355 difference between the reciprocal of the electron cluster energy and the reciprocal of its track
 356 momentum ($1/E - 1/p$). These conditions mimic the electron identification criteria applied at
 357 trigger level.

358 3.2 Hadronic τ decays

359 Hadronic τ decays are reconstructed by the “hadrons plus strips” (HPS) algorithm [78, 79].
 360 The algorithm allows to reconstruct individual hadronic decay modes of the τ : “one-prong”
 361 τ decays ($h^\pm, h^\pm + 1\pi^0, h^\pm + 2\pi^0$), “two-prong” τ decays ($h^\pm h^\mp, h^\pm h^\mp + 1\pi^0, h^\pm h^\mp + 2\pi^0$) and
 362 “three-prong” τ decays ($h^\pm h^\mp h^\pm, h^\pm h^\mp h^\pm + 1\pi^0$). Here h^\pm denotes either a charged pion or
 363 kaon. The decay modes of τ^+ are the charge conjugate of the τ^- decay modes. Hadronic τ
 364 candidates are built by combining the charged hadrons reconstructed by the PF algorithm with
 365 neutral pions. The latter are reconstructed by clustering the photons reconstructed by the PF
 366 algorithm within rectangular strips, that are narrow in η -, but wide in ϕ -direction, which ac-
 367 counts for the broadening of energy deposits in the ECAL in case one of the photons produced
 368 in $\pi^0 \rightarrow \gamma\gamma$ decays converts within the tracking detector. The size of the strip is adjusted as
 369 function of p_T , taking into consideration that the bending of charged particles in the magnetic
 370 field increases inversely proportional to p_T [80]. Photon conversions within the silicon tracking
 371 detector are accounted for by considering both the photons and the electrons reconstructed by
 372 the PF algorithm when reconstructing the neutral pions.

373 A multiclass algorithm based on a convolutional deep neural network (DNN), referred to as
 374 “Deep Tau v2.1”, is used to separate hadronic τ decays from the quark and gluon jet back-
 375 ground, muons and electrons [81]. This algorithm outperforms significantly previous discrim-
 376 ination methods in terms of misidentification probability of jets. It combines information from
 377 the high-level reconstructed τ features together with the low level information from the in-
 378 inner tracker, calorimeters and muon subdetectors using particle flow candidates, electrons and
 379 muons reconstructed within the τ isolation cone. The DNN has been trained with $t\bar{t}$ and $W+jets$
 380 MC samples in 2017 detector conditions. Different WPs are defined by the Tau POG based on
 381 the τ_h identification efficiencies and misidentification rates when varying the DNN output

Observable	Electrons		
	Loose	Fakeable	Tight
Cone- p_T	$> 7 \text{ GeV}$	$> 10 \text{ GeV}$	$> 10 \text{ GeV}$
$ \eta $	< 2.5	< 2.5	< 2.5
$ d_{xy} $	$< 0.05 \text{ cm}$	$< 0.05 \text{ cm}$	$< 0.05 \text{ cm}$
$ d_z $	$< 0.1 \text{ cm}$	$< 0.1 \text{ cm}$	$< 0.1 \text{ cm}$
d/σ_d	< 8	< 8	< 8
I_e	$< 0.4 \times p_T$	$< 0.4 \times p_T$	$< 0.4 \times p_T$
$\sigma_{i\eta i\eta}$	—	$< \{ 0.011 / 0.030 \}^1$	$< \{ 0.011 / 0.030 \}^1$
H/E	—	< 0.10	< 0.10
$1/E - 1/p$	—	> -0.04	> -0.04
Conversion rejection	—	✓	✓
Missing hits	≤ 1	$= 0$	$= 0$
EGamma POG MVA	$>\text{WP-loose}^2$	$>\text{WP-80} (>\text{WP-loose})^2 \dagger$	$>\text{WP-loose}^2$
Deep Jet of nearby jet	—	$<\text{WP-medium}^3$	$<\text{WP-medium}^3$
Jet relative isolation ⁴	—	$< 0.7 (-) \dagger$	—
Prompt-e MVA	—	$< 0.80 (> 0.80)$	> 0.80

¹ Barrel / endcaps.

² WPs as defined by EGamma POG (see Section 3.1.1).

³ WPs as defined by JetMET POG (see Section 3.3).

⁴ Defined as $1/p_T^{ratio}-1$ if the electron is matched to a jet within $\Delta R < 0.4$ or as the PF relative isolation with $\Delta R=0.4$ otherwise.

† Fails (passes) the requirement prompt-e MVA > 0.80 .

Table 20: Loose, fakeable, and tight selection criteria for electrons. The requirement on the output of the BDT trained by the EGamma POG (see Section 3.1.1) and on the observables $\sigma_{i\eta i\eta}$, H/E, and $1/E - 1/p$ are varied as function of η of the electron candidate. The conditions on the EGamma POG MVA, the Deep Jet discriminant and the relative isolation of the nearest jet to the electron are tightened (relaxed) for fakeable electrons that fail (pass) the requirement prompt-e MVA > 0.80 , in order to reduce the systematic uncertainty on the fake lepton background estimate on the jet flavour composition (see Section 7.4.1 in Ref. [77]). A hyphen (–) indicates selection criteria that are not applied.

382 scores. Eight WPs are defined in the discriminator against jets (VVVLoose, VVLoose, VLoose,
 383 Loose, Medium, Tight, VTight, VVTight), four WPs are defined in the discriminator against
 384 muons (VLoose, Loose, Medium, Tight) and eight WPs are defined in the discriminator against
 385 electrons (VVVLoose, VVLoose, VLoose, Loose, Medium, Tight, VTight, VVTight).

386 Three levels of τ_h identification criteria are used in the analysis: the "loose", the "fakeable"
 387 and the "tight". Loose τ_h 's are used for cleaning against jets and veto between the different
 388 channels in the analysis. Fakeable τ_h 's are used for the purpose of obtaining a data-driven
 389 estimate of the fake τ_h background, as in the case of the leptons. Finally, tight τ_h 's are used
 390 for the selection of events in the signal region. The selection criteria applied to loose, fakeable
 391 and τ_h are given in Table 22. The observables used for such classification include the kinematic
 392 properties of the τ_h (p_T , $|\eta|$), the impact parameters ($|d_{xy}|$, $|d_z|$), the τ_h decay mode and the
 393 output of the Deep Tau DNN to discriminate against jets, muons and electrons. For this last
 394 one, the WP of the discriminant against jets chosen in the signal regions is channel specific, as
 395 will be detailed in Section 5. The τ_h are required to be reconstructed with one of the "new"
 396 decay modes, as is recommended for analysis using the Deep Tau discriminator. Additionally,
 397 the τ_h are required not to overlap, within $\Delta R < 0.3$, with any electron or muon passing the

Observable	Muons		
	Loose	Fakeable	Tight
p_T	$> 5 \text{ GeV}$	$> 10 \text{ GeV}$	$> 10 \text{ GeV}$
$ \eta $	< 2.4	< 2.4	< 2.4
$ d_{xy} $	$< 0.05 \text{ cm}$	$< 0.05 \text{ cm}$	$< 0.05 \text{ cm}$
$ d_z $	$< 0.1 \text{ cm}$	$< 0.1 \text{ cm}$	$< 0.1 \text{ cm}$
d/σ_d	< 8	< 8	< 8
I_μ	$< 0.4 \times p_T$	$< 0.4 \times p_T$	$< 0.4 \times p_T$
PF muon	$>\text{WP-loose}^1$	$>\text{WP-loose}^1$	$>\text{WP-medium}^1$
Deep Jet of nearby jet	—	$<\text{WP-interp. } (<\text{WP-medium})^2$	$<\text{WP-medium}^2$
Jet relative isolation ³	—	$<0.5 \text{ (--) } \dagger$	—
Prompt- μ MVA	—	$< 0.85 \text{ } (> 0.85)$	> 0.85

¹ WPs as defined by Muon POG (see Section 3.1.2).

² Upper cut on the Deep Jet score defined with a linear interpolation from Deep Jet WP-medium at cone- p_T 20 GeV to Deep Jet WP-loose at cone- p_T 45 GeV, taking the Deep Jet WPs as defined by JetMET POG (see Section 3.3).

³ Defined as $1/\text{jetPtRatio} > 1$ if the muon is matched to a jet within $\Delta R < 0.4$ or as the PF relative isolation with $\Delta R = 0.4$ otherwise.

\dagger Fails (passes) the requirement prompt- μ MVA > 0.85 .

Table 21: Loose, fakeable, and tight selection criteria for muons. The conditions on the Deep Jet discriminant and the relative isolation of the nearest jet to the muon are tightened (relaxed) for fakeable muons that fail (pass) the requirement prompt- μ MVA > 0.85 , in order to reduce the systematic uncertainty on the fake lepton background estimate on the jet flavour composition (see Section 7.4.1 in Ref. [77]). A hyphen (—) indicates selection criteria that are not applied.

398 loose lepton selection criteria.

3.3 Jets

400 Jets are reconstructed using the anti- k_t algorithm [82] with a distance parameter $R = 0.4$.
 401 Charged particles not originating from the PV are excluded from the jet clustering. Fake jets,
 402 mainly arising from calorimeter noise, are rejected by requiring reconstructed jets to pass the
 403 loose WP of the PF jet identification criteria in 2016 and the tight WP in 2017 and 2018, following
 404 the recommendations of the JetMET POG [83]. The energy of reconstructed jets is calibrated as
 405 function jet p_T and η [84]. Corrections based on jet area and energy density [73, 74] are applied
 406 in order to compensate for PU effects, denoted as Jet-Energy-Corrections (JEC). The global tags
 407 used to apply these JEC to data and simulated events for the three years of data-taking can be
 408 found in Table 23.

409 Jets selected in this analysis are required to satisfy the conditions $p_T > 25 \text{ GeV}$ and $|\eta| < 2.4$,
 410 as is shown in Table 24. They are required not to overlap with fakeable electrons/muons or
 411 loose τ_h 's. In this context, two objects are considered to be overlapping if they share a packed
 412 PF candidate. We refer to this collection as "jets" in what follows.

413 We consider an additional collection of jets expected in tH topologies, which we refer to as
 414 "forward jets", whose selection criteria are shown in Table 24. These are required to pass the
 415 same p_T threshold as the central ones but to be within the region $2.4 < |\eta| < 5$. For the forward
 416 jets within $2.7 < |\eta| < 3$, an additional requirement of $p_T > 60 \text{ GeV}$ is applied in order to
 417 suppress the noise in the ECAL-HCAL transition region, which is not properly accounted for
 418 by the JEC factors. Forward jets are also required not to overlap with electrons, muons or τ_h
 419 that pass the fakeable object selection criteria. As before, two objects are considered to overlap

Hadronic τ			
Observable	Loose	Fakeable	Tight
p_T	> 20 GeV	> 20 GeV	> 20 GeV
$ \eta $	< 2.3	< 2.3	< 2.3
$ d_{xy} $	< 1000 cm	< 1000 cm	< 1000 cm
$ d_z $	< 0.2 cm	< 0.2 cm	< 0.2 cm
Decay mode finding	New	New	New
Decay modes	All	All except 2-prong($+\pi^0$) ¹	All except 2-prong($+\pi^0$) ¹
DeepTau vs. jets	> WP-VVLoose	> WP-VVLoose	Channel-dependent
DeepTau vs. muons	—	> WP-VLoose	> WP-VLoose
DeepTau vs. electrons	—	> WP-VVVLoose	> WP-VVVLoose

¹ TauPOG recommends to use the 2-prong and 2-prong+ π^0 decay modes only in analysis containing high- $p_T \tau_h$'s.

Table 22: Loose, fakeable and tight selection criteria for hadronic τ decays. A hyphen (—) indicates selection criteria that are not applied.

Event type	Global tag		
	2016	2017	2018
Simulation	102X_mcRun2_asymptotic_v6	102X_mc2017_realistic_v6	102X_upgrade2018_realistic_v20
Data	102X_dataRun2_nanoAOD_2016_v1	102X_dataRun2_v8	102X_dataRun2_v12 102X_dataRun2_Prompt_v15

Table 23: Global tags used to apply jet energy corrections to data and simulated events in the three years of data-taking.

420 if they share a packed PF candidate.

421 Jets originating from the hadronization of b quarks are identified by the “Deep Flavour” or
 422 “Deep Jet” algorithm [85, 86]. This DNN-based algorithm exploits high- and low-level observ-
 423 ables related to the long lifetime of b hadrons and the high particle multiplicity and mass of
 424 b-jets compared to light quark and gluon jets. Three levels of b-tagging selection are provided
 425 by the BTV POG [87] based on the b-jet selection efficiency and misidentification rates. In this
 426 analysis, we use the loose and medium b-tagging WPs, as will be detailed in Section 5.

4 Reconstruction of event level quantities

428 The missing transverse momentum vector is computed as the negative sum of the transverse
 429 momentum vectors of all the Particle-Flow candidates reconstructed in the event. The differ-
 430 ence in momentum between calibrated and uncalibrated jets is applied as correction (“Type-1

Observable	Jets	Forward jets
$ \eta $	0.0 - 2.4	2.4 - 5.0
p_T	> 25 GeV	> 25 GeV (> 60 GeV ¹)
PFJet ID	Loose-WP (Tight-WP) ²	Loose-WP (Tight-WP) ²

¹ Applied in the $2.7 < |\eta| < 3.0$ range.

² Applied in 2016 (2017/2018) data and simulation.

Table 24: Jets and forward jets selection criteria.

431 corrected PFMET") [88]. The magnitude of the missing transverse momentum vector is re-
 432 ferred to as E_T^{miss} . In 2017 data-taking period, the effect of the noise in the ECAL endcap at high
 433 η is reduced by applying the EE noise mitigation technique provided by the JetMET POG [89].

434 To mitigate the influence of PU on the missing transverse energy, the H_T^{miss} variable is consid-
 435 ered as well and is defined in the same way as E_T^{miss} , but considering only jets of $p_T > 25$ GeV
 436 and $|\eta| < 2.4$ as well as electrons, muons and τ_h passing the fakeable object selection criteria
 437 when evaluating the sum of transverse momenta. While the resolution in H_T^{miss} is worse com-
 438 pared to the resolution in E_T^{miss} , the observable H_T^{miss} has the advantage to be less sensitive to
 439 PU, as soft hadrons which predominantly originate from PU do not enter its computation.

440 A linear combination of E_T^{miss} and H_T^{miss} is used in the event selection, making use of the fact
 441 that the two observables are less correlated for events in which the reconstructed missing trans-
 442 verse momentum arises from instrumental effects compared to events with genuine missing
 443 transverse momentum. The linear combination, referred to as $E_T^{\text{miss}}LD$, is defined as:

$$E_T^{\text{miss}}LD = 0.6 \times E_T^{\text{miss}} + 0.4 \times H_T^{\text{miss}}. \quad (3)$$

444 Moreover, we exploit the different jet multiplicities of the ttH and tH topologies by making
 445 use of the number of light jets in the event. This quantity, which is used in event selection, is
 446 computed as the sum of the central jets which are not b-tagged and the forward jets:

$$N_{\text{light jets}} = (N_{\text{jets}} - N_{\text{loose } b\text{-jets}}) + N_{\text{fwd jets}} \quad (4)$$

447 where N_{jets} is the number of central jets, $N_{\text{loose } b\text{-jets}}$ is the number of central jets passing the
 448 loose WP of the Deep Jet b-tagging discriminant and $N_{\text{fwd jets}}$ is the number of forward jets.

449 5 Event selection

450 The event selection aims to target events in which the Higgs boson is produced through the
 451 $t\bar{t}H$, tHq or tHW process, and which decays into a pair of W bosons, Z bosons or τ leptons.
 452 The W and Z bosons can subsequently decay either hadronically or into electrons or muons,
 453 while the τ can decay to electrons, muons or τ_h . Events with a pair of loose leptons with an
 454 invariant mass smaller than 12 GeV are rejected, as they are not well modeled by the simulation.
 455 Moreover, events are required to contain at least one jet of $p_T > 25$ GeV. The triggers used
 456 to select events in all channels are detailed in Section 5.1. Following the recommendation of
 457 the JetMET POG [90], events selected in any of the channels are required to pass certain filter
 458 algorithms which remove events that are subject to different types of spurious detector signals.
 459 These algorithms are referred to as " E_T^{miss} filters" and are described in Section 5.2. Further
 460 channel specific event selection criteria are described in Section 5.3.

461 5.1 Triggers

462 The HLT paths used to record events are given in Table 25. Double τ_h trigger are used to
 463 record events containing zero leptons and two τ_h . A combination of single lepton triggers and
 464 triggers based on the presence of a lepton and a τ_h (also known as lepton+ τ_h "cross-triggers")
 465 are used to record events in the channels containing one lepton. A combination of single and
 466 double lepton triggers are used to record events in the channels containing two leptons, where
 467 the inclusion of single lepton triggers boosts the events acceptance. Similarly, a mix of single,

468 double and triple lepton triggers is used to record events in the channels containing at least
469 three leptons.

470 For some triggers, we use a combination of HLT paths with different p_T thresholds or a com-
471 bination of paths with and without a d_z requirement applied to the leptons. In the case of the
472 double muon triggers we further use a mix of HLT paths with and without a requirement on
473 the invariant mass of the di-muon pair, namely $m_{\mu\mu} > 3.8$ GeV. The motivation for choos-
474 ing such a mix is to use the trigger with highest efficiency whenever available and to employ
475 triggers of lower efficiency whenever the most efficient ones are disabled or prescaled.

476 Events recorded in any data-taking period as well as in simulated samples are selected in case
477 they pass any of the HLT paths that are required for each category. The effect of triggers that are
478 disabled or prescaled in some part of the analyzed data is accounted for by applying suitably
479 chosen weights to simulated events, as is detailed in Section 6.2.

480 5.2 E_T^{miss} filters

481 Events selected in any of the channels are required to pass the filter algorithms given in Ta-
482 ble 26, as recommended by the JetMET POG [90]. These filters perform additional event clean-
483 ing according to beam halo effects, detector noise, etc. All of them are applied in both data and
484 simulation, except the `Flag.eeBadScFilter` filter, which is applied to data events only.

485 5.3 Event channels

486 The events are analyzed in mutually exclusive categories, also referred to as “channels”, based
487 on the multiplicity of light leptons and τ_h , with requirements on the charge of the light leptons
488 in some cases. The ten different channels covered in this analysis are $0\ell + 2\tau_h$, $1\ell + 1\tau_h$, $1\ell +$
489 $2\tau_h$, $2\ell ss + 0\tau_h$, $2\ell ss + 1\tau_h$, $2\ell os + 1\tau_h$, $2\ell + 2\tau_h$, $3\ell + 0\tau_h$, $3\ell + 1\tau_h$ and $4\ell + 0\tau_h$, where ℓ refers
490 to an electron or muon and the τ_h refers to a hadronic τ , while the “ss” (“os”) refers to same
491 sign (opposite sign) electrons or muons. Details on the selections applied to each channel will
492 be shown in what follows, and a summary can be found in Tables 27, 28 and 29.

493 5.3.1 $0\ell + 2\tau_h$ category

494 The $0\ell + 2\tau_h$ category aims to select $t\bar{t}H$ signal events in which the two top quarks decay
495 hadronically and the H boson decays into two τ_h . Events selected in this category are required
496 to contain zero electrons or muons passing the tight object selection criteria and two τ_h , both
497 passing the fakeable selection criteria and the loose WP of the τ_h identification discriminant.
498 The two τ_h must have opposite charge, as expected for a τ_h pair produced in a H boson decay,
499 and must be within the geometric acceptance of the double τ_h triggers, i.e. within $|\eta| < 2.1$. The
500 contribution of the dominant background, arising from $t\bar{t}$ +jets events in which one or two jets
501 are misidentified as τ_h , is reduced by requiring that both τ_h satisfy the condition $p_T > 40$ GeV
502 and that the event contains at least four jets with $p_T > 25$ GeV and $|\eta| < 2.4$. Within those jets,
503 at least two must pass the loose WP of the b-tagging discriminator or at least one must pass
504 the medium WP. Events with at least one electron or muon passing the tight object selection
505 criteria are vetoed to avoid overlap with the $1\ell + 2\tau_h$ and $2\ell + 2\tau_h$ categories.

506

507 5.3.2 $1\ell + 1\tau_h$ category

508 The $1\ell + 1\tau_h$ category targets $t\bar{t}H$ signal events in which the two top quarks decay hadron-
509 ically and the H boson decays into two τ , one of which decays hadronically while the other
510 one decays leptonically. Events selected in this category must contain one electron or muon

Double τ_h triggers	HLT_DoubleMediumIsoPFTau35_Trk1_eta2p1_Reg ($\checkmark/-/-$) HLT_DoubleMediumCombinedIsoPFTau35_Trk1_eta2p1_Reg ($\checkmark/-/-$) HLT_DoubleMediumChargedIsoPFTau35_Trk1_eta2p1_Reg ($-/\checkmark/-$) HLT_DoubleTightChargedIsoPFTau35_Trk1_TightID_eta2p1_Reg ($-/\checkmark/\checkmark$) HLT_DoubleMediumChargedIsoPFTau40_Trk1_TightID_eta2p1_Reg ($-/\checkmark/\checkmark$) HLT_DoubleTightChargedIsoPFTau40_Trk1_eta2p1_Reg ($-/\checkmark/\checkmark$) HLT_DoubleMediumChargedIsoPFTauHPS35_Trk1_eta2p1_Reg ($-/-/\checkmark$)
Single lepton triggers	HLT_Ele25_eta2p1_WPTight_Gsf ($\checkmark/-/-$) HLT_Ele27_WPTight_Gsf ($\checkmark/-/-$) HLT_Ele27_eta2p1_WPLoose_Gsf ($\checkmark/-/-$) HLT_Ele32_WPTight_Gsf ($-/\checkmark/\checkmark$) HLT_Ele35_WPTight_Gsf ($-/\checkmark/-$) HLT_IsoMu22 ($\checkmark/-/-$) HLT_IsoTkMu22 ($\checkmark/-/-$) HLT_IsoMu22_eta2p1 ($\checkmark/-/-$) HLT_IsoTkMu22_eta2p1 ($\checkmark/-/-$) HLT_IsoMu24 ($\checkmark/\checkmark/\checkmark$) HLT_IsoTkMu24 ($\checkmark/-/-$) HLT_IsoMu27 ($-/\checkmark/\checkmark$)
Lepton+ τ_h cross-triggers	HLT_Ele24_eta2p1_WPLoose_Gsf_LooseIsoPFTau20 ($\checkmark/-/-$) HLT_Ele24_eta2p1_WPLoose_Gsf_LooseIsoPFTau20_SingleL1 ($\checkmark/-/-$) HLT_Ele24_eta2p1_WPLoose_Gsf_LooseIsoPFTau30 ($\checkmark/-/-$) HLT_Ele24_eta2p1_WPTight_Gsf_LooseChargedIsoPFTau30_eta2p1_CrossL1 ($-/\checkmark/\checkmark$) HLT_Ele24_eta2p1_WPLoose_Gsf_LooseChargedIsoPFTauHPS30_eta2p1_CrossL1 ($-/-/\checkmark$) HLT_IsoMu19_eta2p1_LooseIsoPFTau20_SingleL1 ($\checkmark/-/-$) HLT_IsoMu20_eta2p1_LooseChargedIsoPFTau27_eta2p1_CrossL1 ($-/\checkmark/\checkmark$) HLT_IsoMu20_eta2p1_LooseChargedIsoPFTauHPS27_eta2p1_CrossL1 ($-/-/\checkmark$)
Double lepton triggers	HLT_Ele23_Ele12_CaloIdL_TrackIdL_IsoVL_DZ ($\checkmark/-/-$) HLT_Ele23_Ele12_CaloIdL_TrackIdL_IsoVL ($-/\checkmark/\checkmark$) HLT_Mu17_TrkIsoVVL_Mu8_TrkIsoVVL ($\checkmark/-/-$) HLT_Mu17_TrkIsoVVL_Mu8_TrkIsoVVL_DZ ($\checkmark/-/-$) HLT_Mu17_TrkIsoVVL_TkMu8_TrkIsoVVL ($\checkmark/-/-$) HLT_Mu17_TrkIsoVVL_TkMu8_TrkIsoVVL_DZ ($\checkmark/-/-$) HLT_Mu17_TrkIsoVVL_Mu8_TrkIsoVVL_DZ_Mass8 ($-/\checkmark/-$) HLT_Mu17_TrkIsoVVL_Mu8_TrkIsoVVL_DZ_Mass3p8 ($-/\checkmark/\checkmark$) HLT_Mu8_TrkIsoVVL_Ele23_CaloIdL_TrackIdL_IsoVL_DZ ($\checkmark/-/-$) HLT_Mu8_TrkIsoVVL_Ele23_CaloIdL_TrackIdL_IsoVL ($\checkmark/\checkmark/\checkmark$) HLT_Mu23_TrkIsoVVL_Ele8_CaloIdL_TrackIdL_IsoVL_DZ ($\checkmark/-/-$) HLT_Mu23_TrkIsoVVL_Ele8_CaloIdL_TrackIdL_IsoVL ($\checkmark/-/-$) HLT_Mu12_TrkIsoVVL_Ele23_CaloIdL_TrackIdL_IsoVL_DZ ($\checkmark/\checkmark/-$) HLT_Mu23_TrkIsoVVL_Ele12_CaloIdL_TrackIdL_IsoVL ($\checkmark/\checkmark/-$) HLT_Mu23_TrkIsoVVL_Ele12_CaloIdL_TrackIdL_IsoVL_DZ ($-/\checkmark/-$)
Triple lepton triggers	HLT_Ele16_Ele12_Ele8_CaloIdL_TrackIdL ($\checkmark/\checkmark/\checkmark$) HLT_TripleMu_12_10_5 ($\checkmark/\checkmark/\checkmark$) HLT_Mu8_DiEle12_CaloIdL_TrackIdL ($\checkmark/\checkmark/\checkmark$) HLT_DiMu9_Ele9_CaloIdL_TrackIdL ($\checkmark/-/-$) HLT_DiMu9_Ele9_CaloIdL_TrackIdL_DZ ($-/\checkmark/\checkmark$)

Table 25: Triggers (2016/2017/2018) used to record events. A hyphen ($-$) indicates the trigger is not used in the corresponding data-taking year.

Filter name	Applied to data	Applied to simulation
Flag_goodVertices	✓	✓
Flag_globalSuperTightHalo2016Filter	✓	✓
Flag_HBHENoiseFilter	✓	✓
Flag_HBHENoiseIsoFilter	✓	✓
Flag_EcalDeadCellTriggerPrimitiveFilter	✓	✓
Flag_BadPFMuonFilter	✓	✓
Flag_ecalBadCalibReducedMINIAODfilter [†]	✓	✓
Flag_eeBadScFilter	✓	—

[†] applied only in 2017 and 2018 data-taking years

Table 26: E_T^{miss} filters applied to events selected in data and to simulated events, a hyphen (–) indicates the filter is not applied.

511 passing the tight object selection criteria and one τ_h the passing fakeable selection criteria and
 512 the medium WP of the τ_h identification discriminant. The lepton is required to be within the
 513 geometric acceptance of the lepton+ τ_h cross-trigger, i.e. $|\eta| < 2.1$, and to have $p_T > 30$ GeV
 514 (> 25 GeV) if it is an electron (muon). We further require that the τ_h satisfies the condition
 515 $p_T > 30$ GeV and that the event contains at least four jets with $p_T > 25$ GeV and $|\eta| < 2.4$,
 516 among which at least two pass the loose WP of the b-tagging discriminator or at least one
 517 passes the medium WP. Events with more than one electron or muon passing the tight object
 518 selection criteria or more than one loose τ_h passing the medium WP of the τ_h identification dis-
 519 criminant are vetoed to avoid overlap with the $1\ell + 2\tau_h$, $2\ell(\text{os}/\text{ss}) + 1\tau_h$, $2\ell + 2\tau_h$ and $3\ell + 1\tau_h$
 520 categories.
 521

522 5.3.3 $1\ell + 2\tau_h$ category

523 The $1\ell + 2\tau_h$ category predominantly selects $t\bar{t}H$ signal events in which one top quark de-
 524 cays leptonically and the other one decays hadronically, while the H boson decays into two
 525 τ_h . Events selected in this category are required to contain one electron or muon passing the
 526 tight object selection criteria and two τ_h , both passing the medium WP of the τ_h identification
 527 discriminant. The lepton is required to be within the geometric acceptance of the lepton+ τ_h
 528 cross-trigger, i.e. $|\eta| < 2.1$, and to have $p_T > 30$ GeV (> 25 GeV) if it is an electron (muon).
 529 The two τ_h are required to have opposite charge, as expected for a τ_h pair produced in a H bo-
 530 son decay. The contribution of the dominant background, arising from $t\bar{t}$ +jets events in which
 531 one or two jets are misidentified as τ_h , is reduced by demanding that the τ_h of higher p_T satis-
 532 fies the condition $p_T > 30$ GeV and that the event contains at least three jets with $p_T > 25$ GeV
 533 and $|\eta| < 2.4$, out of which at least two satisfy the loose WP of the b-tagging discriminator or
 534 at least one passes the medium WP. Events with more than one electron or muon passing the
 535 tight object selection criteria are vetoed to avoid overlap with the $2\ell + 2\tau_h$ category.

536 5.3.4 $2\ell\text{ss} + 0\tau_h$ category

537 The $2\ell\text{ss} + 0\tau_h$ category targets $t\bar{t}H$ or tH signal events in which the H boson decays into a pair
 538 of W bosons, one of which decays leptonically while the other one decays hadronically. In the
 539 $t\bar{t}H$ case, one top quark decays to leptons and the other one decays to hadrons, while in the tH
 540 case, the single top quark decays leptonically. Additionally, the lepton from the W boson and
 541 the lepton from the top quark have the same sign. Selected events are therefore required to con-
 542 tain two leptons of the same charge and passing the tight object selection criteria. The lepton
 543 of highest (lowest) p_T is required to have $p_T > 25$ GeV (> 15 GeV). The requirement on both

leptons to be of the same charge cuts half of the $t\bar{t}H$ signal events away, but removes almost all of the large $t\bar{t} + \text{jets}$ background. Residual $t\bar{t} + \text{jets}$ background contributions are further suppressed by requiring the charge of all fakeable electrons and muons in the event to be well measured. Electrons must satisfy two conditions (namely `isGsfCtfScPixChargeConsistent` and `isGsfScPixChargeConsistent`) which test the consistency between the independent measurements of the electron charge obtained from the position of the ECAL cluster and from its track, while muons must satisfy the condition that the estimated uncertainty on the p_T of the muon track is below 0.2 times its p_T . The latter is equivalent to requiring that the sign of the curvature of the muon track, which determines its charge, is measured with a significance of 5σ . After applying these conditions, the charge misidentification rate is on the per-mille level for electrons and negligible for muons [91]. The background from $t\bar{t}Z$ production is suppressed by requiring that the event contains no pair of same-flavor opposite-sign loose leptons with mass close to the mass of the Z boson, i.e. $|m_{ll} - m_Z| < 10$ GeV, where $m_Z = 91.2$ GeV [92]. In the case where the two selected leptons in the event are electrons, the invariant mass of electron pair is required not to be close to the mass of Z boson, i.e. $|m_{ee} - m_Z| < 10$ GeV, and the event must satisfy the condition $E_T^{\text{miss}} \text{LD} > 30$ GeV.

For what concerns the jet multiplicity, we select any event containing at least one of the two following topologies, which are expected from either the $t\bar{t}H$ or the tH process, respectively:

- To target the $t\bar{t}H$ signal, we select events that have at least three jets of $p_T > 25$ GeV and $|\eta| < 2.4$, among which at least two satisfy the loose WP of the b-tagging discriminator or that at least one satisfies the medium WP.
- To target the tH signal, we select events that have at least one jet of $p_T > 25$ GeV and $|\eta| < 2.4$ which passes the medium WP of the b-tagging discriminant and at least one light jet as defined in Section 3.3.

Events containing more than two tight leptons or a loose τ_h passing the very loose WP of the τ_h identification discriminant are vetoed. The former avoids overlap with the $3\ell + 0\tau_h$ category, while the latter avoids overlap with the $2\ell ss + 1\tau_h$ category.

5.3.5 $2\ell ss + 1\tau_h$ category

The $2\ell ss + 1\tau_h$ category targets $t\bar{t}H$ or tH signal events in which the H boson decays into a pair of τ leptons, where one decays leptonically while the other one decays into a τ_h . In the $t\bar{t}H$ case, one top quark decays to leptons and the other one decays to hadrons, while in the tH case, the single top quark decays leptonically. Additionally, the lepton from the τ decay and the lepton from the top quark decay have the same sign. The event selection criteria applied in the $2\ell ss + 1\tau_h$ category are identical to those applied in the $2\ell ss + 0\tau_h$ category, except that events selected in this category are required to contain one τ_h passing the very loose WP of the τ_h identification discriminant, and there is no requirement on the mass of the selected electron pair m_{ee} . Also, if the second highest p_T lepton is a muon, the p_T requirement is relaxed to $p_T > 10$ GeV. The charge of the τ_h is required to be opposite to the charge of the leptons. Overlap with the $2\ell + 2\tau_h$ category is avoided by applying a modified τ_h veto, which requires that the events selected in the $2\ell ss + 1\tau_h$ category do not contain two loose τ_h passing the medium WP of the τ_h identification discriminant.

5.3.6 $2\ell os + 1\tau_h$ category

The $2\ell os + 1\tau_h$ category targets $t\bar{t}H$ signal events in which the H boson decays into a pair of τ leptons, one of which decays leptonically, while the other one decays into a τ_h . One of the

589 top quarks decays to leptons and the other one decays to hadrons. In addition, the lepton from
 590 the τ and the lepton from the top quark have opposite sign. Events selected in this category
 591 are required to contain two electrons or muons passing the tight object selection criteria and
 592 one τ_h passing the fakeable selection criteria and the very tight WP of the τ_h identification
 593 discriminant. The two leptons are required to have opposite charge. The leading lepton must
 594 pass the requirement of $p_T > 25$ GeV, while the subleading lepton must pass $p_T > 30$ GeV
 595 (> 25 GeV) if it is an electron (muon). The background from $t\bar{t}Z$ production is suppressed
 596 by requiring that the event contains no pair of same-flavor opposite-sign loose leptons with
 597 invariant mass close to the mass of the Z boson, i.e. $|m_{ll} - m_Z| < 10$ GeV, where $m_Z =$
 598 91.2 GeV [92]. In case the two selected leptons in the event are of the same flavor, the event is
 599 further required to satisfy the condition $E_T^{miss} LD > 30$ GeV. Finally, the events must contain the
 600 at least three jets of $p_T > 25$ GeV and $|\eta| < 2.4$, among which at least two satisfy the loose WP
 601 of the b-tagging discriminant or that at least one satisfies the medium WP. Events with more
 602 than one lepton passing the tight object selection criteria or more than one loose τ_h passing the
 603 medium WP of the τ_h identification discriminant are vetoed to avoid overlap with the $3\ell + 1\tau_h$
 604 category and the $2\ell + 2\tau_h$ category.

605 5.3.7 $2\ell + 2\tau_h$ category

606 The $2\ell + 2\tau_h$ category aims at selecting $t\bar{t}H$ signal events in which both of the top quarks
 607 decay leptonically, while the H boson decays into two τ_h . Events selected in this category are
 608 required to contain two leptons that pass the tight selection criteria. The lepton of highest p_T
 609 is required to have $p_T > 25$ GeV, while the lowest p_T lepton is required to have $p_T > 10$ GeV
 610 ($p_T > 15$ GeV) if it is a muon (an electron). To suppress the background from the $t\bar{t}Z$ process,
 611 events containing a pair of loose leptons of the same flavor and opposite charge with mass
 612 $|m_{\ell\ell} - m_Z| < 10$ GeV are vetoed. Two τ_h passing the medium WP of the τ_h identification
 613 discriminant are required, and the charge sum of the two leptons and the two τ_h is required to
 614 be zero. Events must contain at least two jets, among which at least two satisfy the loose WP
 615 of the b-tagging discriminant or at least one satisfies the medium WP. Events containing less
 616 than four jets are required to satisfy the condition $E_T^{miss} LD > 45$ GeV in case the event contains
 617 a pair of fakeable leptons of the same flavor and opposite charge, and $E_T^{miss} LD > 30$ GeV if the
 618 event does not contain such lepton pair. If the event contains four or more jets, no requirement
 619 on $E_T^{miss} LD$ is applied, as the contributions of background processes are negligible in this case.

620 5.3.8 $3\ell + 0\tau_h$ category

621 The $3\ell + 0\tau_h$ category targets $t\bar{t}H$ or tH signal events in which the H boson decays into a
 622 pair of W bosons. In the $t\bar{t}H$ case, two final states are covered: those in which only one top
 623 quark and the two W bosons decay leptonically, and those in which both top quarks but only
 624 one W boson decays leptonically. In the tH case, the single top quark and both W bosons
 625 decay leptonically. Selected events are required to contain exactly three leptons passing the
 626 tight object selection criteria. The lepton of highest, second and third highest p_T is required to
 627 have $p_T > 25$ GeV, > 15 GeV and > 10 GeV, respectively. The charge sum of the leptons is
 628 required to be either $+1$ or -1 . The background from $t\bar{t}Z$ production is suppressed by vetoing
 629 events containing a pair of loose leptons of the same flavor and opposite charge with invariant
 630 mass $|m_{\ell\ell} - m_Z| < 10$ GeV.

631 For what concerns the jet multiplicity, we select any event containing at least one of the two
 632 following topologies, which are expected from either the $t\bar{t}H$ or the tH process, respectively:

- 633 • To target the $t\bar{t}H$ signal, we selected events that have at least two jets, among which
 634 at least two satisfy the loose WP of the b-tagging discriminant or at least one satisfies

635 the medium WP. Events containing less than four jets are required to satisfy the
 636 condition $E_T^{\text{miss}} \text{LD} > 45$ GeV in case the event contains a pair of loose leptons of
 637 the same flavor and opposite charge, and $E_T^{\text{miss}} \text{LD} > 30$ GeV if the event does not
 638 contain such lepton pair. If the event contains four or more jets, no requirement on
 639 $E_T^{\text{miss}} \text{LD}$ is applied, as the contributions of background processes are negligible in
 640 this case.

- 641 • To target the tH signal, we select events that have at least one jet passing medium
 642 WP of the b-tagging discriminant and at least one light jet as defined in Section 3.3.

643 Events containing a loose τ_h passing the very loose WP of the τ_h identification discriminant
 644 are vetoed, as are events containing two pairs of loose leptons of the same flavor and opposite
 645 charge which satisfy the condition $m_{\ell\ell\ell\ell} < 140$ GeV. While the first condition avoids overlap
 646 with the $3\ell + 1\tau_h$ category, the second condition avoids overlap with the t̄H-tagged category
 647 of the $H \rightarrow ZZ^* \rightarrow 4\ell$ analysis [93].

648 5.3.9 $3\ell + 1\tau_h$ category

649 The $3\ell + 1\tau_h$ category targets t̄H signal events in which the H boson decays into a pair of τ
 650 leptons, out of which one decays leptonically while the other one decays into a τ_h , and the
 651 two top quarks decay leptonically. The event selection criteria applied in the $3\ell + 1\tau_h$ category
 652 are identical to those applied in the $3\ell + 0\tau_h$ category, except that no τ_h veto is applied in the
 653 $3\ell + 1\tau_h$ category and the events selected in this category are instead required to contain one
 654 τ_h passing the very loose WP of the τ_h identification discriminant. The jet multiplicity and
 655 $E_T^{\text{miss}} \text{LD}$ requirements are also modified. In this case, events are required to have at least two
 656 jets, among which at least two satisfy the loose WP of the b-tagging discriminant or at least
 657 one satisfies the medium WP. Events containing less than four jets are required to satisfy the
 658 condition $E_T^{\text{miss}} \text{LD} > 45$ GeV in case the event contains a pair of loose leptons of the same
 659 flavor and opposite charge, and $E_T^{\text{miss}} \text{LD} > 30$ GeV if the event does not contain such lepton
 660 pair. If the event contains four or more jets, no requirement on $E_T^{\text{miss}} \text{LD}$ is applied, as the
 661 contributions of background processes are negligible in this case. The acceptance for the t̄H
 662 signal is increased by lowering the p_T thresholds for the leptons to $p_T > 20$ GeV, > 15 GeV and
 663 > 10 GeV for the lepton of highest, second and third highest p_T , respectively. Additionally, the
 664 charge sum of the three leptons and the τ_h is required to be zero.

665 5.3.10 $4\ell + 0\tau_h$ category

666 The $4\ell + 0\tau_h$ category targets events in which the H boson decays into a pair of W bosons
 667 or Z bosons, with the two top quarks decaying leptonically. When the H decays into two
 668 W bosons, we cover the cases in which both decay leptonically, whereas when the H decays
 669 into two Z bosons, we cover the cases in which one decays into two leptons and the other
 670 decays into neutrinos or quarks. Events selected in this category are required to contain four
 671 leptons passing the tight object selection criteria and passing p_T thresholds of $p_T > 25$ GeV,
 672 > 15 GeV, > 15 GeV and > 10 GeV, for the lepton of highest, second, third and fourth highest
 673 p_T , respectively. Remaining event selection criteria are similar to those of the $3\ell + 0\tau_h$ category.
 674 The charge sum of the leptons is required to be zero. Events containing a pair of loose leptons
 675 of the same flavor opposite charge with mass $|m_{\ell\ell} - m_Z| < 10$ GeV are vetoed. Events are
 676 required to have at least two jets, among which at least two satisfy the loose WP of the b-
 677 tagging discriminant or at least one satisfies the medium WP. Events containing less than four
 678 jets are required to satisfy the condition $E_T^{\text{miss}} \text{LD} > 45$ GeV in case the event contains a pair of
 679 fakeable leptons of the same flavor and opposite charge, and $E_T^{\text{miss}} \text{LD} > 30$ GeV if the event
 680 does not contain such lepton pair. Events containing two pairs of loose leptons of the same

681 flavor and opposite charge which satisfy the condition $m_{\ell\ell\ell\ell} < 140$ GeV are also vetoed.

Table 27: Event selections applied in the $0\ell + 2\tau_h$, $1\ell + 1\tau_h$ and $2\ell os + 1\tau_h$ categories.

Selection	$0\ell + 2\tau_h$	$1\ell + 1\tau_h$
Targeted $t\bar{t}H$ decays	$t \rightarrow b\bar{q}q$, $t \rightarrow b\bar{q}q$, $H \rightarrow \tau_h\tau_h$	$t \rightarrow b\bar{q}q$, $t \rightarrow b\bar{q}q$, $H \rightarrow \tau\tau \rightarrow \ell\tau_h + \nu's$
Trigger	Double- τ_h trigger	Single-lepton trigger and lepton- τ_h cross trigger
Lepton p_T	—	$p_T > 30$ GeV(e) or $p_T > 25$ GeV(μ)
Lepton η	—	$ \eta < 2.1$
$\tau_h p_T$	$p_T > 40$ GeV	$p_T > 30$ GeV
$\tau_h \eta$	$ \eta < 2.1$	$ \eta < 2.3$
Charge requirements	$\sum_{\tau_h} q = 0$	—
Jet multiplicity	≥ 4 jets	
b tagging requirements	≥ 1 medium b-tagged jet or ≥ 2 loose b-tagged jets	
Missing transverse momentum	—	—
Dilepton mass	$m_{\ell\ell} > 12$ GeV *	
Four-lepton mass	—	
Selection	$2\ell os + 1\tau_h$	
Targeted $t\bar{t}H$ decays	$t \rightarrow b\ell\nu$, $t \rightarrow b\bar{q}q$, $H \rightarrow \tau\tau \rightarrow \ell\tau_h + \nu's$	
Trigger	Single- and double- lepton triggers	
Lepton p_T	$p_T > 25 / 15$ (e) or 10 (μ) GeV	
Lepton η	$ \eta < 2.5$ (e) or 2.4 (μ)	
$\tau_h p_T$	$p_T > 20$ GeV	
$\tau_h \eta$	$ \eta < 2.3$	
Charge requirements	$\sum_{\ell} q = 0$	
Jet multiplicity	≥ 3 jets	
b tagging requirements	≥ 1 medium b-tagged jet or ≥ 2 loose b-tagged jets	
Missing transverse momentum	$E_T^{miss} LD > 30$ GeV **	
Dilepton mass	$m_{\ell\ell} > 12$ GeV * and $ m_{\ell\ell} - m_Z > 10$ GeV †	
Four-lepton mass	—	

* Applied on all pairs of leptons that pass loose selection.

** If both leptons are same flavor.

† Applied on all SFOS pair of leptons that pass loose selection.

6 Data-to-MC corrections

683 In order to improve the modeling of the data, we apply corrections to simulated events, which
684 we denote as "data-to-MC" corrections. The corrections considered in this analysis will be
685 described in the next subsections, and mainly concern differences in data and MC regarding
686 the following:

- 687 • pileup reweighting

Table 28: Event selections applied in the $2\ell ss + 0\tau_h$, $2\ell ss + 1\tau_h$, $1\ell + 2\tau_h$ and $2\ell + 2\tau_h$ categories.

Selection	$2\ell ss + 0\tau_h$	$2\ell ss + 1\tau_h$
Targeted $t\bar{t}H$ decays	$t \rightarrow b\ell\nu, t \rightarrow bqq,$ $H \rightarrow WW \rightarrow \ell\nu qq$	$t \rightarrow b\ell\nu, t \rightarrow bqq,$ $H \rightarrow \tau\tau \rightarrow \ell\tau_h + \nu's$
Targeted tH decays	$t \rightarrow b\ell\nu,$ $H \rightarrow WW \rightarrow \ell\nu qq$	$t \rightarrow b\ell\nu,$ $H \rightarrow \tau\tau \rightarrow \ell\tau_h + \nu's$
Trigger	Single- and double-lepton triggers	
Lepton p_T	$p_T > 25 / 15 \text{ GeV}$	$p_T > 25 / 15 (\text{e}) \text{ or } 10 \text{ GeV } (\mu)$
Lepton η	$ \eta < 2.5 (\text{e}) \text{ or } 2.4 (\mu)$	
$\tau_h p_T$	—	$p_T > 20 \text{ GeV}$
$\tau_h \eta$	—	$ \eta < 2.3$
Charge requirements	2 same-sign leptons and charge quality requirements $\sum_{\ell, \tau_h} q = \pm 1$	
Jet multiplicity and b-tag [†]	$\geq 3 \text{ jets}, \geq 1 \text{ medium b-tagged jet or } \geq 2 \text{ loose b-tagged jets}$	
Light jet and b-tag [†]	$\geq 1 \text{ light jets}, \geq 1 \text{ medium b-tagged jet}$	
Missing transverse momentum	$E_T^{\text{miss}} LD > 30 \text{ GeV } ^{**}$	
Dilepton mass	$m_{\ell\ell} > 12 \text{ GeV } ^*, m_{\ell\ell} - m_Z > 10 \text{ GeV } ^{***}, m_{ee} - m_Z > 10 \text{ GeV } ^{**}$	
Selection	$1\ell + 2\tau_h$	$2\ell + 2\tau_h$
Targeted $t\bar{t}H$ decays	$t \rightarrow b\ell\nu, t \rightarrow bqq,$ $H \rightarrow \tau\tau \rightarrow \tau_h\tau_h + \nu's$	$t \rightarrow b\ell\nu, t \rightarrow b\ell\nu,$ $H \rightarrow \tau\tau \rightarrow \tau_h\tau_h + \nu's$
Trigger	Single-lepton and lepton+ τ_h triggers	
Lepton p_T	$p_T > 30 (\text{e}) \text{ or } 25 \text{ GeV } (\mu)$	$p_T > 25 / 15 (\text{e}) \text{ or } 10 \text{ GeV } (\mu)$
Lepton η	$ \eta < 2.1$	$ \eta < 2.5 (\text{e}) \text{ or } 2.4 (\mu)$
$\tau_h p_T$	$p_T > 30 / 20 \text{ GeV}$	$p_T > 20 \text{ GeV}$
$\tau_h \eta$	$ \eta < 2.3$	$ \eta < 2.3$
Charge requirements	$\sum_{\tau_h} q = 0$	$\sum_{\ell, \tau_h} q = 0$
Jet multiplicity	$\geq 3 \text{ jets}$	$\geq 2 \text{ jets}$
b tagging requirements	$\geq 1 \text{ medium b-tagged jet or } \geq 2 \text{ loose b-tagged jets}$	
Missing transverse momentum	—	No requirement if $N_j \geq 4$ $E_T^{\text{miss}} LD > 45 \text{ GeV } ^\dagger$ $E_T^{\text{miss}} LD > 30 \text{ GeV otherwise}$
Dilepton mass	$m_{\ell\ell} > 12 \text{ GeV } ^*$ $ m_{\ell\ell} - m_Z > 10 \text{ GeV } ^{***},$ $ m_{ee} - m_Z > 10 \text{ GeV } ^{**}$	

* Applied on all pairs of leptons that pass loose selection.

** If both leptons are electrons.

*** Applied on all SFOS pairs of leptons that pass loose selection.

[†] Pass at least one of these two jet and b-tag cuts.

[‡] If the event contains a SFOS lepton pair and $N_j \leq 3$.

- 688 • trigger efficiency
- 689 • e and μ identification and isolation efficiency
- 690 • τ_h identification efficiency
- 691 • τ_h energy scale

Table 29: Event selections applied in the $3\ell + 0\tau_h$, $3\ell + 1\tau_h$ and $4\ell + 0\tau_h$ categories.

Selection	$3\ell + 0\tau_h$	$3\ell + 1\tau_h$
Targeted $t\bar{t}H$ decays	$t \rightarrow b\ell\nu, t \rightarrow b\ell\nu,$ $H \rightarrow WW \rightarrow \ell\nu qq$ $t \rightarrow b\ell\nu, t \rightarrow bq\bar{q},$ $H \rightarrow WW \rightarrow \ell\nu\ell\nu$	$t \rightarrow b\ell\nu, t \rightarrow b\ell\nu,$ $H \rightarrow \tau\tau \rightarrow \ell\tau_h + \nu's$
Targeted tH decays	$t \rightarrow b\ell\nu, H \rightarrow WW \rightarrow \ell\nu\ell\nu$	—
Trigger	Single-, double- and triple-lepton triggers	
Lepton p_T	$p_T > 25 / 15 / 10 \text{ GeV}$	$p_T > 20 / 15 / 10 \text{ GeV}$
Lepton η	$ \eta < 2.5 (\text{e}) \text{ or } 2.4 (\mu)$	
$\tau_h p_T$	—	$p_T > 20 \text{ GeV}$
$\tau_h \eta$	—	$ \eta < 2.3$
Charge requirements	$\sum_\ell q = \pm 1$	$\sum_{\ell, \tau_h} q = 0$
Jet multiplicity**	≥ 2 jets	
b tagging requirements**	≥ 1 medium b-tagged jet or ≥ 2 loose b-tagged jets	
Light jet and b-tag***	≥ 1 light jets, ≥ 1 medium b-tagged jet	
Missing transverse** momentum	No requirement if $N_j \geq 4$ $E_T^{\text{miss}} LD > 45 \text{ GeV}^\dagger$ $E_T^{\text{miss}} LD > 30 \text{ GeV otherwise}$	
Dilepton mass	$m_{\ell\ell} > 12 \text{ GeV}^*$ and $ m_{\ell\ell} - m_Z > 10 \text{ GeV}^\ddagger$	
Four-lepton mass	$m_{4\ell} > 140 \text{ GeV}^\S$	—
Selection	$4\ell + 0\tau_h$	
Targeted $t\bar{t}H$ decays	$t \rightarrow b\ell\nu, t \rightarrow b\ell\nu,$ $H \rightarrow WW \rightarrow \ell\nu\ell\nu$ $t \rightarrow b\ell\nu, t \rightarrow b\ell\nu,$ $H \rightarrow ZZ \rightarrow \ell\ell qq \text{ or } \ell\ell\nu\nu$	
Trigger	Single-, double- and triple-lepton triggers	
Lepton p_T	$p_T > 25 / 15 / 15 / 10 \text{ GeV}$	
Lepton η	$ \eta < 2.5 (\text{e}) \text{ or } 2.4 (\mu)$	
$\tau_h p_T$	—	
$\tau_h \eta$	—	
Charge requirements	$\sum_\ell q = 0$	
Jet multiplicity	≥ 2 jets	
b tagging requirements	≥ 1 medium b-tagged jet or ≥ 2 loose b-tagged jets	
Missing transverse momentum	No requirement if $N_j \geq 4$ $E_T^{\text{miss}} LD > 45 \text{ GeV}^\dagger$ $E_T^{\text{miss}} LD > 30 \text{ GeV otherwise}$	
Dilepton mass	$m_{\ell\ell} > 12 \text{ GeV}^*$ and $ m_{\ell\ell} - m_Z > 10 \text{ GeV}^\ddagger$	
Four-lepton mass	$m_{4\ell} > 140 \text{ GeV}^\S$	

* Applied on all pairs of leptons that pass loose selection.

** In 3ℓ category, if events do not pass these cuts, *** is required.† If the event contains a SFOS lepton pair and $N_j \leq 3$.

‡ Applied to all SFOS lepton pairs.

§ Applied only if the event contains 2 SFOS lepton pairs.

Lepton multiplicity and flavor	Leading lepton p_T	2016 SF	2017 SF	2018 SF
2μ	$p_T < 35 \text{ GeV}$ $p_T \geq 35 \text{ GeV}$	1.010 ± 0.010	0.972 ± 0.006 0.994 ± 0.001	$\mathbf{XXX} \pm \mathbf{XXX}$
$e + \mu$	$p_T < 35 \text{ GeV}$ $35 \leq p_T < 50 \text{ GeV}$ $p_T \geq 50 \text{ GeV}$	1.020 ± 0.010	0.952 ± 0.008 0.983 ± 0.003 1.000 ± 0.001	$\mathbf{XXX} \pm \mathbf{XXX}$
$2e$	$p_T < 30 \text{ GeV}$ $p_T \geq 30 \text{ GeV}$	1.020 ± 0.020	0.937 ± 0.027 0.991 ± 0.002	$\mathbf{XXX} \pm \mathbf{XXX}$
$\geq 3\ell$	—	1.000 ± 0.060	1.000 ± 0.050	$\mathbf{XXX} \pm \mathbf{XXX}$

Table 30: Trigger efficiency SF applied to simulated events selected in different categories. The SF applied to events selected in $0\ell + 2\tau_h$, $1\ell + 1\tau_h$ and $1\ell + 2\tau_h$ channels are described in the text.

- b-tag efficiency and mistag rate
- E_T^{miss} resolution and response
- prefiring probability of Level-1 ECAL trigger
- reweighting of Drell-Yan events
- reweighting of $t\bar{t}$ events

6.1 Pileup reweighting

The PU present in the MC samples does not exactly match the PU present in the data. The difference is corrected by reweighting simulated events to match the PU distribution in data [94]. We use the PU reweighting based on the mean of the Poisson distribution. The corresponding PU distribution in data is computed as described in Ref. [95], using a value of 69.2 mb for the inelastic pp scattering cross section [96]. A problem has been reported with the simulation of PU in the RunIIIFall17MiniAOD MC production [97]. The issue still persisted in samples produced in RunIIIFall17MiniAODv2 production campaign. We work around the problem using the distribution of `PileupSummaryInfo::getTrueNumInteractions`, obtained individually for each MC sample before any cuts are applied, as input to the PU reweighting.

6.2 Trigger efficiency

Difference in efficiency for events in data and MC simulation to pass the triggers given in Table 25 are corrected by applying the ratio of the efficiency in data to the efficiency in the MC simulation as weight to simulated events. We refer to these weights as “scale factors” (SF).

In $2\ell ss + 0\tau_h$, $2\ell ss + 1\tau_h$, $2\ell os + 1\tau_h$, $2\ell + 2\tau_h$, $3\ell + 0\tau_h$, $3\ell + 1\tau_h$ and $4\ell + 0\tau_h$ channels, the SF are measured as function of lepton multiplicity and type of the leptons as well as of the leading lepton p_T [98]. An additional uncertainty of 2% is attributed to 2ℓ -triggered events, associated with the parametrization of the trigger efficiency as a function of the leading lepton p_T alone. The SF are determined by comparing the combined efficiencies of single, double and triple lepton triggers between data and $t\bar{t}$ +jets events using events recorded by E_T^{miss} triggers. The SF are shown in Table 30.

In $1\ell + 1\tau_h$ and $1\ell + 2\tau_h$ channels, we parametrize the efficiency for lepton to pass the single lepton trigger and lepton “legs” of the lepton+ τ_h cross-triggers as function of p_T and η of the lepton. In $0\ell + 2\tau_h$, $1\ell + 1\tau_h$ and $1\ell + 2\tau_h$ channels, the efficiency for τ_h to pass the τ_h “legs” is parametrized as function of p_T , η , ϕ , decay mode of the τ_h and WP of the τ_h

identification discriminant. In $0\ell + 2\tau_h$ channel, the efficiency for events to pass double τ_h is expressed as the product of the efficiencies for each τ_h to pass either leg of the double τ_h trigger. The efficiency of these triggers has been measured via the Tag-and-Probe technique [99], using $Z/\gamma^* \rightarrow ee$, $Z/\gamma^* \rightarrow \mu\mu$ and $Z/\gamma^* \rightarrow \tau\tau$ events. The measurement has been performed by the Tau POG [100–102].

The efficiency for an event containing one lepton and one τ_h or one lepton and two τ_h to pass the combination of single lepton trigger and lepton+ τ_h cross-trigger is given by:

$$\epsilon = \begin{cases} \epsilon_L - \min(\epsilon_L, \epsilon_\ell) \times \epsilon_\tau & \text{if only the single lepton trigger fires} \\ (\epsilon_\ell - \epsilon_L) \times \epsilon_\tau & \text{if only the cross-trigger fires} \\ \min(\epsilon_L, \epsilon_\ell) \times \epsilon_\tau & \text{if both triggers fire} \end{cases}, \quad (5)$$

where

$$\epsilon_\tau = \begin{cases} \epsilon_{\tau 1} & \text{in the } 1\ell + 1\tau_h \text{ channel} \\ 1 - (1 - \epsilon_{\tau 1})(1 - \epsilon_{\tau 2}) & \text{in the } 1\ell + 2\tau_h \text{ channel} \end{cases}. \quad (6)$$

Here ϵ_L and ϵ_ℓ denote the efficiencies of the lepton to pass the single lepton triggers and the lepton leg of the cross-trigger, respectively, and $\epsilon_{\tau(1)}$ ($\epsilon_{\tau(2)}$) refers to the efficiency for the τ_h of higher (lower) p_T to pass the τ_h leg of the cross-trigger. The efficiencies ϵ_L and ϵ_ℓ ($\epsilon_{\tau(1)}$ and $\epsilon_{\tau(2)}$) depend on p_T and η of the lepton (of the τ_h). Eq. (5) takes into account the fact that any of the selected τ_h present in the event may fire the lepton+ τ_h cross-trigger and that, although the single lepton trigger has a higher p_T threshold compared to the lepton leg of the cross-trigger, the single lepton trigger may nevertheless have a higher efficiency, due to differences in lepton identification and isolation criteria. The SF applied to events selected in $1\ell + 1\tau_h$ and $1\ell + 2\tau_h$ channels is then given by the ratio of the efficiencies for data and MC simulation, computed separately according to Eq. (5).

6.3 Identification and isolation efficiency for e and μ

The efficiency for electrons and muons to pass the loose and the tight selection criteria defined in Tables 20 and 21 have been measured via the Tag-and-Probe technique using samples of $Z/\gamma^* \rightarrow ee$ and $Z/\gamma^* \rightarrow \mu\mu$ events. The measurement described in Ref. [103] has been repeated for each data-taking period. The measurement is performed in two stages: the efficiency for leptons to pass the loose selection criteria is measured first, and then for those leptons that pass the loose selection criteria and also pass the tight selection criteria the loose to tight efficiency is also measured. These latter efficiencies are measured separately for electrons and muons and are parametrized as function of lepton p_T and $|\eta|$ as shown in Figs. 7, 8, 9, 10. The data efficiency is shown with solid points and the MC efficiency with dashed points. The $|\eta|$ bins are defined as [0-0.9, 0.9-1.2, 1.2-2.1, 2.1-2.5 (2.4)] for electrons (muons) and the p_T bins [10-15, 15-20, 20-25, 25-30, 30-35, 35-40, 40-45, 45-60, 60-80, 80-120] GeV.

The ratio of the efficiency measured in data to the efficiency in MC simulation yields a scale factor (SF) per lepton and per era shown in Figs. 11 and 12. The product of per-lepton SF is applied as weight to simulated events. The SF measured for leptons passing the loose selection criteria are also applied to leptons that pass the fakeable lepton selection criteria.

6.4 Identification efficiency for τ

The efficiency for hadronic τ decays to pass the τ_h identification criteria detailed in Section 3.2 has been measured by the Tau POG, using $Z/\gamma^* \rightarrow \tau\tau$ events. The measurement has been carried out for each data-taking period individually. The ratio of the efficiency measured in

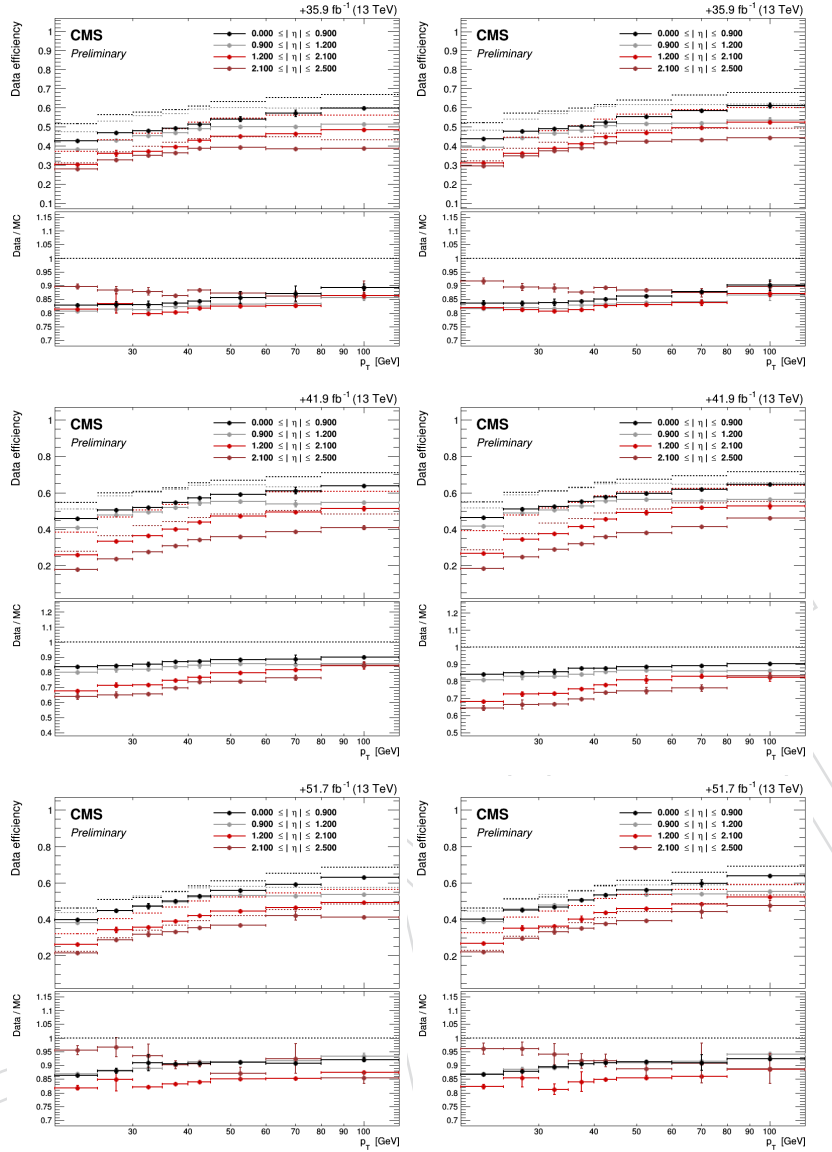


Figure 7: Efficiency of loose electrons to pass the tight selection criteria, as measured in $Z \rightarrow \ell\ell$ events using a tag-and-probe method as a function of p_T in bins of $|\eta|$ for 2016 (top), 2017 (middle) and 2018 (bottom) for 2 lepton same sign (left) and 3 lepton (right) selections.

759 data to the efficiency in MC simulation depends on the τ_h identification discriminant and on
 760 the p_T of the τ_h .

761 **6.5 Energy scale of τ_h**

762 A correction for the energy scale of τ_h (τ_h -ES) is determined by fitting the distribution in the
 763 mass of the τ_h candidate and in the mass of muon and τ_h reconstructed in $Z/\gamma^* \rightarrow \tau\tau$ events
 764 selected in the decay channel $\tau\tau \rightarrow \mu\nu\tau_h\nu\nu$ with shape templates for the $Z/\gamma^* \rightarrow \tau\tau$ signal
 765 and background processes [104]. Separate fits are performed for τ_h candidates reconstructed in
 766 the hadronic τ decay modes $h^\pm, h^\pm + 1\pi^0, h^\pm + 2\pi^0, h^\pm h^\mp h^\pm$ and $h^\pm h^\mp h^\pm + 1\pi^0$ [105, 106].

767 The τ_h -ES is generally lower in data compared to the MC simulation. Depending on the re-
 768 constructed τ_h decay mode, the energy of τ_h that are matched, on generator level, to genuine
 769 hadronic τ decays in simulated signal and background events is scaled by the factors given in

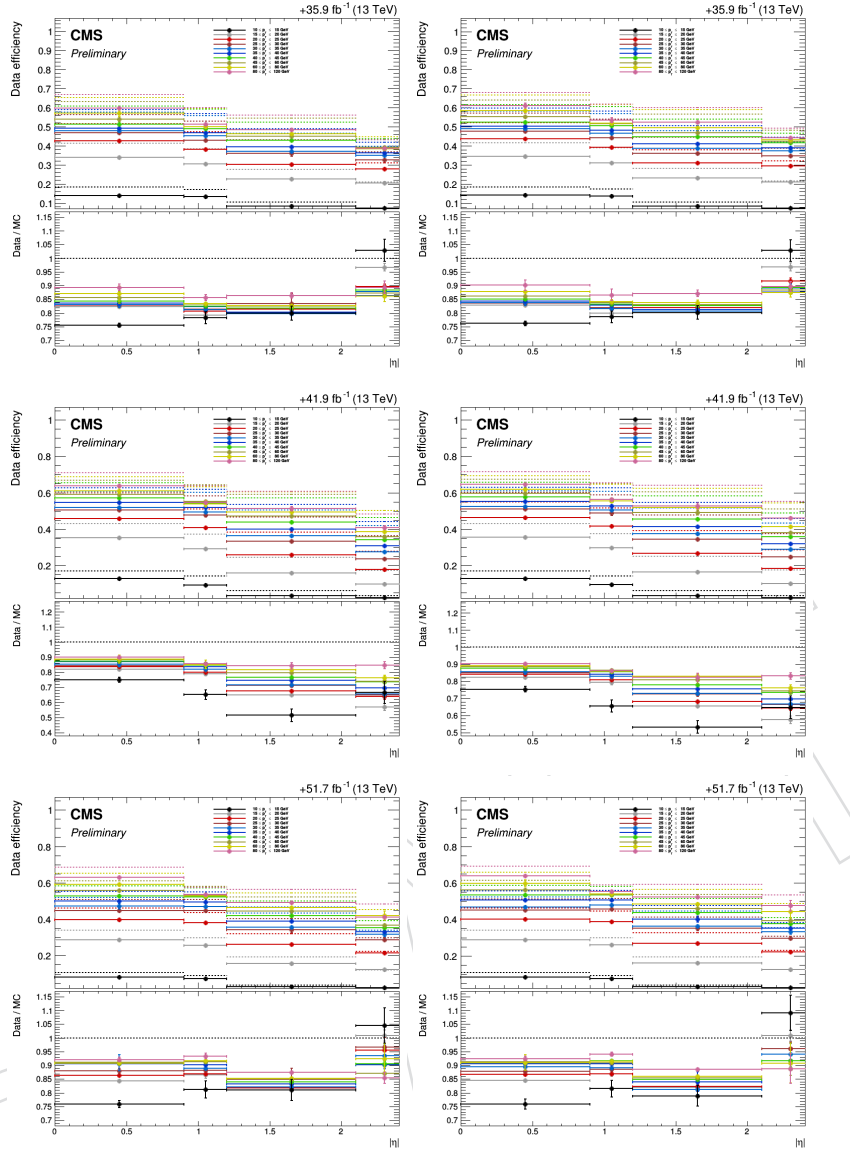


Figure 8: Efficiency of loose electrons to pass the tight selection criteria, as measured in $Z \rightarrow \ell\ell$ events using a tag-and-probe method as a function of $|\eta|$ in bins of p_T for 2016 (top), 2017 (middle) and 2018 (bottom) for 2 lepton same sign (left) and 3 lepton (right) selections.

770 Table 31.

771 6.6 b-tag efficiency and mistag rate

772 Small differences between data and MC simulation in the efficiency for b-jets and c-jets to pass
 773 the loose and medium WPs of the Deep Jet b-tagging algorithm, as well as in the mistag rate
 774 for light flavor (u, d, s) quark and gluon jets, have been observed by the BTV POG. We correct
 775 for the differences by applying suitably chosen weights to simulated events, using SF and tools
 776 (“method 1d”) provided by the BTV POG [107, 108]. The per-jet SF are parametrized as function
 777 of jet p_T and η of the b-tagging discriminant of the jet and of the flavor of the quark or gluon
 778 that is matched to the jet on generator level. The per-event weight is then taken as the product
 779 of per-jet weight of all selected jets in the event.

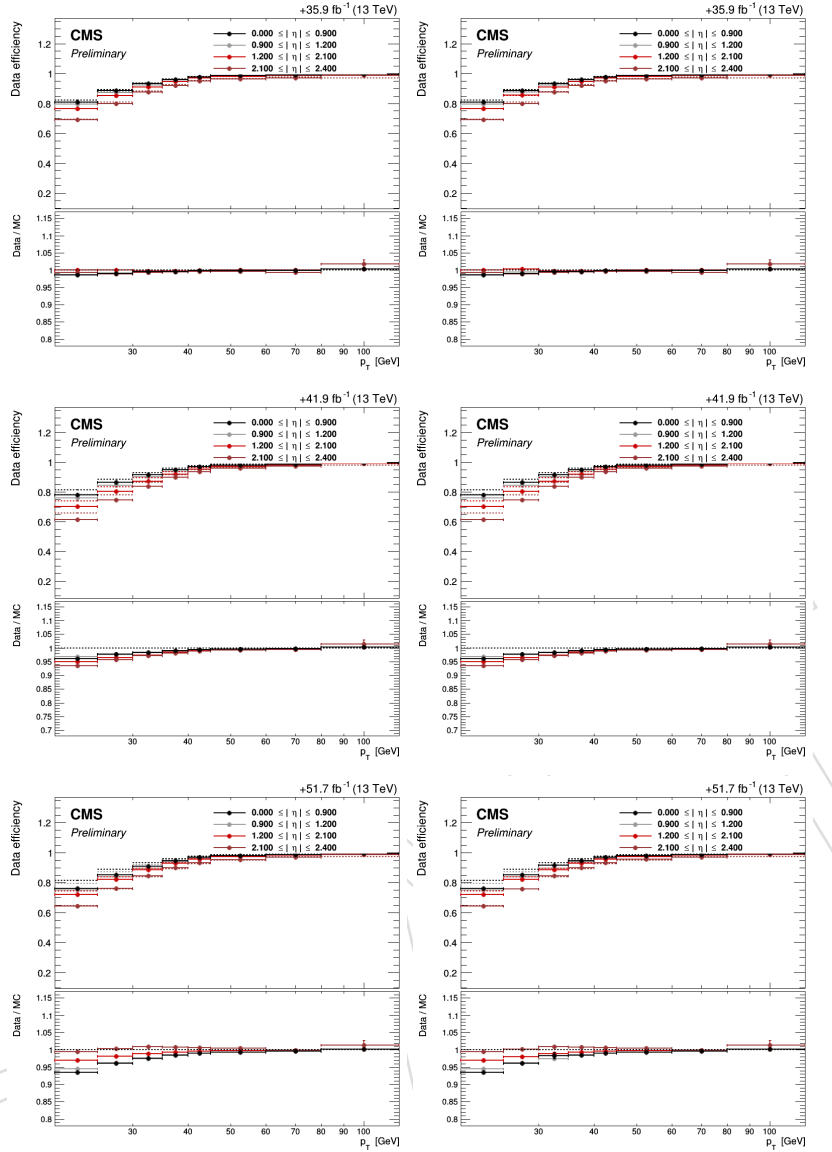


Figure 9: Efficiency of loose muons to pass the tight selection criteria, as measured in $Z \rightarrow \ell\ell$ events using a tag-and-probe method as a function of p_T in bins of $|\eta|$ for 2016 (top), 2017 (middle) and 2018 (bottom) for 2 lepton same sign (left) and 3 lepton (right) selections.

780 6.7 E_T^{miss} resolution and response

781 Differences between data and MC simulation in E_T^{miss} response and resolution are corrected
 782 by “propagating” measured differences in jet response and resolution [109] to the E_T^{miss} , us-
 783 ing the `runMETCorrectionsAndUncertainties` tool provided by the JetMET POG [89].
 784 The validity of the corrections has been verified using $Z/\gamma^* \rightarrow ee$, $Z/\gamma^* \rightarrow \mu\mu$ and $\gamma + \text{jets}$
 785 events [110].

786 6.8 Prefiring probability of L1 ECAL trigger

787 During 2016 and 2017 detector operation, a gradual timing shift of the ECAL was observed,
 788 which was accounted for and corrected before 2018 operation began. This shift was propagated
 789 to the Level-1 (L1) trigger primitives (TP), resulting in a significant fraction of high- $|\eta|$ TP being
 790 mistakenly associated to the previous bunch crossing. Since the L1 rules forbid two consecutive

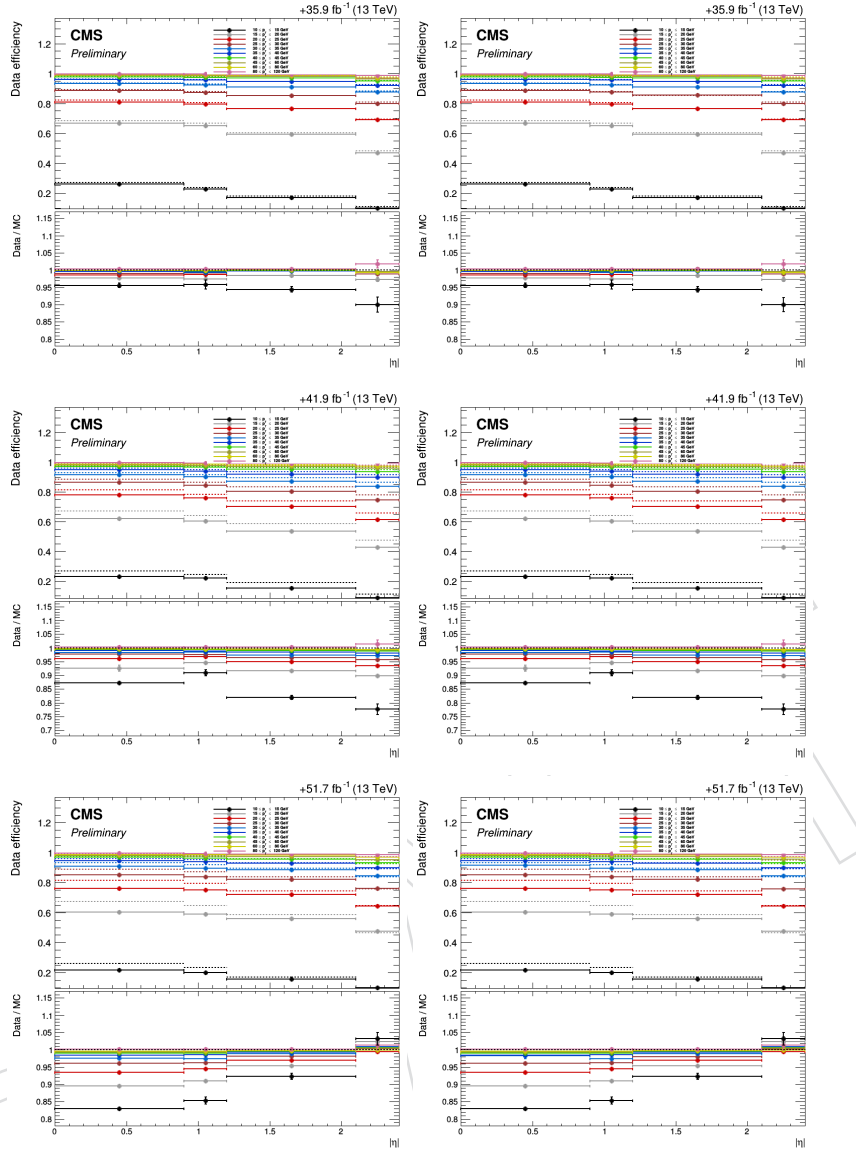


Figure 10: Efficiency of loose muons to pass the tight selection criteria, as measured in $Z \rightarrow \ell\ell$ events using a tag-and-probe method as a function of $|\eta|$ in bins of p_T for 2016 (top), 2017 (middle) and 2018 (bottom) for 2 lepton same sign (left) and 3 lepton (right) selections.

bunch crossings to fire, a consequence of this is that events can self veto if a significant amount of ECAL energy is found in the region $2 < |\eta| < 3$. Further details of the effect can be found in [111].

The effect is not described genuinely by the simulation but taken into account using event weights. These are obtained following the official procedure provided by the ECAL DPG [112, 113]. The recipe assigns a “prefiring” probability to each isolated jet and photon in the ECAL transition region $2 < |\eta| < 3$ with $p_T > 20$ GeV present in the event, parametrized as a function of their p_T and η . The final SF, which is applied to all events before any selection, is taken as the probability for a given MC event not to prefire, which is obtained from the product of non-prefiring probabilities of jets and photons in the event, i.e. $(1 - \text{prefiring weight})$. A more detailed study on the effect of prefire in our analysis can be found in Appendix M.

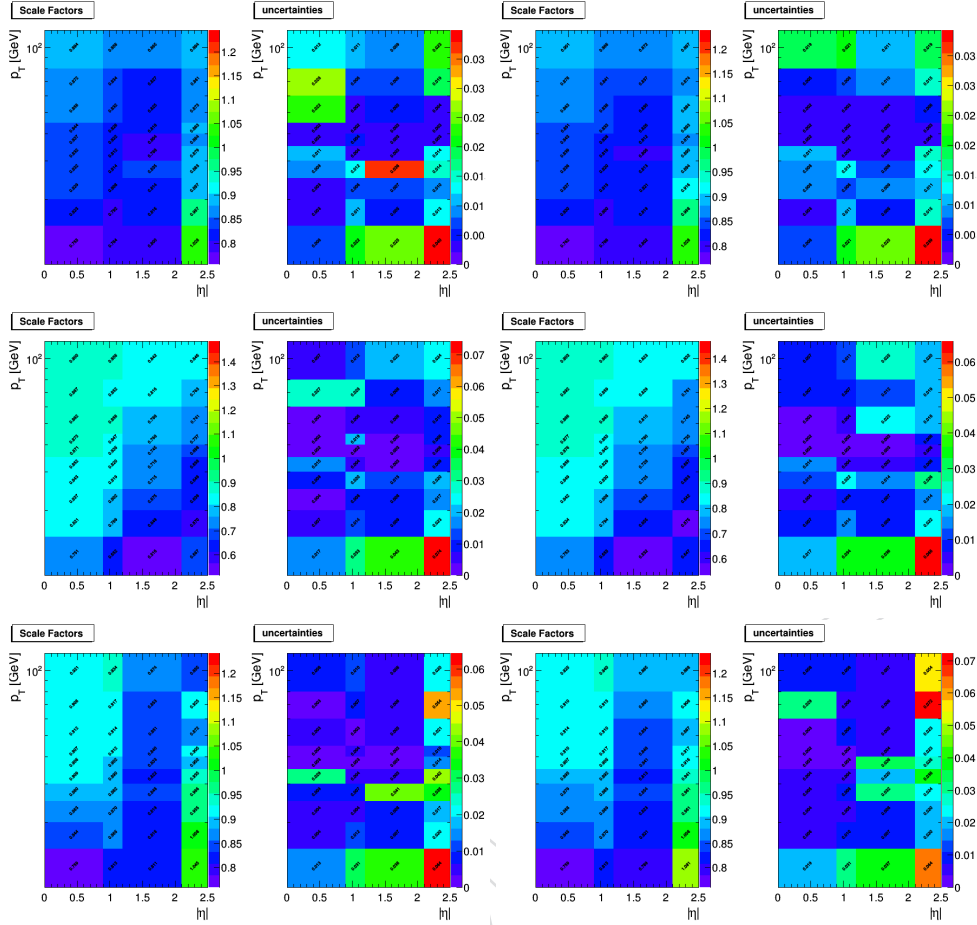


Figure 11: Scale factors and their uncertainties of loose electrons to pass the tight selection criteria, as measured in $Z \rightarrow \ell\ell$ events using a tag-and-probe method as a function of p_T and $|\eta|$ in 2016 (top), 2017 (middle) and 2018 (bottom) for 2 lepton same sign (left) and 3 lepton (right) selections.

Hadronic τ decay mode	2016 SF	2017 SF	2018 SF
h^\pm	0.994 ± 0.010	1.007 ± 0.008	0.987 ± 0.011
$h^\pm + 1\pi^0$ and $h^\pm + 2\pi^0$	0.995 ± 0.009	0.998 ± 0.008	0.995 ± 0.009
$h^\pm h^\mp h^\pm$	1.000 ± 0.011	1.001 ± 0.009	0.988 ± 0.008
$h^\pm h^\mp h^\pm + 1\pi^0$	—	0.999 ± 0.010	—

Table 31: SF for the τ_h -ES. Hyphen (–) indicates that the SF is not measured for a given decay mode.

6.9 Drell-Yan reweighting

The contribution to backgrounds from Drell-Yan process are found to be significant in final states with $0\ell + 2\tau_h$ and $1\ell + 1\tau_h$. The Drell-Yan background that enters to the signal region of $0\ell + 2\tau_h$ and $1\ell + 1\tau_h$ channels primarily consists of $Z \rightarrow \tau\tau + \text{jets}$ events. Thus, a semi-data driven approach is employed to estimate the Drell-Yan background contribution. The yield and the shape of the distributions in the signal region are obtained from the MC samples. However, an additional normalization scale factor is needed to correct for the event yield. The normalization scale factors are estimated in a control region with $Z \rightarrow \ell\ell + \text{jets}$, where $\ell = e$ or μ , and in the bins of jet multiplicity (N_{jets}) and number of b-tagged jets ($N_{\text{b-jets}}$). The control region consisting of $Z \rightarrow \ell\ell + \text{jets}$ events have no overlap with that of the signal region for

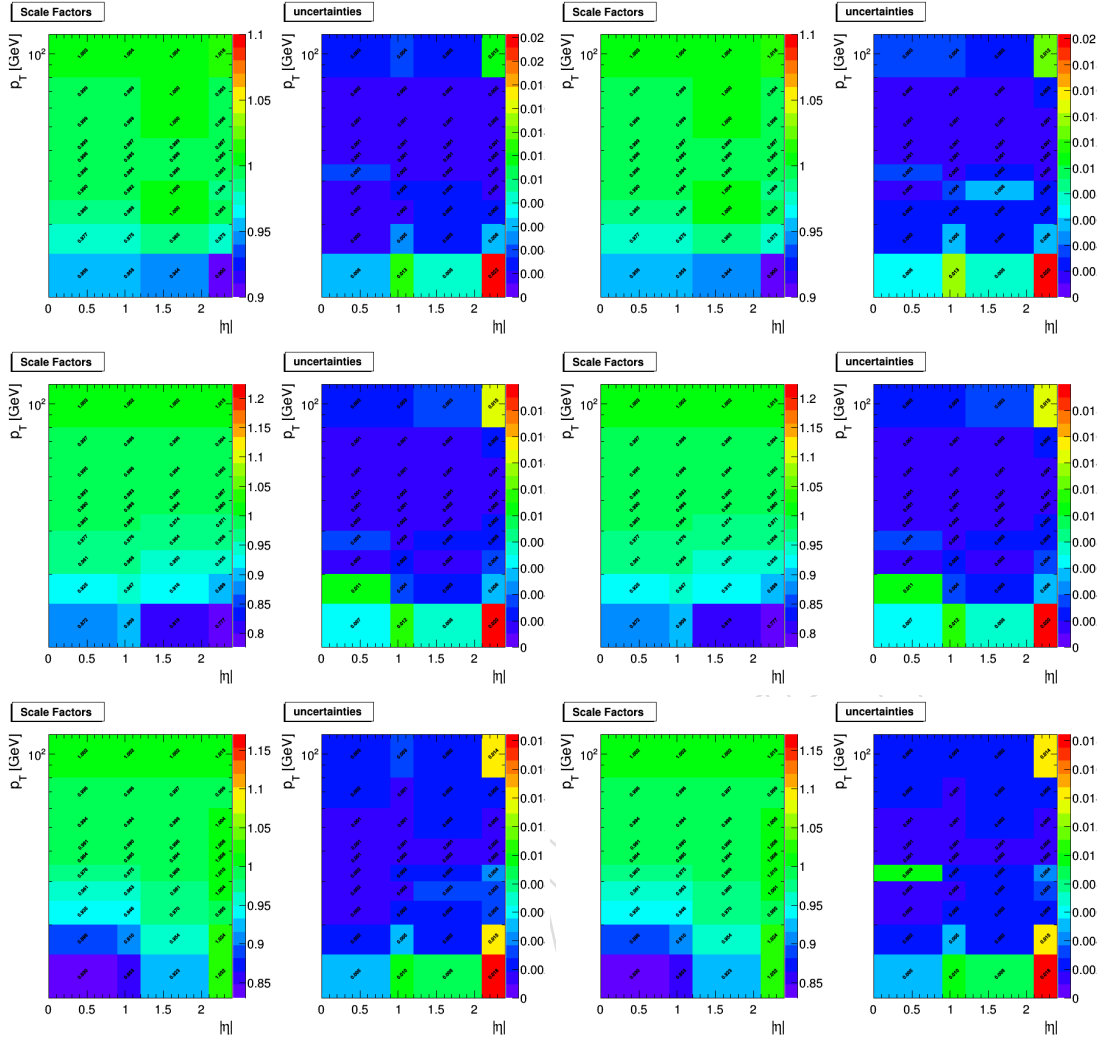


Figure 12: Scale factors and their uncertainties of loose muons to pass the tight selection criteria, as measured in $Z \rightarrow ll$ events using a tag-and-probe method as a function of p_T and $|\eta|$ in 2016 (top), 2017 (middle) and 2018 (bottom) for 2 lepton same sign (left) and 3 lepton (right) selections.

812 $0\ell + 2\tau_h$ and $1\ell + 1\tau_h$ channels. Same selection as that of signal region is applied to count
 813 the number of jets and b-tagged jets. In order to exclude the effects of lepton selection from
 814 the normalization scale factors, the scale factors in individual $N_{\text{jets}}\text{-}N_{\text{b-jets}}$ bins are scaled by
 815 the corresponding factors obtained after inclusive 2ℓ selection. The values of the estimated
 816 scale factors are provided in Table 32 for $N_{\text{jets}} \geq 4$, which corresponds to that of the N_{jets}
 817 requirement in the signal region for $0\ell + 2\tau_h$ and $1\ell + 1\tau_h$ channels.

818 The scale factors are found to be different for di-electron and di-muon final states, where the
 819 scale factors obtained from di-electron final state are often lower than that obtained from di-
 820 muon final state. Therefore, an additional systematic uncertainty is introduced that takes in
 821 to account the difference of the Drell-Yan normalization scale factors obtained from di-electron
 822 and di-muon final states. The value of these additional systematic uncertainties are provided
 823 in Table 33. These systematic uncertainties should be added in quadrature to that of statisti-
 824 cal uncertainties provided in Table 32 to get the total uncertainties on the normalization scale
 825 factors.

Data-taking Years	$N_{\text{b-tagged}}^{\text{medium}} \geq 2$	$N_{\text{b-tagged}}^{\text{medium}} = 1$ $N_{\text{b-tagged}}^{\text{loose}} \geq 2$	$N_{\text{b-tagged}}^{\text{medium}} = 1$ $N_{\text{b-tagged}}^{\text{loose}} = 1$	$N_{\text{b-tagged}}^{\text{medium}} = 0$ $N_{\text{b-tagged}}^{\text{loose}} \geq 2$
2016	0.801 ± 0.04	1.121 ± 0.035	1.145 ± 0.025	1.065 ± 0.019
2017	1.353 ± 0.055	1.55 ± 0.04	1.554 ± 0.03	1.431 ± 0.02
2018	1.261 ± 0.054	1.873 ± 0.057	1.757 ± 0.038	1.769 ± 0.03

Table 32: The normalization scale factors for Drell-Yan background events, estimated in a control region with $\mu^+ \mu^- + \geq 4$ -jets in the bins of number of b-tagged jets. The scale factors are provided for each data-taking period. The uncertainties are due to limited statistics of MC samples.

Data-taking Years	$N_{\text{b-tagged}}^{\text{medium}} \geq 2$	$N_{\text{b-tagged}}^{\text{medium}} = 1$ $N_{\text{b-tagged}}^{\text{loose}} \geq 2$	$N_{\text{b-tagged}}^{\text{medium}} = 1$ $N_{\text{b-tagged}}^{\text{loose}} = 1$	$N_{\text{b-tagged}}^{\text{medium}} = 0$ $N_{\text{b-tagged}}^{\text{loose}} \geq 2$
2016	0.603	0.181	0.071	0.191
2017	0.915	0.140	0.104	0.164
2018	0.529	0.165	0.089	0.153

Table 33: Additional systematic uncertainties on Drell-Yan normalization scale factors. These systematic uncertainties are due to the difference in scale factor values estimated in control regions of $Z \rightarrow ee + \text{jets}$ and $Z \rightarrow \mu\mu + \text{jets}$ events. These uncertainties are to be added in quadrature to that of statistical uncertainties provided in Table 32.

6.10 $t\bar{t}$ reweighting

The irreducible contribution of $t\bar{t}$ events in the signal regions of $0\ell + 2\tau_h$ and $1\ell + 1\tau_h$ categories is found to be significant. In the two event categories, the $t\bar{t}$ background is modeled with POWHEG samples which are listed in Tables 16–18. The p_T spectrum of the top quark is found to be harder in the simulation than in data, which we correct for with an analytic function that takes the p_T of generator level top quarks as input. The analytic expression is derived by the TOP POG from a fit to the ratio between p_T of the top quark measured in data and the theory predictions of POWHEG and PYTHIA [114]. Additional systematic uncertainties are associated with the method by either not weighting the events at all, or by applying square of the scale factor to the events.

7 Background estimation

This section describes the several background processes that are taken into consideration in this analysis. Each background is categorised as either “reducible” or “irreducible” according to the source of the reconstructed leptons passing the tight object selection criteria (see Sections 3.1.4 and 3.2). For all processes, a lepton is considered prompt if it originated from the decay of either a W boson, a Z boson or a τ lepton. A background is considered reducible if one or more of the reconstructed electrons, muons or τ_h leptons passing the tight object selection criteria does not originate from a prompt electron, muon or τ_h . This type of reducible background is known as the “fake” background. In the $2\ell ss + 0\tau_h$ and $2\ell ss + 1\tau_h$ channels there is an additional contribution to the reducible background that comes from processes in which the charge of one of the leptons in an opposite-sign lepton pair is mis-measured leading to a same-sign lepton pair. This reducible background is known as the “flips” background. Both of these reducible backgrounds are estimated using data-driven techniques, the procedures for which can be found in Sections 7.1 and 7.2. Furthermore, the estimation of the fake background is validated in dedicated control regions as shown in the Appendix A.

851 Due to the low signal rate, additional small background contributions must also be taken into
852 consideration. A small additional reducible background contribution arises from $t\bar{t}$ pair pro-
853 duction in association with real or virtual photons (see Refs [77, 103, 115, 116] for more detailed
854 studies of this process). The contribution from $t\bar{t}$ events with real photons is typically due
855 to a $\gamma \rightarrow e^+e^-$ conversion where one of the leptons carries most of the energy of the pho-
856 ton meaning the other fails to get reconstructed. Such events are suppressed by the photon
857 conversion rejection criteria and by requiring that the electron candidate tracks have hits in
858 each layer of the pixel detector it traverses, as shown in Table 20. The contribution from $t\bar{t}$
859 events with virtual photons typically produce low-mass electron or muon pairs which can be
860 effectively suppressed by requiring that the invariant mass of the dilepton pair be greater than
861 some minimal value $m_{\ell\ell} > 12$ GeV in all channels. Consequently, the number of $t\bar{t}$ events
862 produced in association with photons that actually passes the events selection is small in the
863 $2\ell ss + 0\tau_h$ and $2\ell ss + 1\tau_h$ channels, and negligible in all other channels. The contribution from
864 this background is modeled using MC simulation.

865 We refer to the background contribution from events in which at least one reconstructed elec-
866 tron is matched to a photon ($\Delta R(e, \gamma) < 0.3$) at generator level as the “conversion” background.
867 The p_T of the generator level photon is required to be greater than 0.5 p_T of the reconstructed
868 electron. All simulated samples used in the analysis are also used to estimate the contribution
869 from this background. All simulated events in which at least one reconstructed electron is due
870 to a photon conversion are included in this estimate unless the event qualifies as coming from
871 a fake or flip process to avoid double counting. We treat the uncertainties on the background
872 contributions that are due to conversions of real photons into e^+e^- as fully correlated between
873 all background processes in which the reconstructed electrons are due to photon conversions.

874 As mentioned above, we also have the irreducible background contribution which comes pre-
875 dominantly from $t\bar{t}W$ and $t\bar{t}Z$ processes, as well as processes in which a diboson pair (WW,
876 WZ or ZZ) is produced in association with jets. There is also a minor contribution coming
877 from triboson production and from the production of single top quarks in association with a
878 W or Z boson. All of these irreducible backgrounds are modeled using Monte Carlo simulated
879 samples.

880 To check that the simulated samples accurately model the data without biasing the analysis we
881 define several control regions where the agreement between data and simulation can be eval-
882 uated. The event selection in each control aims to enrich it in a particular irreducible background
883 process. Two control regions (3 ℓ -CR and 4 ℓ -CR) are defined to target three of the dominant ir-
884 reducible processes: $t\bar{t}Z$, WZ and ZZ, as is described in Section 9.3. A specific node in the
885 multi-classification DNN used for signal extraction in the $2\ell ss + 0\tau_h$ channel targets the irre-
886ducible $t\bar{t}W$ process, making a control region for this process difficult to define. However,
887 we do ensure we have good modelling of all processes used in the multivariate analysis by
888 checking the data-simulation agreement in all DNN input variables distributions and the cor-
889 relations between two-dimensional variables. Results of these studies are described in Section 9
890 and Appendix A.

891 To avoid double counting of the contributions to the total background that are included both
892 in the data-driven fake and flip estimates and in the Monte Carlo simulation, reconstructed
893 electrons (muons) are required to be matched to a prompt generator level electron (muon) and
894 reconstructed hadronic τ particles are required to be matched to a generator level τ_h . The
895 ΔR between a generator level object and a reconstructed object is required to be less than 0.3.
896 Further requirements on the transverse momentum of the reconstructed lepton relative to the
897 generator level lepton are imposed such that $|(p_T^{reco} - p_T^{gen})| / p_T^{gen} < 0.5$ for reconstructed elec-

898 trons/muons and τ_h matching generator level electrons and muons, and $|(\vec{p}_T^{reco} - \vec{p}_T^{gen})|/p_T^{gen} <$
 899 1.0 for reconstructed τ_h matching a generator level τ . Generator level electrons (muons) matching
 900 to reconstructed electrons (muons) are also required to be stable. Each generator level object
 901 is matched to no more than one reconstructed object. A reconstructed electron, muon or τ_h not
 902 satisfying the above criteria is considered fake.

903 All simulated background samples are processed, and we take the background contribution
 904 from simulation in the cases where the number of tight and matched leptons and τ_h matches
 905 the event selection. The background contribution from events where at least one of the tight
 906 leptons or τ_h is not matched to a generator level object is taken from data. Events with a
 907 reconstructed τ_h matched to a generator level electron or muon are considered part of the
 908 irreducible background. The background contribution arising from the misidentification of
 909 electrons and muons as τ_h particles is small because electrons and muons that fail the loose
 910 object selection criteria get considered as τ_h .

911 7.1 “Fake” background

912 The estimation of the fake background is based on the fake-factor (FF) method. The method is
 913 applied to each of the channels separately. In the $0\ell + 2\tau_h$, $1\ell + 1\tau_h$, $1\ell + 2\tau_h$, $2\ell ss + 0\tau_h$, $2\ell os +$
 914 $1\tau_h$, $2\ell + 2\tau_h$, $3\ell + 0\tau_h$ and $4\ell + 0\tau_h$ channels the method selects events which pass all selection
 915 criteria for the respective category, as detailed in Section 5, except that the electrons, muons
 916 and τ_h in these events are required to pass the fakeable instead of the tight object selection
 917 criteria. The selected event sample is referred to as the “application region” (AR) of the FF
 918 method. Events in which all e , μ and τ_h pass the tight object selection criteria are vetoed in
 919 order to avoid overlap with the signal region (SR). An estimate of the fake background in the
 920 SR is obtained by applying appropriately chosen weights to the events selected in the AR.
 921 The applied weights are a function of the so called fake-factors that are derived in another
 922 orthogonal region described later.

923 The weights applied depends on the number of e , μ and τ_h in the event that pass the fakeable
 924 but fail the tight object selection criteria. Expressions for the weights are derived in Refs. [115,
 925 117]. For events containing a total of 2, 3 or 4 fakeable “objects” (where “object” refers to either
 926 electrons, muons or τ_h), the expressions read as follows:

$$\begin{aligned}
 N_{pp}^{\text{fake}} &= \sum_{fp} F_1 + \sum_{pf} F_2 - \sum_{ff} F_1 F_2 \\
 N_{ppp}^{\text{fake}} &= \sum_{fpp} F_1 + \sum_{pfp} F_2 + \sum_{ppf} F_3 \\
 &\quad - \sum_{ffp} F_1 F_2 - \sum_{fpf} F_1 F_3 - \sum_{pff} F_2 F_3 + \sum_{fff} F_1 F_2 F_3 \\
 N_{pppp}^{\text{fake}} &= \sum_{fppp} F_1 + \sum_{pfpp} F_2 + \sum_{ppfp} F_3 + \sum_{pppf} F_4 \\
 &\quad - \sum_{ffpp} F_1 F_2 - \sum_{fpfp} F_1 F_3 - \sum_{fppf} F_1 F_4 - \sum_{pfpf} F_2 F_3 - \sum_{ppff} F_2 F_4 - \sum_{ppff} F_3 F_4 \\
 &\quad + \sum_{ffff} F_1 F_2 F_3 + \sum_{ffpf} F_1 F_2 F_4 + \sum_{fpff} F_1 F_3 F_4 + \sum_{pfff} F_2 F_3 F_4 - \sum_{ffff} F_1 F_2 F_3 F_4. \tag{7}
 \end{aligned}$$

927 The symbols N_{pp}^{fake} and N_{ppp}^{fake} on the left-hand-side of the equations represent the estimated con-
 928 tributions of the fake background in the signal region from events containing 2 and 3 electrons,

929 muons and τ_h , respectively, as determined by the method. The symbol F_i is a short-hand nota-
 930 tion for $F_i \equiv \frac{f_i}{1-f_i}$. The label “pfpp” refers to events in which the object of highest, third-highest,
 931 and fourth-highest p_T passes the tight selection criteria, while the object of second highest p_T
 932 fails the tight selection criteria, and similarly for the other labels. The FF f_i represents the prob-
 933 ability for an electron, muon or τ_h that passes the fakeable selection criteria to pass the tight
 934 selection criteria, where i refers to the i -th electron, muon or τ_h , sorted by decreasing p_T . The
 935 different sums correspond to specific combinations of leptons and hadronic τ decays passing
 936 and failing the tight selection criteria. Events enter the sums with a weight equal to a product
 937 of factors F_i , each factor F_i representing a single lepton or hadronic τ decay that passes the
 938 fakeable, but fails the tight selection criteria. For example, the sum \sum_{fpf} extends over all events
 939 that contain three electrons, muons or τ_h passing the fakeable selection criteria, of which the
 940 highest and third highest p_T objects fail and the second highest p_T object passes the tight se-
 941 lection criteria, and the events in the sum are weighted by the product $F_1 F_3$. The sign of the
 942 weights alternates for events with different numbers of electrons, muons or τ_h failing the tight
 943 selection criteria. The contamination from irreducible backgrounds with prompt leptons and
 944 genuine τ_h in the application region is taken from simulation and subtracted from this estimate
 945 to avoid double-counting in the signal region.

946 The FF f_i are measured separately for electrons, muons and τ_h and are parametrised as func-
 947 tion of η and cone- p_T of the lepton. The measurement of the FF is described in Appendices I
 948 and J. The control regions used to measure the FF are referred to as “measurement regions”
 949 (MR). The event selection criteria that are applied in the MR used to measure the FF for leptons
 950 (τ_h) are chosen such that the relative fractions of non-prompt leptons and hadrons (of quark
 951 jets of different flavor and gluon jets) are similar between AR and MR. Likewise, the fakeable
 952 lepton selection criteria are chosen so the difference between the FF for non-prompt leptons
 953 and hadrons is reduced. These choices guarantee that the FF method yields an unbiased es-
 954 timate of the fake background in the SR when the weights given by Eq. 7 are applied to the
 955 events in the AR. Remaining differences of the fake factors for electrons and muons between
 956 the measurement and application regions have been studied in simulated events and found to
 957 be small (see Fig. 48 in Ref. [115] for illustration). The FF for τ_h are measured separately for the
 958 loose and medium τ_h identification discriminants.

959 In the $2\ell ss + 1\tau_h$ and $3\ell + 1\tau_h$ channels, a modified version of the FF method is used. In this
 960 case, only the lepton selection criteria are relaxed in the AR, while the τ_h selection criteria are
 961 kept tight, and the FF are applied to the leptons only. The estimate of the fake background ob-
 962 tained in the $2\ell ss + 1\tau_h$ ($3\ell + 1\tau_h$) channel is given by the expression $N_{\text{pp}}^{\text{fake}}$ ($N_{\text{ppp}}^{\text{fake}}$) in Eq. 7. The
 963 τ_h is not considered in the count of fakeable objects, the expression suitable for events contain-
 964 ing 2 (3) fakeable objects is used, and the factors F_i refer to the leptons only. The contribution
 965 of background events in which the reconstructed leptons match prompt leptons at generator
 966 level and in which the reconstructed τ_h is due to the misidentification of a quark and gluon
 967 jet is taken from Monte Carlo simulation. The latter background contribution predominantly
 968 arises from $t\bar{t}W$, $t\bar{t}WW$, $t\bar{t}Z$ and diboson production. The motivation for this modification is
 969 that, in the $2\ell ss + 1\tau_h$ and $3\ell + 1\tau_h$ categories, in about one third of the selected $t\bar{t}H$ signal
 970 events the reconstructed τ_h is a misidentified quark or gluon jet (mainly for $H \rightarrow WW$ decays).
 971 These events would be included in the estimate of the fake background if the FF method were
 972 to be applied to the $2\ell ss + 1\tau_h$ and $3\ell + 1\tau_h$ channels without this modification. Therefore,
 973 these events could not be used for the purpose of inferring the production rate of the $t\bar{t}H$ sig-
 974 nal, which would reduce the signal-rate parameter (μ) sensitivity by $\sim 30\%$ in these channels.
 975 The loss in sensitivity can be reduced by applying tighter τ_h identification discriminants but
 976 the sensitivity would still be suboptimal compared to the one achieved using the modified FF

977 method for these channels.

978 7.2 Charge “flip” background

979 The charge “flip” background in the $2\ell ss + 0\tau_h$ and $2\ell ss + 1\tau_h$ categories is dominated by
 980 $t\bar{t} + \text{jets}$ events with two prompt leptons, produced in the decay $t\bar{t} \rightarrow bW^+\bar{b}W^- \rightarrow b\ell^+\nu\bar{b}\ell^-\bar{\nu}$,
 981 in which the charge of either prompt lepton is mis-measured. The background is estimated
 982 from data, following a strategy similar to the one used for the estimation of the fake back-
 983 ground. The control region used to estimate the charge flip background contains events that
 984 pass all selection criteria of the SR, except that the two leptons are required to be of opposite
 985 charge. The sum of the probabilities to mis-measure the charge of either one of the two leptons
 986 is then applied as an event weight. The charge misidentification rates for electrons are mea-
 987 sured using $Z/\gamma^* \rightarrow ee$ events and are parametrised as function of p_T and η of the electron.
 988 The measurement is described in Appendix K. The charge misidentification rates for muons are
 989 negligible [91]. As a consequence, the charge flip background in the $2\ell ss + 0\tau_h$ and $2\ell ss + 1\tau_h$
 990 categories is significantly higher for events containing either two electrons or one electron and
 991 one muon compared to events that contain two muons.

992 8 Systematic uncertainties

993 Various imprecisely-known or simulated effects may alter the event yield of the $t\bar{t}H$ and tH
 994 signals and of background processes, as well as the shape of the distributions in the discrim-
 995 inating observables that are used for the signal extraction. In this section we describe these
 996 effects, commonly called systematic uncertainties, and their impact on the yields in the various
 997 final states. The systematic uncertainties are modelled as nuisance parameters in a maximum-
 998 likelihood fit to extract the $t\bar{t}H$ and tH cross section which is detailed in Section 11. The nuisance
 999 parameters are allowed to change the event yield, accounting also for the migration of events
 1000 among regions and among different bins in the distributions fitted in each region. We consider
 1001 broadly two categories of nuisance parameters: those which purely affect the yield in a cate-
 1002 gory (*rate uncertainties*) are assigned a log-normal probability density function, whereas those
 1003 which affect also the shape of the distributions (*shape uncertainties*) are modelled via a polyno-
 1004 mial interpolation with a Gaussian constraint and are also allowed to change the event yields
 1005 in a category.

1006 The correlations between the various uncertainty sources across the three years of data-taking
 1007 are detailed in the text and summarized in Table 34.

- 1008 • **Trigger efficiency**

1009 The impact on the final discriminants due to the trigger efficiency is estimated by
 1010 varying the scale factors within its uncertainties. For events in the $2\ell ss + 0\tau_h$, $2\ell ss +$
 1011 $1\tau_h$, $2\ell ss + 1\tau_h$, $2\ell + 2\tau_h$, $3\ell + 0\tau_h$, $3\ell + 1\tau_h$ and $4\ell + 0\tau_h$ categories, these uncertain-
 1012 ties can be found in Table 30. For events in the $0\ell + 2\tau_h$, $1\ell + 1\tau_h$ and $1\ell + 2\tau_h$ chan-
 1013 nels, we consider the uncertainty in the τ_h legs of the lepton+ τ_h cross-triggers and
 1014 the di- τ_h triggers, which are provided by the TauPOG as a function of the p_T , η , ϕ
 1015 and decay mode of the hadronic τ . The uncertainty in the efficiency of the lepton leg
 1016 of the lepton+ τ_h cross-trigger, which we use in the $1\ell + 1\tau_h$ and $1\ell + 2\tau_h$ channels,
 1017 is neglected. The resulting effect on the signal (background) rates amounts to about
 1018 $XXX(YYY)\%$, while the effect on the shapes is found to be small and neglected in
 1019 the analysis. The trigger efficiency uncertainties are treated as uncorrelated across
 1020 the data taking years.

1021 • **Identification and isolation efficiency for e and μ**

1022 The loose electron and muon identification criteria defined in Tables 20 and 21 are
 1023 affected by uncertainties which we estimate according to the recommendations of
 1024 the Muon and EGamma POGs. For muons a total shape uncertainty is assigned
 1025 to the muon identification and isolation scale factors, while for the electrons the
 1026 uncertainties correspond to the electron identification and GSF tracking efficiency.
 1027 In both cases, the uncertainties are derived as a function of the lepton p_T and η .

1028 A second uncertainty source is associated to the tight lepton selection criteria de-
 1029 fined in Tables 20 and 21. This uncertainty is estimated in closure tests performed
 1030 separately for the three years and as a function of the lepton p_T and η . Details on
 1031 these closure tests can be found in Appendix L.

1032 The total uncertainty in the lepton identification and isolation efficiency is taken as
 1033 shape uncertainty. These uncertainties are correlated across years.

1034 • **Identification efficiency for τ_h**

1035 The uncertainty associated to the τ_h identification efficiency is estimated by the Tau
 1036 POG as a function of the p_T and decay mode of the τ leptons. This uncertainty is
 1037 dominated by statistical effects and is treated as uncorrelated across years, p_T bins
 1038 and decay modes.

1039 The uncertainty in reconstructing and identifying hadronic τ decays amounts to
 1040 XXX% [81] and is treated as fully correlated among the $0\ell + 2\tau_h$, $1\ell + 2\tau_h$, $2\ell ss +$
 1041 $1\tau_h$, $2\ell + 2\tau_h$ and $3\ell + 1\tau_h$ channels. The resulting effect on the normalization
 1042 amounts to XXX% (XXXX%) in the $1\ell + 1\tau_h$, $2\ell ss + 1\tau_h$ and $3\ell + 1\tau_h$ ($1\ell + 2\tau_h$
 1043 and $2\ell + 2\tau_h$) channels. This uncertainty is treated as correlated across the years.

1044 • **Energy scale of e, μ and τ_h**

1045 The energy scales of electrons and muons are known with an uncertainty of less than
 1046 1% and are neglected in the analysis.

1047 The uncertainties associated to the energy scale of τ_h are obtained by varying the
 1048 corresponding scale factor by its uncertainties, as defined in Table 31. Following the
 1049 recommendations of the Tau POG [105, 106], these uncertainties are uncorrelated
 1050 among different decay modes and years.

1051 • **Jet energy scale**

1052 The jet energy scale (JES) systematic uncertainties are evaluated by shifting the JES
 1053 applied to the reconstructed jets up and down by one standard deviation, following
 1054 the recommendations of the JetMET POG [118]. The events are then re-analyzed,
 1055 including the re-application of the jet-based selection and the computation of all
 1056 relevant kinematic quantities, to derive the varied kinematic distributions, which
 1057 enter as shape uncertainties (including rate effects) in the final fit.

1058 We consider the individual uncorrelated jet energy correction (JEC) uncertainty sources
 1059 provided by the JetMET POG:

- 1060 • Absolute[Stat][Scale][Sample][MPFBias]: flat absolute scale uncertainties
- 1061 • Fragmentation: high p_T extrapolation
- 1062 • SinglePion[ECAL][HCAL]: high p_T extrapolation
- 1063 • FlavorQCD: jet flavor
- 1064 • TimePtEta: JEC time dependence between the different eras
- 1065 • RelativeJER[EC1][EC2][HF] : η -dependence uncertainty from jet p_T reso-
 1066 lution (JER)

- 1067 • RelativePt[BB][EC1][EC2][HF]: half-difference between MPF method log-
1068 linear (default) and constant fits versus p_T
- 1069 • RelativeBal: full difference between log-linear fits of MPF and p_T balance
1070 methods
- 1071 • RelativeFSR: eta-dependence uncertainty due to correction for initial and
1072 final state radiation
- 1073 • RelativeStat[FSR][EC][HF] : statistical uncertainty in determination of η -
1074 dependence
- 1075 • PileUpDataMC: estimating 5% uncertainty on the data/MC scale factor
1076 for offset correction
- 1077 • PileUpPt[Ref][BB][EC1/2][HF]: pile-up offset dependence on jet p_T is es-
1078 timated from matched MC with and without PU overlay

1079 Since this analysis is moderately sensitive to the JEC mentioned above, we follow the
1080 prototype of the reduced set of uncertainty sources provided by the JetMET POG.
1081 This reduction groups the aforementioned uncertainties by detector regions, such
1082 that analyses using both central and forward jets get a reasonable modeling of the
1083 correlations between central and forward jets, without taking into account the full
1084 set of sources. This procedure results in a set of 11 JEC uncertainty sources which
1085 are treated as uncorrelated among themselves and across the years.

- 1086 • **b-tag efficiency and mistag rate**

1087 Uncertainties in the b tagging efficiencies and mistag rates as function of the jet p_T
1088 and η are provided by the BTV POG [108]. The effect of these uncertainties on the
1089 yields is evaluated by varying the data-to-MC correction factors described in Sec-
1090 tion 6.6 within their uncertainties and reanalyzing the events. We consider the three
1091 sources of b-tagging systematic uncertainty recommended by the BTV POG, which
1092 concern the impact of the JES uncertainties, the purity in the control sample used to
1093 derive the scale factors, and the statistics of the sample used to derive the scale fac-
1094 tors. We build separate shape templates for each individual source of uncertainty in
1095 the b-tag efficiency and in the mistag rate. The effect of the uncertainties on the b-tag
1096 efficiency and mistag rate is small compared to the statistical uncertainties, and the
1097 splitting of the uncertainties into individual sources is not absolutely necessary for
1098 our analysis. Considering these effects simplifies however future combinations with
1099 $t\bar{t}H$ analyses performed in other decay channels, notably $H \rightarrow b\bar{b}$, $H \rightarrow \gamma\gamma$ and
1100 $H \rightarrow ZZ \rightarrow 4\ell$. b-tag efficiency uncertainties of statistical origin are uncorrelated
1101 across years, while the experimental ones are correlated.

- 1102 • **E_T^{miss} resolution and response**

1103 Uncertainties in the E_T^{miss} resolution and response are accounted for by varying the
1104 jet energy scale and resolution within their respective uncertainties and recomputing
1105 E_T^{miss} and all E_T^{miss} related observables after each variation. The variations are
1106 performed using the `runMETCorrectionsAndUncertainties` tool developed
1107 by the JetMET POG [89].

- 1108 • **Signal rate**

1109 The signal rate is measured in units of the SM $t\bar{t}H$ and tH production rates; the
1110 measurement is therefore affected by uncertainties in the $t\bar{t}H$ and tH cross sections.
1111 The uncertainties associated to these processes are the following:

- 1112 • The uncertainty in the SM $t\bar{t}H$ cross section, computed at NLO accuracy,
1113 amounts to $^{+6.8\%}_{-10.0\%}$, of which $^{+5.8\%}_{-9.3\%}$ are due to missing higher orders and

1114 3.6% arises from uncertainties in the PDF and α_s [119].

- 1115 • The uncertainty in the SM tH cross section, computed at NLO accuracy,
 1116 amounts to $^{+XX\%}_{-YY\%}$, of which $^{+4.1\%}_{-6.7\%}$ are due to missing higher orders and
 1117 1.0% arises from uncertainties in the PDF and α_s [119]. The uncertainty in
 1118 the ITC tH cross section, computed at NLO accuracy, amounts to $^{+XX\%}_{-YY\%}$,
 1119 of which $^{+XXX\%}_{-XXXX\%}$ are due to missing higher orders and XXXXX% arises
 1120 from uncertainties in the PDF and α_s [119].
- 1121 • The uncertainty in the branching fraction for the H boson to decay into
 1122 WW and ZZ ($\tau\tau$) amounts to 1.54% (1.65%).
- 1123 • Uncertainties in the acceptance that are due to missing higher orders are
 1124 treated as shape systematics, as they affect the shape of the distribution in
 1125 the observable used for signal extraction. They are estimated by varying
 1126 the renormalization (μ_R) and factorization (μ_F) scales between 0.5 and 2
 1127 times their default values, with the constraint that $0.5 \leq \mu_F/\mu_R < 2$.

1128 Theoretical uncertainties associated to the signal rates and branching ratios are cor-
 1129 related across years.

1130 • Background rates

1131 The uncertainties associated to each of the background contributions are the follow-
 1132 ing:

- 1133 • The contribution of the WZ+jets background is known with an uncer-
 1134 tainty of 50%. The uncertainty represents the uncertainty in the extrap-
 1135 olation to the SR from the WZ+jets dominated control region described
 1136 in Section 9.3. It includes: the statistical uncertainty in the data yields in
 1137 the control region; the uncertainty in the b-tag efficiency and mistag rate;
 1138 and the uncertainty in the relative composition of light quark and gluon,
 1139 c quark and b quark jets in WZ+jets events contributing to the control
 1140 region and to the signal region. The relative compositions are estimated
 1141 in simulated events [103].
- 1142 • The uncertainty in the background arising from production of top quark
 1143 pairs in association with real or virtual photons amounts to 50%.
- 1144 • The yield of the fake background amounts to 30% in the $2\ell ss + 0\tau_h$, $2\ell ss +$
 1145 $1\tau_h$, $3\ell + 0\tau_h$, $3\ell + 1\tau_h$ and $4\ell + 0\tau_h$ categories and to 50% in the $0\ell + 2\tau_h$,
 1146 $1\ell + 1\tau_h$, $1\ell + 2\tau_h$, $2\ell os + 1\tau_h$ and $2\ell + 2\tau_h$ categories. Uncertainties in
 1147 the shape of the fake background arise from statistical uncertainties in
 1148 the MR and AR, from the subtraction of the prompt lepton contamination
 1149 in the MR, and from differences in the background composition between
 1150 MR (dominated by multijet background) and AR (dominated by $t\bar{t}+j$ jets
 1151 background). The latter is quantified by comparing the shape templates
 1152 obtained by selecting simulated $t\bar{t}+j$ jets in the AR and applying the event
 1153 weights obtained through Eq. (7) to the shape templates obtained by re-
 1154 quiring simulated $t\bar{t}+j$ jets to pass the event selection criteria of the SR. The
 1155 FF f_i for leptons are obtained from simulated multijet events that pass the
 1156 event selection criteria detailed in Section I, while the f_i for τ_h are ob-
 1157 tained from simulated $t\bar{t}+j$ jets that pass the selection criteria detailed in
 1158 Section J. We refer to the shape templates obtained from simulated $t\bar{t}+j$ jets
 1159 events passing the selection criteria of the SR as “nominal MC” shape
 1160 templates, and to those obtained from simulated $t\bar{t}+j$ jets events selected
 1161 in the AR and weighted by the expressions given by Eq. (7) as the “MC

closure” shape templates. The ratio of the nominal MC to the MC closure shape templates in each channel is fitted with a linear function and the deviation of the constant term (i.e. the slope) from 1 (0) is taken as an additional uncertainty. The fit is illustrated in Fig. 13 for the $1\ell + 2\tau_h$ channel.

- The yield of the charge flip background in the $2\ell ss + 0\tau_h$ and $2\ell ss + 1\tau_h$ categories is known with an uncertainty of 30%.
- No assumption is made on the rates of the irreducible $t\bar{t}W$, $t\bar{t}WW$, and $t\bar{t}Z$ backgrounds. The yield of these backgrounds is instead determined simultaneously with the rate of the $t\bar{t}H$ and tH signals by the maximum-likelihood fit used for the signal extraction, described in Section 9.
- An additional uncertainty of 30% is assigned to the contribution of $t\bar{t}W$, $t\bar{t}WW$, and $t\bar{t}Z$ backgrounds which arises in the $2\ell ss + 1\tau_h$ and $3\ell + 1\tau_h$ categories from events in which the reconstructed leptons are genuine prompt leptons and the reconstructed τ_h originates from the misidentification of a quark or gluon jet. These events are modelled using the MC simulation.
- An uncertainty of 50% is assigned to other, rare, backgrounds the contribution of which is modeled using the MC simulation.

The uncertainties associated to the fake background estimation techniques are treated as uncorrelated across the years, while the ones associated to the charge flips and conversions are treated as correlated. The uncertainties associated to electroweak and rare processes are treated as correlated across the years.

• **Luminosity**

The uncertainty in the integrated luminosity is split among correlated and uncorrelated effects across the years. The uncorrelated effects amount to 2.2% in 2016, 2.0% in 2017, and 1.5% in 2018 [120] [update ref?]. The correlated effects amount to 1.4% in 2015, 1.3% in 2017, and 2.1% in 2018. These effects are applied as rate uncertainties to all processes fully estimated from simulation (*prompt* processes).

• **Pileup**

Uncertainties in the instantaneous luminosity and on the pp inelastic cross section may affect the event yield of the $t\bar{t}H$ and tH signals and of backgrounds obtained from the MC simulation, as the efficiency to pass the event selection criteria detailed in Section 5 may vary with PU conditions. We vary the product of instantaneous luminosity and pp inelastic cross section, i.e. the number of PU interactions, by 5%, reweight simulated events to the different PU conditions, and rerun the analysis. We find that the effect on the signal and of background yields amounts to less than 1%.

• **L1 ECAL prefiring**

The effects due to the uncertainty in the L1 prefiring correction are taken into account by propagating the POG-provided uncertainties in the event weights to the event yield scale factors. Varied scale factors are obtained using event weights varied by their uncertainty.

Figure 13: Closure test of the FF method in the $1\ell + 2\tau_h$ channel. The distribution in the MVA discriminant that is used for the signal extraction in the SR, is obtained in two ways: by requiring simulated events (including $t\bar{t}$ +jets background) to pass the tight lepton and τ_h selection criteria (“fakes_mc”) and by requiring simulated events to pass the fakeable lepton and τ_h selection criteria and weighting the events by the FF f_i (“mcClosure”). The FF f_i are obtained from simulated events. The ratio of the two shape templates is fitted by a linear function and the deviation of the function from a constant of value one is considered as systematic uncertainty.

Uncertainty source	Correlated between years
Trigger efficiency	Yes/No
Identification and isolation efficiency for e and μ	Yes/No
Identification efficiency for τ_h	Yes/No
Energy scale of e , μ , and τ_h	Yes/No
Jet energy scale	Yes/No
b-tag efficiency and mistag rate	Yes/No
E_T^{miss} resolution and response	Yes/No
Signal rates	Yes/No
Background rates	Yes/No
Luminosity	Yes/No
Pileup	Yes/No
L1 ECAL prefiring	Yes/No

Table 34: Summary of the uncertainty source correlations across the three data-taking years.

Table 35: List of channels and methods used for signal extraction in the signal regions and in the control regions. The event categorization of the 3ℓ and 4ℓ control regions (CR) is described in Sec. 9.3.

Region	Signal extraction method	Channel
Signal regions	Multiclass Neural Networks	$2\ell ss + 0\tau_h$
		$2\ell ss + 1\tau_h$
		$3\ell + 0\tau_h$
	Boosted Decision Trees	$0\ell + 2\tau_h$
		$1\ell + 1\tau_h$
		$1\ell + 2\tau_h$
		$2\ell os + 1\tau_h$
		$2\ell + 2\tau_h$
Control regions	Object multiplicity	$3\ell + 1\tau_h$
		$4\ell + 0\tau_h$
Control regions	Object multiplicity	3ℓ -CR 4ℓ -CR

9 Signal extraction

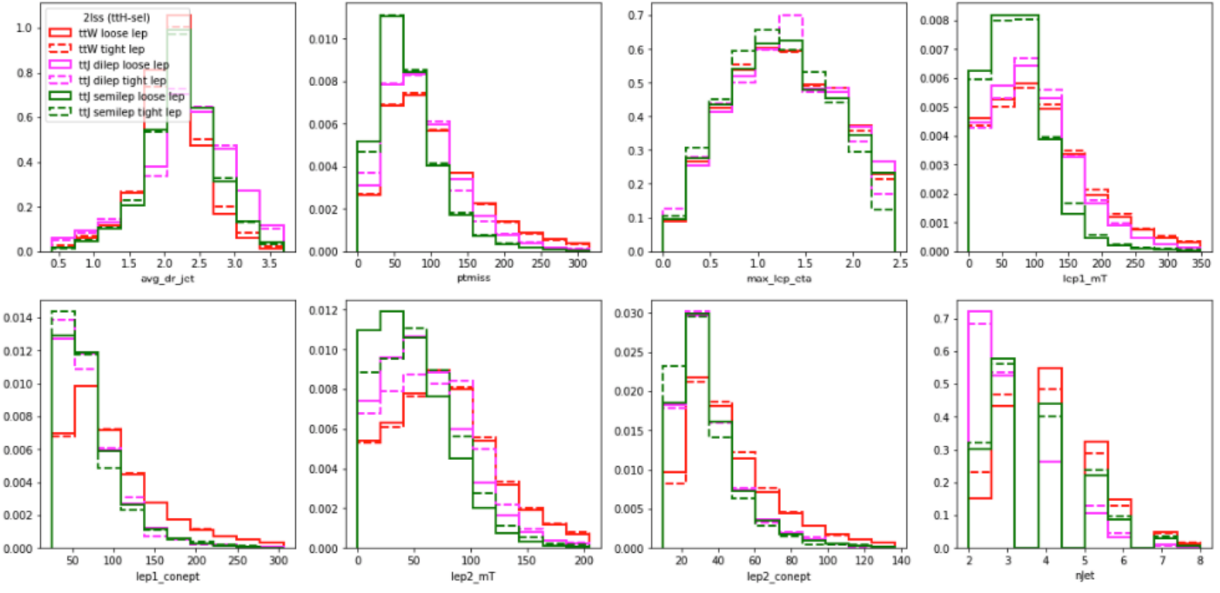
The rate of the tH and $t\bar{t}H$ signals is determined by means of a maximum-likelihood (ML) fit to the distributions in "discriminating" observables. The observables are chosen such that the maximal separation in a shape of the distribution is attained between the signals and the backgrounds. The differences in shape allows the fit to determine the signal rates more precisely compared to simply counting events, thereby improving the sensitivity of the analysis. The observables used in the different channels are explained in this section.

This analysis employs dedicated MVA-based signal extraction methods in each category, as the dominant signal and backgrounds vary within the different channels. The output of those MVA discriminators are the observables that will be used as discriminating variables in each of the categories. The MVA method used in each channel is designed based on the relative contribution of the signal processes and the reducible and irreducible backgrounds, as can be seen in Tables 56 to 59 of Appendix O, where the prefit yields are shown. For the majority of categories, the main background contributions come from irreducible $t\bar{t}W+jets$ and $t\bar{t}Z+jets$ processes, as well as from the reducible fake backgrounds detailed in Section 7, which mostly arise from $t\bar{t}$ decaying either semi-leptonically or di-leptonically.

One can split the ten channels in three groups based on the signal and background components. The first group corresponds to those categories that have a non-negligible tH contribution and are not completely dominated by the fake backgrounds ($2\ell ss + 0\tau_h$, $2\ell ss + 1\tau_h$ and $3\ell + 0\tau_h$). The second group corresponds to those categories that again have a non-negligible tH contribution, but where the fake background is more than ten times higher than the yield of the $t\bar{t}H$ and tH processes ($0\ell + 2\tau_h$, $1\ell + 1\tau_h$, $1\ell + 2\tau_h$ and $2\ell os + 1\tau_h$). Finally, the third group of categories are those containing a total of four objects, meaning leptons and τ_h , which have very limited statistics and also a negligible tH contribution ($2\ell + 2\tau_h$, $3\ell + 1\tau_h$ and $4\ell + 0\tau_h$). A summary of the signal extraction method used in each category can be found in Table 35.

For the first group of categories, which have considerable $t\bar{t}H$ and tH yields, as well as negligible fake background contributions, we employ dedicated multi-classification Deep Neural Networks (DNN) in order to exploit the different kinematics of the three signal processes ($t\bar{t}H$, tHq and tHW) and better constraint each of them. This allows to simultaneously separate the $t\bar{t}H$ and tH signals, as well as to separate the signals from the rest of the backgrounds. More

Figure 14: Normalized distributions of different input variables to the DNN in $2\ell ss + 0\tau_h$ for the dominant backgrounds $t\bar{t}W$ and $t\bar{t}+jets$, with the loose and tight lepton selections applied. An explanation of the variable naming can be found in Table 36.



1235 details on the methods used are shown in Section 9.1.

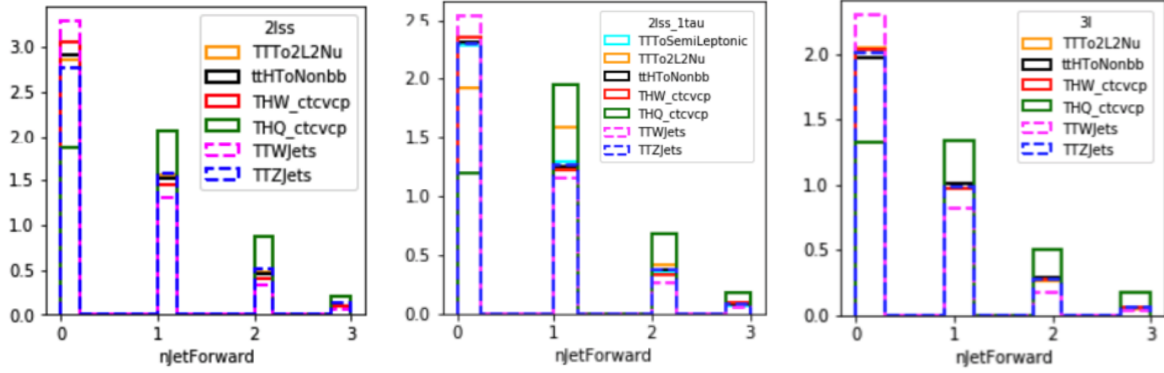
1236 For the second and third groups of categories, which are either dominated by fakes or have
 1237 very low statistics, we use dedicated MVA techniques based on Boosted Decision Trees (BDT),
 1238 in order to separate the sum of $t\bar{t}H$, tHq and tHW against the sum of the corresponding back-
 1239 grounds in each channel. More details on the methods used are shown in Appendix C.

1240 To enhance the sensitivity, we add in the final fit a 3ℓ and a 4ℓ control region, which are enriched
 1241 in the main irreducible backgrounds $t\bar{t}Z/WZ$ and ZZ , respectively, as will be described in
 1242 Section 9.3. Moreover, a dedicated $t\bar{t}W$ node is included in the $2\ell ss + 0\tau_h$ multiclassifier, which
 1243 is also added in the final fit to constrain this important background.

1244 For the training of the MVAs mentioned above, we make use of Monte Carlo samples based on
 1245 2016, 2017 and 2018 detector conditions. The list of such samples can be found in Tables 16, 17
 1246 and 18. In order to profit from an enlarged statistical sample in the training, we relax the lepton
 1247 and τ_h selections to the loose selection criteria. The kinematics and correlations amongst the
 1248 basic variables used in the MVAs are not significantly affected by this relaxation, as can be seen
 1249 in Figure 14 for the $2\ell ss + 0\tau_h$ category for illustration.

1250 When relevant for the category, we make use of two BDT-based taggers that are designed to
 1251 identify the jets arising from hadronic top decays and the jets arising from the decays of the
 1252 Higgs, namely the “Hadronic top tagger” (HTT) and the “Higgs jet tagger” (Hj), respectively.
 1253 The former aims to identify those cases in which the top quark decays to a bottom quark and
 1254 a W boson, which in turns decays hadronically. Its output score is employed as input to the
 1255 signal extraction methods in the categories a hadronic top is expected, i.e., $0\ell + 2\tau_h$, $1\ell + 1\tau_h$,
 1256 $1\ell + 2\tau_h$, $2\ell ss + 0\tau_h$, $2\ell ss + 1\tau_h$, $2\ell os + 1\tau_h$ and $3\ell + 0\tau_h$. The latter is designed to identify the
 1257 jets originating from a H boson decaying into two W bosons. Its output score is used as input to

Figure 15: Number of forward jets in the $t\bar{t}H$, tH and background processes for $2\ell ss + 0\tau_h$, $2\ell ss + 1\tau_h$ and $3\ell + 0\tau_h$ categories, respectively.



1258 the signal extraction methods in the $2\ell ss + 0\tau_h$ category. Details on training and performance
 1259 of both taggers can be found in the Appendices E and D.

1260 In the case of the $2\ell ss + 1\tau_h$ and $3\ell + 0\tau_h$ categories, discriminants based on the matrix element
 1261 method (MEM) are used as an alternative signal extraction method. These are designed to
 1262 increase the separation between the $t\bar{t}H$ signal and the $t\bar{t}W$, $t\bar{t}Z$ and $t\bar{t}$ backgrounds. Details
 1263 on the MEM computation and performance can be found in Appendix F.

1264 A simplified version of the signal extraction strategy is also designed to serve both as a cross-
 1265 check of the main procedure as well as to highlight the improvement obtained from the usage
 1266 of MVA techniques over an optimized approach relying only on the discriminant power of a
 1267 single variable in the multileptonic categories. More details on this approach can be found in
 1268 Appendix G.

1269 9.1 Signal regions with DNNs

1270 In this section, we describe the usage of multi-classification Deep Neural Networks (DNNs)
 1271 in the analysis. DNNs are utilised in the higher statistics categories where we also expect a
 1272 relatively large yield of the tH signal process, namely: $2\ell ss + 0\tau_h$, $2\ell ss + 1\tau_h$ and $3\ell + 0\tau_h$. The
 1273 architecture of the multi-class DNNs is designed such that each output node is used to target
 1274 a particular process as signal and the other processes used in the training as background. This
 1275 not only helps maximise the separation between the signal and the backgrounds, but allows for
 1276 categorisation by process (described later) allowing for categories that are optimally enriched
 1277 in the targeted process. This also provides a framework in which it's possible to simultaneously
 1278 separate the $t\bar{t}H$, tH and background processes. For that reason, we allocate separate classes
 1279 for the signals $t\bar{t}H$ and tH in all three categories. To achieve a better separation of the tH
 1280 signal, we use as target only the tHq component which has both a higher cross section in the
 1281 SM scenario and typically contains an enhanced quantity of forward jets, as can be seen in
 1282 Figure 15. This makes the it more distinct and a better target to the DNN. The background
 1283 classes in each category are chosen according to the most relevant background in each. In the
 1284 $2\ell ss + 0\tau_h$ channel, the DNN classifies the backgrounds as either $t\bar{t}W$ or $t\bar{t}+jets$ (labelled as
 1285 "other" seeing as in the signal region this category tends to be dominated by events from fake,
 1286 flip and conversion processes). In the $3\ell + 0\tau_h$ channel, the $t\bar{t}W$, $t\bar{t}Z$ and $t\bar{t}+jets$ backgrounds
 1287 are grouped in one class ("other"). In the case of the $2\ell ss + 1\tau_h$ category, all the backgrounds
 1288 are grouped in one class ("other").

1289 The networks take 25-40 input variables, which are detailed in Table 36. They consist on both
1290 low level variables, such as the three-momenta of the different objects, as well as high-level
1291 variables, such as angular variables, summed momenta and MT2 variables [?]. In general,
1292 these variables are related to the kinematic properties of the individual objects, lepton flavors,
1293 central and forward jet multiplicities, b-tagging discriminator, the Hadronic Top Tagger and
1294 the Higgs Jet Tagger and global variables. The choice of the input variables has been optimised
1295 according to the confusion matrices, the variable rankings, the ROC curves and the expected
1296 limits. For all variables, the agreement between Monte Carlo simulation and data has been
1297 checked, and only variables with good agreement are used as inputs to the DNN. Several plots
1298 showing the data-MC comparison for some input variables can be found in Section 9.3.

DRAFT

Table 36: List of variables used for the multi-classification DNNs for the $2\ell ss + 0\tau_h$, $2\ell ss + 1\tau_h$ and $3\ell + 0\tau_h$ categories.

Input variable	$2\ell ss + 0\tau_h$	$2\ell ss + 1\tau_h$	$3\ell + 0\tau_h$	Naming convention
Number of electrons	X	X	X	nElectron
Cone- p_T of selected leptons	X	X	X	lepX.conept
η of selected leptons	X	X	X	lepX.eta
ϕ of selected leptons	X	X	X	lepX.phi
Transverse mass of selected leptons	X	X	X	lepX.mT
Leading lepton charge	X	X	X	lep1_charge
Dilepton channel	X	X	X	Dilep_pdgId
p_T of selected tau	X	X	X	tau1_pt
η of selected tau	X	X	X	tau1_eta
ϕ of selected tau	X	X	X	tau1_phi
Invariant mass lepton+tau	X	X	X	mTauTauvisX
Charge sum of leptons+taus	X	X	X	sumLep-charge
Maximum lepton η	X	X	X	maxLep-eta
Minimum ΔR leptons+taus	X	X	X	minDr-Lep
Minimum ΔR leptons+jets	X	X	X	lepX-minDr-jet, mindr_lepX_jet
Minimum ΔR tau+jets	X	X	X	mindr_tau_jet
m_{T2}	X	X	X	mT2_top-2particle
Number of jets	X	X	X	nJet
p_T of the jets	X	X	X	jetX_pt
η of the jets	X	X	X	jetX_eta
ϕ of the jets	X	X	X	jetX_phi
Jets average ΔR	X	X	X	avg_dr_jet
Number of forward jets	X	X	X	nJetForward
p_T of leading forward jet	X	X	X	jetForward1_pt, leadFwdJet_pt
η of leading forward jet	X	X	X	jetForward1_eta, leadFwdJet_eta
Minimum $\Delta\eta$ leading fwd jet + jet	X	X	X	minDeltaLeadfwdJet-jet
Number of loose b-jets	X	X	X	nBJetLoose
Number of medium b-jets	X	X	X	nBJetMedium
Invariant mass of loose b-jets	X	X	X	mbb_loose
Invariant mass of medium b-jets	X	X	X	mbb_medium
MET _{LD}	X	X	X	MET_LD
Hadronic top tagger	X	X	X	res_HTT, res_HTT-CSVSORT4rd
Hadronic top p_T	X	X	X	HadTop_pt, HadTop_pt-CSVSORT4rd
Higgs jet tagger	X	X	X	Hjtagger, mvaOutPut_Hjtagger
Number of variables	40	37	37	

1299 A sequential deep neural network architecture was constructed using 5 fully-connected hidden
1300 layers with 16 node per layer. These were interspersed with a dropout layers between each to
1301 reduce the amount of overtraining. This was followed by 5 fully-connected hidden layers with
1302 16 node per layer without dropout layers. Finally 5 fully-connected hidden layers with 8 nodes
1303 per layer were added in series to reduce the dimensionality of the network slowly before the
1304 4 output nodes. Additional information on hyper-parameters used and loss functions can be
1305 found on the Appendix B. All final hyper-parameter settings are tuned to ensure maximum
1306 performance of the network.

1307 To train the networks, we populate a training region using an event selection that is the same
1308 selection as for the signal region but with a relaxed lepton selection to increase the statistics.
1309 To avoid over-training this dataset is divided into 2 statistically independent 'training' (80% of
1310 the dataset) and 'testing' (20% dataset) samples. Several tests are then performed that compare
1311 the performance of the network on the two datasets to ensure the training of a generalised
1312 neural network. The suppression of over-training is verified based on a comparison of several
1313 metrics evaluated in the training and testing datasets, namely: the area under the ROC curves,
1314 confusion matrices and distributions of events on the output nodes. The confusion matrices for
1315 the three channels can be found in Fig. 16. The ROC curves for the separation of each process
1316 from the rest of the regions in each of the DNNs can be found in Fig. 17 and 18.

1317 The DNN provides an output score associated to each node, which are then normalised using a
1318 softmax transformation. This allows for a direct interpretation of these scores as the probability
1319 an event belongs to a certain class. The process with the highest output score is then interpreted
1320 as the most probable process. Events are categorised according to their most probable process
1321 ensuring each event is only used in once. The distributions of the maximum output of the
1322 DNN's are the discriminants used as input to the fit.

1323 The number of events in the $2\ell ss + 0\tau_h$ and $3\ell + 0\tau_h$ categories is high enough to allow for sub-
1324 categorisation. This is used to enhance the signal and background separation. This choice of
1325 subcategorisation improves the expected limits and helps validate the data-driven fake back-
1326 ground estimation. The sub-categorisation is done as follows:

- 1327 • In the $2\ell ss + 0\tau_h$ category, events are sub-categorised depending on the flavour of
1328 the leptons ($ee/e\mu/\mu\mu$). This exploits the fact that the identification efficiencies are
1329 lower and misidentification rates are higher for electrons compared to muons, and
1330 the charge misidentification rates are sizeable for electrons and negligible for muons.
1331 It is intended to separate further the $t\bar{t}W$ component of the background from the $t\bar{t}H$
1332 and $t\bar{t}Z$ components.
- 1333 • In the $3\ell ss + 0\tau_h$ category, events are separated according to the number of jets
1334 that pass the medium WP of the b-tagging discriminant ($2b$ and $1b$). In the back-
1335 ground region of the $1b$ subcategory, which is by construction dominated by fakes,
1336 we further separate events according to the lepton flavour ($eee/ee\mu/e\mu\mu/\mu\mu\mu$), for
1337 the same reasons outlined before.

1338 To build the final distributions in each of the subcategories, we bin the discriminants construct-
1339 ing quantiles in the quantity of backgrounds. The number of bins is then decided upon based
1340 on both the error over content on the last bin and the total statistics, and the achieved expected
1341 limit.

Figure 16: Confusion matrices in the $2\ell ss + 0\tau_h$ (training region then application region), $2\ell ss + 1\tau_h$ and $3\ell + 0\tau_h$ categories, respectively.

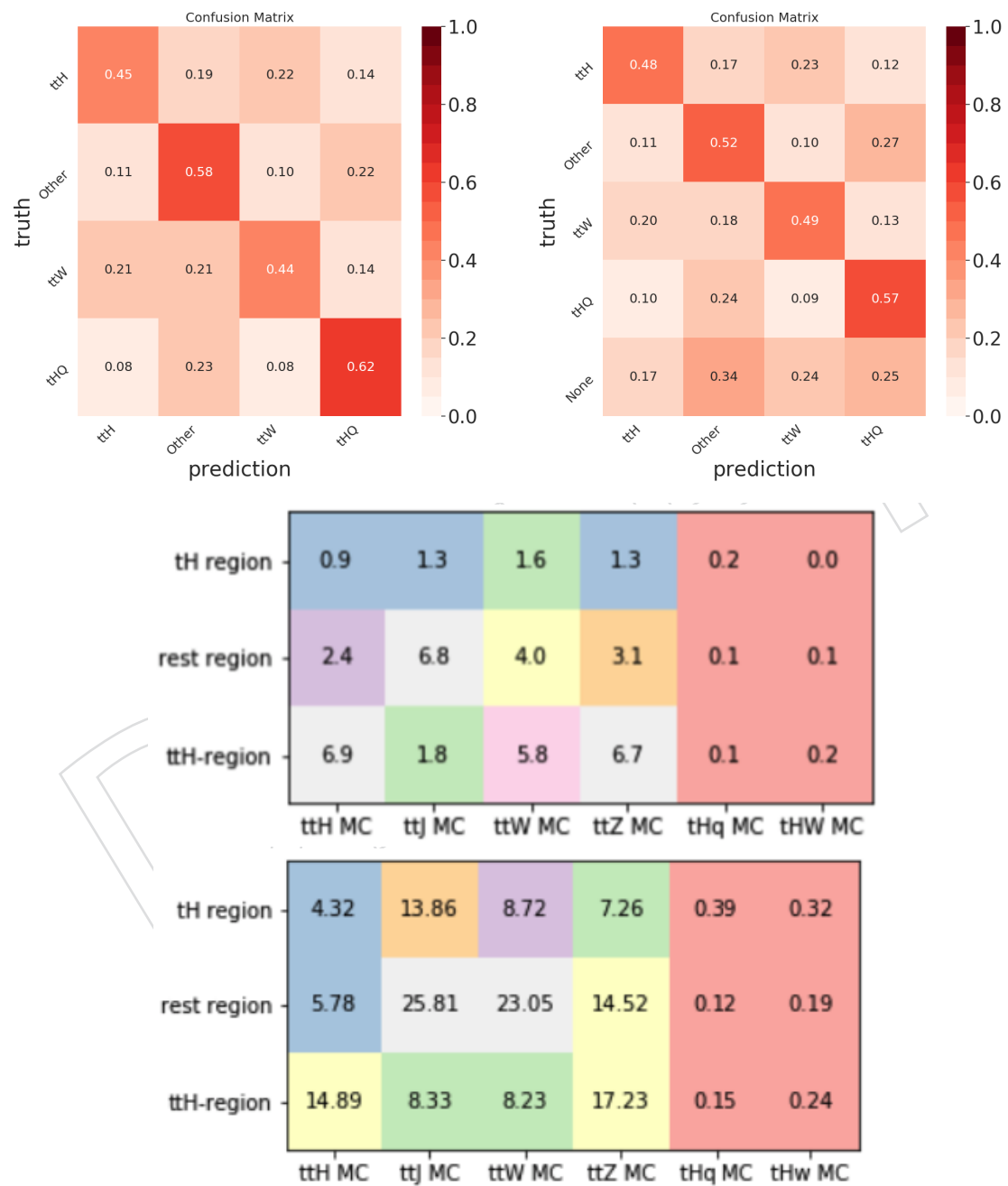


Figure 17: ROC curves for the separation of the process that define the DNN region from the rest of the processes considered on the DNN training in the $2\ell ss + 0\tau_h$ category.

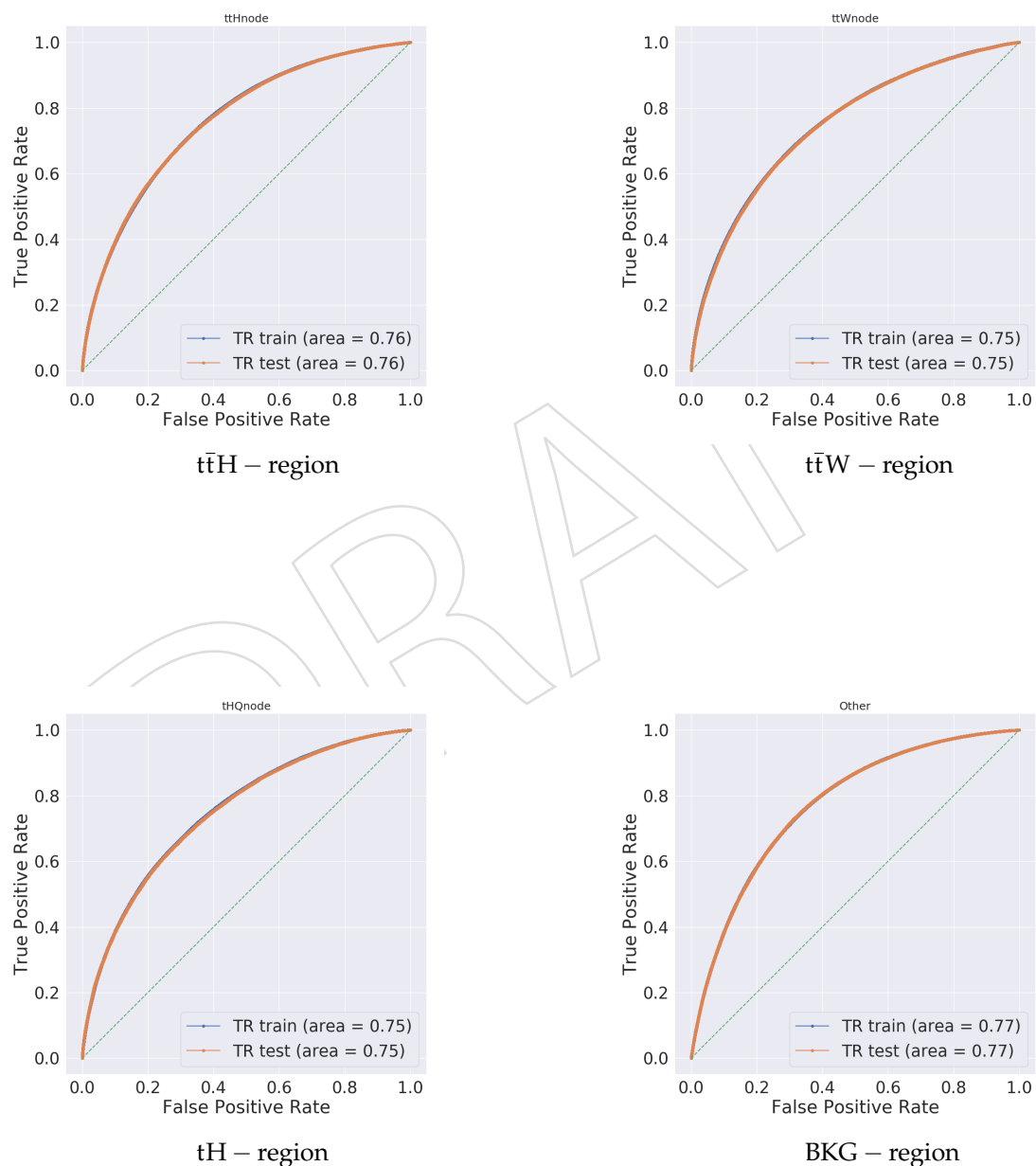
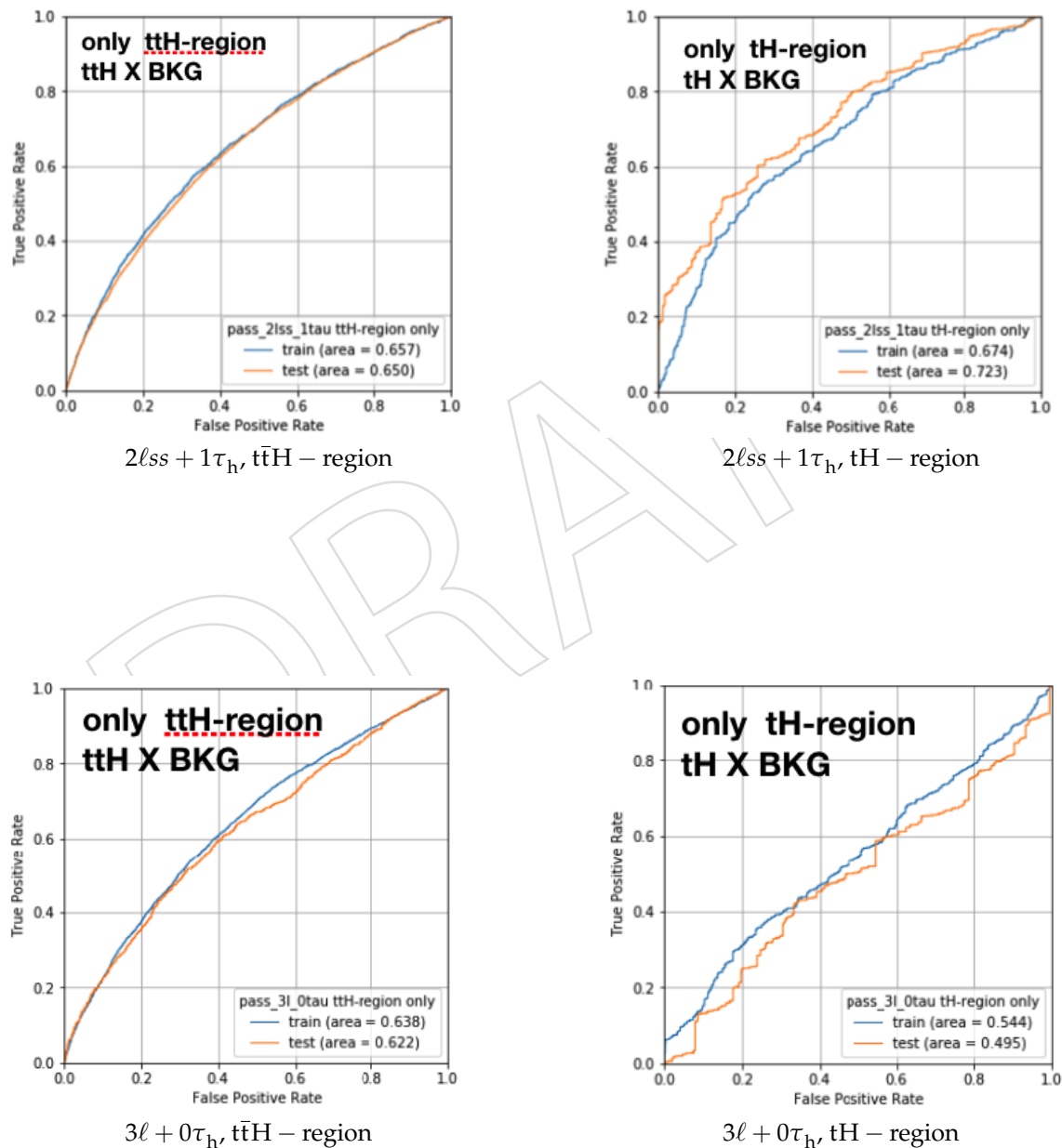


Figure 18: ROC curves for the separation of the process that define the DNN region from the rest of the processes considered on the DNN training for $2\ell ss + 1\tau_h$ category in the first two and $3\ell + 0\tau_h$ in the second row.



9.2 Signal regions with BDTs

In this section, we describe the Boosted Decision Trees (BDTs) that are used in the second and third group of categories detailed in Section 9. This concerns those categories that have a non-negligible $t\bar{H}$ contribution but also a large fake background ($0\ell + 2\tau_h$, $1\ell + 1\tau_h$, $1\ell + 2\tau_h$ and $2\ell os + 1\tau_h$), as well as those categories which are statistically limited and have a negligible $t\bar{H}$ contribution ($2\ell + 2\tau_h$, $3\ell + 1\tau_h$ and $4\ell + 0\tau_h$). In this section we describe the implementation of these BDTs, the input variables used and the performance achieved.

A single BDT is trained in each category, and is aimed to separate the $t\bar{H}$ signal from the sum of the backgrounds. The list of samples used for the training can be found in Tables 16, 17 and 18. In the $1\ell + 1\tau_h$ and $0\ell + 2\tau_h$ categories, the background processes used for training are $t\bar{t}W$, $t\bar{t}Z$, $t\bar{t}$ and Drell-Yan. For the rest of the channels, we train against the $t\bar{t}W$, $t\bar{t}Z$ and $t\bar{t}$ backgrounds. For the training we balance the signal and the sum of the backgrounds to the same sum of weights.

The BDTs take input variables related to the object multiplicities, the jet b-tagging score, the flavor of the leptons, some basic kinematic properties of the objects, geometrical relations between the objects, the Hadronic Top Tagger score and other global variables. In the $0\ell + 2\tau_h$ and $1\ell + 1\tau_h$ category, the jets that have not entered the computation of the hadronic top are used to reconstruct a second hadronic top, which also enters as input to the BDTs in these categories. In the $0\ell + 2\tau_h$, $1\ell + 1\tau_h$, $1\ell + 2\tau_h$, $2\ell os + 1\tau_h$ and $2\ell + 2\tau_h$ categories, we make use of the SVFit mass of the leading $\tau_h + \tau_h$ or $\ell + \tau_h$ collection pair, as introduced by the $gg \rightarrow H \rightarrow \tau\tau$ analysis [121].

The BDTs have been trained with the `xgboost` algorithm. The choice of variables has been optimized according to their relative importance in terms of signal/background discriminating power. This variable ranking can be found in Fig. 19. The choice of the hyperparameters used in the training has been done evaluating the ROC curves and the expected limits. The ROC curves showing the separation of the $t\bar{H}$ process from the rest of backgrounds can be found in Fig. 20. In these same figures information on the choice of hyperparameters can be found.

Table 37: List of variables used for the multi-classification BDTs.

Input variable	0 $\ell + 2\tau_h$	1 $\ell + 1\tau_h$	1 $\ell + 2\tau_h$	2 $\ell + 2\tau_h$	2 $\ell os + 1\tau_h$	2 $\ell + 2\tau_h$	3 $\ell + 1\tau_h$	4 $\ell + 0\tau_h$	Naming convention
Cone- p_T of $\ell(s)$	X	X	X	X	X	X	X	X	lepX.conept
p_T of $\tau_h(s)$	X	X	X	X	X	X	X	X	tauX.pt
Transverse mass of $\ell(s)$	X	X	X	X	X	X	X	X	lepX.mT
Transverse mass of $\tau_h(s)$	X	X	X	X	X	X	X	X	lepX.mT
Transverse mass of $\ell+\tau_h$'s system	X	X	X	X	X	X	X	X	massL3
Visible mass of leading τ_h/ℓ and τ_h pair	X	X	X	X	X	X	X	X	mTauTauVis
SVFit mass of leading τ_h/ℓ and τ_h pair	X	X	X	X	X	X	X	X	mTauTau
Charge sum of ℓ and τ_h	X	X	X	X	X	X	X	X	charge_lep-tau
Maximum η of $\ell(s) / \tau_h(s)$	X	X	X	X	X	X	X	X	max_Lep-eta
ΔR between $\ell''s$	X	X	X	X	X	X	X	X	dr_leps
ΔR between $\tau_h''s$									drtaus, dr_tau
ΔR between ℓ and τ_h									dr_lep-tau
ΔR between OS ℓ and τ_h									dr_lep-tau_OS
ΔR between SS ℓ and τ_h									dr_lep_tau_SS
Minimum ΔR between $\ell(s)$ and $\tau_h(s)$	X	X	X	X	X	X	X	X	min_dr_Lep
Minimum ΔR between $\ell(s)$ and jets	X	X	X	X	X	X	X	X	Lep_min_dr_jet, mindr_lepX_jet
Minimum ΔR between $\tau_h(s)$ and jets	X	X	X	X	X	X	X	X	mindr_tauX_jet
$\cos^*\theta$ of τ_h/ℓ and τ_h pair	X	X	X	X	X	X	X	X	cosThetaS_hadTau, costS_tau
Number of jets	X	X	X	X	X	X	X	X	nJet
Average ΔR between jets	X	X	X	X	X	X	X	X	avg_dr_jet
Number of loose b-jets	X	X	X	X	X	X	X	X	nBJetLoose
Number of medium b-jets	X	X	X	X	X	X	X	X	nBJetMedium
Invariant mass of loose b-jets	X	X	X	X	X	X	X	X	mbb_loose
MET_{LD}	X	X	X	X	X	X	X	X	MET_LD
Has pair of SFOS loose $\ell''s$									has_SFOS
Minimum invariant mass of loose ℓ pairs									massL,massL4
Hadronic top tagger	X	X	X	X	X	X	X	X	res_HTT
Second Hadronic top tagger	X	X	X	X	X	X	X	X	res_HTT_2
Hadronic top p_T	X								HadTop_pt
Second Hadronic top p_T									HadTop_pt_2
Number of variables	18	18	17	18	18	9	9	7	

9.3 Control regions

Several regions are defined in order to test the Monte Carlo modeling of the most relevant backgrounds that are estimated using simulations: $t\bar{t}Z$, WZ and ZZ . A $t\bar{t}W$ control region is also built in the $2\ell ss + 0\tau_h$ region using the DNN discriminant, as has been described in Section 9.1. These regions are included in the signal extraction fit, providing an *in situ* estimation of these backgrounds.

The two control regions included in the analysis consist of 3 and 4 reconstructed leptons in the final state, denoted as 3ℓ - and 4ℓ -CR, respectively. These regions are defined by removing and inverting some of the selection cuts in the $3\ell + 0\tau_h$ and $4\ell + 0\tau_h$ categories, and are therefore orthogonal to all the regions of the analysis. The sensitivity to these background processes is driven by the 3ℓ -CR, however, the 4ℓ -CR provides a reasonably sensitive alternative measurement of these processes.

Additionally, three control regions enriched in $t\bar{t}Z$, WZ , and $t\bar{t}Z$ and non-prompt leptons are defined to check the modeling of the input variables to the $3\ell + 0\tau_h$ and $2\ell ss + 0\tau_h$ signal extraction discriminants. These regions are not included as they are in the signal extraction fit, as they overlap with some of the other regions.

9.3.1 3ℓ control region

This region targets events from the $t\bar{t}Z$ and the WZ processes. The event selection criteria applied in this region are identical to those applied in the $3\ell + 0\tau_h$ category, except that events containing a pair of loose leptons of the same flavor and opposite charge with mass $|m_{\ell\ell} - m_Z| < 10$ GeV are not vetoed. Moreover, the jet and b-tagging discriminator selections are not applied in this case.

For the signal extraction fit, events are classified in 12 different categories according to the number of jets and medium WP b-tagged jets: 0 b-tagged jets with 1, 2, 3 or more than 3 jets; 1 b-tagged jet with 2, 3, 4 or more than 4 jets, and more than 1 b-tagged jets with 2, 3, 4 or more than 4 jets. Additionally, events are categorized according to the flavor of the leptons as eee , $e\mu\mu$ or $\mu\mu\mu$. The categories with lower jet and b-jet multiplicities are sensitive to WZ , while categories with higher jet and b-jet multiplicities are enriched in $t\bar{t}Z$ events.

9.3.2 4ℓ control region

This region targets events from the ZZ process. The event selection criteria applied in this region are identical to those applied in the $4\ell + 0\tau_h$ category, except that events must contain a pair of loose leptons of the same flavor and opposite charge with mass $|m_{\ell\ell} - m_Z| < 10$ GeV. Moreover, the jet and b-tagging discriminator selections are not applied in this case.

For the signal extraction fit, events are classified in 4 different categories:

- Events with two pairs of opposite-sign same flavor leptons with masses compatible with the Z boson.
- Events with exactly one pair of opposite-sign same flavor leptons with a mass compatible with the Z boson and no jets.
- Events with exactly one pair of opposite-sign same flavor leptons with a mass compatible with the Z boson and exactly 1 medium WP b-tagged jet.
- Events with exactly one pair of opposite-sign same flavor leptons with a mass compatible with the Z boson and more than one medium WP b-tagged jet.

Figure 19: Ranking of importance of the variables used in the training of the BDTs used for signal extraction. The naming convention for the variables follow the last column of Table 37.

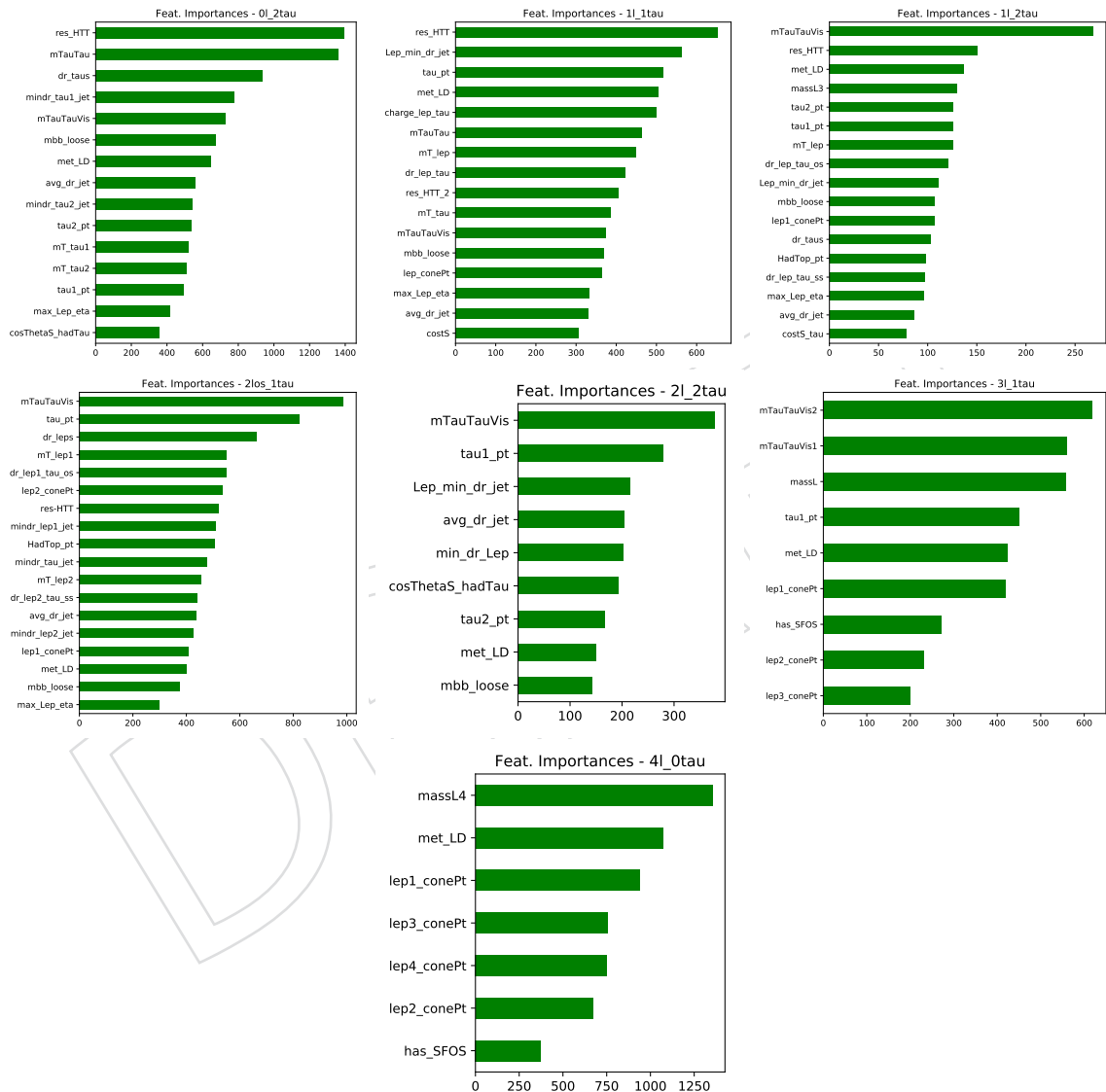


Figure 20: ROC curves for separation of the $t\bar{t}H$ process from the rest of the backgrounds for the the BDTs used for signal extraction. The hyperparameters used on the training that are not the default on XGBoost are marked inside the figures.

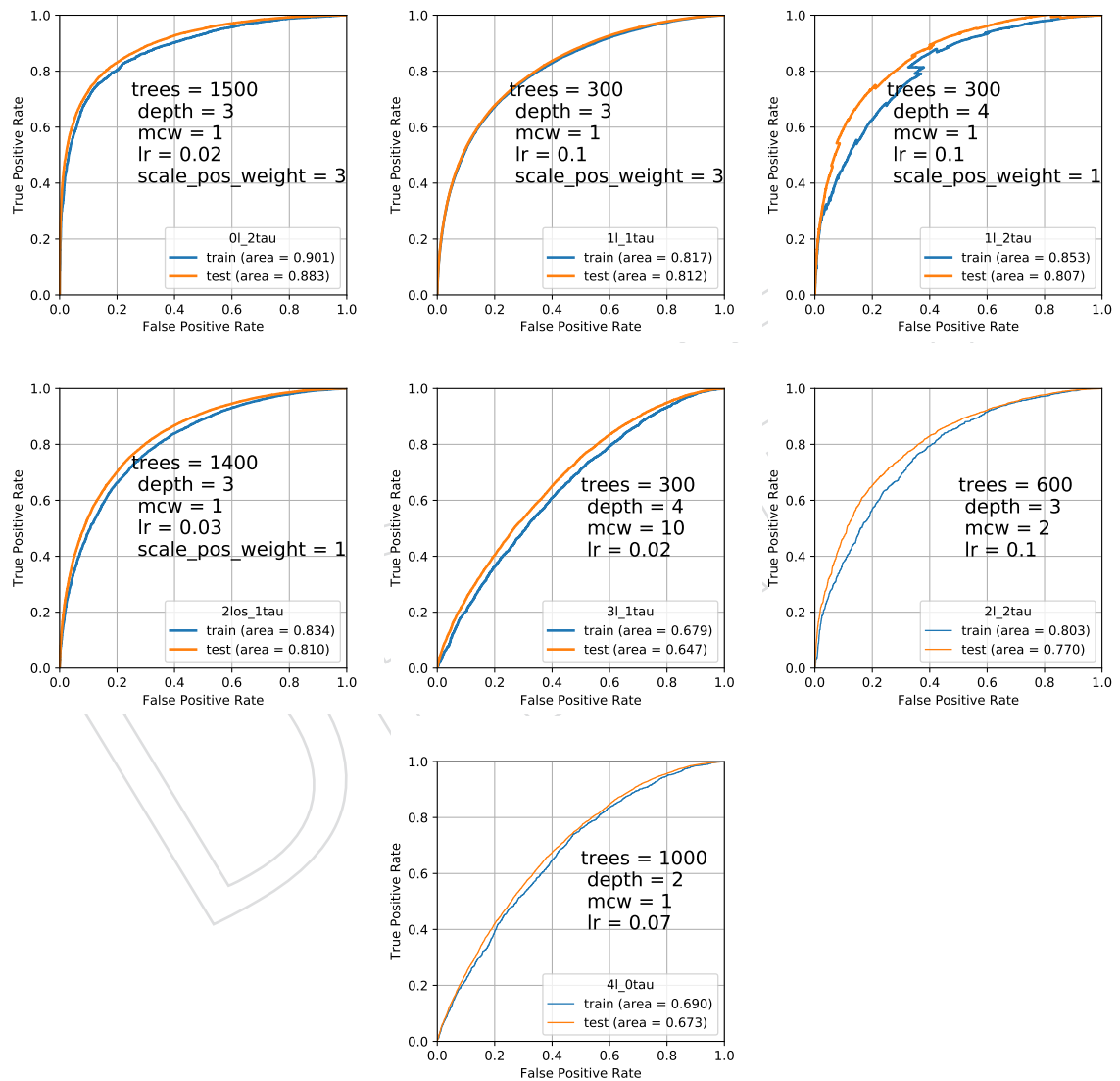
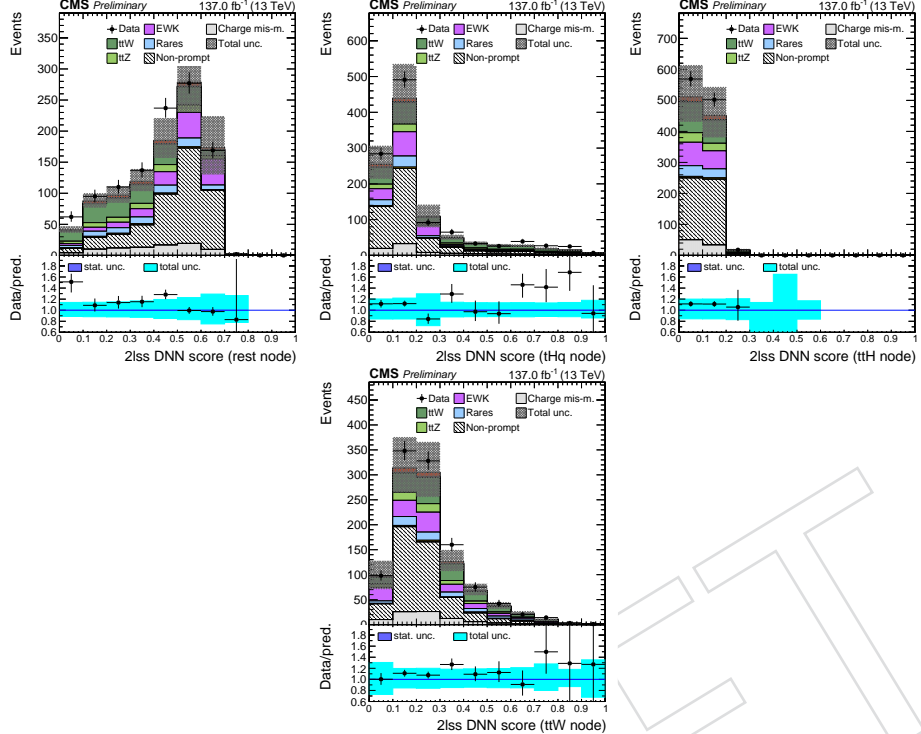


Figure 21: Data/SM agreement plots for some input variables of the $2\ell ss + 0\tau_h$ DNN in a region with 3 jets.



1411 9.3.3 Modeling of DNN inputs

1412 **9.3.3.1 Modeling $2\ell ss + 0\tau_h$ DNN** The modeling of the input variables to the $2\ell ss + 0\tau_h$
 1413 in checked in a region enriched in non-prompt leptons and $t\bar{t}Z$. Such a region is defined by
 1414 vetoing events in the $2\ell ss$ signal region that have a jet multiplicity, including forward jets,
 1415 different from 3. The data/SM agreement plots for the output scores of the $2\ell ss + 0\tau_h$ DNN can
 1416 be seen in Fig. 21. The modeling of each one of the input variables can be found in Appendix A.

1417 **9.3.3.2 Modeling $3\ell ss + 0\tau_h$ DNN** Two regions are defined to check the input variables
 1418 of the $3\ell ss + 0\tau_h$ DNN in $t\bar{t}Z$ and WZ events. The first is checked by reversing the Z veto in
 1419 the $3\ell ss + 0\tau_h$ signal region and selecting only events with at least two central jets. The control
 1420 region enriched in WZ events is defined by inverting the b tagged jet multiplicity requirement
 1421 in the $t\bar{t}Z$ region.

1422 Data/SM agreement in these two regions for the score of the DNNs is shown in Figs. 22 and
 1423 23. The modeling of each one of the input variables can be found in Appendix. A.

Figure 22: Data/SM agreement plots for the output scores of the 3ℓ in $t\bar{t}Z$ events.

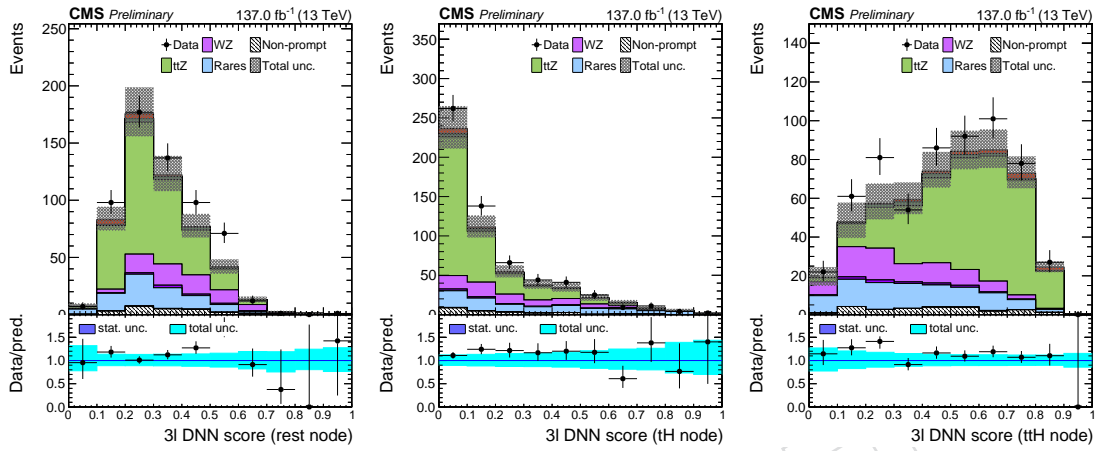
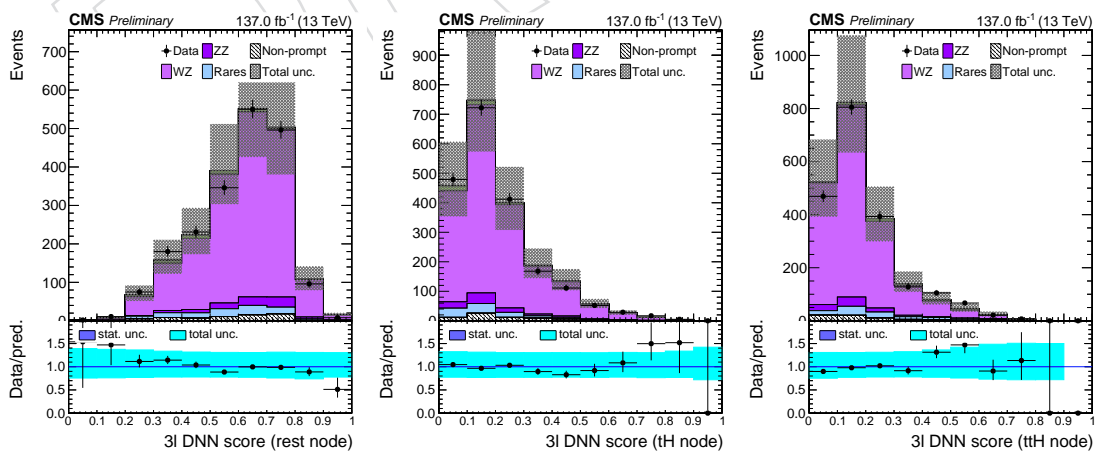


Figure 23: Data/SM agreement plots for the output scores of the 3ℓ in WZ events.



1424 10 Theory elements to BSM interpretation

1425 In the context of a simultaneous tH and tt>H signal extraction and in order to explore possible
 1426 BSM scenarios, we interpret the Higgs couplings results in this analysis in the so-called κ -
 1427 framework. For that, we introduce the Higgs-W and Higgs-top coupling modifiers¹, labelled
 1428 κ_V and κ_t , respectively, which scale the cross-sections and partial widths relative to the SM,
 1429 allowing for BSM contributions to enter the relevant loops and decays. The variations of these
 1430 κ -coefficients lead to different cross-section values in tH and tt>H and different event kinematics
 1431 in the tH processes. We assume that the reader is familiar with the κ -framework: a more
 1432 comprehensive description can be found in [123].

1433 In the following, the parametrization and modeling of the three process of interest (tt>H, tHq
 1434 and tHW), as a function of κ_V and κ_t is described. The tt>H cross section scales as $\sigma_{t\bar{t}H} \propto \kappa_t^2$,
 1435 while the tHq and tHW cross section dependencies take the expressions:

$$\sigma_{tHq} = (2.63 \kappa_t^2 + 3.58 \kappa_V^2 - 5.21 \kappa_t \kappa_V) \times \sigma_{tHq}^{SM} \quad (8)$$

$$\sigma_{tHW} = (2.91 \kappa_t^2 + 2.31 \kappa_V^2 - 4.22 \kappa_t \kappa_V) \times \sigma_{tHW}^{SM} \quad (9)$$

1436 The coefficients in Eqs. 8 and 9 have been calculated in with MadWeight using the model
 1437 from [124].

1438 Regarding the different Higgs production modes, we take into account additional single Higgs
 1439 processes that have non-negligible yields resulting from the coupling modifier variations. These
 1440 processes are the associated production of the Higgs with gauge bosons (VH), the gluon fusion
 1441 (ggH) and Vector Boson Fusion (VBF) processes. The yields for such processes can be found
 1442 in Table[XXX], where pre-fit yields are shown. The ggH process can, in general, be modified
 1443 by κ_g , but for the simplification here we set it to $\kappa_g = 1.0$. Moreover, we assume a uniform
 1444 coupling of the Higgs boson to the weak sector, i.e., $\kappa_V = \kappa_Z = \kappa_W$.

1445 In what regards the Higgs decays, the branching ratios are κ -dependent. In this analysis, the
 1446 relevant κ values are κ_τ , κ_V , κ_μ and $\kappa_{Z\gamma}$. Since we expect negligible contributions from the
 1447 H $\rightarrow \mu\mu$ and H $\rightarrow Z\gamma$ processes in our signal regions, we consider $\kappa_{Z\gamma} = 1.0$. Moreover, light
 1448 fermions are treated universally with the parameter κ_f , defined as $\kappa_f = \kappa_\tau = \kappa_\mu$.

1449 To account for the κ_V and κ_t variations, the tH Monte Carlo samples are generated with a set of
 1450 event weights corresponding to different values of the Higgs-top and Higgs-W coupling modi-
 1451 fiers. We consider k_T variations which span from -3 to 3 in steps of 0.25, and κ_V variations which
 1452 span between 0.5 and 1.5 in the steps of 0.5. As an illustration of the kinematical variations in
 1453 the tH processes as a function of the coupling modifiers can be found in Fig. 24. It should be
 1454 noted that the dedicated multivariate discriminants described in Section 9 were developed
 1455 for the SM case ($\kappa_t = 1.0$ and $\kappa_V = 1.0$).

1456 In Fig. 25 we show the variation the total cross section of the Higgs processes when κ_t and κ_V
 1457 are varied within the considered range. For completeness, in Table 38 we show the present
 1458 precision of the combined ATLAS + CMS measurement of the Higgs coupling modifiers con-
 1459 sidering no BSM physics contributing to the invisible Higgs decays [125].

¹ At one loop level, corrections to the Higgs trilinear coupling κ_λ are important for the Higgs production [122]. Since we do not have sensitivity to such modifications, we ignore the tt>H dependency on κ_λ in this document.

Figure 24: Variation of the kinematics of the tHq (upper row) and tHW (bottom row) processes in the $2\ell ss + 0\tau_h$ category for several values of κ_t .

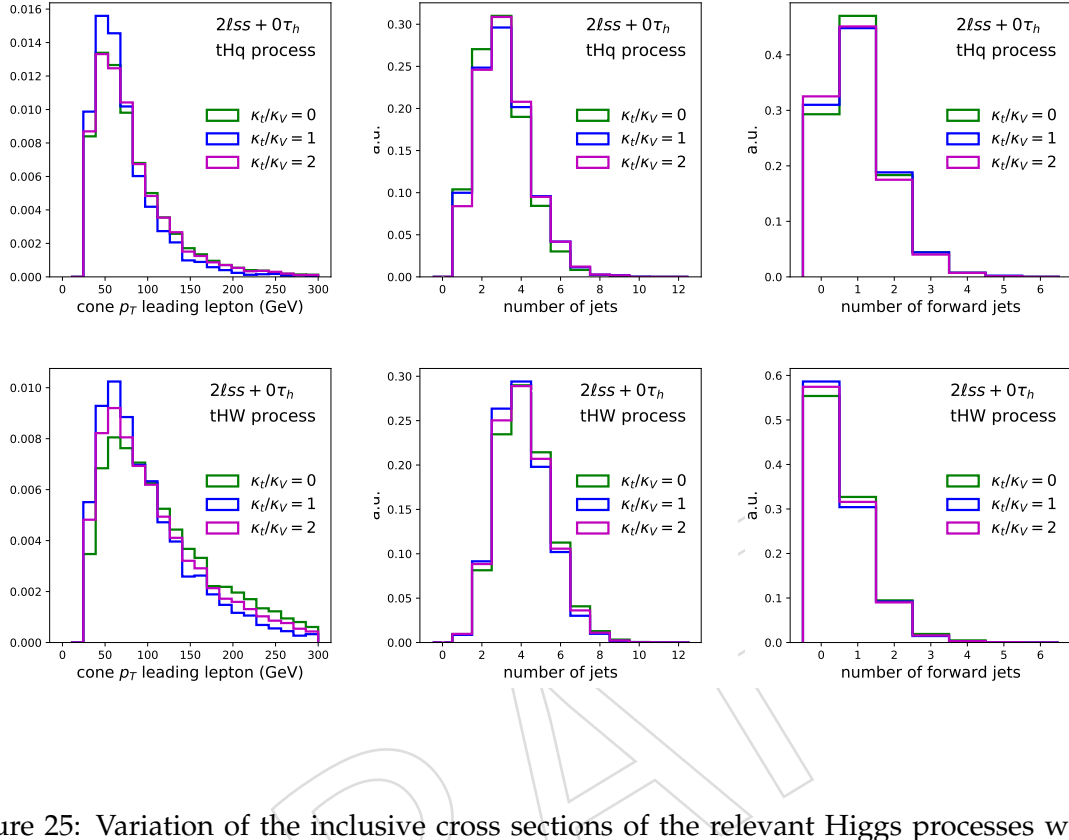


Figure 25: Variation of the inclusive cross sections of the relevant Higgs processes when (a) varying κ_t and keeping $\kappa_V = 1.0$ and (b) varying κ_V and keeping $\kappa_t = 1.0$.

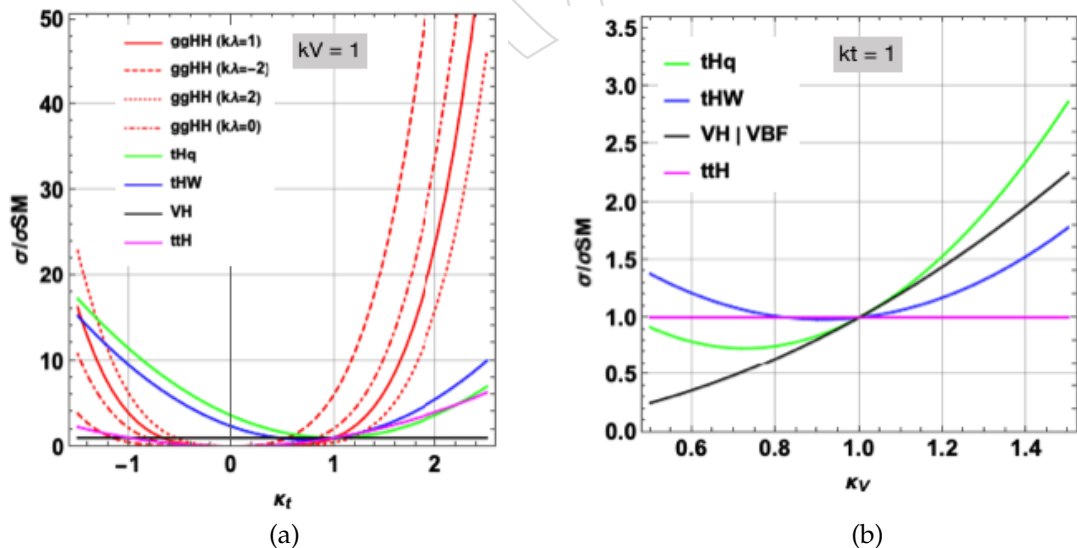


Table 38: Experimental constraints from ATLAS + CMS on the Higgs coupling multipliers considering no BSM physics contributing to invisible Higgs decays [125].

Coupling modifier	Measured value
κ_t	$1.40^{+0.24}_{-0.21}$
κ_Z	$[-1.08, -0.88]$ or $[0.94, 1.13]$
κ_W	$0.87^{+0.21}_{-0.13}$
$\kappa_{Z\gamma}$	1.09 ± 0.28
κ_μ	—
$ \kappa_\tau $	$0.84^{+0.15}_{-0.11}$
$ \kappa_g $	$0.78^{+0.13}_{-0.10}$

1460 11 Results

1461 The signal strength modifier $\mu = \sigma/\sigma_{SM}$ of the tH and $t\bar{t}H$ production cross-sections are deter-
 1462 mined in a simultaneous binned profile likelihood fit to the data across all analysis categories.
 1463 The systematic uncertainties described in Section 8 are taken into account via nuisance param-
 1464 eters, which allow for variations in the shape and the normalization of the final discriminant
 1465 distributions during the fit. In Section 11.1 we show the results assuming the SM scenario (k_T
 1466 $= \kappa_V = 1$), while in Section 11.2 we extend the results to BSM interpretations through the Higgs
 1467 couplings modifiers, as described in Section 10.

1468 In all the results presented the background components are divided in a consistent way. For
 1469 the $t\bar{t}W$, $t\bar{t}Z$, WZ and ZZ processes, which have sizable yields in the leptonic categories, we
 1470 include enriched control regions which are added into the final fit. The sum of background con-
 1471 tributions from Z+jets, W+jets, WW and Drell-Yan production is referred to as “electroweak”
 1472 (EWK) background in all categories, but in the case of the $0\ell + 2\tau_h$ and $1\ell + 1\tau_h$ categories, we
 1473 consider the Drell-Yan as a separate process in order to add the associated nuisance parameters
 1474 described in Section 8. The contribution of triboson production and of the few other “exotic”
 1475 processes described in Section 2 is referred to as “other” background. Background contribu-
 1476 tions arising from single top and top quark pair production are fully covered by the estimates
 1477 of the charge flip backgrounds. With the exception of the $0\ell + 2\tau_h$ and $1\ell + 1\tau_h$ categories, the
 1478 top quark pair production is fully covered by the estimates of the fake background.

1479 In the following sections we present a selected set of results. For the full results, the reader
 1480 can refer to Appendix O. Additionally, preliminary results on the measurement of the $t\bar{t}H$
 1481 differential cross-section as a function of the Higgs boson transverse momentum can be found
 1482 in Appendix H. The impact of the nuisances on the fits with full run II and per era can be found
 1483 on Figs. ?? to ?? in Appendix ??.

1484 11.1 Standard Model interpretation

1485 The number of events selected in different categories and in the control regions included in
 1486 the fit is compared to the contributions of the $t\bar{t}H$ and tH signals and of different background
 1487 processes in Tables 56 to 59 of Appendix O. The pre-fit distributions of the discriminating
 1488 observables that are used for signal extraction in the signal regions and in the control regions
 1489 can be found in Section O. The post-fit distributions of the discriminating observables that
 1490 are used for signal extraction in the signal regions and in the control regions can be found in
 1491 Figures 26 to 31 below.

1492 In Fig. 32 and Table 39 we show the measured signal rate multipliers ($\mu = \sigma/\sigma_{SM}$) under the
 1493 hypothesis that the processes $t\bar{t}H$ and tH are SM-like for all ten signal regions separately and
 1494 for the combination of signal regions with the control regions in the fit. In Fig. 33 we show
 1495 the same, but from fits considering separately each era. In Table 40 we show μ for the $t\bar{t}H$, tH,
 1496 $t\bar{t}W$ and $t\bar{t}Z$, processes individually extracted from the fit with all signal and control regions. In
 1497 Fig. 34 we show the 2D likelihoods between the $t\bar{t}H$ process and the tH, $t\bar{t}W$ and $t\bar{t}Z$ processes.

1498 11.2 Beyond the Standard Model interpretation

1499 In this section we show the constraints on the Higgs coupling within the κ framework described
 1500 in Section 10, considering the kinematic modifications on the tH processes as a function of the
 1501 different k_T and κ_V values. As an illustration of the impact of the couplings modifications on
 1502 the tH processes, in Fig. 35 we show the evolution of acceptance \times efficiency of the tHq and
 1503 tHW processes in terms of k_T/κ_V . In Fig. 36 we show the limits on the signal strength of the

Figure 26: Distributions in the discriminating observables used for the signal extraction in the $2\ell ss + 0\tau_h$ category in the different regions: (a) the $t\bar{t}H$ – region, (b) the tH – region, (c) the $t\bar{t}W$ – region and the (d) BKG – region. The post-fit rates and uncertainties are used. [PLACEHOLDER - PREFIT, BLINDED - THERE IS A BUG IN THE IMPLEMENTATION OF THE DNN WEIGHTS, MOSTLY AFFECTING THE THQ NODE]

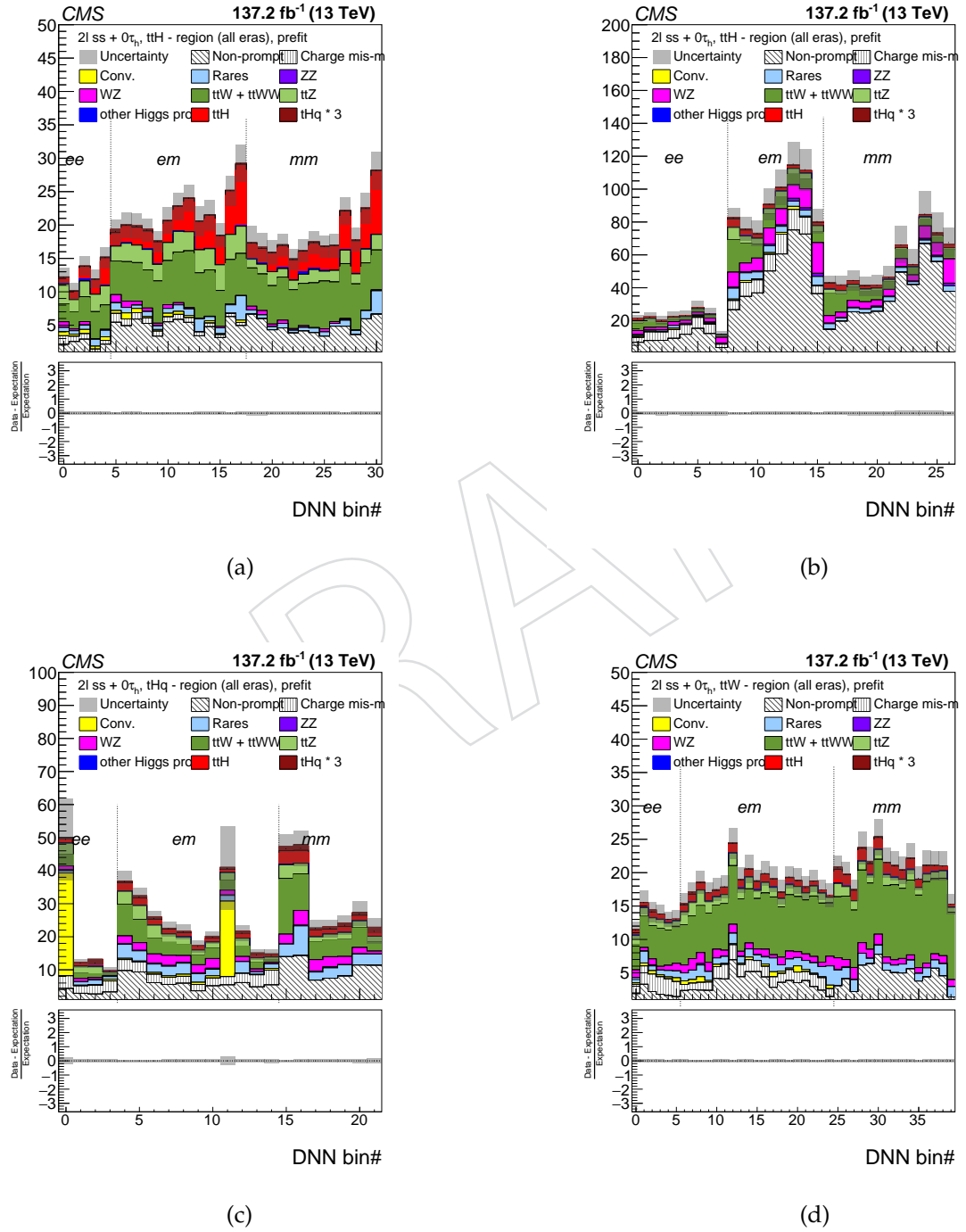


Figure 27: Distributions in the discriminating observables used for the signal extraction in the $3\ell + 0\tau_h$ category in the different regions: (a) the $t\bar{t}H$ – region and (b) the tH – region and (c) the BKG – region. The post-fit rates and uncertainties are used. [PLACEHOLDER - PREFIT, BLINDED - THE DNN WEIGHTS ARE GOING TO BE UPDATED]

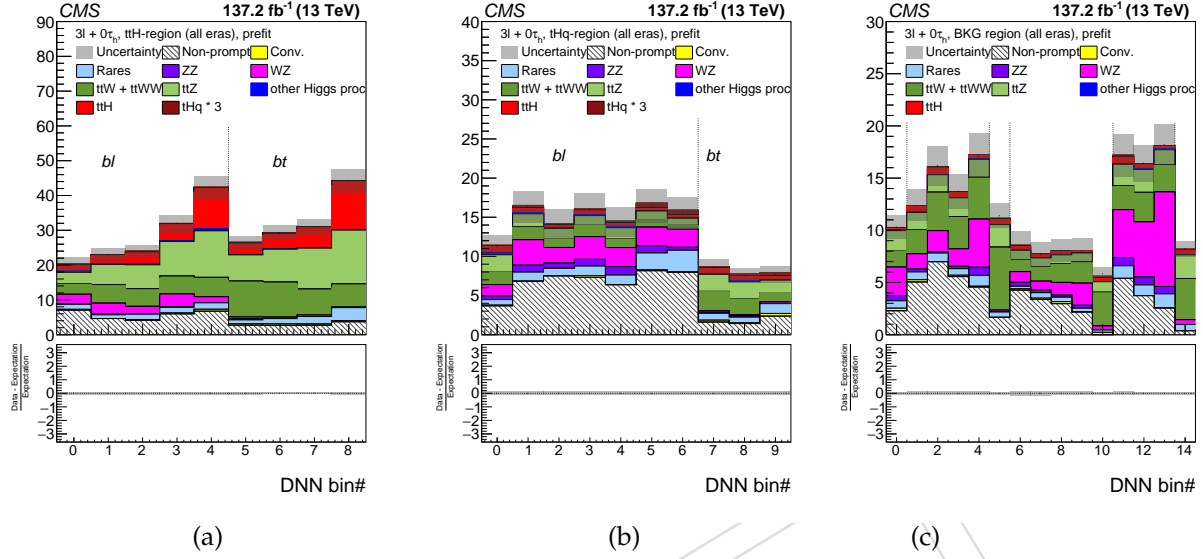


Table 39: The measured and expected signal rates are presented as signal-rate multipliers for the SM-like $t\bar{t}H$ and tH processes, μ , which are normalized to the SM $t\bar{t}H$ production rate, for the individual categories and for the combination of all seven categories with an inclusion of a simultaneous fit to $t\bar{t}W$ and $t\bar{t}Z$ for the full run II luminosity. [PLACEHOLDER]

Category	signal strength $\pm 1\sigma$		significance
	Measured	Expected	
0ℓ + 2τ _h	---	---	---
1ℓ + 2τ _h	---	---	---
2ℓss + 0τ _h	---	---	---
2ℓss + 1τ _h	---	---	---
2ℓos + 1τ _h	---	---	---
2ℓ + 2τ _h	---	---	---
1ℓ + 1τ _h	---	---	---
3ℓ + 0τ _h	---	---	---
3ℓ + 1τ _h	---	---	---
4ℓ + 0τ _h	---	---	---
Combined	---	---	XX σ (XXσ)

Figure 28: Distributions in the discriminating observables used for the signal extraction in the $2\ell ss + 1\tau_h$ category in the different regions: (a) the $t\bar{t}H$ – region and (b) the tH – region and (c) the BKG – region. The post-fit rates and uncertainties are used. [PLACEHOLDER - PREFIT, BLINDED - THE DNN WEIGHTS ARE GOING TO BE UPDATED]

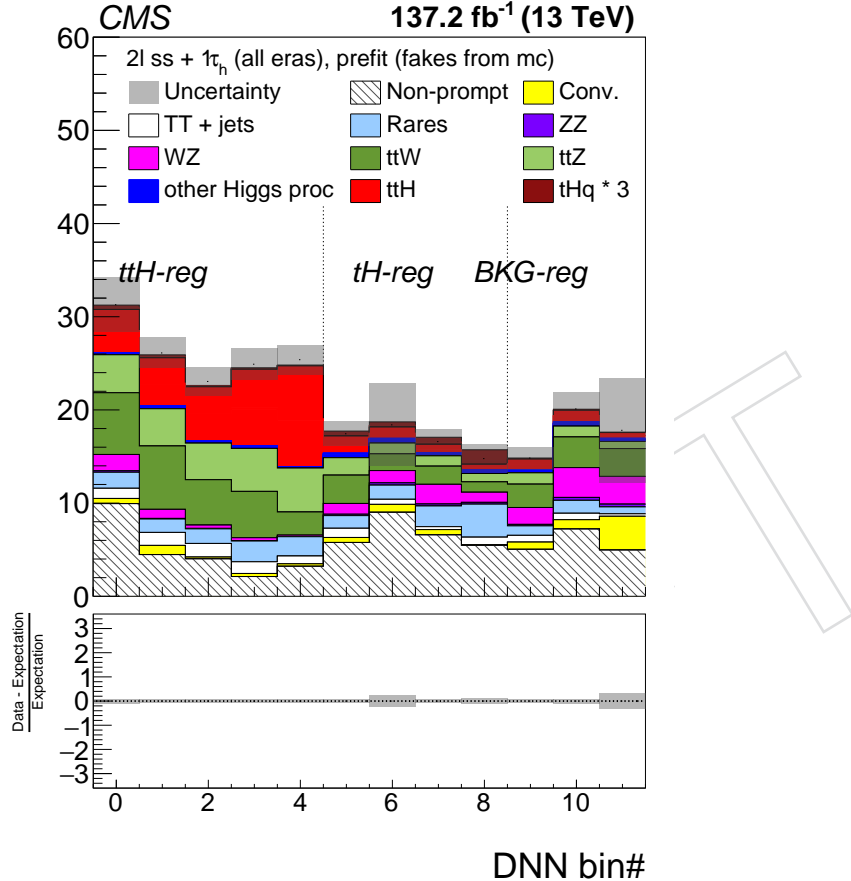


Table 40: Signal rates μ , in units of the SM $t\bar{t}H$ and $t\bar{t}Z$ and $t\bar{t}W + t\bar{t}WW$ production rates, measured including the $t\bar{t}Z$ and $t\bar{t}W(W)$ control regions extracted with the full run II luminosity. [PLACEHOLDER - ONLY EXPECTED, BLINDED - INPUTS WILL BE UPDATED]

	signal strength $\pm 1\sigma$	
	Measured	Expected
$\mu_{t\bar{t}H}$	---	+1.0 -0.195/+0.231
μ_{tH}	---	+1.0 -2.737/+2.956
$\mu_{t\bar{t}W}$	---	+1.0 -0.161/+0.186
$\mu_{t\bar{t}Z}$	---	+1.0 -0.189/+0.213

Figure 29: Distributions in the discriminating observables used for the signal extraction in the (a) $0\ell + 2\tau_h$, (b) $1\ell + 1\tau_h$, (c) $1\ell + 2\tau_h$ and (d) $2\ell os + 1\tau_h$ categories. The post-fit rates and uncertainties are used. [PLACEHOLDER - PREFIT, BLINDED - CALCULATE IT WITH DATA DRIVEN FAKES ESTIMATION - REVISIT 0L_2TAU BINNING (EMPTY DY BINS IN SOME ERAS)]

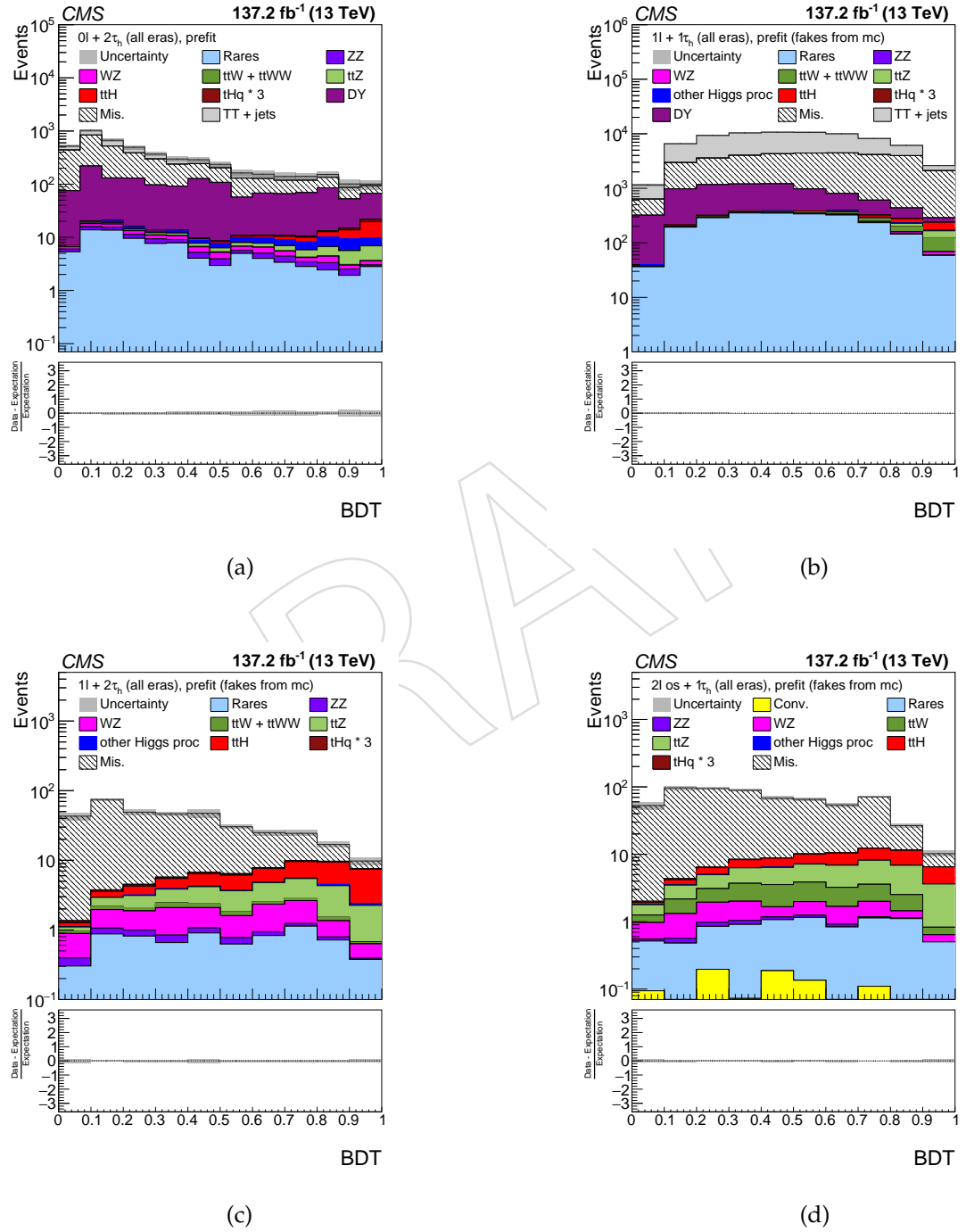


Figure 30: Distributions in the discriminating observables used for the signal extraction in the (a) $2l + 2\tau_h$, (b) $3l + 1\tau_h$ and (d) $4l + 0\tau_h$ categories. The post-fit rates and uncertainties are used. [PLACEHOLDER - PREFIT, BLINDED - INCORPORATE TT+JETS TO THE TTZ COMPONENT]

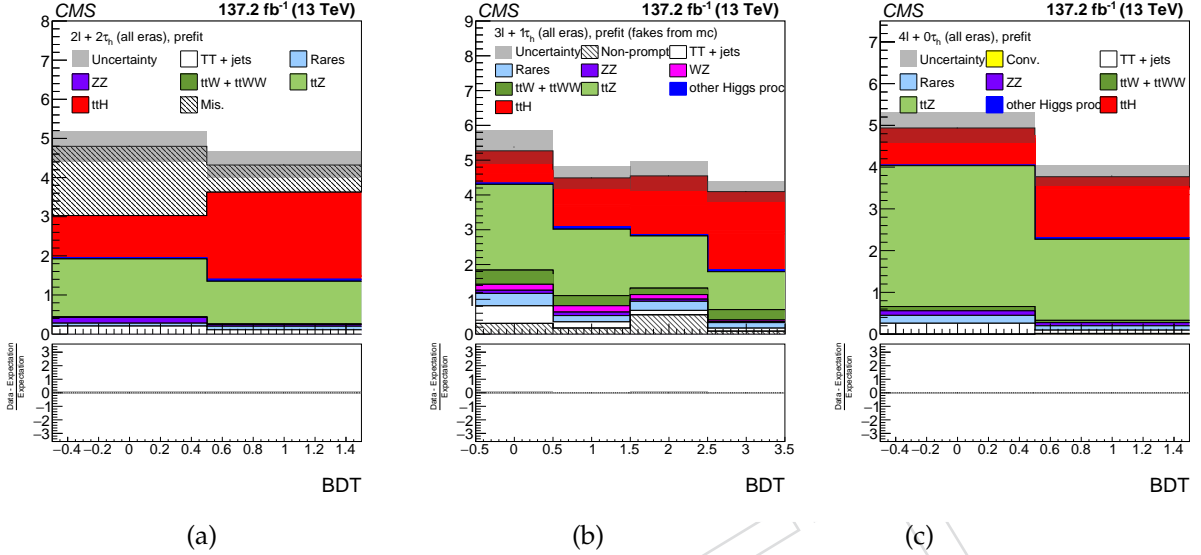


Table 41: Signal rates μ , in units of the SM $t\bar{t}H$ and $t\bar{t}Z$ and $t\bar{t}W + t\bar{t}WW$ production rates, measured including the $t\bar{t}Z$ and $t\bar{t}W(W)$ control regions extracted with the full run II luminosity. [PLACEHOLDER - ONLY EXPECTED, BLINDED - INPUTS WILL BE UPDATED]

	signal strength $\pm 1\sigma$		
	2016 luminosity		2017 luminosity
	Measured	Expected	2018 luminosity
$\mu_{t\bar{t}H}$	--	+1.0 -0.347 / +0.389	--
μ_{tH}	--	+1.0 -5.043 / +5.360	+1.0 -6.816 / +7.094
$\mu_{t\bar{t}W}$	--	+1.0 -0.238 / +0.272	+1.0 -0.222 / +0.255
$\mu_{t\bar{t}Z}$	--	+1.0 -0.245 / +0.279	+1.0 -0.249 / +0.283

Table 42: Significance for the $t\bar{t}H$ and tH processes extracted with the full run II luminosity, and with the luminosity of individual eras. [PLACEHOLDER - ONLY EXPECTED, BLINDED - INPUTS WILL BE UPDATED]

	significance			
	2016 luminosity	2017 luminosity	2018 luminosity	full run II
$t\bar{t}H$	3.06	3.49	4.03	5.84
tH	0.20	0.15	0.28	0.36

Figure 31: Distributions in the discriminating observables used for the signal extraction in the control regions 3ℓ -CR and 4ℓ -CR. The post-fit rates and uncertainties are used. The shapes are from binning on the number of jets and number of b-jets for the 3ℓ -CR and number of SFOS leptons and bjets on 4ℓ -CR (see Sec. 9.3).

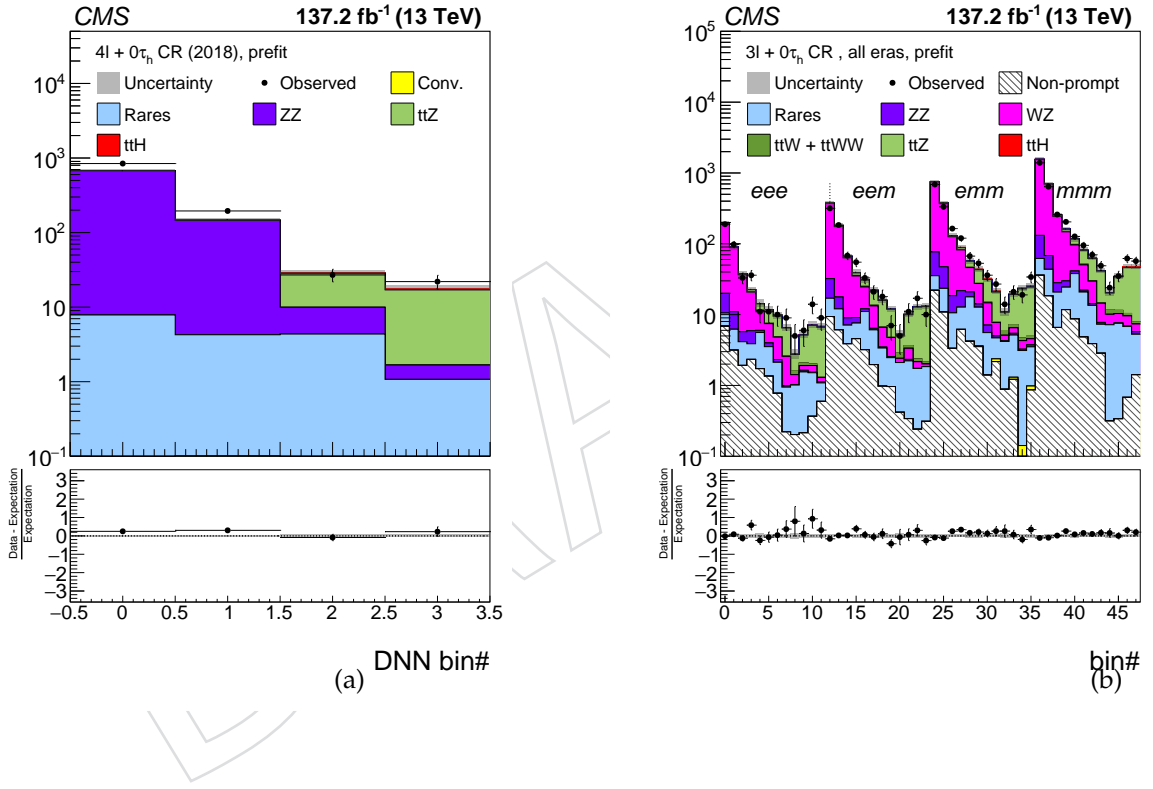


Figure 32: Measured signal rate multipliers ($\mu = \sigma/\sigma_{SM}$) under the hypothesis that the processes $t\bar{t}H$ and tH are SM-like for all ten signal regions separately and for the combination of signal regions with the control regions in the fit. [PLACEHOLDER - ONLY EXPECTED, BLINDED - INPUTS WILL BE UPDATED]

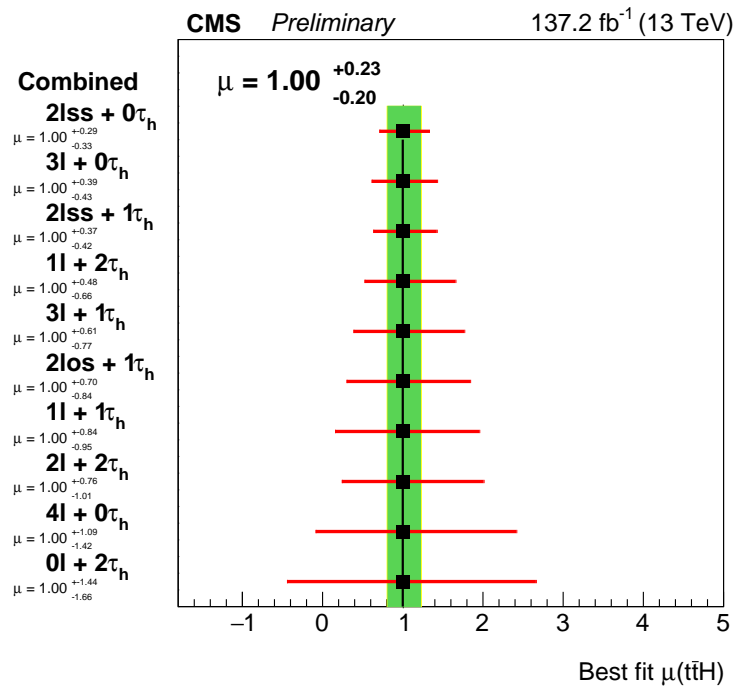


Figure 33: Measured signal rate multipliers ($\mu = \sigma/\sigma_{SM}$) under the hypothesis that the processes $t\bar{t}H$ and tH are SM-like for all ten signal regions separately and for the combination of signal regions with the control regions in the fit. For the luminosity of 2016 era (a), 2017 era (b) and 2018 era (c). [PLACEHOLDER - ONLY EXPECTED, BLINDED - INPUTS WILL BE UPDATED]

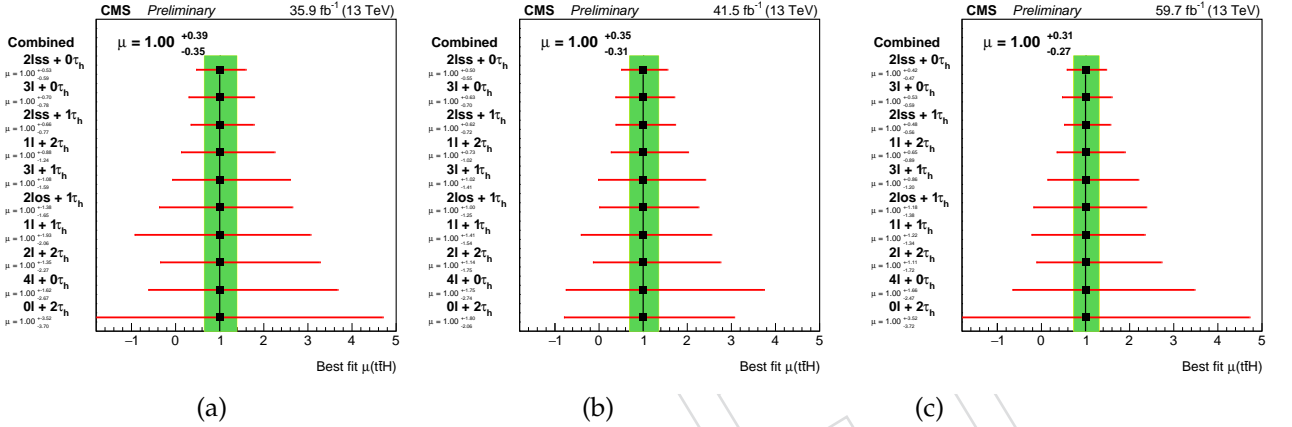


Figure 34: Two-dimensional likelihood for the signal extraction on the different processes considered on the final fit for the case were we consider SM-like kinematics to all processes. [PLACEHOLDER]

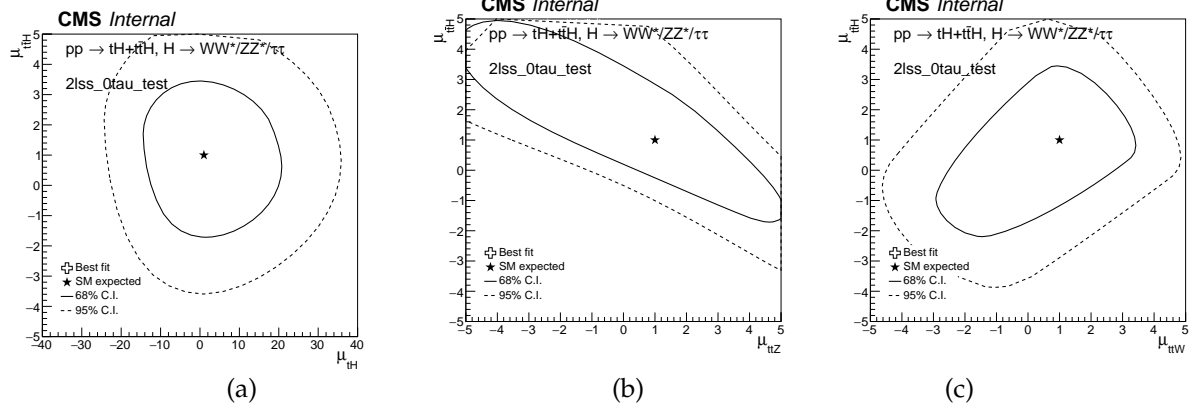
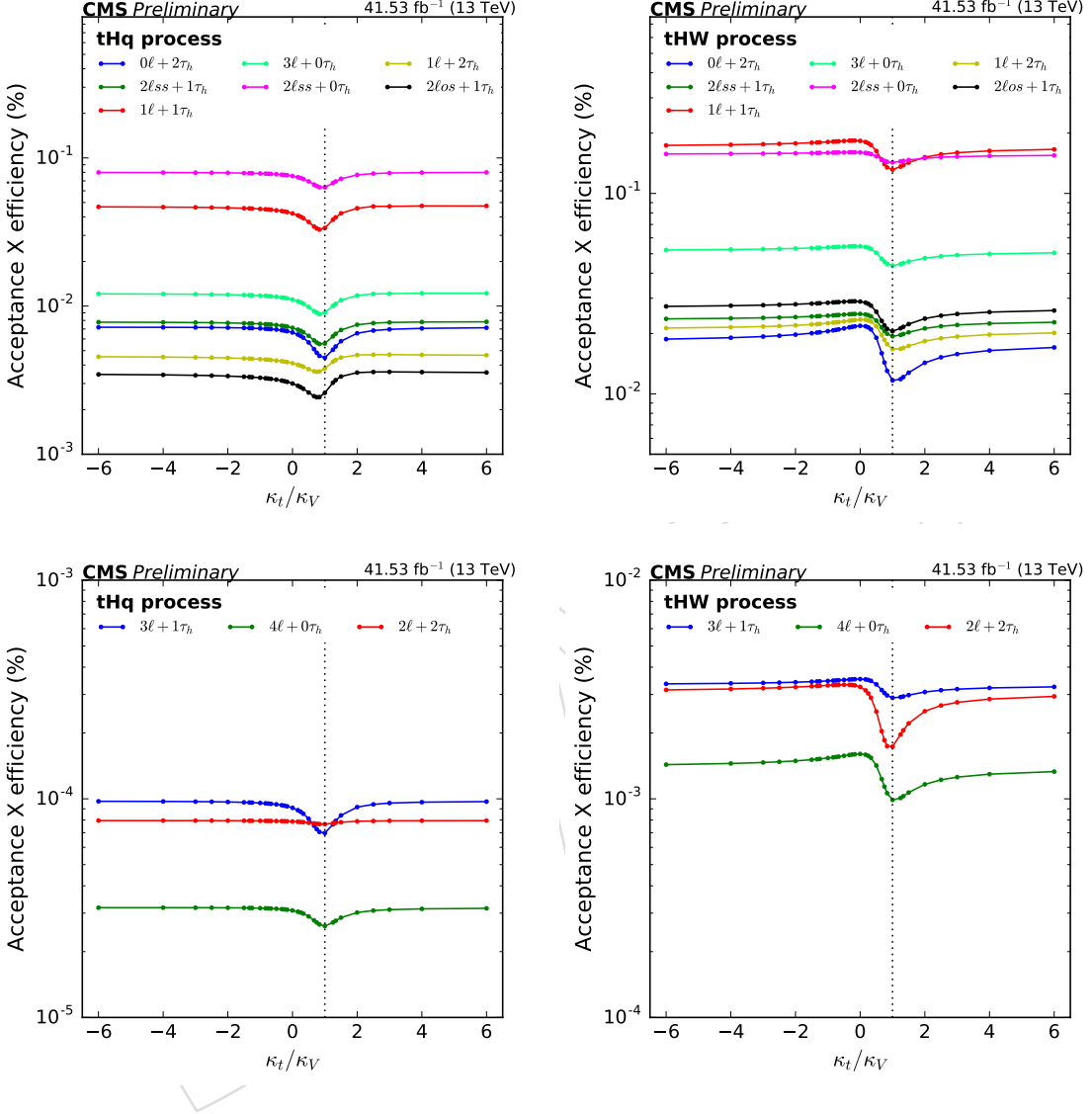


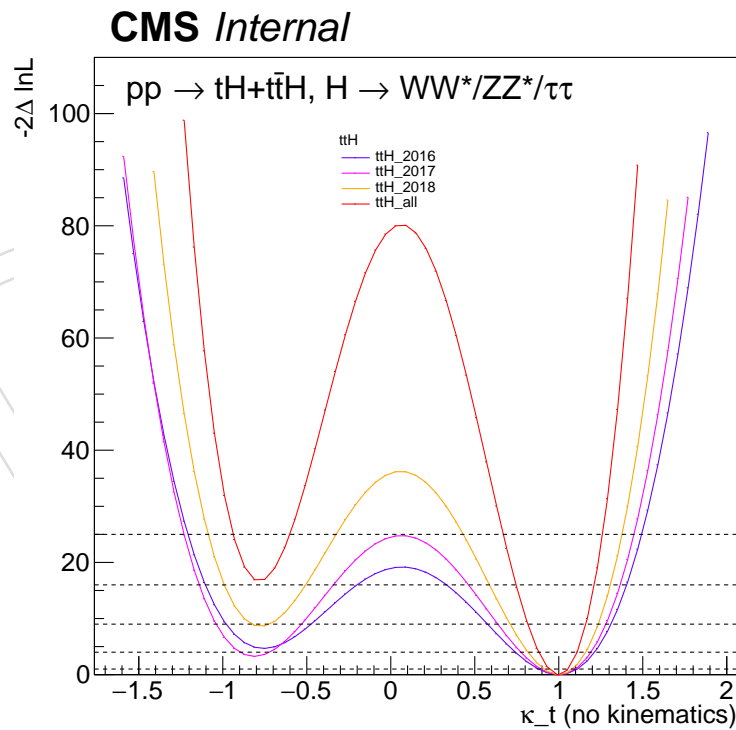
Figure 35: Acceptance X efficiency for the tHq (left) and tHW (right) processes k_T/κ_V . For the sake of visualization we show separately the figure for the categories that have Acceptance X efficiency at the order of 0.1% (upper row) and the ones that this is 2-3 orders of magnitude lower (lower row). [PLACEHOLDER]



1504 ttH and tH processes in terms of k_T/κ_V . In Fig. 37 we show a 2D-likelihood scan as a function
 1505 of k_T and κ_V .

Figure 36: Limit for the $t\bar{t}H + tH$ process in terms of k_T/κ_V . [PLACEHOLDER]

Figure 37: Likelihood scan as a function of k_T for the resolved couplings model is shown in the left plot for $\kappa_V = 0.5$, $\kappa_V = 1.0$ and $\kappa_V = 1.5$ while all the other Higgs coupling multipliers are taken to be as the SM. [PLACEHOLDER – WE SHOW THE SCAN COMPARING THE RESULTS WITH FULL RUN II LUMI WITH THE ONE FROM THE INDIVIDUAL ERAS] [IGNORING KT KINEMATICS AT THE MOMENT]



1506 12 Summary

1507 The production of the Higgs boson in association with either one (tH) or two (ttH) top quarks
 1508 has been measured in events that contain electrons, muons and hadronically decaying taus in
 1509 the final state. Events are analyzed in ten different categories ($0\ell + 2\tau_h$, $1\ell + 1\tau_h$, $1\ell + 2\tau_h$,
 1510 $2\ell ss + 0\tau_h$, $2\ell ss + 1\tau_h$, $2\ell os + 1\tau_h$, $2\ell + 2\tau_h$, $3\ell + 0\tau_h$, $3\ell + 1\tau_h$ and $4\ell + 0\tau_h$), covering the
 1511 decay channels $H \rightarrow WW, ZZ$ (excluding $ZZ \rightarrow 4\ell$), and $\tau\tau$.

1512 The analyzed data has been recorded in pp collisions at $\sqrt{s} = 13$ TeV center-of-mass energy
 1513 during the period 2016 to 2018, corresponding to an integrated luminosity of 137.2 fb^{-1} . The
 1514 sensitivity of the analysis has been improved by using matrix element and machine learning
 1515 methods (DNN, BDT) to separate the signals (tH , ttH) from the backgrounds, but also to sepa-
 1516 rate tH from ttH .

1517 For the Standard Model scenario ($\kappa_t=+1$, $\kappa_V=+1$), the measured signal rates for tH and ttH
 1518 production amount to $\mu_{ttH} = X.XX_{-Z.ZZ}^{+Y.YY} (1.00_{-Z.ZZ}^{+Y.YY})$ and $\mu_{tH} = X.XX_{-Z.ZZ}^{+Y.YY} (1.00_{-Z.ZZ}^{+Y.YY})$ times
 1519 the production rate expected in the Standard Model, corresponding to an observed (expected)
 1520 significance of XX (YY) over the background-only hypothesis.

1521 Similarly, for the ITC scenario ($\kappa_t=-1$, $\kappa_V=+1$), the measured signal rates for tH and ttH pro-
 1522 duction amount to $\mu_{ttH} = X.XX_{-Z.ZZ}^{+Y.YY} (1.00_{-Z.ZZ}^{+Y.YY})$ and $\mu_{tH} = X.XX_{-Z.ZZ}^{+Y.YY} (1.00_{-Z.ZZ}^{+Y.YY})$ times the
 1523 production rate expected in the ITC scenario, corresponding to an observed (expected) signifi-
 1524 cance of XX (YY) over the background-only hypothesis.

DRAFT

1525 A Background control regions

1526 The modeling of irreducible background contributions in the SR, which are obtained from the
 1527 MC simulation, is validated in two CRs, one dedicated to $t\bar{t}Z$, and $WZ+jets$ and $WZ+jets$.
 1528 Additionally, a region is designed in the $2lss$ region to check the modeling of $t\bar{t}W$ and processes
 1529 containing non-prompt leptons. Events in these CRs are selected as described in Sections 9.3.3.
 1530 Distributions in selected kinematic observables are shown in Figs. 41-43, Figs. 38-40, and 44-46.
 1531 Good agreement between data and simulation is observed in modeling the yields of events
 1532 selected in the $t\bar{t}W$, $t\bar{t}Z$, and $WZ+jets$ CRs as well as in modeling the shape of distributions.

1533 A.1 $t\bar{t}W$

1534 Events in the CR enriched in the contribution of the $t\bar{t}W$ background are selected by applying
 1535 the event selection criteria for the SR of the $2lss$ category, described in Section 9.3, but requiring
 1536 exactly three jets of $p_T > 25$ GeV and $|\eta| < 2.4$ for events selected in the CR.

1537 A.2 $t\bar{t}Z$

1538 Events in the CR enriched in the contribution of the $t\bar{t}Z$ background are selected by applying
 1539 the event selection criteria for the SR of the 3ℓ category, described in Section 5.3.8, except that
 1540 events selected in the CR are required to contain a pair of fakeable leptons of the same flavor,
 1541 opposite charge, and mass $|m_{\ell\ell} - m_Z| < 10$ GeV.

1542 A.3 $WZ+jets$

1543 Events in the CR enriched in the contribution of the $t\bar{t}Z$ background are selected by applying
 1544 the event selection criteria for the SR of the 3ℓ category, but requiring the events selected in
 1545 the CR to contain a pair of fakeable leptons of the same flavor, opposite charge, and mass
 1546 $|m_{\ell\ell} - m_Z| < 10$ GeV and no jets of $p_T > 25$ GeV, $|\eta| < 2.4$, and passing the medium WP of
 1547 the DeepCSV discriminant.

1548 A.4 “Fake” background control plots

1549 A.5 $1\ell + 2ss\tau_h$

1550 Events in this control region are selected similarly as $1\ell + 2\tau_h$ signal region except the two
 1551 τ_h are required to be of same charge. The “fake” background in this CR is estimated with FF
 1552 method described in 7.1 from an application region that is the same as AR used to estimate
 1553 “fake” background in $1\ell + 2\tau_h$ SR, but with the requirement that the two τ_h are same sign
 1554 instead of opposite sign.

1555 A.6 $t\bar{t}$ background

1556 The production of top quark pairs represents an irreducible background in the $0\ell + 2\tau_h$ and
 1557 $1\ell + 1\tau_h$ categories only. In all other categories, $t\bar{t}$ events only contribute as background, in
 1558 case at least one lepton or τ_h is either misidentified (all categories) or at least the charge of
 1559 one lepton is mismeasured ($2lss + 0\tau_h$ and $2lss + 1\tau_h$ categories). The modeling by the MC
 1560 simulation of the irreducible $t\bar{t}$ background in the $0\ell + 2\tau_h$ and $1\ell + 1\tau_h$ categories is validated
 1561 in a CR dominated by $t\bar{t}$ dilepton events. The events are selected as described in Appendix J,
 1562 except that no requirements are imposed on the presence or absence of τ_h . Distributions in

Figure 38: Data/SM agreement plots for some input variables of the $2\ell ss + 0\tau_h$ DNN in a region with 3 jets.

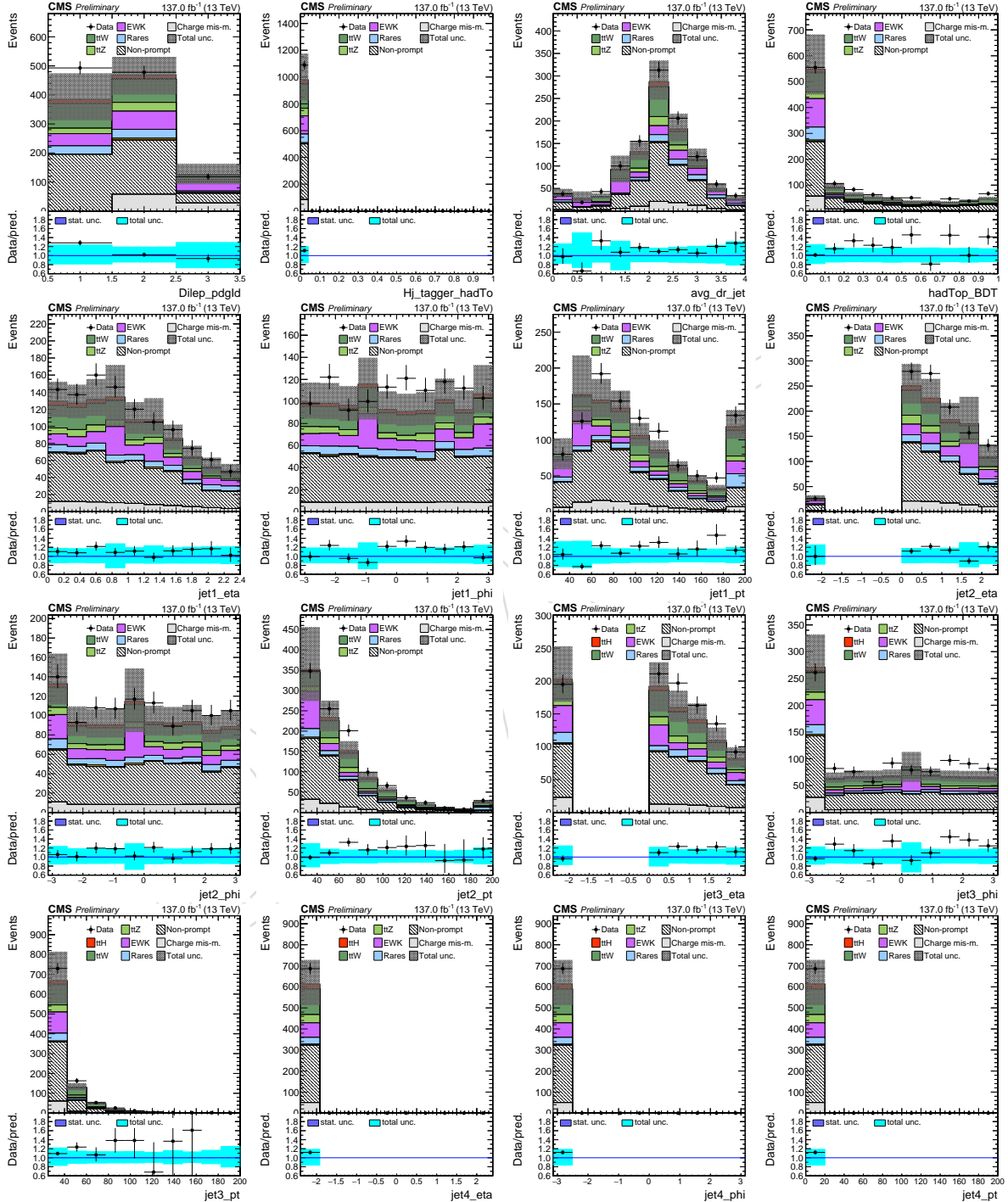


Figure 39: Data/SM agreement plots for some input variables of the $2\ell ss + 0\tau_h$ DNN in a region with 3 jets.

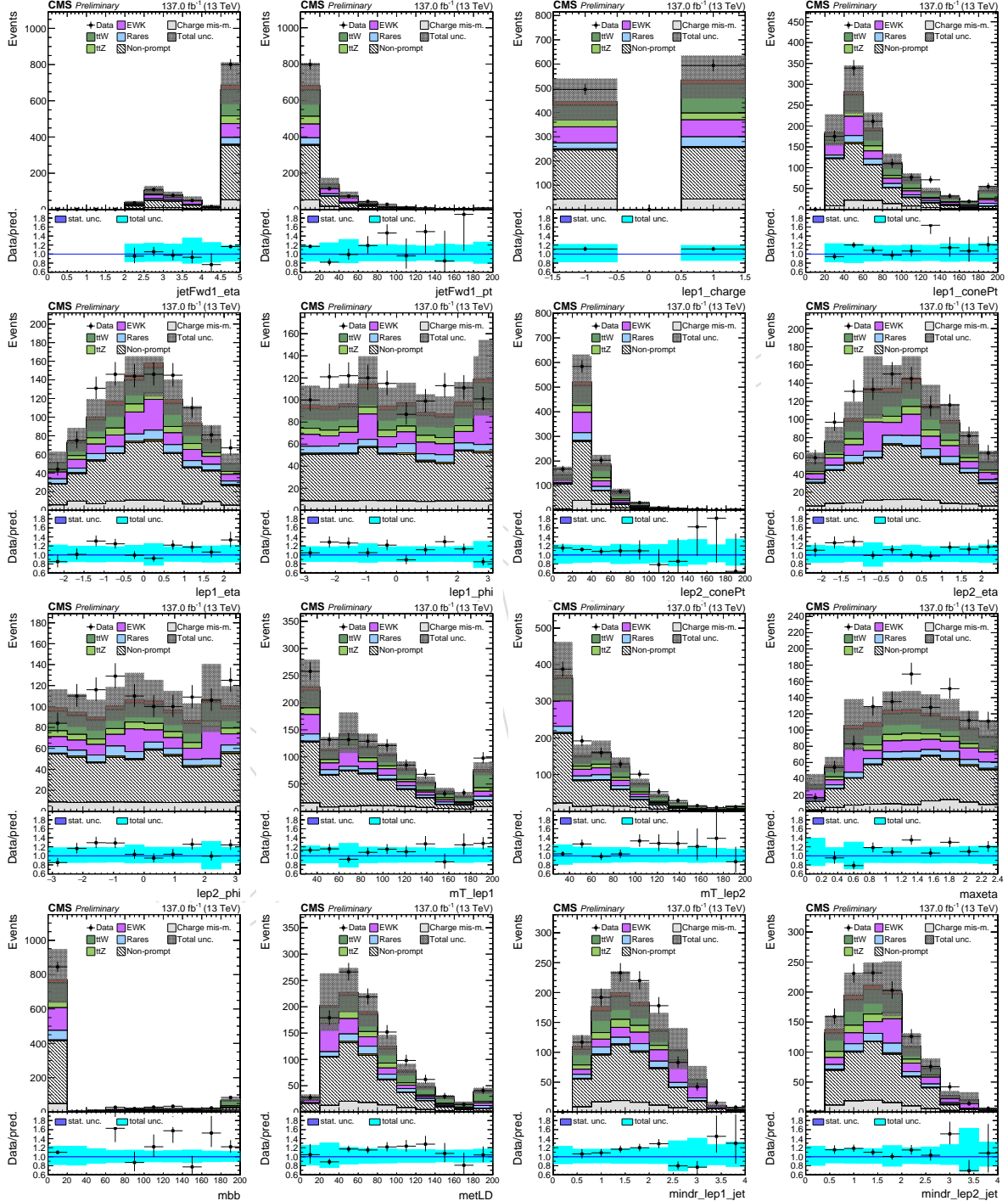
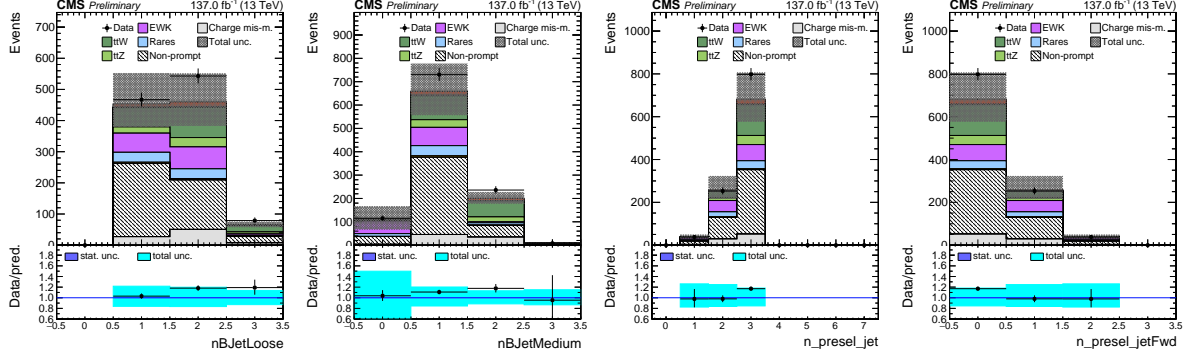


Figure 40: Data/SM agreement plots for some input variables of the $2\ell ss + 0\tau_h$ DNN in a region with 3 jets.



1563 selected kinematic observables for events selected in the $t\bar{t}$ CR are shown in Fig. 48. The uncer-
 1564 tainty bands shown in the figure represent statistical uncertainties only. Satisfactory agreement
 1565 between data and expectation is observed.

DRAFT

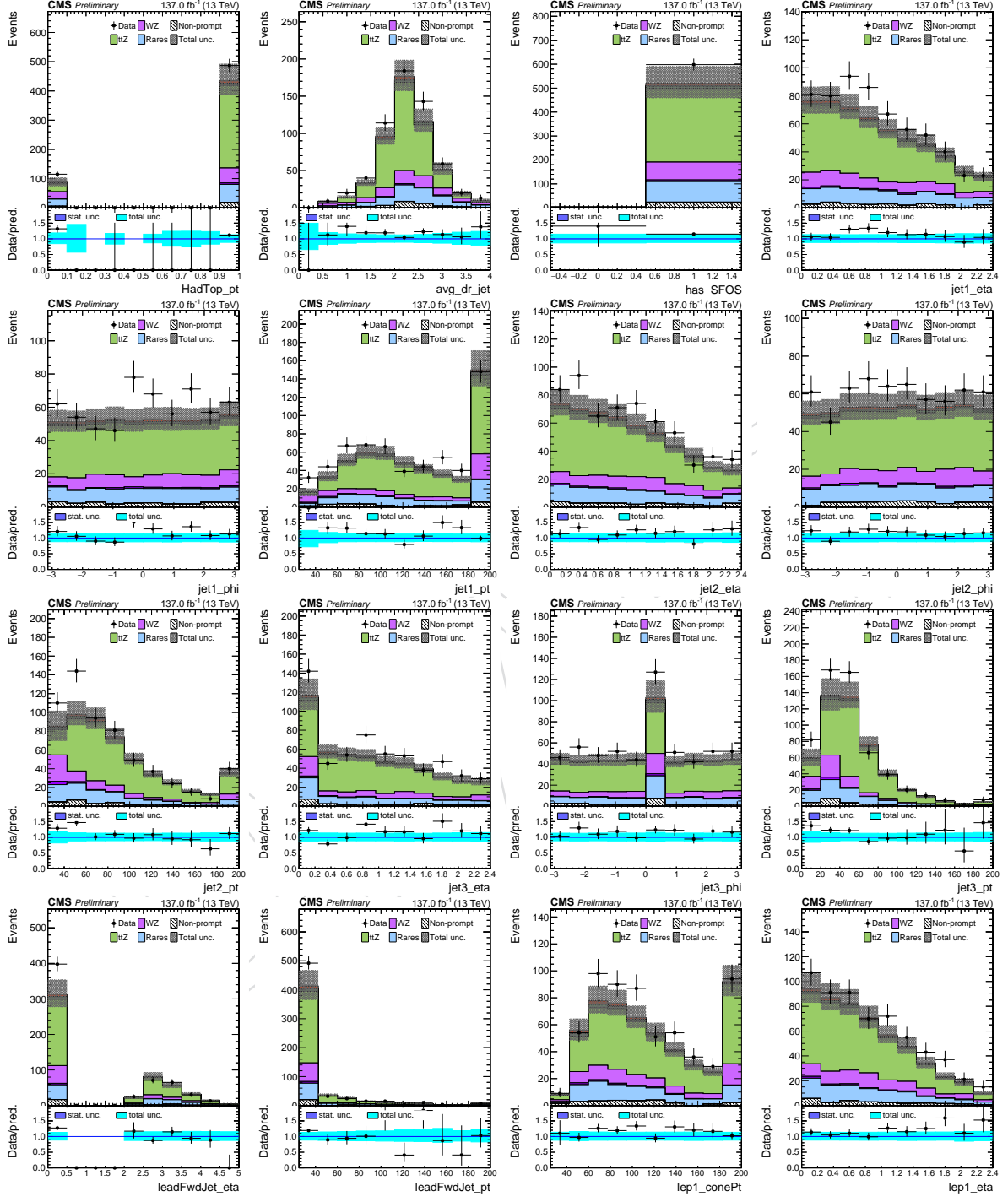


Figure 41: Distributions in selected kinematic observables in events selected in the CR enriched in the contribution of $t\bar{t}Z$ background.

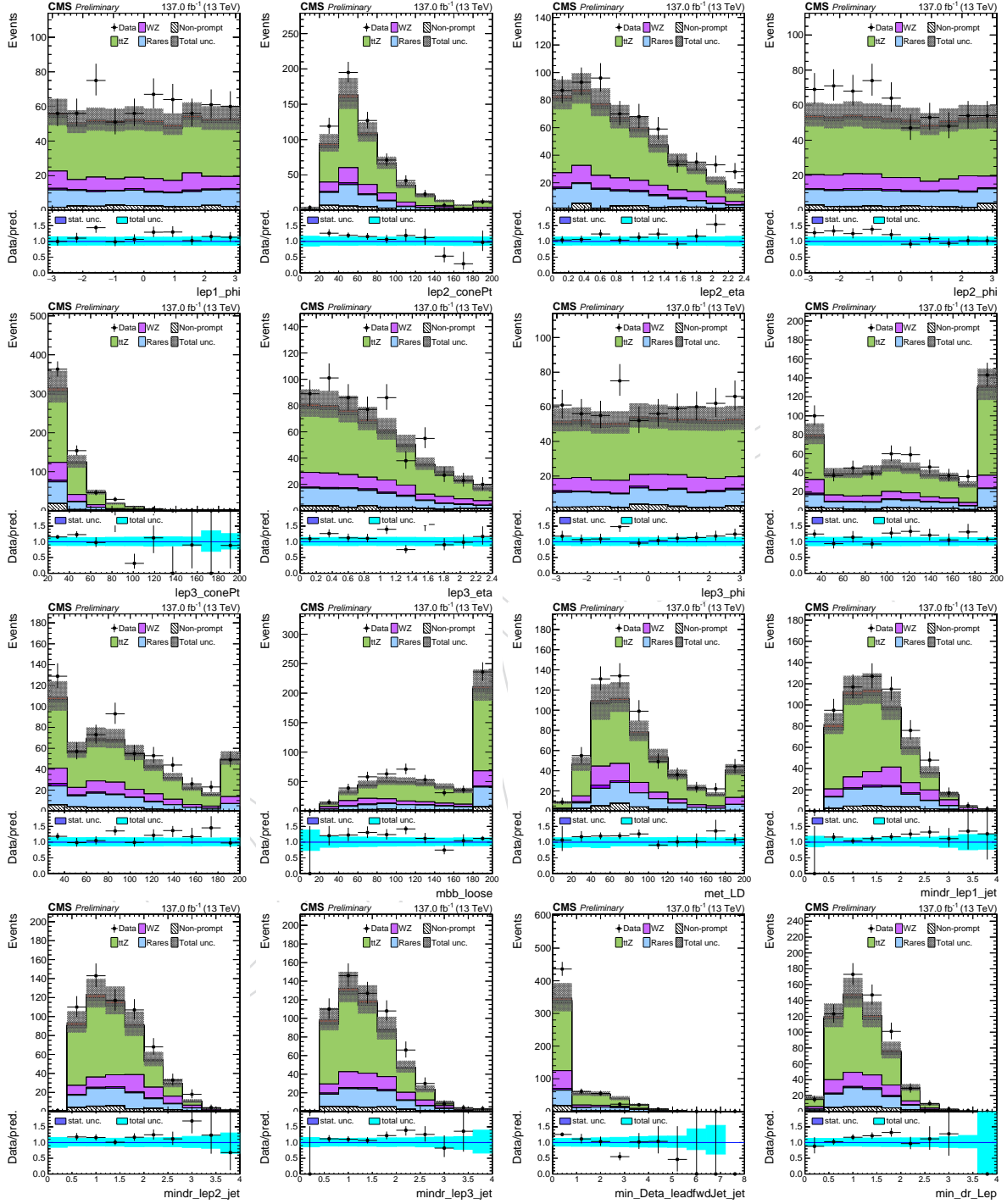


Figure 42: Distributions in selected kinematic observables in events selected in the CR enriched in the contribution of $t\bar{t}Z$ background.

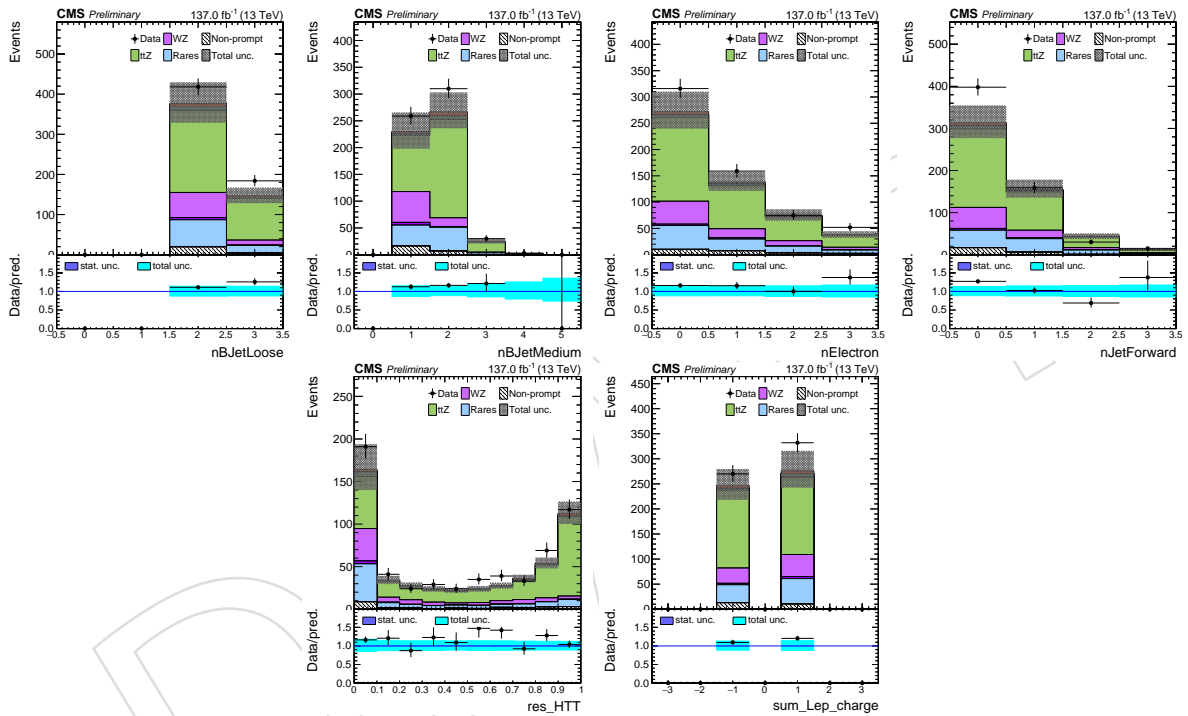


Figure 43: Distributions in selected kinematic observables in events selected in the CR enriched in the contribution of $t\bar{t}Z$ background.

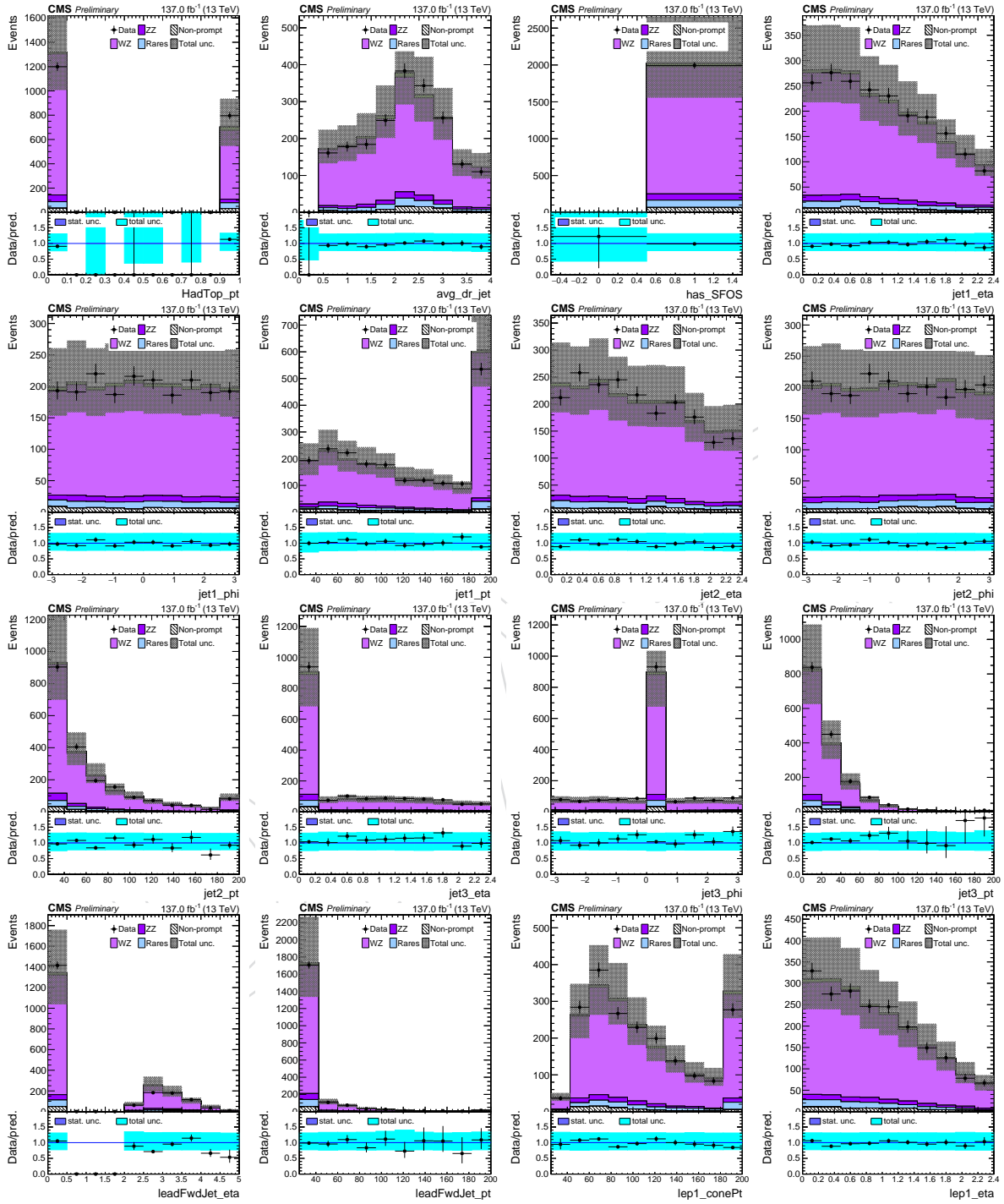


Figure 44: Distributions in selected kinematic observables in events selected in the CR enriched in the contribution of WZ+jets background.

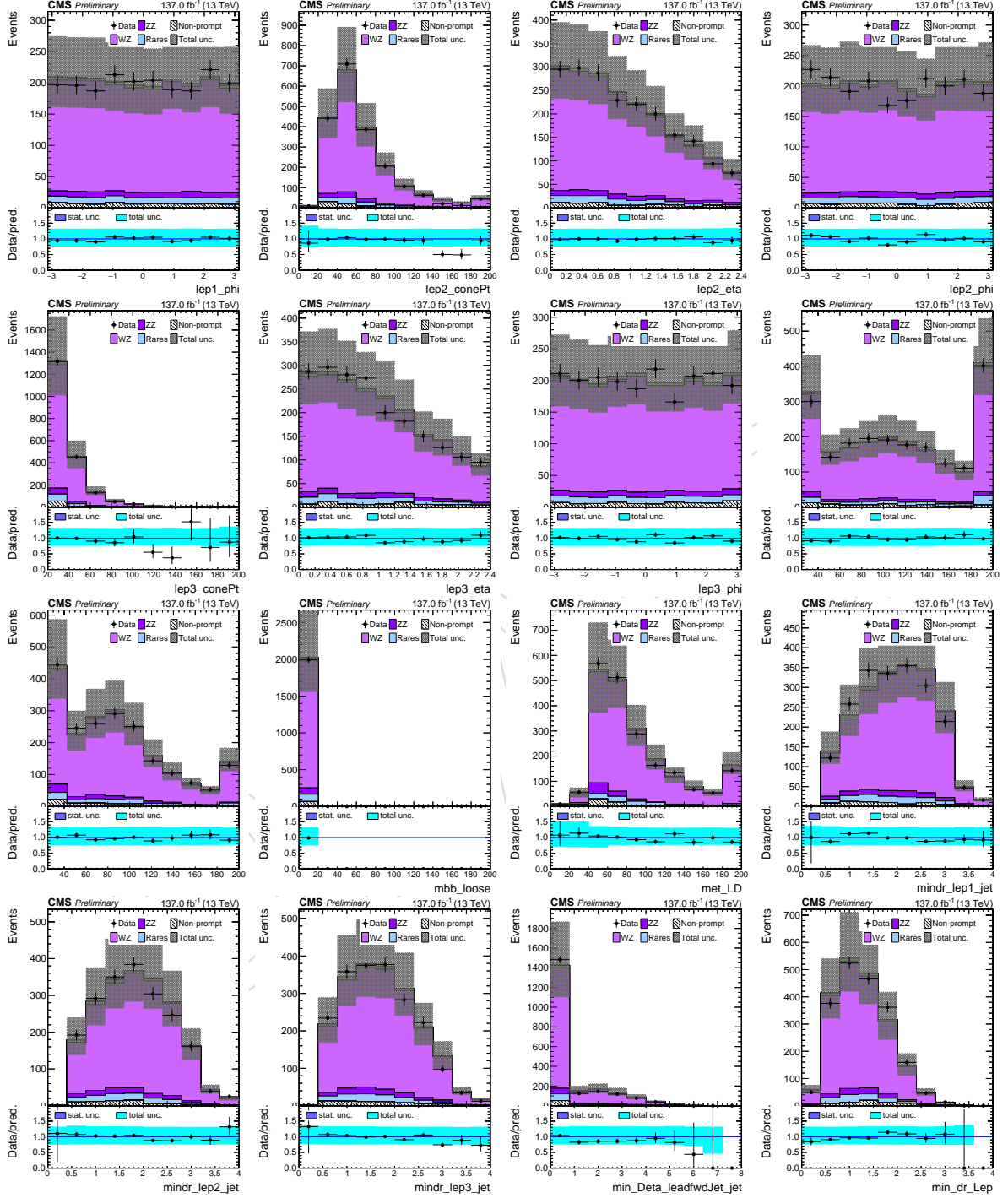


Figure 45: Distributions in selected kinematic observables in events selected in the CR enriched in the contribution of WZ+jets background.

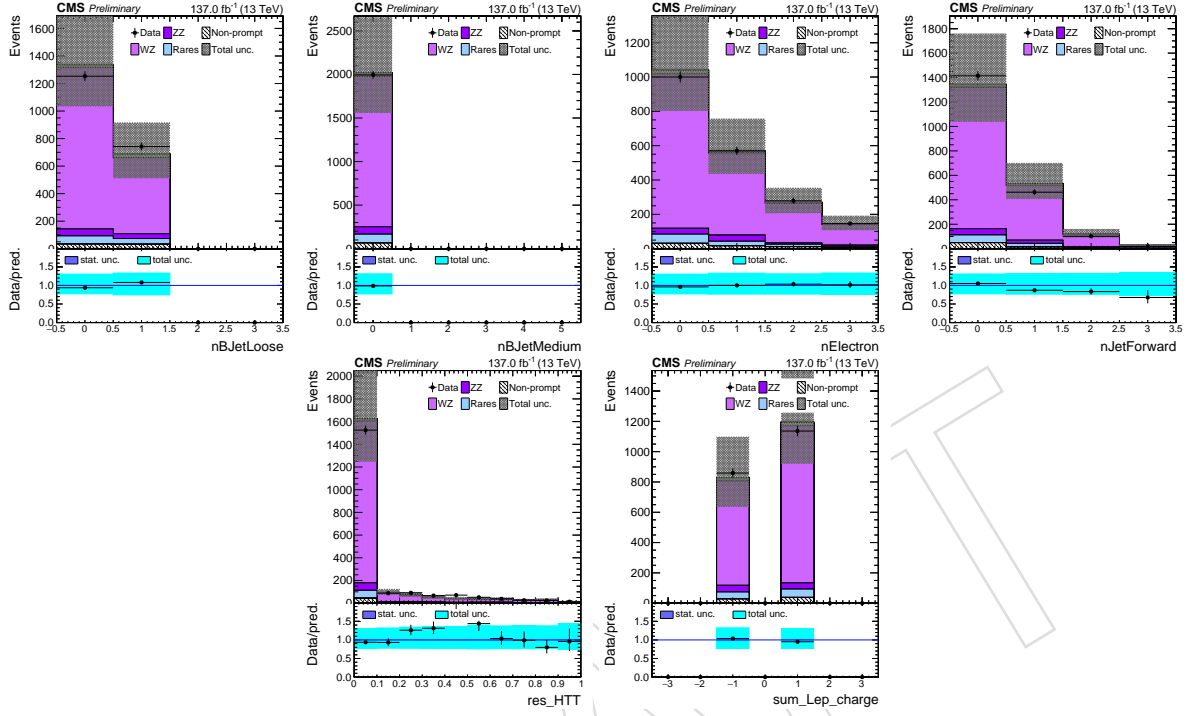


Figure 46: Distributions in selected kinematic observables in events selected in the CR enriched in the contribution of $WZ + \text{jets}$ background.



Figure 47: Distributions in the BDT output and visible mass of the τ_h pair, as well as the event count in $1\ell + 2s\bar{s}\tau_h$ control region.

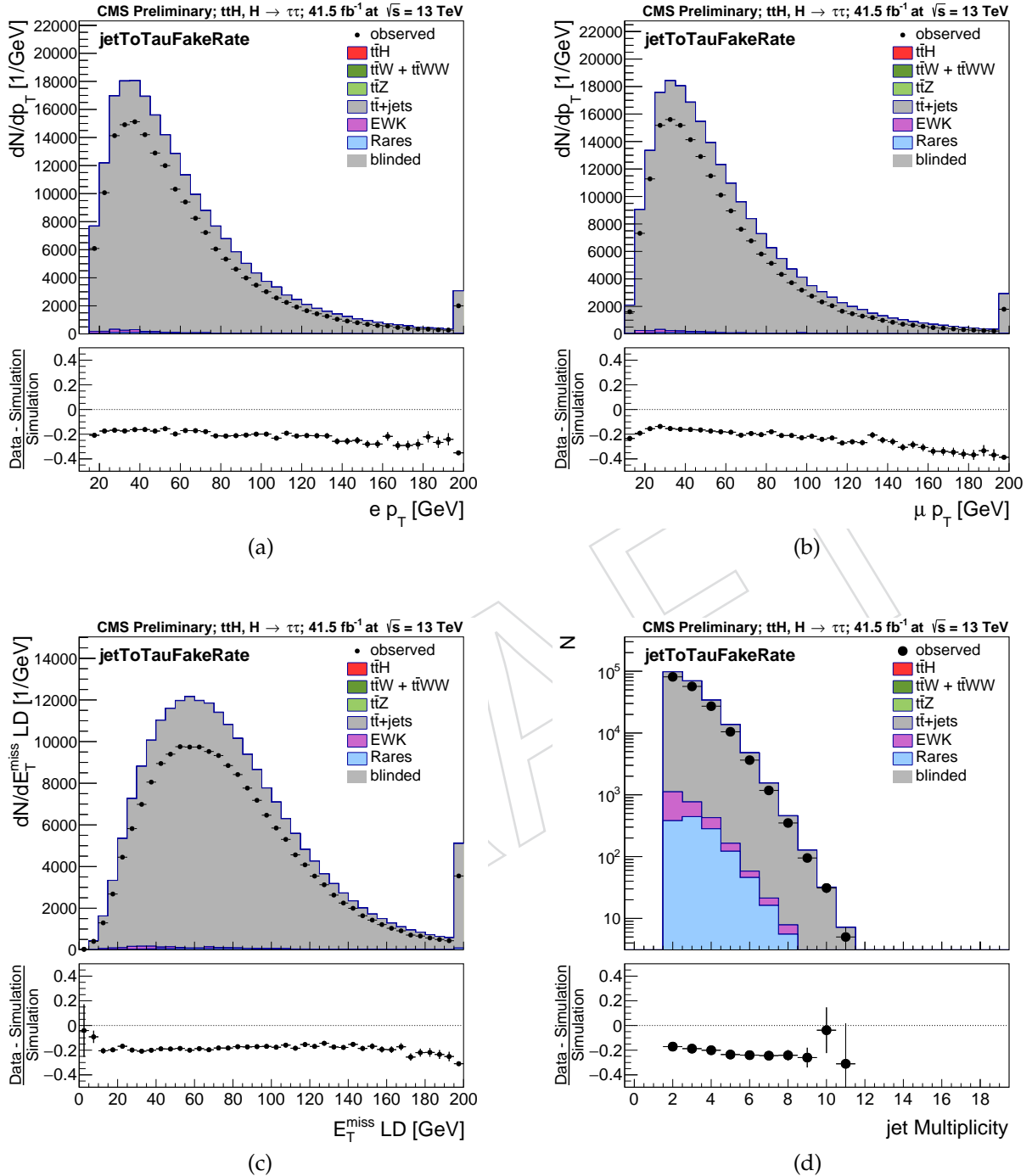


Figure 48: Distributions in p_T of (a) electrons and (b) muons, (c) $E_T^{\text{miss}} \text{ LD}$, and (d) the number of jets in events selected in the $t\bar{t}$ dominated CR used to validate the modeling of the irreducible $t\bar{t}$ background in the $0\ell + 2\tau_h$ and $1\ell + 1\tau_h$ categories.

1566 **B Deep Neural Networks**

Table 43: Hyperparameters used in the training of the DNN's for each category. [PLACEHOLDER]

Variable	$2\ell_{ss} + 0\tau_h$	$2\ell_{ss} + 1\tau_h$	$3\ell + 0\tau_h$
Number of hidden layers	3 (32, 16, 16 nodes)		
Hidden layer initialization	"he.uniform"		
Activation on hidden layers	ReLU		
Between hidden layers	batch normalization 0.2 dropout.		
Optimizer	Nadam (lr= 7e-4, decay 1e-5)	Nadam	
Number of epochs	30		
Batch size	264		
Balancing of classes	$t\bar{t}H = 0.2$ $tH = 0.4$ $BKG = 0.3$	$t\bar{t}H =$ tH $t\bar{t}W =$ $BKG =$	

Figure 49: Evolution of loss with the DNN training epochs for the three considered categories. Each plot corresponds respectively from left to right to $2\ell_{ss} + 1\tau_h$, $2\ell_{ss} + 0\tau_h$ and $3\ell + 0\tau_h$ categories. [PLACEHOLDER]

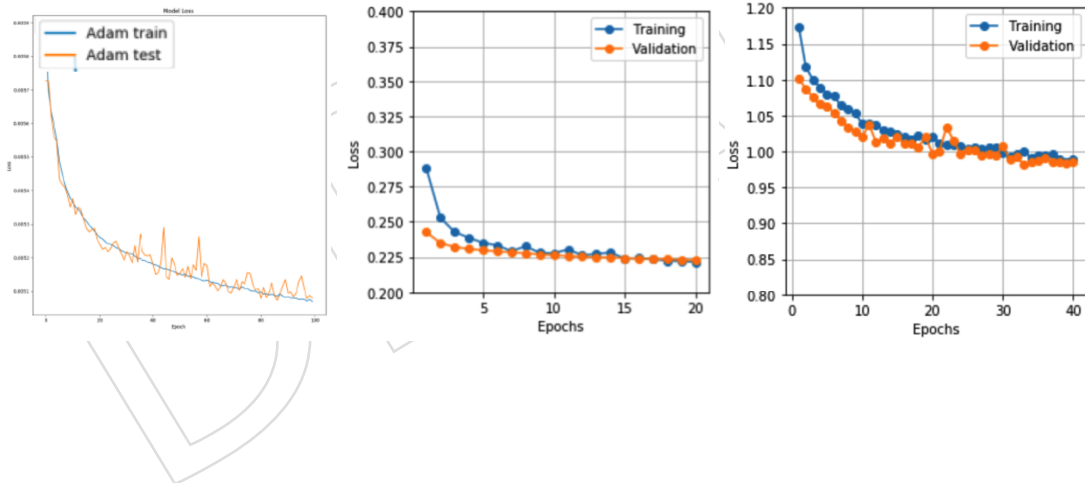


Figure 50: Ranking of the variables on the DNN constructed with variable permutation for the three considered categories. The reference of each variable naming can be found in Table 36. [PLACEHOLDER]

Weight	Feature	Weight	Feature	Weight	Feature
0.0810 ± 0.0003	lep2_mT	0.2180 ± 0.0030	HadTop_pt_CSVsort4rd	0.0871 ± 0.0020	ptmiss
0.0775 ± 0.0006	lep1_conept	0.1832 ± 0.0029	lep1_mT	0.0604 ± 0.0015	lep1_mT
0.0609 ± 0.0010	mbb_loose	0.1426 ± 0.0024	met_LD	0.0352 ± 0.0015	lep2_mT
0.0603 ± 0.0013	jet1_pt	0.1194 ± 0.0029	jet1_pt	0.0314 ± 0.0010	lep3_mT
0.0564 ± 0.0002	massL	0.1002 ± 0.0027	mVis_lep_tau_OS	0.0253 ± 0.0010	jet1_pt
0.0557 ± 0.0004	sum_lep_charge	0.0978 ± 0.0027	lep2_mT	0.0192 ± 0.0013	max_lep_eta
0.0555 ± 0.0006	jetForward1_pt	0.0977 ± 0.0028	jetForward1_pt	0.0183 ± 0.0005	lep1_conept
0.0540 ± 0.0005	met_LD	0.0926 ± 0.0024	mVis_lep2_tau	0.0180 ± 0.0010	jetForward1_pt
0.0524 ± 0.0006	nElectron	0.0843 ± 0.0029	massL	0.0146 ± 0.0007	jet2_pt
0.0500 ± 0.0009	lep1_mT	0.0798 ± 0.0028	mbb_loose	0.0136 ± 0.0007	avg_dr_jet
0.0441 ± 0.0013	jet2_pt	0.0784 ± 0.0033	lep1_conept	0.0114 ± 0.0007	lep2_conept
0.0428 ± 0.0010	nBJetLoose	0.0532 ± 0.0014	tau1_pt	0.0100 ± 0.0010	jet3_pt
0.0423 ± 0.0006	avg_dr_jet	0.0497 ± 0.0019	jet2_pt	0.0094 ± 0.0006	mbb_medium
0.0408 ± 0.0005	jet3_pt	0.0393 ± 0.0014	lep2_conept	0.0073 ± 0.0008	nBJetLoose
0.0346 ± 0.0006	lep2_conept	0.0037 ± 0.0008	nJet	0.0072 ± 0.0004	HadTop_pt_CSVsort4rd
0.0335 ± 0.0009	HadTop_pt_CSVsort4rd	0.0031 ± 0.0005	nJetForward	0.0068 ± 0.0006	sum_lep_charge
0.0283 ± 0.0007	nJet	0.0028 ± 0.0003	jetForward1_eta_abs	0.0068 ± 0.0009	nElectron
0.0227 ± 0.0004	dr_leps	0.0028 ± 0.0005	sum_Lep_charge	0.0057 ± 0.0004	lep3_conept
0.0206 ± 0.0006	res-HTT_CSVsort4rd	0.0027 ± 0.0004	avg_dr_jet	0.0041 ± 0.0005	jet4_pt
0.0188 ± 0.0004	lep_min_dr_jet	0.0017 ± 0.0004	dr_leps	0.0038 ± 0.0007	nJet
0.0141 ± 0.0004	mvaOutput_Ht_tagger	0.0010 ± 0.0001	Lep_min_dr_jet	0.0026 ± 0.0005	res-HTT_CSVsort4rd
0.0062 ± 0.0002	jetForward1_eta_abs	0.0005 ± 0.0002	res-HTT_CSVsort4rd	0.0014 ± 0.0001	nJetForward
0.0051 ± 0.0001	nBJetMedium			0.0008 ± 0.0001	nBJetMedium
0.0010 ± 0.0000	nJetForward				

1567 C Boosted Decision Trees

1568 In this appendix we add complementary plots to what is presented in Section 9.2. We show
 1569 the correlation matrices of the variables used for BDT trainings in Figs. 51 to 53. In Figs. 54
 1570 to 57 we show the shape normalized distributions of those variables, and compare the shapes
 1571 between the 2016 simulation and 2017/2018 simulations.

Figure 51: Correlation matrices of the variables used as inputs to the BDTs for signal extraction for the $0\ell + 2\tau_h$ (top) and $1\ell + 1\tau_h$ (bottom) categories. The plots on the left concern the $t\bar{t}H$ process, while the ones on the right concern the rest of the backgrounds. For the naming convention of the variables please refer to Table 37.

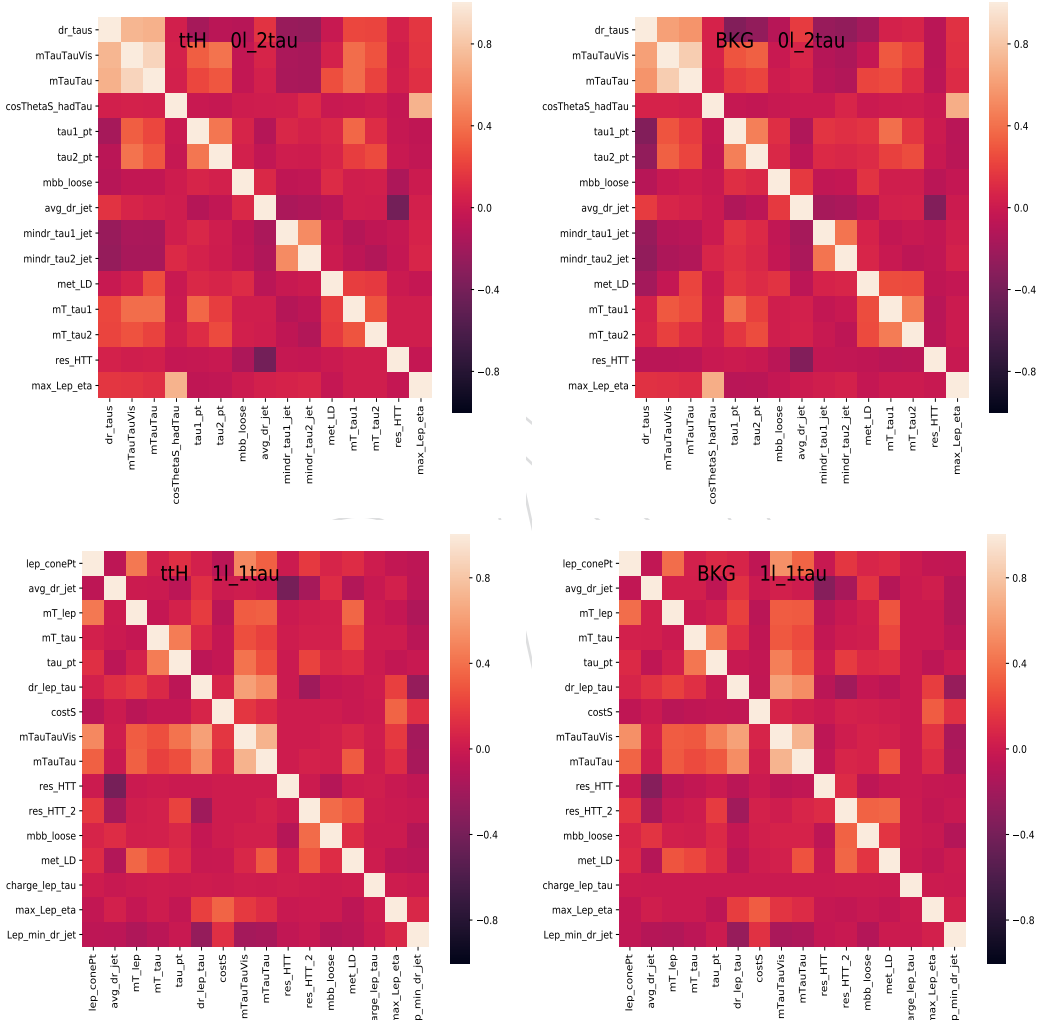


Figure 52: Correlation matrices of the variables used as inputs to the BDTs for signal extraction for the $1\ell + 2\tau_h$ (top) and $2\ell os + 1\tau_h$ (bottom) categories. The plots on the left concern the $t\bar{t}H$ process, while the ones on the right concern the rest of the backgrounds. For the naming convention of the variables please refer to Table 37.

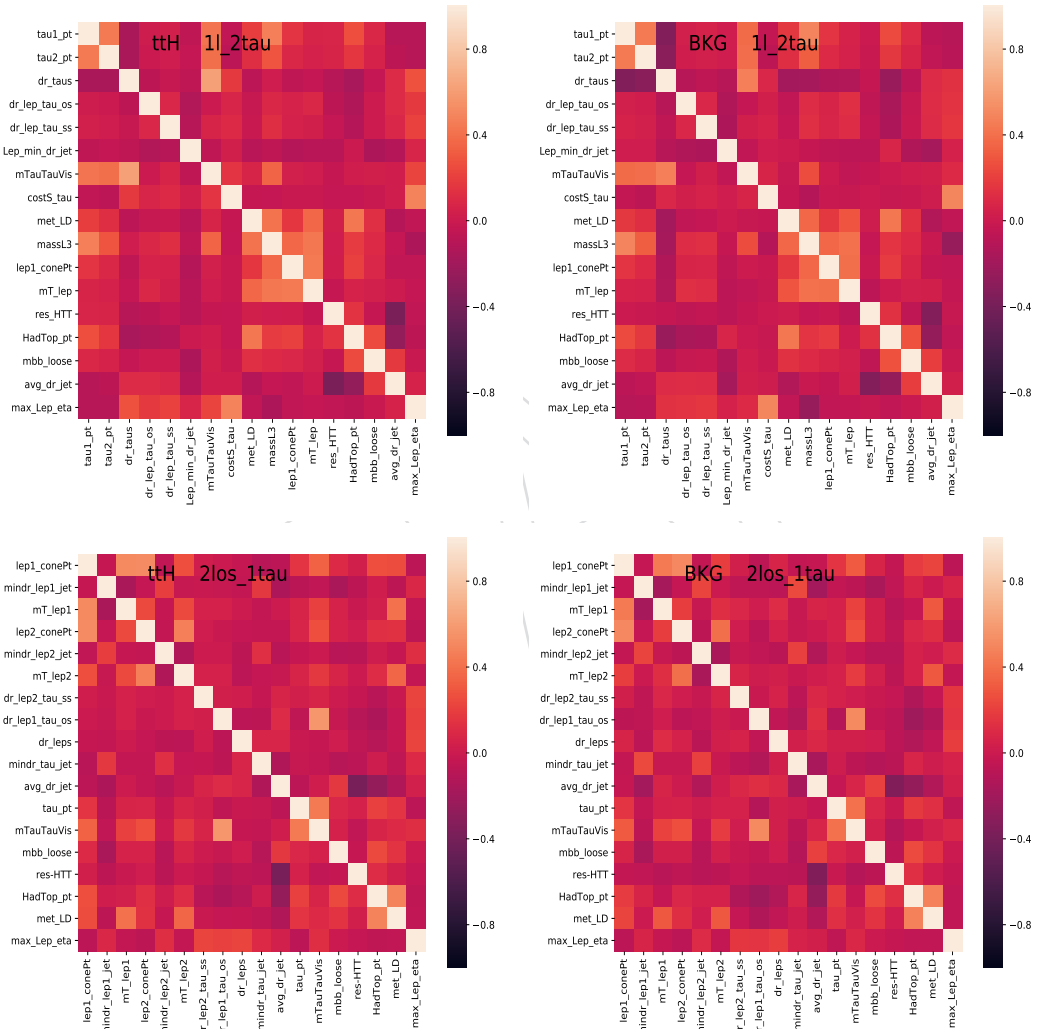


Figure 53: Correlation matrices of the variables used as inputs to the BDTs for signal extraction for the $2\ell + 2\tau_h$ (left), $3\ell + 1\tau_h$ (center) and $4\ell + 0\tau_h$ (right) categories. The plots in the top row concern the $t\bar{t}H$ process, while the ones in the bottom row concern the rest of the backgrounds. For the naming convention of the variables please refer to Table 37.

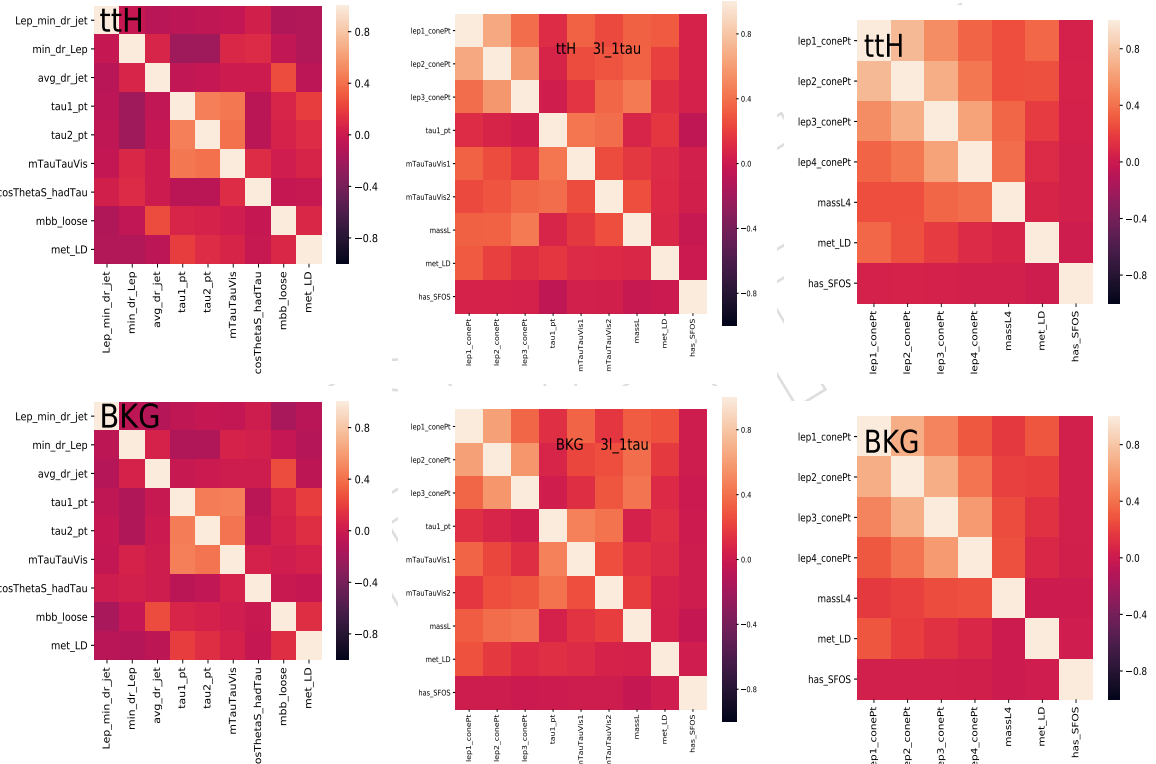


Figure 54: Shape normalized distributions of the variables used as input to the BDTs for signal extraction for the $0\ell + 2\tau_h$ (top) and $1\ell + 2\tau_h$ (bottom) categories. The plots correspond to the training region. The dashed lines correspond to the 2016 simulation while the continuous one to the 2017+2018 simulations. For the naming convention of the variables please refer to Table 37.

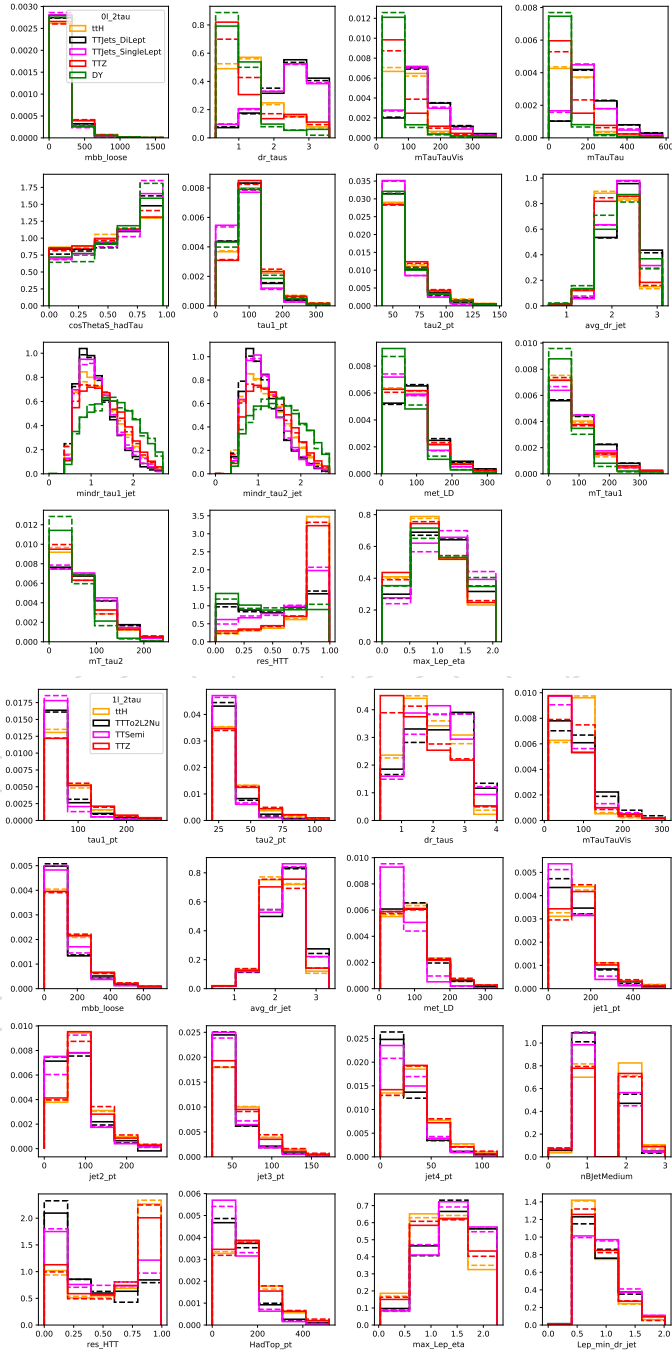


Figure 55: Shape normalized distributions of the variables used as input to the BDTs for signal extraction for the $1\ell + 1\tau_h$ category. The plots correspond to the training region. The dashed lines correspond to the 2016 simulation while the continuous one to the 2017+2018 simulations. For the naming convention of the variables please refer to Table 37.

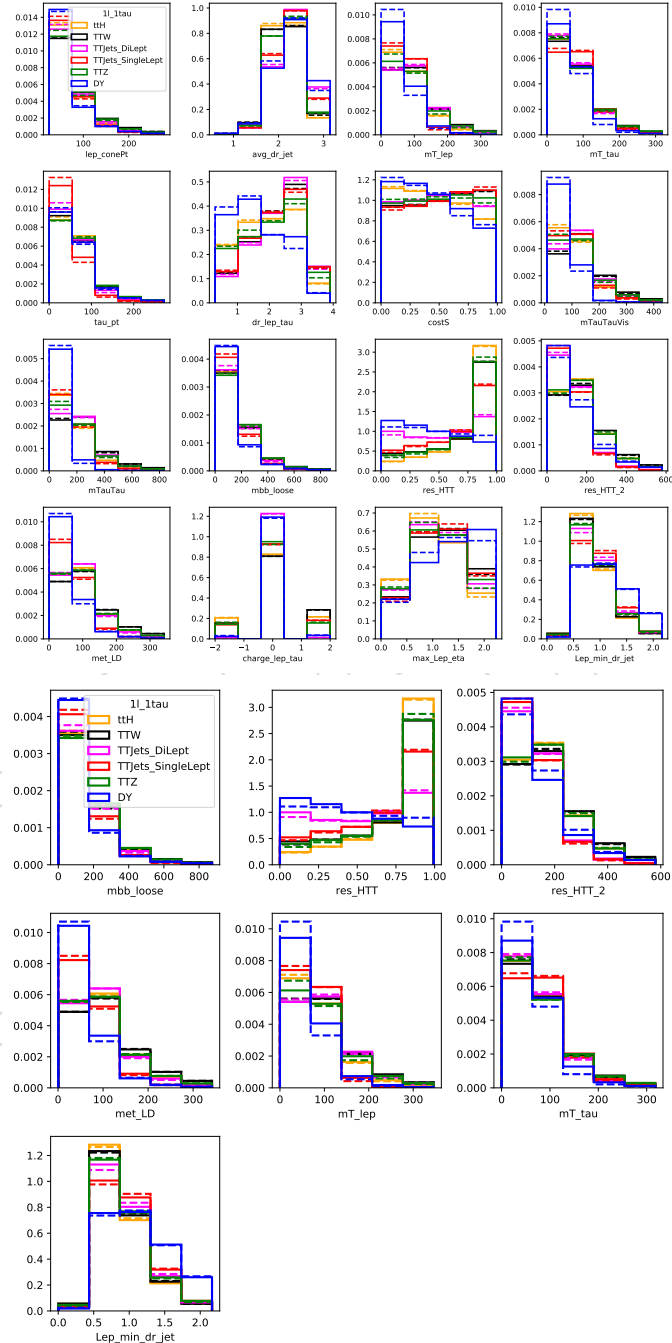
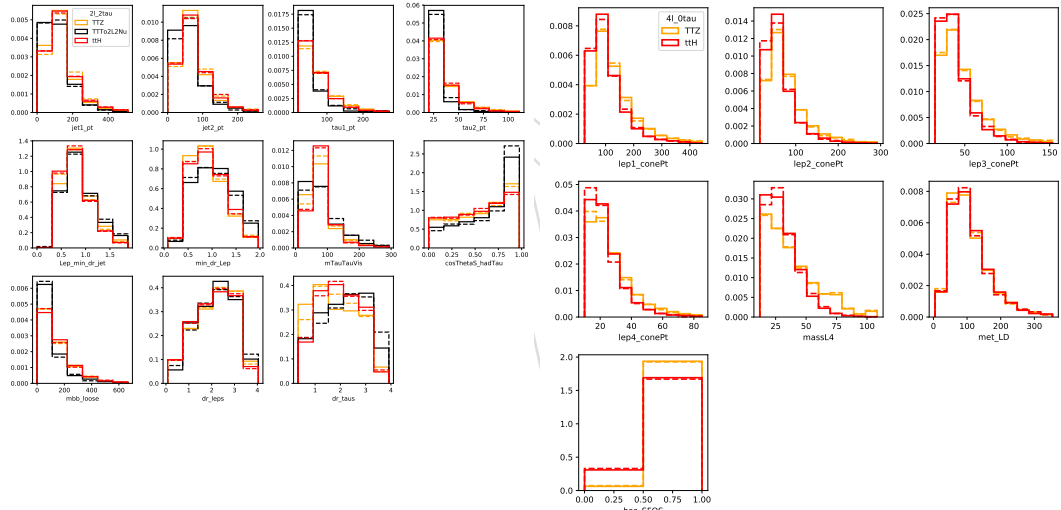


Figure 56: Shape normalized distributions of the variables used as input to the BDTs for signal extraction for the $2\ell_{\text{los}} + 1\tau_h$ (top) and $3\ell + 1\tau_h$ (bottom) categories. The plots correspond to the training region. The dashed lines correspond to the 2016 simulation while the continuous one to the 2017+2018 simulations. For the naming convention of the variables please refer to Table 37.



Figure 57: Shape normalized distributions of the variables used as input to the BDTs for signal extraction for the $2\ell + 2\tau_h$ (left) and $4\ell + 0\tau_h$ (right) categories. The plots correspond to the training region. The dashed lines correspond to the 2016 simulation while the continuous one to the 2017+2018 simulations. For the naming convention of the variables please refer to Table 37.



1572 D Higgs Jet Tagger

1573 The “Higgs-jet” (H_j) tagger is a BDT-based discriminant that targets the identification of jets
 1574 originating from a H boson decaying into two W bosons. Jets that are identified as originating
 1575 from had-top decays by the algorithm described in Section E are not considered by the H_j
 1576 tagger. The algorithm presented in this paragraph has been first developed and used in the
 1577 analysis with 2016 data. The TMVA package [29] was used to train the tagger in the analysis
 1578 with 2016 and 2017 data. The xgboost [30] algorithm, implemented using the scikit-learn [31]
 1579 package, is first introduced to train event level BDT-based discriminant in 2017 analysis in
 1580 channels with τ_h . It has been found to improve the sensitivity by $10 \sim 15\%$ [126]. Therefore
 1581 we move to xgboost algorithm to train the H_j tagger in this version of analysis. In the following,
 1582 we present updated results for the H_j tagger trained in legacy samples condition using xgboost.
 1583 The H_j tagger focuses on the $2\ell ss$ category, where the H boson decays to two W bosons via:
 1584 $t\bar{t}H \rightarrow bW, b\bar{W}, WW \rightarrow jj, b\ell\nu, b\bar{\nu}jj$. The selection criteria described in Section 5.3.4 require
 1585 the presence of two same-sign leptons and at least four jets, which means that one of the two W
 1586 bosons originating from the H boson decay decays hadronically. The two jets do not necessarily
 1587 both pass the $p_T > 25$ GeV and $|\eta| < 2.4$ cuts. Allowing for one of the two jets to fail the p_T
 1588 and η cuts, we have developed the H_j tagger to assess the likelihood for a jet to originate from
 1589 the decay chain $H \rightarrow WW^* \rightarrow \ell\nu_{\ell}jj$.

1590 The algorithm is trained on simulated samples of $t\bar{t}H$ and $t\bar{t}W$ events. Jets originating from
 1591 $H \rightarrow WW^* \rightarrow \ell\nu_{\ell}jj$ decays are considered as “signal” and jets that do not originate from
 1592 such decays are considered as “background”. Jets that are originating from had-top decays are
 1593 excluded from the training.

1594 The following observables are used as input to the BDT:

- 1595 • minimum ΔR between the jet and any electron or muon passing the fakeable lepton
 1596 selection criteria
- 1597 • maximum ΔR between the jet and any electron or muon passing the fakeable lepton
 1598 selection criteria
- 1599 • jet p_T
- 1600 • DeepFlavour b-tagging discriminant
- 1601 • quark-gluon discriminant [127] of the jet

1602 The distribution in BDT output of the H_j tagger for signal and background jets and the corre-
 1603 sponding feature importance are shown in Fig. 58. There is no evidence of overtrain from the
 1604 kolmogrov-smirnov test.

1605 The corresponding ROC curves are shown in Fig. 59. The ROC curve shows that the perfor-
 1606 mance of the H_j tagger to separate signal from background jets is similar in 2016 and 2017 and
 1607 is slightly different in 2018.

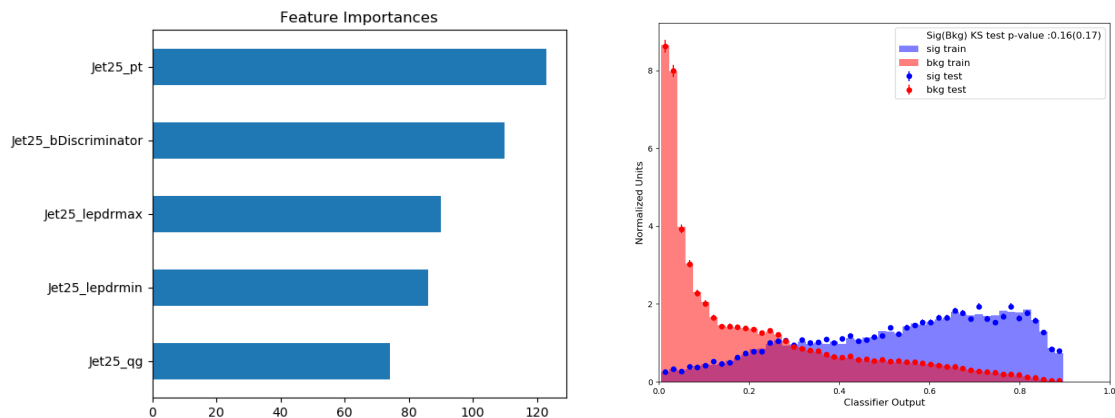


Figure 58: The feature importance (left) and distributions in the H_j discriminant (right)

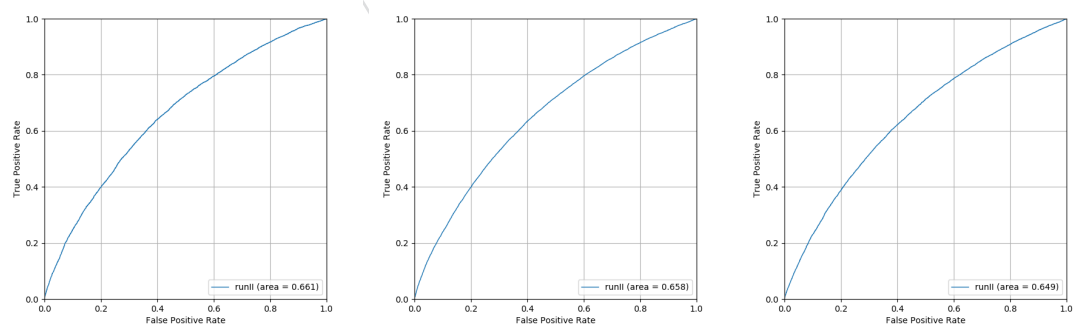


Figure 59: ROC curve for the separation between signal and background jets for the H_j taggers used in the 2016 (left), 2017 (middle) and 2018 (right) data-taken period.

1608 E Hadronic Top Tagger

1609 The Resolved Hadronic Top Tagger algorithm, referred to as “resHTT”, targets the case that the
 1610 b quark and the two quarks produced in the W boson decay are reconstructed as separate jets.
 1611 It computes the likelihood of three jets passing the selection criteria described in Section 3.3
 1612 and not overlapping, within $\Delta R < 0.4$, with an electron, muon, or τ_h passing the fakeable
 1613 object selection criteria to be compatible with originating from a had-top decay. We refer to
 1614 the combination of three such jets as “jet triplet”. The algorithm uses a BDT to discriminate
 1615 triplets of jets in which all jets are generator-level matched to quarks from a had-top decay (the
 1616 “signal”) from jet triplets in which one or more jets fail to satisfy this matching criterion (the
 1617 “background”).

1618 The following variables are used as input to the BDT:

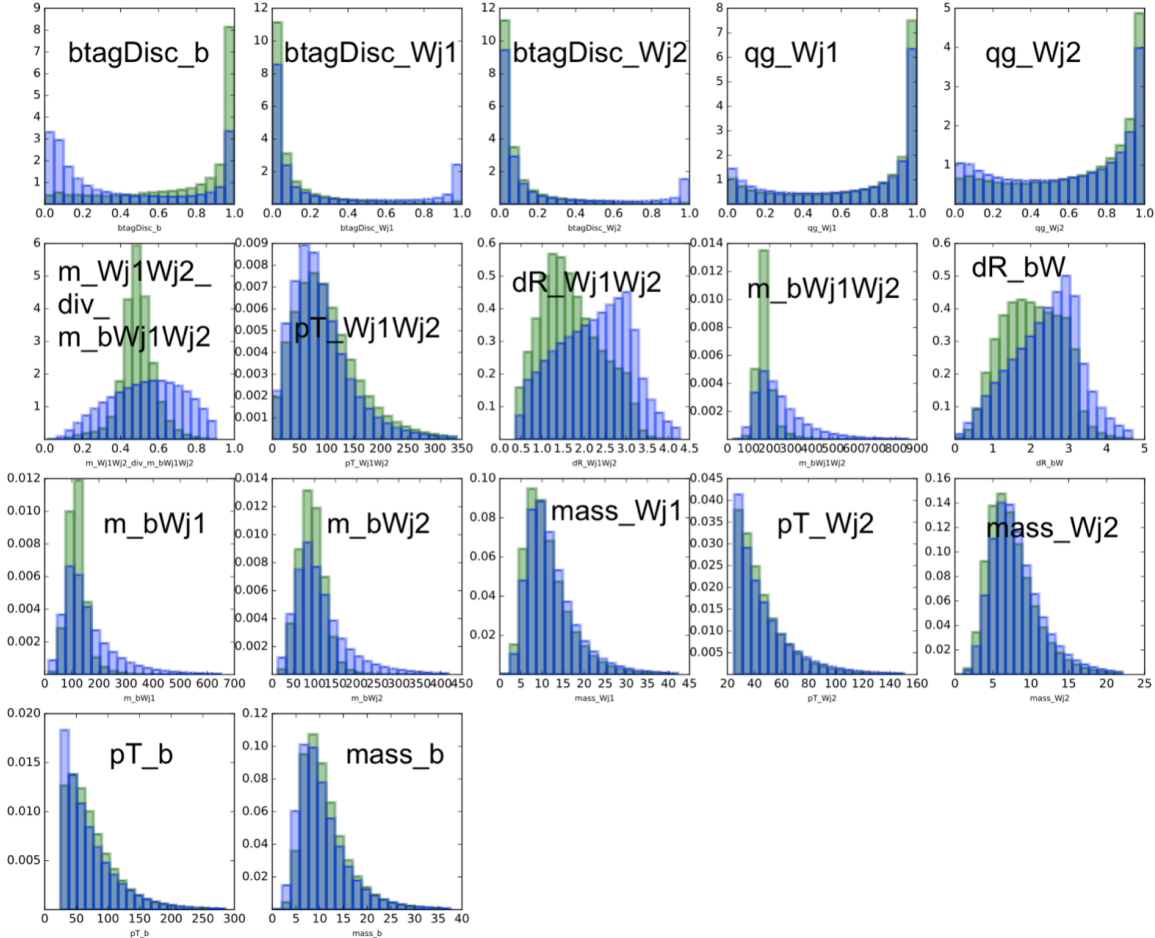
- 1619 • `btagDisc_b`, b-tag discriminator of the BJet-candidate.
- 1620 • `btagDisc_Wj1`, b-tag discriminator of the Wj1-candidate.
- 1621 • `btagDisc_Wj2`, b-tag discriminator of the Wj2-candidate.
- 1622 • `qg_Wj1`, quark-gluon discriminator of the Wj1-candidate.
- 1623 • `qg_Wj2`, quark-gluon discriminator of the Wj2-candidate.
- 1624 • `m_bWj1Wj2`, mass of $(b + W1 + W2)$.
- 1625 • `m_Wj1Wj2_div_m_bWj1Wj2`, ratio between mass of mass of $(W1 + W2)$ and mass of
 $(b + W1 + W2)$.
- 1626 • `pT_Wj1Wj2`, p_T of $(b + W1 + W2)$.
- 1627 • `dR_Wj1Wj2`, delta radii between $W1$ and $W2$.
- 1628 • `dR_bW`, delta radii between b and $(W1 + W2)$.
- 1629 • `m_bWj1`, mass of $(b + W1)$.
- 1630 • `m_bWj2`, mass of $(b + W2)$.
- 1631 • `mass_Wj1`, mass of WJet1-candidate.
- 1632 • `pT_Wj2`, p_T of WJet2-candidate.
- 1633 • `mass_Wj2`, mass of WJet2-candidate.
- 1634 • `pT_b`, p_T of BJet-candidate.
- 1635 • `mass_b`, mass of BJet-candidate.

1637 where the symbol b refers to the jet corresponding to the b quark, and the symbols $W1$ and
 1638 $W2$ refer to the quarks of higher and lower p_T that are produced in the decay of the W boson,
 1639 respectively. The b-tag discriminator used on training was DeepCSV. The distributions of
 1640 these variables for jet triplets considered as signal and background are shown in Fig. 60, their
 1641 correlations are shown in Fig. 61.

1642 The BDT is trained using a mixture of $t\bar{t}H$, $t\bar{t}W$, $t\bar{t}Z$, and $t\bar{t}$ +jets samples, produced by the
 1643 MC simulation. No further event selection criteria are applied to the events used for the BDT
 1644 training, the idea being that the res-HTT algorithm is trained once for all categories in which
 1645 $t\bar{t}H$ signal events are expected to contain top quarks that decay hadronically ($2\ell ss + 0\tau_h$, $2\ell ss +$
 1646 $1\tau_h$, $3\ell ss + 0\tau_h$, $0\ell + 2\tau_h$, $1\ell + 1\tau_h$, $1\ell + 2\tau_h$ and $2\ell os + 1\tau_h$).

1647 For the training stage we do some selections to be able to keep the quantity of signal and back-
 1648 ground (matched and non-matched jet triplets) within a reasonable quantity of representative
 1649 triplets to the training be feasible (the number of entries stay within 1-2M for each MC compo-

Figure 60: Distribution of BDT input variables used for reconstructing had-top decays for signal (green) and background (blue) jet triplets in simulated $t\bar{t}+jets$ events produced with the full CMS detector simulation for 2017 detector conditions.



1650 nent), from which we use 0.8 (0.2) for training (testing): The first obvious selection is to only
 1651 accept events with three jets or more. The other practical selections that are done in the training
 1652 stage is to only consider events where there is at least one generation level W-boson (at least
 1653 one potential "signal") and to accept the triplets formed where the b-jet candidate is up to
 1654 the fourth ranked with respect to the highest b-tag discriminator. Such selections is not used
 1655 on application. For application we loop on all the possible jet triplets and chose as the hadronic
 1656 top candidate is the one in which the BDT returned the highest score. If there are no three jets
 1657 a sentinel value is set to the res-HTT at event level.

1658 The choice of variables, hyperparameters BDTs and overtraining tests are optimized consider-
 1659 ing the ROC curves between "signal" and "background". The Area Under the Curve (AUC)
 1660 for the ROC curve of the final training is 0.907 (0.898) for training (testing)². In Fig. 62 we show
 1661 the ranking of variable importance for the final BDT.

1662 The performance of the algorithm is quantified by the separation power between the $t\bar{t}H$ -signal

² During the decision making of the algorithm different methods for the screening of the training/testing dataset, among the options where a mass selection around the top or W candidate mass, and the usage of kinematic fit variables. It is not on the scope of the AN to discuss those methods, for the interested reader more details can be found on this presentation https://indico.cern.ch/event/762838/contributions/3175553/attachments/1735115/2806113/HTT_2017_ttHmeeting.pdf

Figure 61: Correlation between variables used for reconstructing had-top decays.

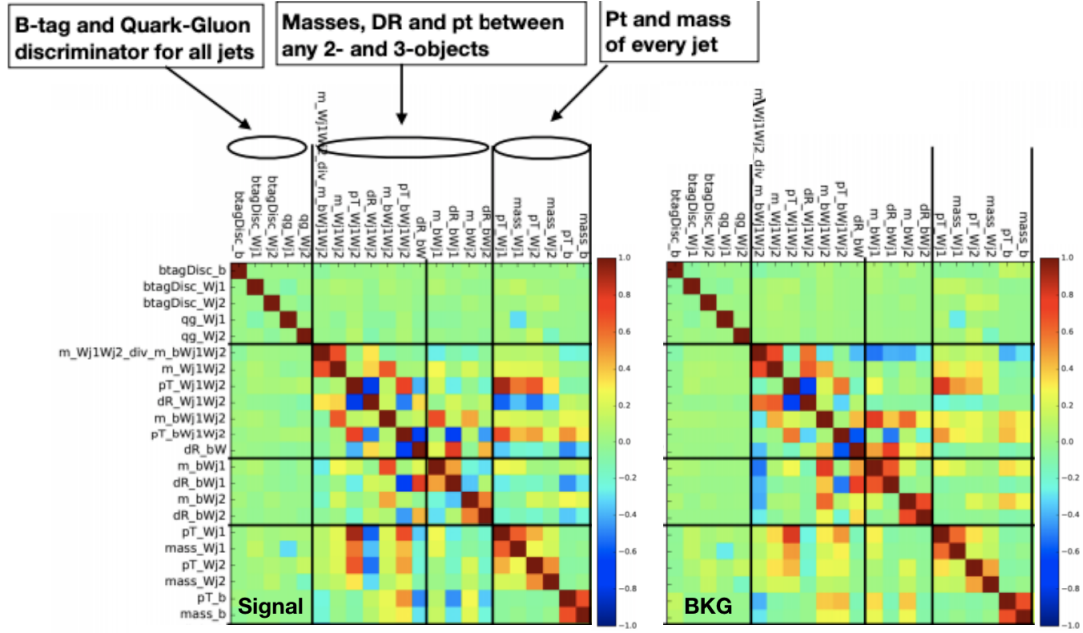
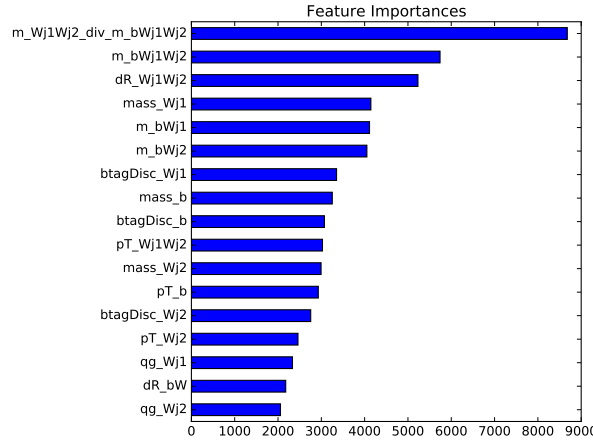
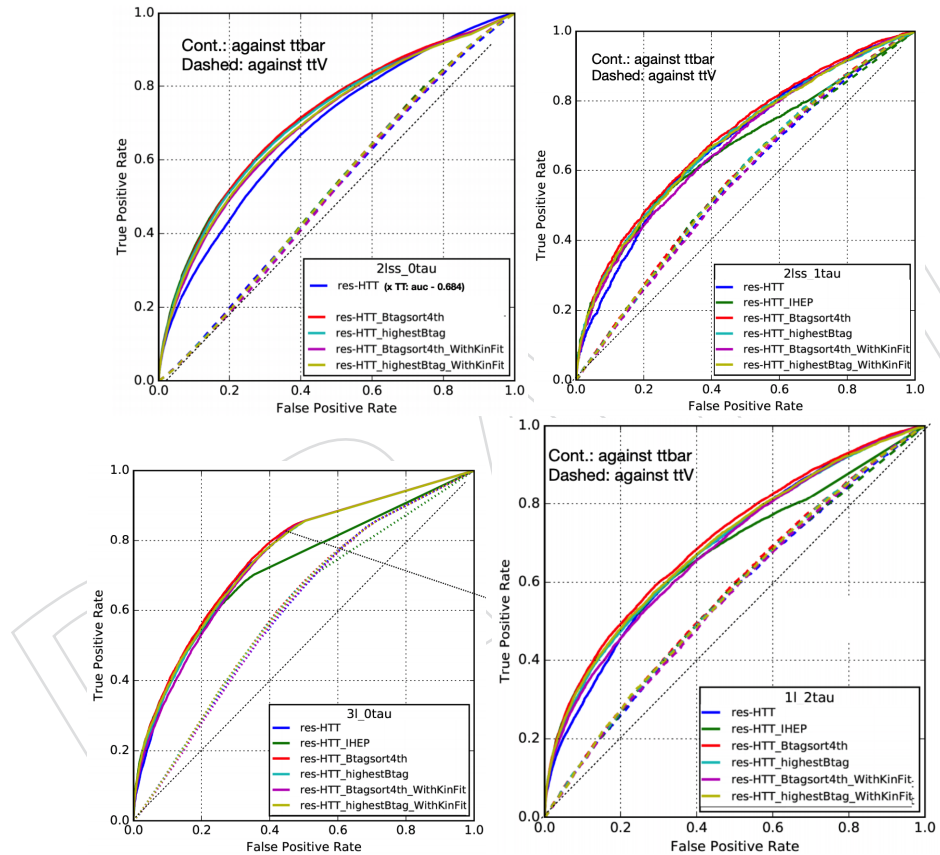


Figure 62: Ranking of variables importance for the BDT reconstructing had-top decays from the hypothesis of resolved decays.



and the main backgrounds (ROC) to each category separately. In the $0\ell + 2\tau_h$ and $1\ell + 1\tau_h$ that means $t\bar{t}$, DY and $(t\bar{t}Z + t\bar{t}W)$, for all the other categories that means only $t\bar{t}$ and $(t\bar{t}Z + t\bar{t}W)$. On Fig. 63 we show the ROC curves where tth -signal is taken as signal and the other or $t\bar{t}$ or DY (when relevant) or $(t\bar{t}Z + t\bar{t}W)$. On Figure It is clear that the res-HTT is a tool to deal with $t\bar{t}$ and DY as the first is expected to have top quarks with more discriminant and the second is not expected to have top quarks at all.

Figure 63: ROC curves for the different categories where the res-HTT is used. The corresponding category can be found in the legend.



1669 F Matrix Element Method

1670 For the $2\ell ss + 1\tau_h$ and $3\ell + 0\tau_h$ categories, discriminants based on the matrix element method
 1671 (MEM) are used to increase the separation of the tH and $t\bar{t}H$ signals from the main back-
 1672 grounds. In the case of the $2\ell ss + 1\tau_h$ category, the MEM implementation has been optimized
 1673 to separate $t\bar{t}H$, $H \rightarrow \tau\tau$ events from several kinds of background: $t\bar{t}Z$ events (including an
 1674 irreducible component with $Z \rightarrow \tau\tau \rightarrow \ell\tau_h$ decays and a reducible component with $Z \rightarrow \ell\ell$
 1675 where one lepton is misreconstructed as a τ_h) and semileptonic $t\bar{t}$ events with an additional
 1676 non-prompt lepton from b quark hadronization. In the case of the $3\ell + 0\tau_h$ category, the MEM
 1677 implementation has been optimized to separate tH and $t\bar{t}H$ from the irreducible $t\bar{t}Z$ and $t\bar{t}W$
 1678 backgrounds.

1679 The MEM makes use of the differential decay widths predicted by the theory by using the
 1680 matrix element $\mathcal{M}_\Omega(\mathbf{x})$ associated to a given process Ω , which depends on a set of variables \mathbf{x}
 1681 which describes the initial- and the final- state particles at a parton level. The squared matrix
 1682 element is then convoluted with a function $W(\mathbf{y}||\mathbf{x})$ associated to the event reconstruction in the
 1683 detector and called transfer function. It represents the probability that a set of event observables
 1684 \mathbf{y} (lepton, τ_h , jet and E_T^{miss} 4-momenta) is measured given a parton-level configuration \mathbf{x} .

More specifically, the MEM aims at computing the differential cross-section of the process Ω with respect to the observables \mathbf{y} , while integrating over the unmeasured or poorly measured parton-level quantities \mathbf{x} , as well as the Bjorken fractions of the incoming partons x_a and x_b . The differential cross-section, also called weight in the case of the MEM, is computed as:

$$w_\Omega(\mathbf{y}) = \frac{1}{\sigma_\Omega} \sum_p \int d\mathbf{x} dx_a dx_b \frac{f_i(x_a, Q) f_j(x_b, Q)}{x_a x_b s} \delta^2(x_a P_a + x_b P_b - \sum p_k) |\mathcal{M}_\Omega(\mathbf{x})|^2 W(\mathbf{y}||\mathbf{x}) \quad (10)$$

1685 The factor σ_Ω can be fixed by the condition $\int d\mathbf{y} w_\Omega(\mathbf{y}) = 1$ and corresponds to the product of
 1686 the cross-section of the process Ω with the acceptance of the analysis. The sum \sum_p corresponds
 1687 to a sum over all the possible assignments of the reconstructed objects to the parton-level ob-
 1688 jects p (a so-called permutation). The functions $f_i(x, Q)$ are the parton distribution functions
 1689 associated to the incoming parton of flavor i , depending on their Bjorken fraction x and the
 1690 scale of the process Q . As the reconstructions in CMS of the different objects are mostly un-
 1691 correlated, the overall transfer function $W(\mathbf{y}||\mathbf{x})$ can be split into a product of different transfer
 1692 functions associated to each individual object.

Each weight $w_\Omega(\mathbf{y})$ represents the probability to measure the set of observables \mathbf{y} given the process Ω . The weights associated to signal and background processes are then combined in a likelihood ratio of the form

$$\mathcal{L}(\mathbf{y}) = \frac{w_{tH/t\bar{t}H}(\mathbf{y})}{w_{tH/t\bar{t}H}(\mathbf{y}) + w_{\mathcal{B}}(\mathbf{y})} \quad (11)$$

1693 which is optimized to discriminate the $tH/t\bar{t}H$ signals from the the background \mathcal{B} . A combined
 1694 likelihood ratio is also defined to provide discrimination against the different backgrounds
 1695 simultaneously, using the sum of the background weights instead of the individual ones. This
 1696 variable, whose value is between 0 and 1, can then be interpreted as the probability that a
 1697 given event associated to \mathbf{y} originates from the $tH/t\bar{t}H$ process rather than from one of the
 1698 background processes \mathcal{B} .

1699 In the $2\ell ss + 1\tau_h$ category, two subcategories of events are defined base on the compatibility of
 1700 the event with the $t\bar{t}H$ hypothesis. The so-called "no missing jet" events correspond to events

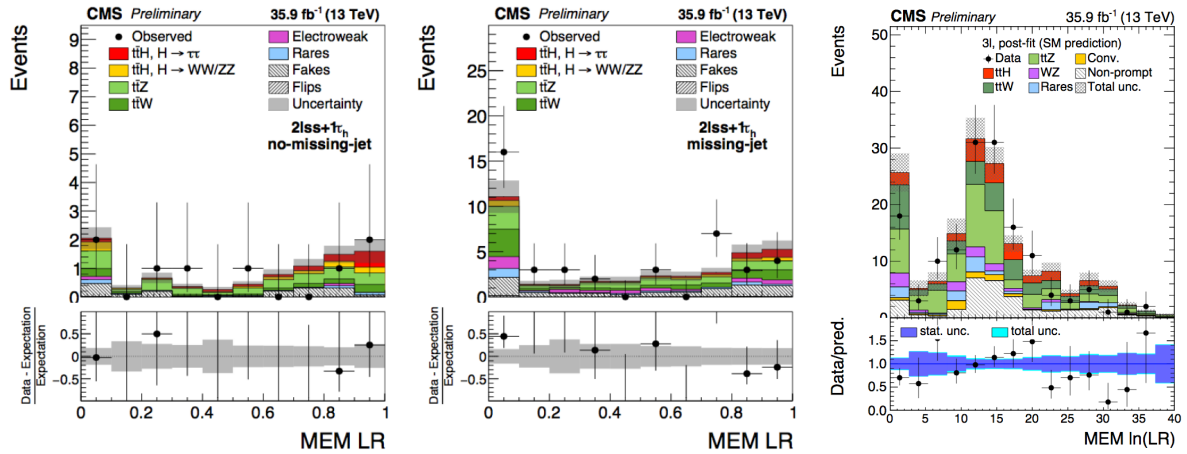


Figure 64: MEM LR scores for $2\ell\text{ss} + 1\tau_h$ category (two left plots) and $3\ell + 0\tau_h$ (right plot). [PLACEHOLDER]

where it is possible to find reconstructed jets to be associated to each of the final-state quarks from the top decays, while the "missing jet" events correspond to those where one of the jets from a light quark is not reconstructed, either because it falls out of the detector acceptance or because it is merged into another reconstructed jet. In the case of the latter, an integration over the direction of the missing jet is performed to compute the weights.

The distributions of the combined likelihood ratio are presented in Fig. 64 and the discrimination obtained in each of those categories of events with the different likelihood ratios is presented in the ROC curves in Fig. ???. It can be seen that the specific likelihood ratios have the expected behavior and provide a good discrimination between the signal(s) and the background for which they are optimized, while the combined likelihood ratio is relatively performant against each of the background components.

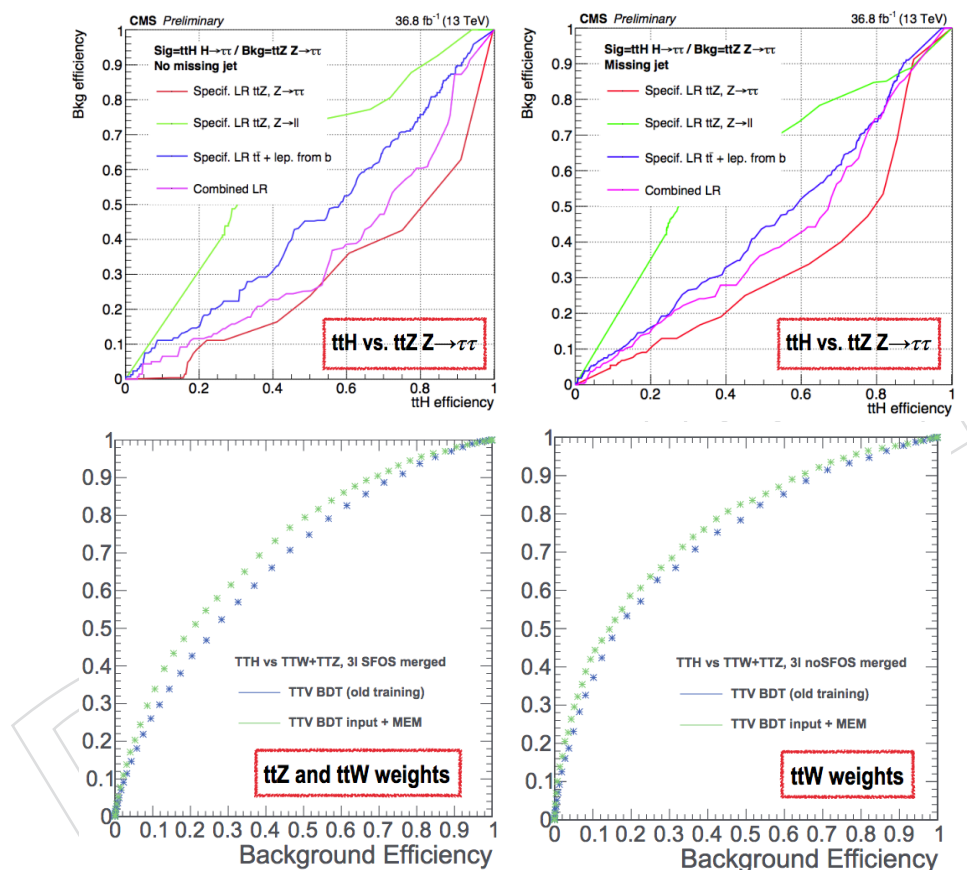


Figure 65: ROC curves for the $2\ell_{ss} + 1\tau_h$ and $3\ell + 0\tau_h$ categories. [PLACEHOLDER]

1712 G Single variable analysis

1713 A simplified version of the signal extraction strategy described in Section 9 has been designed
 1714 to serve as both a cross-check of the main procedure as well as to highlight the improvement
 1715 obtained from the usage of MVA techniques over an optimized approach relying only on the
 1716 discriminant power of a single variable in the multileptonic (without taus) categories.

1717 The strategy relies on the subcategorization approach used in the previous iterations of the
 1718 analysis and described in [128]. The $2\ell ss + 0\tau_h$ and $3\ell + 0\tau_h$ statistically rich categories are
 1719 first splitted into subcategories of different sensitivity and background composition. Then, a
 1720 common single discriminant variable and binning is chosen across all subcategories and years
 1721 to define the set of bins that will be used for the joint maximum likelihood fit used for the
 1722 signal extraction. Categories are defined as described in Section 5 with some additional tighter
 1723 cuts corresponding to phase spaces of low sensitivity in which no benefit is found by using the
 1724 single variable approach, mostly due to very low signal presence.

1725 The $2\ell ss + 0\tau_h$ category is first tightened by requiring at least 4 selected jets to further suppress
 1726 the non-prompt and $t\bar{t}W$ backgrounds. It is then further classified in terms of the flavor of the
 1727 leptons ($ee, e\mu$ and $\mu\mu$) to profit from the flavor asymmetry of processes like the charge flips
 1728 and photon conversions. Each of these subcategories is then split according the number of total
 1729 selected jets ($N_{jet} < 6$ and $N_{jet} \geq 6$) to clearly separate the phase spaces dominated by either the
 1730 non-prompt or $t\bar{t}W + t\bar{t}Z$ backgrounds. The $e\mu$ and $\mu\mu$ categories -for which enough statistical
 1731 power is available- are then split by the total charge of the final state, to take advantage of the
 1732 charge asymmetry in the $t\bar{t}W$ process.

1733 A similar approach is employed for the $3\ell + 0\tau_h$ category which is first required to have at
 1734 least two selected jets. It is then splitted in terms of jet multiplicity ($N_{jet} < 4$ and $N_{jet} \geq 4$) and
 1735 then based on the final state total charge; the motivations being similar to those of the previous
 1736 category.

1737 The $4\ell + 0\tau_h$ category is included in the fit but no subcategorization is considered due to the
 1738 expected low amount of statistical power.

1739 An alternative subcategorization in line with that of [128] -based on the usage of b tagging sub-
 1740 categories instead of jetmultiplicity ones- has been tested extensively and found to be slightly
 1741 underperforming (at the 10-15% level) as the increased presence of signal in high sensitivity
 1742 regions was suppressed by the uncertainties associated to higher amounts of the non-prompt
 1743 background.

1744 A summary of the yields in the subcategories used for the single variable analysis can be seen
 1745 in Figure 66.

1746 Multiple variables related to lepton kinematics (leading and trailing leptons p_T and η , minimum
 1747 and maximum η , invariant mass of the leptonic system, minimum angular distance between
 1748 leptons, minimum invariant mass of any dilepton pair), jet properties (total hadronic energy, jet
 1749 multiplicity, b tagged jet multiplicity) and global event quantities (missing transverse energy,
 1750 minimum and maximum angular distance between any lepton-jet pair or leading lepton and
 1751 jet pair) are considered as candidates to single best variable.

1752 The width in a best fit to the signal strength performed over the distribution of each variable
 1753 across all categories is computed for each variable as a figure of merit to choose the final one.
 1754 For each variable three different possible binnings are considered: uniform binning between
 1755 minimum and maximum value, bins of uniform background content and bins of uniform signal
 1756 content. The same number of bins is chosen for each case: 9 bins for the $2\ell ss + 0\tau_h$ category,

Figure 66: Distributions of the subcategories used for the single variable analysis. From left to right: 2016, 2017 and 2018 year. From top to bottom: $4\ell + 0\tau_h$, $3\ell + 0\tau_h$ and $2\ell ss + 0\tau_h$ categories

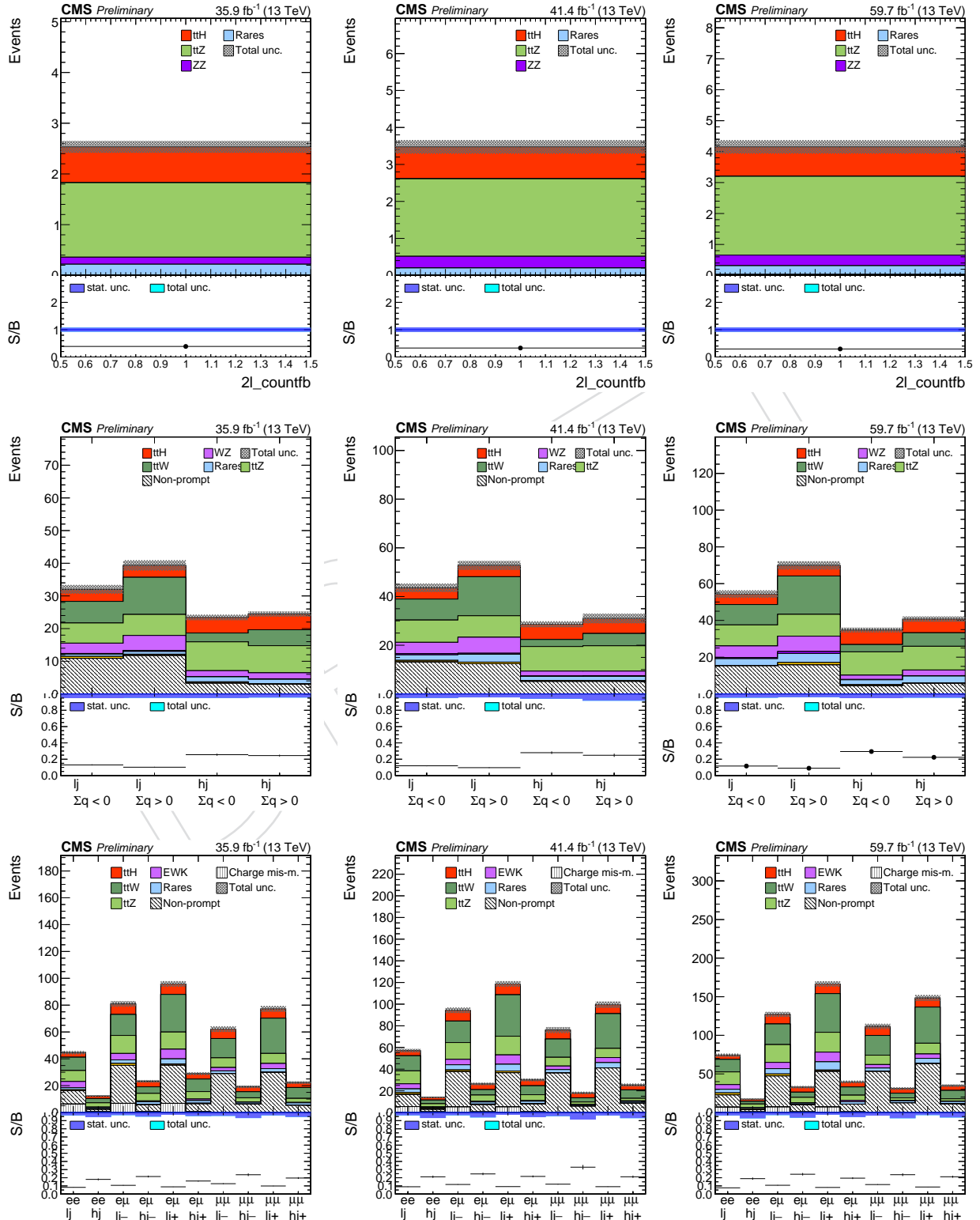


Table 44: Expected signal strength confidence interval width ($\Delta\mu$) and median significance (σ) for the SM-like $t\bar{t}H$ process for each year and category based on the single variable analysis as well as the combination of all categories with and without the different control regions. Results are obtained with the Asimov dataset under the background plus signal hypothesis.

	$\Delta\mu(2016)$	$\Delta\mu(2017)$	$\Delta\mu(2018)$	$\Delta\mu(\text{Comb.})$	$\sigma(2016)$	$\sigma(2017)$	$\sigma(2018)$	$\sigma(\text{Comb.})$
$2\ell ss + 0\tau_h$	0.75	0.67	0.63	--	1.42	1.60	1.70	--
$3\ell + 0\tau_h$	0.96	0.91	0.75	--	1.23	1.30	1.50	--
$4\ell + 0\tau_h$	3.15	3.08	2.56	--	0.40	0.41	0.44	--
Comb.	--	--	--	0.43	--	--	--	3.00
Comb. + CR	--	--	--	0.38	--	--	--	3.56

1757 5 bins for the $3\ell + 0\tau_h$ category and 3 bins for the $4\ell + 0\tau_h$ category. Bins are defined to be
 1758 consistent across subcategories for each category. The final best value of the figure of merit is
 1759 finally selected to select the final best one.

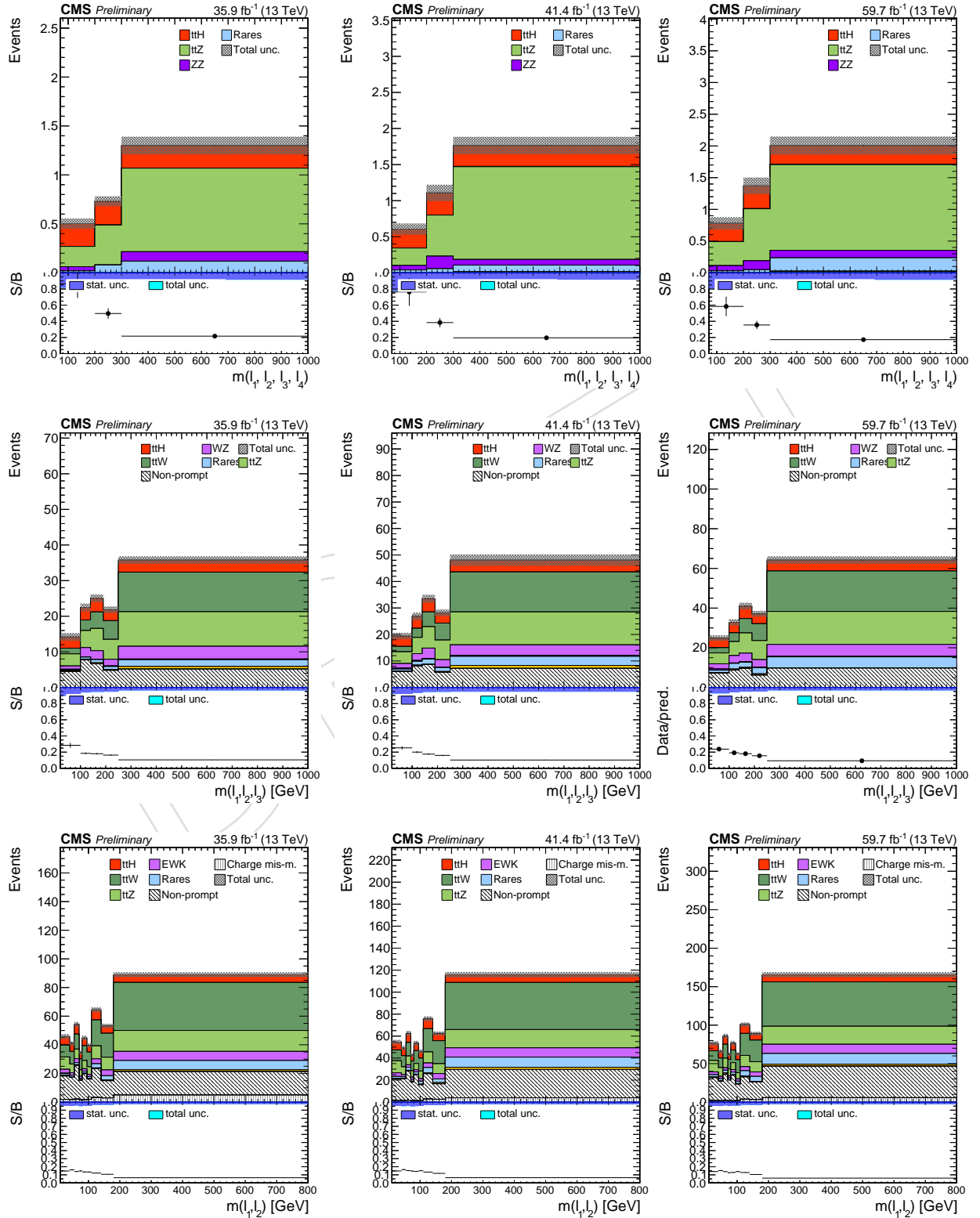
1760 The final variable selected for the single variable analysis is the invariant mass of the total
 1761 lepton system, which shows strong discriminance against both the $t\bar{t}W$ and $t\bar{t}Z$ processes, thus
 1762 easily complementing the separation against the non-prompt background provided by the sub-
 1763 categorization strategy, slightly overperforming (by a 5%) the whole N_{jets} and $\min(\Delta R(l, j))$
 1764 distributions, which offer a better separation from the non-prompt background but worse per-
 1765 formance against prompt lepton processes.

1766 The distributions of the chosen variable -using bins of uniform signal presence- can be observed
 1767 in Figure 67.

1768 The final result with the single variable analysis is obtained through a maximum likelihood fit
 1769 to the distribution of the invariant mass of the leptonic system across all subcategories previ-
 1770 ously detailed. Table 44 contains the final values of the best fit uncertainty and significance
 1771 obtained through this fit. A final result is obtained combinint this distributions with the in-
 1772 formation from the ZZ, $t\bar{t}Z$, WZcontrol regions and the -excluded from the categorization-
 1773 $2\ell ss + 0\tau_h + 3\text{jet}$ region. In this last case each of the control regions becomes one single bin in
 1774 the fit.

1775 An alternative study in which consistency was sacrificed by allowing the variable used for each
 1776 possible subcategory to vary independently was also developed, finding a possible improve-
 1777 ment of up to a significance of 3.82σ when combined with the control regions detailed above.
 1778 Such method resulted in the use of a mixture of the number of jets, total hadronic energy and
 1779 minimum distance between a lepton and a jet in the event and the invariant mass of the leptonic
 1780 system for the different categories in the analysis.

Figure 67: Distributions of the invariant mass of the leptonic system used for the signal extraction in the single variable analysis. From left to right: 2016, 2017 and 2018 year. From top to bottom: $4\ell + 0\tau_h$, $3\ell + 0\tau_h$ and $2\ell ss + 0\tau_h$ categories



1781 H Differential cross-section measurements

1782 The measurement of the $t\bar{t}H$ differential cross section as a function of the Higgs boson trans-
 1783 verse momentum, p_T^H , allows to disentangle the effects of modified Higgs boson self-coupling
 1784 values from other effects such as the presence of anomalous top-Higgs couplings [122]. More-
 1785 over, such measurements are proven to provide a strong handle on relevant Effective Field
 1786 Theory (EFT) dimension-six operators through the constraint of the corresponding Wilson co-
 1787 efficients [129]. Differential results within a Simplified Template Cross Section (STXS) frame-
 1788 work are also very important in that they permit the integration of top-Higgs coupling results
 1789 in the global fits for the properties of the Higgs(125) boson. Preliminary results on the $t\bar{t}H$
 1790 cross-section measurements are therefore of uttermost importance, as they anticipate strategic
 1791 decisions within the HEP community.

1792 H.1 Available final states

1793 The decision on which final state must be investigated first is driven by two main considera-
 1794 tions: the amount of events expected in each final state, and the possibility of performing a full
 1795 or approximately full kinematic reconstruction of each final state. The ability of performing
 1796 an approximately full kinematic reconstruction of the final state is crucial to disentangle the
 1797 top-quark-related portion of the event from the Higgs-boson-related part of the event.

1798 The $2\ell ss + 0\tau_h$ final state is characterized by the largest expected yields. Its kinematics is de-
 1799 termined by 40 free parameters:

$$\begin{aligned} P(t) &= P(b) + P(W) & P(W) &= P(\ell_1) + P(v_1) \\ P(\bar{t}) &= P(b) + P(W) & P(W) &= P(q_1) + P(q_2) \\ P(H) &= P(W) + P(W) & P(W) &= P(\ell_2) + P(v_2), \\ & & P(W) &= P(q_3) + P(q_4). \end{aligned} \tag{12}$$

1800 This final state can be determined by using 39 measurements and constraints, as outlined in
 1801 Table 45. A last constraint can be added using experimental hypotheses, such as adding a
 1802 longitudinal momentum hypothesis for the neutrinos, or splitting the E_T^{miss} into components
 1803 assigned to the two neutrinos.

Object	Parameter	Type	N_{pars}	Total (incremental)
Charged leptons	(E, \vec{p})	measurement	2×4	8
Jets	(E, \vec{p})	measurement	6×4	32
Neutrinos	E_T^{miss}	measurement	2	34
W (had)	window on/off shell	constraint	2×1	36
Top mass	$m_t = 174.3 \text{ GeV}, m_t = m_{\bar{t}}$	constraint	2	38
Higgs mass	$m_H = 125.1 \text{ GeV}$	constraint	1	39

Table 45: Measurements and constraints for the $2\ell ss + 0\tau_h$ final state.

1804 The $3\ell + 0\tau_h$ final state is also characterized by quite large expected yields. Its kinematics is
 1805 described by 40 parameters:

$$\begin{aligned}
P(t) &= P(b) + P(W) & P(W) &= P(\ell_1) + P(v_1) \\
P(\bar{t}) &= P(b) + P(W) & P(W) &= P(q_1) + P(q_2) \\
P(H) &= P(Z) + P(Z) & P(Z) &= P(\ell_2) + P(\ell_3), \\
&& P(Z) &= P(q_3) + P(q_4),
\end{aligned} \tag{13}$$

and the measurements and constraints that can be set result in an overconstrained system, as outlined in Table 46. A big difficulty lies however in the problem of assigning each object to its parent particle, due to combinatorics effects. This final state is therefore not examined in this version of the analysis.

Object	Parameter	Type	N_{pars}	Total (incremental)
Charged leptons	(E, \vec{p})	measurement	3×4	12
Jets	(E, \vec{p})	measurement	6×4	36
Neutrinos	E_T^{miss}	measurement	2	38
Z (lep)	window on/off shell	constraint	1	39
Z (had)	window on/off shell	constraint	1	40
W (had)	window on/off shell	constraint	1	41
Top mass	$m_t = 174.3 \text{ GeV}, m_{\bar{t}} = m_t$	constraint	2	43
Higgs mass	$m_H = 125.1 \text{ GeV}$	constraint	1	44

Table 46: Measurements and constraints for the $3\ell + 0\tau_h$ final state.

The $4\ell + 0\tau_h$ final state is characterized by very low expected yields, making it not useful for a differential measurement with the available luminosity. Furthermore, it is still determined by 40 parameters:

$$\begin{aligned}
P(t) &= P(b) + P(W) & P(W) &= P(\ell_1) + P(v_1) \\
P(\bar{t}) &= P(b) + P(W) & P(W) &= P(q_1) + P(q_2) \\
P(H) &= P(W) + P(W) & P(W) &= P(\ell_2) + P(v_2), \\
&& P(W) &= P(q_3) + P(q_4),
\end{aligned} \tag{14}$$

but this time the system is severely underconstrained, as outlined in Table 47. Even when imposing constraints on the mass of the parent objects the system remains severely underconstrained. The combination of the low expected yields and of the lack of enough constraints led to the decision of not considering this final state for this preliminary differential analysis.

Object	Parameter	Type	N_{pars}	Total (incremental)
Charged leptons	(E, \vec{p})	measurement	4×4	16
Jets	(E, \vec{p})	measurement	2×4	24
Neutrinos	E_T^{miss}	measurement	2	26

Table 47: Measurements and constraints for the $4\ell + 0\tau_h$ final state.

Final states with hadronic taus are a natural extension of this study, but will be pursued in this round only after the basic method outlined in the following part of this section has led to results in the $2\ell ss + 0\tau_h$ final state.

1820 H.2 Reconstructing the Higgs boson p_T in the $2\ell ss + 0\tau_h$ final state

1821 In this section, we study the $t\bar{t}H$ differential cross-section in the $2\ell ss + 0\tau_h$ final state; as men-
 1822 tioned in the previous paragraphs, this is the final state which contains the largest statistics and
 1823 is characterized by a fully constrained system.

1824 In this category, one top quark decays hadronically and the other decays leptonically. More-
 1825 over, the Higgs boson is assumed to decay to WW^* , where one W decays to hadrons and the
 1826 other one to leptons. This leads to a total of two b jets and four light jets arising from the
 1827 hadronic W decays. The selection requirements of this final state are relaxed with respect to
 1828 the main analysis to allow for higher yields. In this case, we just require the presence of at least
 1829 one top quark and two leptons of the same sign.

1830 The reconstruction and jet and lepton assignments is done in several stages. First, a BDT-based
 1831 discriminant is used to reconstruct the hadronic tops [103], allowing to reject those cases where
 1832 no hadronic tops are found. Then, the W boson candidates are built from light jets whose
 1833 invariant mass is close to that of the W boson. The closest lepton to this two jets, which is
 1834 assumed to be the one originating from the other W boson, recoils against the $t\bar{t}$ system and
 1835 is therefore used to reconstruct the transverse momentum of the Higgs boson. Overall, this
 1836 reconstruction method results in a 50-55% selection efficiency of $t\bar{t}H$ events, corresponding
 1837 to the percentage of events in which the Higgs transverse momentum is reconstructed. The
 1838 efficiency loss is driven by both the mass window requirements and the Top Tagger threshold
 1839 for considering the event. An alternative version of the Higgs p_T reconstruction uses all events
 1840 without considering the Top Tagger information. When using NanoAOD_v4 the Top Tagger
 1841 BDT score is not available, therefore the algorithm runs without accounting for the Top Tagger
 1842 information. When using NanoAOD_v[5|6], the Top Tagger BDT score is available, and a
 1843 comparison between the two algorithms can be done. Figure 68 illustrates the relationship
 1844 between the objects considered by our reconstruction algorithm.

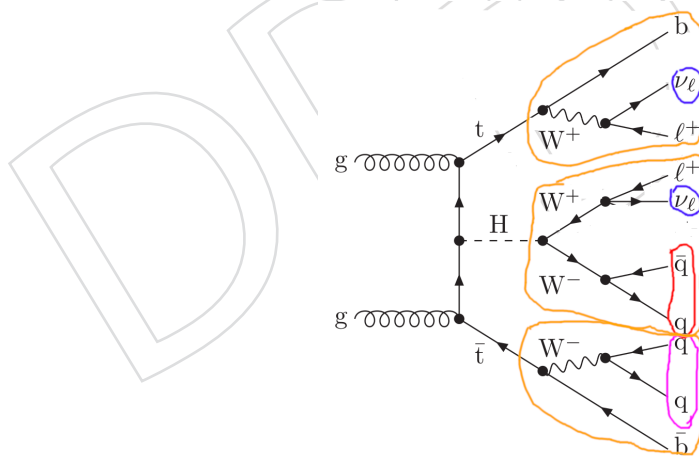


Figure 68: Diagram of the $2\ell ss + 0\tau_h$ final state, highlighting the relationship between the objects.

1845 The event yields for the three years of data-taking are estimated using Monte Carlo simulations
 1846 of the signal ($t\bar{t}H$) and the three dominant background processes ($t\bar{t}$, $t\bar{t}W$, $t\bar{t}Z$). These samples
 1847 are simulated with aMC@NLO and matched to PYTHIA for the parton shower, as is done in the
 1848 main analysis. The reconstructed transverse momentum distributions of the Higgs boson, p_T^H ,
 1849 for different binning schemes can be found in Figs. 69 and 70 for the NanoAOD_v4 production.
 1850 The three-bin scheme corresponds to the latest STXS agreement (Les Houches 2019) for $t\bar{t}H$,

1851 the finer scheme is a test scheme designed to verify in a finely-grained way the quality of our
 1852 reconstruction.

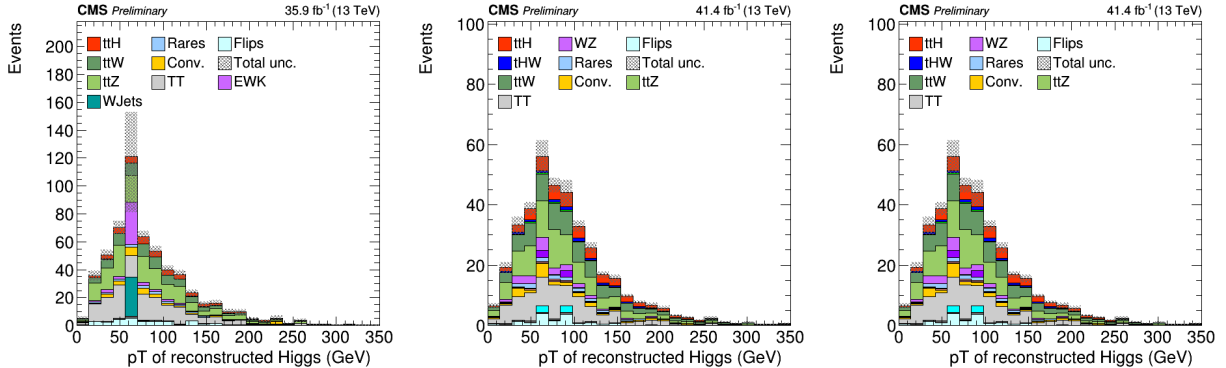


Figure 69: Reconstructed transverse momentum distribution of the Higgs boson, p_T^H , using Monte Carlo (MC) signal and background samples simulating 2016 (left), 2017 (center) and 2018 (right) NanoAOD_v4 datasets.

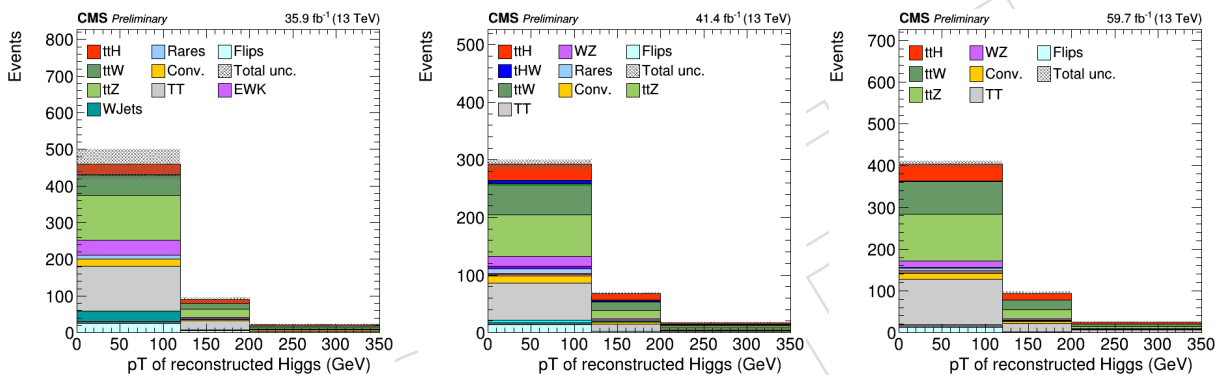


Figure 70: Reconstructed transverse momentum distribution of the Higgs boson, p_T^H , using Monte Carlo (MC) signal and background samples simulating 2016 (left), 2017 (center) and 2018 (right) NanoAOD_v4 datasets.

1853 The estimated backgrounds will then be subtracted from the measured data; the resulting dis-
 1854 tributions will be unfolded to parton level to account for detector effects, such as efficiency and
 1855 resolution, and for the migration of events between neighboring bins. The resulting differential
 1856 cross section measurement will be directly comparable to theoretical predictions.

1857 The first step both in the unfolding procedure and in the estimation of the quality of our Higgs
 1858 boson p_T reconstruction consists in computing a response matrix, which defines the event mi-
 1859 gration probability between the particle-level and reconstructed quantities. This matrix is ob-
 1860 tained using the generator and reconstruction information in the simulated samples. At the
 1861 generator level, the events are required to pass the same kinematic selections used at the re-
 1862 construction level, as described above. As is shown in Figure 71 for the NanoAOD_v4 ntuples,
 1863 there is a reasonable correlation between the reconstructed and the generator-level p_T^H distribu-
 1864 tions, with an unweighted correlation coefficient of 0.29, 0.28 and 0.28 for 2016, 2017 and 2018
 1865 datasets, respectively.

1866 When using the NanoAOD_v [5 | 6] ntuples, the Top Tagger score is available, so its impact on
 1867 the reconstruction algorithm can be checked.

1868 First, the study of the basic algorithm (not making use of the Top Tagger) is reperformed. Fig-
 1869 ures 72 and 73 show, for the v5 ntuples, the reconstructed visible Higgs p_T and the response

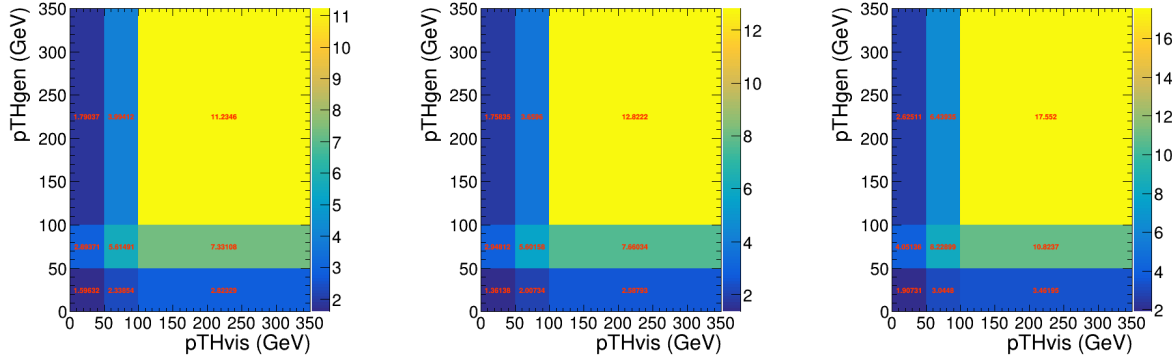


Figure 71: The p_T^H response matrices for the reconstructed-level p_T^H distribution (pTHvis) and the corresponding generator-level p_T^H distribution (pTHgen) for 2016, 2017, and 2018 simulated NanoAOD_v4 datasets, respectively from left to right.

matrices, respectively. Figures 74 and 75 show, for the v6 ntuples, the reconstructed visible Higgs p_T and the response matrices, respectively.

It can be observed that the response matrices exhibit now a large bias towards a dramatic overestimation of the visible p_T . The reconstruction algorithm is exactly the same, and the different NanoAOD versions should differ only by updated Jet Energy Corrections and in the change of generator for the $t\bar{t}H$ samples (from POWHEG to MADGRAPH with fxFx matching). The source of this large bias might be caused by a different definition of the generator level Higgs p_T (defined by the standard Higgs Template Cross Section HTXS module). We are investigating this possibility, but for this we need to run the NanoAOD step on matching samples for the various productions. To highlight the extent of the bias, Figure 76 shows the response matrices with the fine-grained test binning scheme.

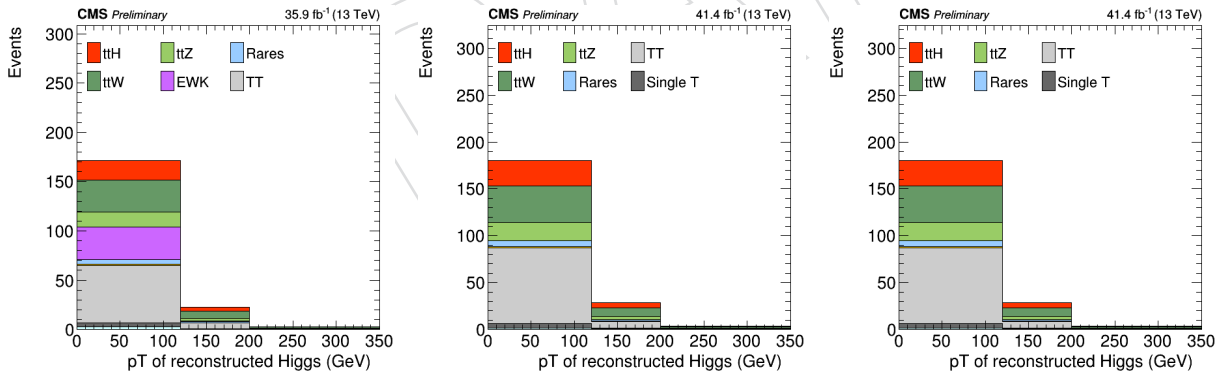


Figure 72: Reconstructed transverse momentum distribution of the Higgs boson, p_T^H , using Monte Carlo (MC) signal and background samples simulating 2016 (left), 2017 (center) and 2018 (right) NanoAOD_v5 datasets.

We reproduced the same study using the information given by the Top Tagger; Figures 77 and 78 show, for the v5 ntuples, the reconstructed visible Higgs p_T and the response matrices, respectively. Figures 79 and 80 show, for the v6 ntuples, the reconstructed visible Higgs p_T and the response matrices, respectively. The same bias is observed as when not using the Top Tagger information. Figure 81 shows the response matrices with the fine-grained test binning scheme.

Besides the bias issue, it can be seen that when the Top Tagger algorithm is not used the response matrices are almost not affected. This is an indication of the fact that the power of the

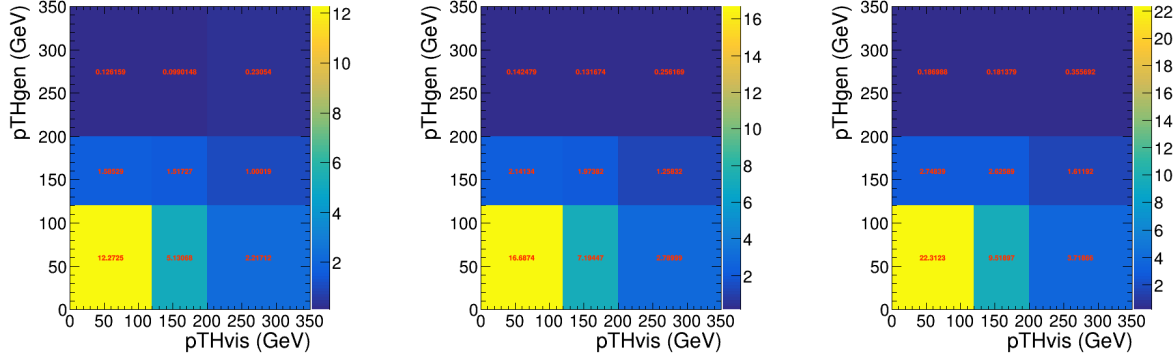


Figure 73: The p_T^H response matrices for the reconstructed-level p_T^H distribution (pTHvis) and the corresponding generator-level p_T^H distribution (pTHgen) for 2016, 2017, and 2018 simulated NanoAOD_v5 datasets, respectively from left to right.

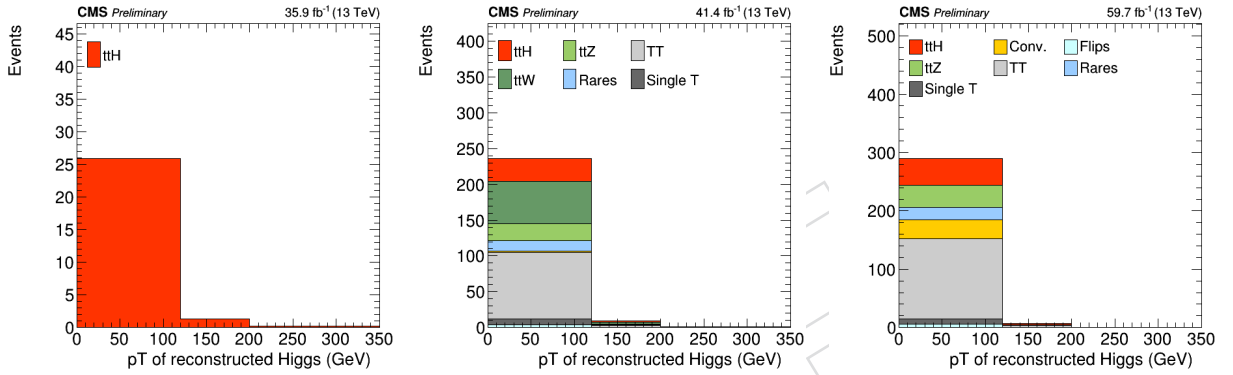


Figure 74: Reconstructed transverse momentum distribution of the Higgs boson, p_T^H , using Monte Carlo (MC) signal and background samples simulating 2016 (left), 2017 (center) and 2018 (right) NanoAOD_v6 datasets.

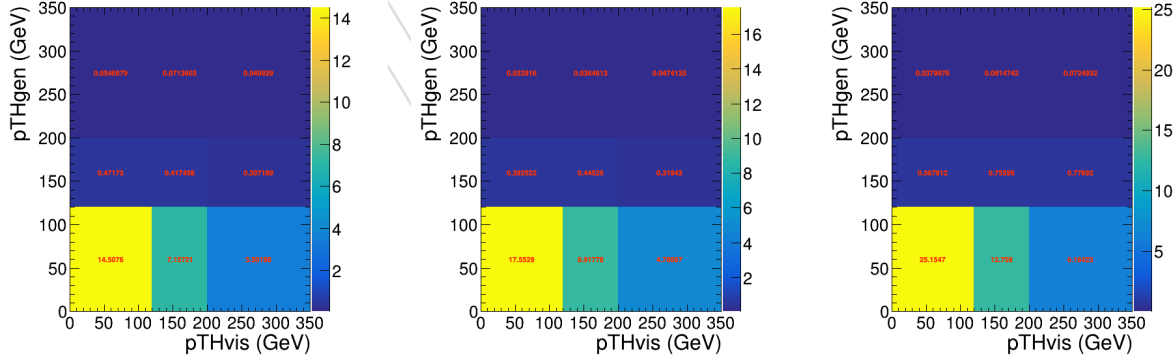


Figure 75: The p_T^H response matrices for the reconstructed-level p_T^H distribution (pTHvis) and the corresponding generator-level p_T^H distribution (pTHgen) for 2016, 2017, and 2018 simulated NanoAOD_v6 datasets, respectively from left to right.

algorithm in assigning the objects properly lies in the $\Delta R(\ell, j)$ -based and mass-window-based algorithm rather than on tagging the decays of the hadronic top quark correctly. The performance of this alternative algorithm results in a partial recovery of reconstruction efficiency (the loss due to the mass windows cuts limits the recovery), but does not improve the correlation between the reconstructed p_T estimate and the true Higgs boson p_T .

Apart from possible different definitions of the true Higgs p_T , part of the missing linear cor-

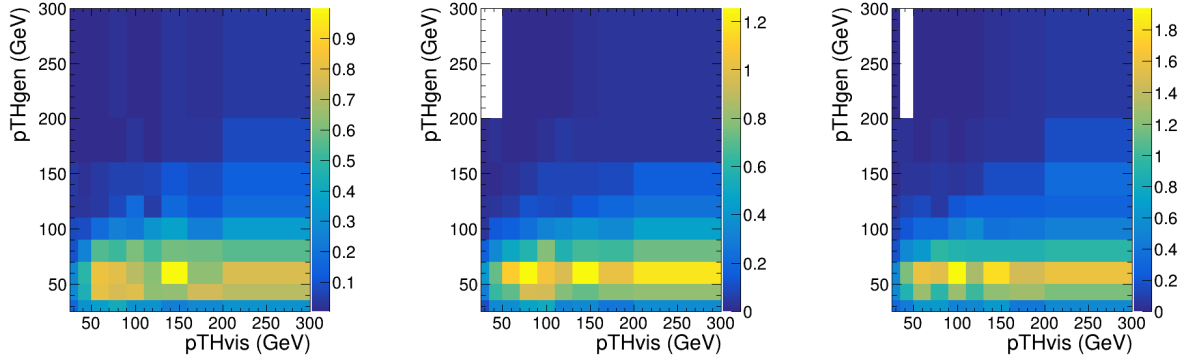


Figure 76: The p_T^H response matrices for the reconstructed-level p_T^H distribution (pTHvis) and the corresponding generator-level p_T^H distribution (pTHgen) for 2016, 2017, and 2018 simulated NanoAOD_v6 datasets, respectively from left to right.

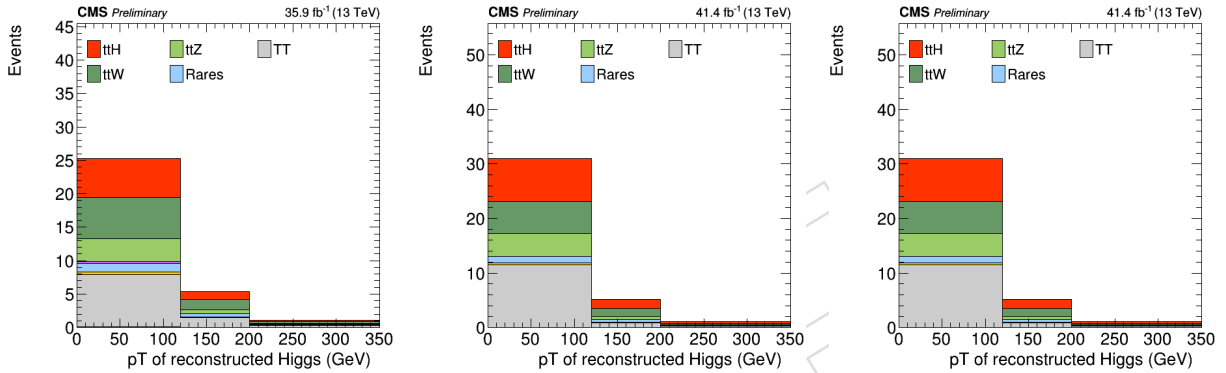


Figure 77: Reconstructed transverse momentum distribution of the Higgs boson, p_T^H , using Monte Carlo (MC) signal and background samples simulating 2016 (left), 2017 (center) and 2018 (right) NanoAOD_v5 datasets. The Top Tagger information is used in the algorithm.

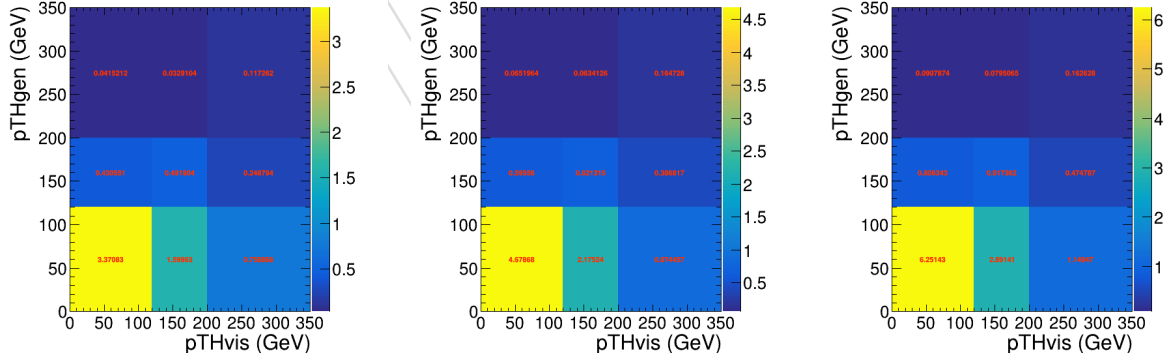


Figure 78: The p_T^H response matrices for the reconstructed-level p_T^H distribution (pTHvis) and the corresponding generator-level p_T^H distribution (pTHgen) for 2016, 2017, and 2018 simulated NanoAOD_v5 datasets, respectively from left to right. The Top Tagger information is used in the algorithm.

relation between the generated and reconstructed Higgs p_T is due to the fact that the E_T^{miss} is shared between the top and the Higgs portions of the event. Our reconstruction algorithm estimates the visible Higgs p_T , and the response matrix compares it to the full true Higgs p_T . To eliminate this effect, we corrected the visible Higgs p_T by artificially adding to it the true neutrino momenta. The resulting response matrices between the true Higgs p_T and the hybrid

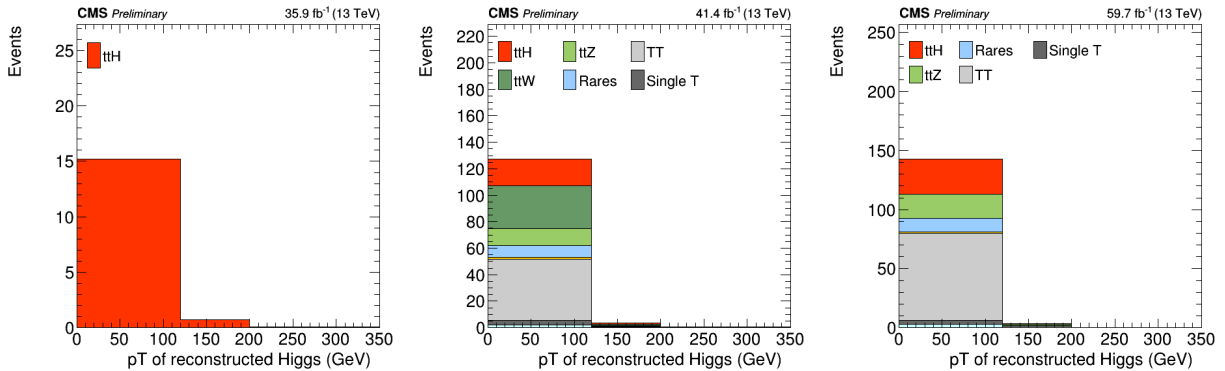


Figure 79: Reconstructed transverse momentum distribution of the Higgs boson, p_T^H , using Monte Carlo (MC) signal and background samples simulating 2016 (left), 2017 (center) and 2018 (right) NanoAOD_v6 datasets. The Top Tagger information is used in the algorithm.

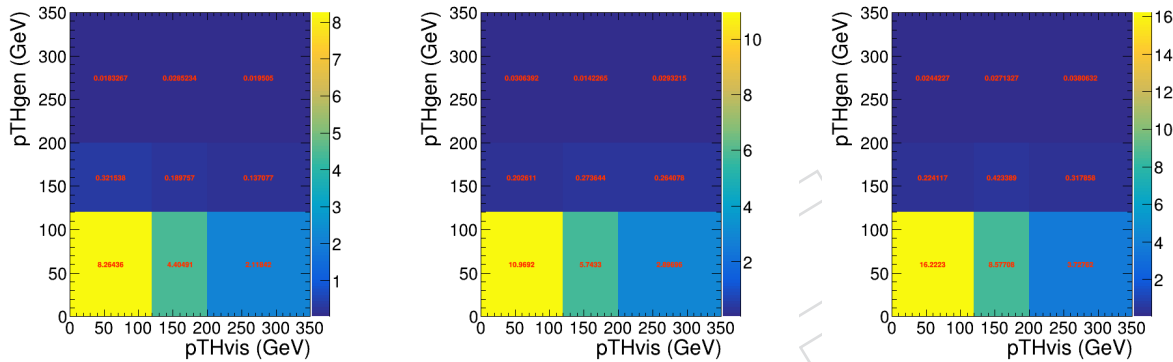


Figure 80: The p_T^H response matrices for the reconstructed-level p_T^H distribution ($pTHvis$) and the corresponding generator-level p_T^H distribution ($pTHgen$) for 2016, 2017, and 2018 simulated NanoAOD_v6 datasets, respectively from left to right. The Top Tagger information is used in the algorithm.

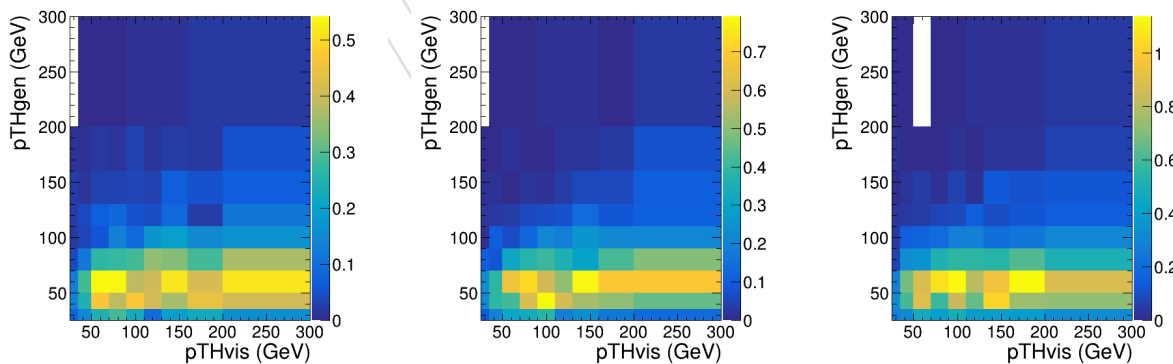


Figure 81: The p_T^H response matrices for the reconstructed-level p_T^H distribution ($pTHvis$) and the corresponding generator-level p_T^H distribution ($pTHgen$) for 2016, 2017, and 2018 simulated NanoAOD_v6 datasets, respectively from left to right. The Top Tagger information is used in the algorithm.

- 1900 reco-gen p_T are shown in Figure 82 for the NanoAOD_v6 production. It can be seen that the
 1901 linear correlation is indeed recovered, leading us to think that there is no intrinsic issue in the
 1902 latest ntuples.
 1903 This is a strong indication that the next step is to investigate ways of solving the equations

1904 which explore the different possible assignments of the E_T^{miss} to the top quark and the Higgs
 1905 boson systems. In case the CMS deadlines for this paper are tighter, as a fallback solution
 1906 we will include in the paper distribution of the visible p_T and the response matrix of the visible
 1907 p_T versus the visible true p_T . This does not allow an immediate interpretation in terms of theory
 1908 parameters, but it is a nice supplement and proof of principle which should be made public
 1909 already in this version of the paper.

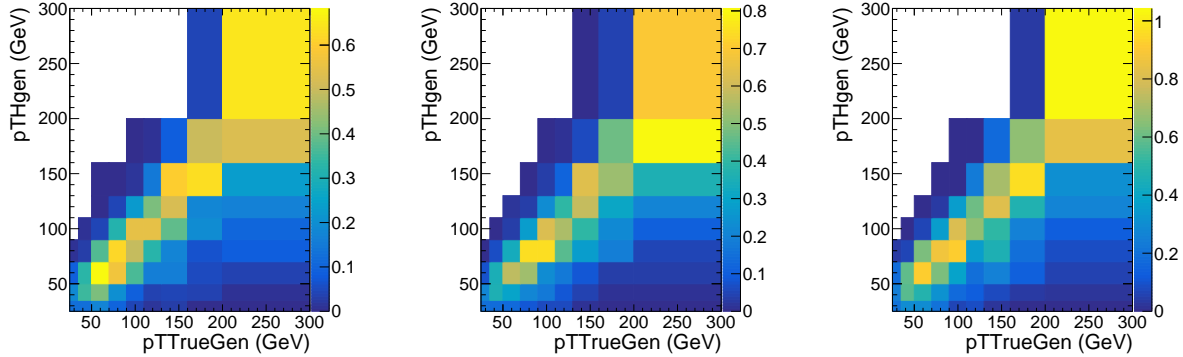


Figure 82: The p_T^H response matrices for the reconstructed-level p_T^H distribution (p_{THvis}) and the corresponding generator-level p_T^H distribution (p_{THgen}) for 2016, 2017, and 2018 simulated datasets, respectively from left to right. The Top Tagger information is used in the algorithm.

1910 We are exploring multiple ways of solving the system for the full Higgs p_T . A first ongoing
 1911 attempt relies on solving the system of equations describing the splitting of the E_T^{miss} ; the class
 1912 of solutions is represented by two ellipses that should intersecate. If the ellipses don't inter-
 1913 secate, this is due to mismeasurement of the E_T^{miss} ; events which exhibit this behaviour can be
 1914 recovered by artificially shifting the E_T^{miss} until the ellipses intersecate. In case this analytic ap-
 1915 proach does not work, toys can be thrown on all the possible assignments, adding top quark
 1916 and Higgs boson mass constraints. The ellipses method is based on Ref. [130].

1917 Another possibility, which we already implemented as a test, is to regress the Higgs boson
 1918 p_T with a neural network.

1919 **H.3 Regressing the Higgs transverse momentum with a Deep Artificial Neural 1920 Network**

1921 The NanoAOD_v6 ntuples are used to regress the Higgs transverse momentum in the $2\ell ss + 0\tau_h$
 1922 final state. Events are not split according to the lepton flavour. Events are split into a training
 1923 dataset of 43975 events and a validation dataset of 29317 events. The Keras frontend [131] is
 1924 used on top of a Tensorflow backend [132] to regress the HTXS Higgs transverse momentum
 1925 p_T and rapidity y .

1926 Various network structures have been tried, converging on the following.

1927 The input features consist in the quadrivectors of the two leptons, the missing transverse
 1928 energy p_T and ϕ , and in two sets of hadronic observables. The Top-Tagger-aware set consists
 1929 in the quadrivectors of the first six jets, the quadrivector of the reconstructed hadronic
 1930 top, and the BDT score associated to the reconstructed hadronic top. The Top-Tagger-unaware
 1931 set consists in the quadrivectors of the first six jets, and the b-tagging discriminator value
 1932 for the first six jets. A mixed set is also explored, consisting in the quadrivectors of non-
 1933 top-tagged jets and their b-tagging word (0/1, non-tagged/tagged), the quadrivectors of the
 1934 reconstructed hadronic top, and the hadronic top BDT score. Results are found to be qualita-
 1935 tively similar among the sets.

1936 The simultaneous regression of the Higgs p_T and y is being tested and will be documented
 1937 shortly.

1938 A simultaneous view of the correlation between the input variables is too heavy to be loaded
 1939 in the current Analysis Note, but can be downloaded from Ref. [133].

1940 Five hidden layers are used in a piramidal scheme. The hidden layers are activated with Rec-
 1941 tified Linear Units (ReLU), and the output node is activated with a linear function. The mean
 1942 absolute error loss function is used, to account for the huge target variable range in the case of
 1943 the Higgs p_T . A test in which the logarithm of the transverse momentum is regressed does not
 1944 yield any significant improvement. A batch size of 128 is chosen, and the network is trained
 1945 for 50 epochs with an initial learning rate of 10^{-4} optimized with the Adam optimizer. No
 1946 overtraining is observed, and the network converges already at around 30 epochs. Figure 83
 1947 details the loss function and an additional monitored metric.

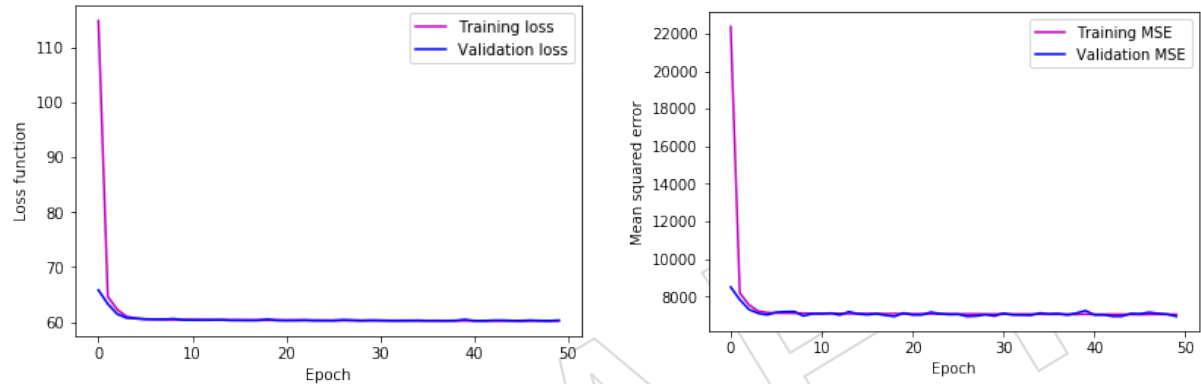


Figure 83: The loss function (left) and the MSE metric (right) for the Higgs p_T^H regression.

1948 The regressed Higgs p_T is affected by a heavy bias. In analogy with the checks performed in
 1949 Section H.2, a new training is performed by removing the E_T^{miss} from the input features of the
 1950 network. The target variable for the regression is then transformed by subtracting the E_T^{miss}
 1951 from it: the regression is performed therefore to $p_T^{\text{Higgs}} - E_T^{miss}$. Figure 84 shows the results of
 1952 the regression to the Higgs p_T and of the regression to the Higgs $p_T - E_T^{miss}$.

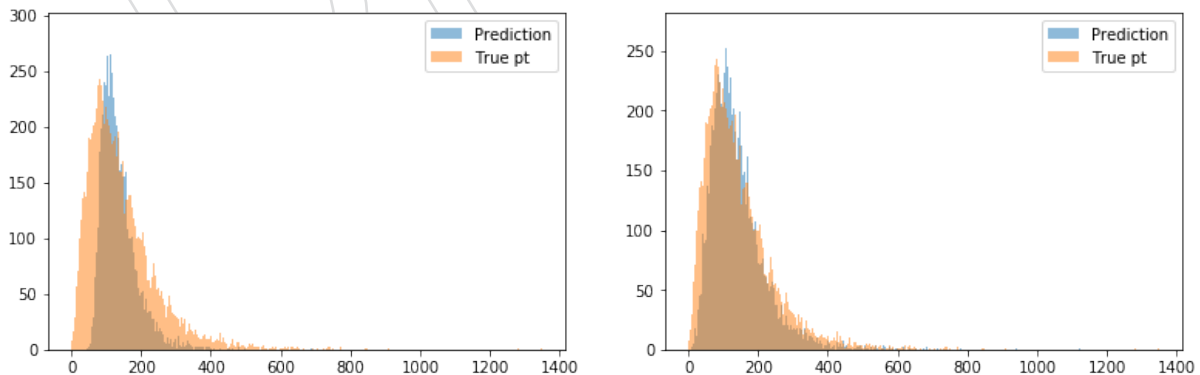


Figure 84: The predicted versus true distribution when regressing to the Higgs p_T (left) and when regressing to the Higgs $p_T - E_T^{miss}$ (right).

1953 The linear correlation between reconstructed and true variable in these tests is about 0.56–0.60,
 1954 representing a large improvement with respect to the basic reconstruction technique. How-
 1955 ever, the assignment problem of the E_T^{miss} is still present. Currently we are trying solving the

1956 problem of splitting the E_T^{miss} among the neutrinos with a Generative Adversarial Network
 1957 approach. The generator network attempts to generate assignments of the neutrino momenta
 1958 constrained by the total E_T^{miss} , and the discriminator network tests these assignments against
 1959 the true splitting. We will update shortly the documentation with the result of this ongoing
 1960 attempt.

1961 The prediction is evaluated in background events to test if we recover the shape differences
 1962 we observe with the basic algorithm. Figure 86 shows the result, which matches the generator
 1963 studies done for the basic algorithm.

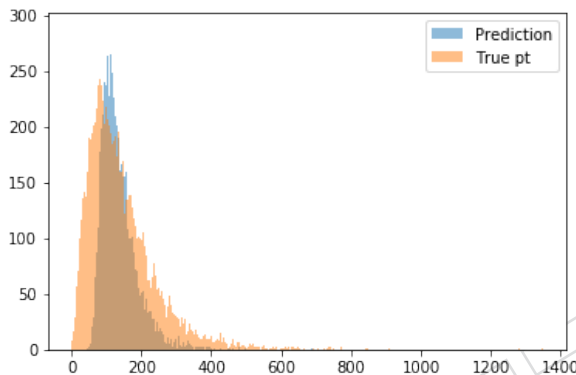


Figure 85: The prediction for the regressed momentum, computed for events with a true Higgs (ttH), events with a vector boson (ttV), and events with fake leptons not originating from the decay of a particle (ttbar).

1964 A regression to the Higgs rapidity is shown in Figure reffig:diff:ytt to result in a distribution
 1965 better matching the target feature. However, correlation studies highlighted some issues that
 1966 we are addressing.

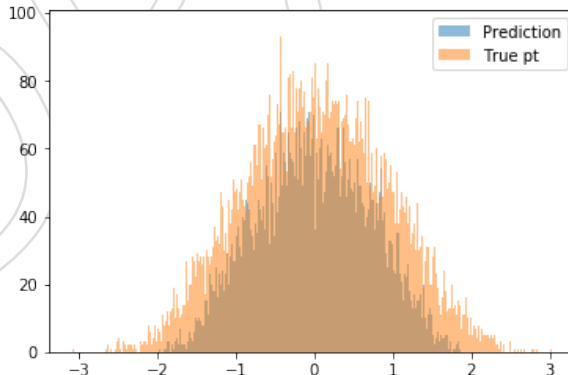


Figure 86: The prediction for the regressed rapidity.

1967 More studies are needed to obtain a reliable Higgs transverse momentum and rapidity regres-
 1968 sion to solve some technical issues. We will update this Section with a robust version of the
 1969 network very soon.

I Measurement of lepton misidentification rates

The lepton misidentification rates are measured using an event sample enriched in the contribution from multijet production. The sample is selected by requiring the presence of exactly one electron or muon that passes the fakeable lepton selection criteria given by Tables 20 and 21 and at least one jet, which is separated from the lepton by $\Delta R > 0.7$. The events are recorded using single electron and muon triggers of various p_T thresholds. The corresponding HLT paths are given in Table 48. Some of the triggers require the presence of a jet on trigger level, where the jet p_T threshold varies by HLT path. Events selected in the multijet sample, referred to as MR, are required to contain at least one “offline” reconstructed jet with a p_T above the p_T threshold of the trigger. None of the triggers demands that the lepton satisfies an isolation condition on trigger level, which results in high trigger rates and necessitate to apply prescales to the triggers, in order to satisfy the bandwidth limitations of the data-acquisition system. The values of the prescales are given in the Table.

HLT path	Prescale	Lepton cone- p_T	Lepton reco- p_T	Jet p_T
HLT_Ele8_CaloIdM_TrackIdM_PFJet30	1.14×10^4	15-45 GeV	> 27 GeV	> 30 GeV
HLT_Ele17_CaloIdM_TrackIdM_PFJet30	1.17×10^3	25-100 GeV	> 17 GeV	> 30 GeV
HLT_Ele23_CaloIdM_TrackIdM_PFJet30	1.07×10^3	32-100 GeV	> 23 GeV	> 30 GeV
HLT_Mu3_PFJet40	8.99×10^3	10-32 GeV	> 3 GeV	> 45 GeV
HLT_Mu8	1.59×10^4	15-45 GeV	> 8 GeV	> 30 GeV
HLT_Mu17	5.94×10^2	32-100 GeV	> 17 GeV	> 30 GeV
HLT_Mu20	2.25×10^2	32-100 GeV	> 20 GeV	> 30 GeV
HLT_Mu27	2.25×10^2	45-100 GeV	> 27 GeV	> 30 GeV

Table 48: Triggers used to record events for the measurement of the lepton misidentification rate. A hyphen (–) indicates requirements that are not applied.

The offline reconstructed leptons are required to satisfy conditions on the reco- p_T and on the cone- p_T , depending on the HLT path that triggers the event. The requirement on the reco- p_T is applied to ensure that the trigger is fully efficient, while the condition on the cone- p_T is applied to reduce biases in the measurement of the lepton misidentification rates. The issue is that the p_T thresholds that are applied on trigger level impose an implicit condition on the isolation of the lepton, because the lepton misidentification rates are parametrized by the cone- p_T , and not the reco- p_T , of the lepton. Such bias on the isolation of the lepton would cause a bias on the output of the BDT that is used to separate prompt leptons from non-prompt and fake leptons, increasing the probability for fakeable leptons to pass the tight lepton selection criteria. This in turn would cause the estimate of the fake background in the SR to be overestimated, as all leptons selected in the MR are required to pass the trigger requirements, whereas events selected in the AR contain multiple leptons and only one of these leptons must pass the trigger requirements. A bias of this kind is avoided by requiring that the cone- p_T of the offline reconstructed lepton exceeds the p_T threshold applied on trigger level by about a factor two. The condition $I_\ell < 0.4 \times \text{reco-}p_T$ that is applied in the selection of fakeable electrons and muons then ensures that leptons passing the threshold on the cone- p_T pass the p_T threshold of the trigger regardless of their isolation, avoiding the aforementioned bias. A small residual bias, which is caused by the electron identification criteria applied on trigger level, is reduced by requiring fakeable electrons to satisfy conditions on $\sigma_{\eta\eta}$, H/E, and 1/E - 1/p (cf. Table 20).

The p_T cuts that are applied in the offline event selection on the p_T of the jet and on the reco- p_T and cone- p_T of the lepton are also given in Table 48. For events selected in the MR, we demand that at least one of the HLT paths given in Table 48 triggered the event and the event contains at least one pair of fakeable lepton plus jet, which satisfies the conditions on cone- p_T as well as reco- p_T of the lepton and on the p_T of the jet p_T for any of the HLT paths that triggered the

2007 event.

The event yield of processes that are modeled by the MC simulation is corrected for the effect of the trigger prescales by applying suitable chosen weights to the simulated events. As the prescales are applied independently for each HLT path, the weights are given by the expression:

$$w = 1 - \prod_p \left(1 - \frac{1}{\text{prescale}_p} \right), \quad (15)$$

2008 where the product extends over all HLT paths p that “fired” for a given event.

The fake-factors (FF) are measured in bins of η and cone- p_T of the lepton. In each bin, the FF is measured by determining the number of multijet events with fakeable leptons that pass the tight lepton selection criteria and those that fail. The number of multijet events in the pass and fail regions, denoted by N_{pass} and N_{fail} , is determined by a maximum-likelihood (ML) fit of the distribution of the observable:

$$m_T^{\text{fix}} = \sqrt{2 p_T^{\text{fix}} E_T^{\text{miss}} (1 - \cos \Delta\phi)} \quad (16)$$

with shape templates for W+jets, Z+jets, diboson, top quark pair, and multijet production. Given the event yields N_{pass} and N_{fail} of multijet production in the pass and fail regions, the FF f_i for a given bin i in η and cone- p_T of the lepton is then computed as:

$$f_i = \frac{N_{\text{pass}}}{N_{\text{pass}} + N_{\text{fail}}}. \quad (17)$$

2009 The symbol $\Delta\phi$ in Eq. (16) refers to the angle in the transverse plane between the lepton momentum and the E_T^{miss} vector, while the symbol p_T^{fix} denotes a constant of value 35 GeV. The
 2010 observable m_T^{fix} exploits the fact that the E_T^{miss} reconstructed in multijet events is mainly due
 2011 to resolution effects and is typically small, resulting in a falling distribution in m_T^{fix} , while the
 2012 distribution in W+jets events, which constitute the main background for the FF measurement,
 2013 exhibits a broad maximum around $m_W \approx 80$ GeV. Compared to the usual transverse mass,
 2014 the observable m_T^{fix} has the advantage of not depending on the p_T of the lepton, which is better
 2015 suited for the purpose of measuring the FF in bins of lepton p_T [103]. The contributions from
 2016 W+jets, Z+jets, and diboson production are assumed to scale by a common factor with respect
 2017 to their MC expectation in the fit, and their sum is referred to as “electroweak” background.
 2018 The shape templates for multijet production are obtained from the MC simulation, using the
 2019 samples given in Tables 49-51. The contributions of other processes to the pass and fail regions
 2020 is small. These contributions are estimated using the MC simulation and subtracted from the
 2021 data before the fit. The pass and fail regions for each p_T and η bin are fitted simultaneously,
 2022 taking correlations between the systematic uncertainties between both regions into account,
 2023 while individual p_T and η bins are fitted independently. The fit is illustrated for two example
 2024 p_T and η bins, one for electrons and one for muons, in Fig. 87.

2026 A correction needs to be applied to the measured FF for electrons to account for the contribution
 2027 of photon conversions to the pass and fail regions. The event yields N_{pass} and N_{fail} obtained by
 2028 the fit are scaled by the relative fraction of multijet events in which the reconstructed fakeable
 2029 electron is matched, within $\Delta R < 0.3$, to a generator level prompt photon (i.e. not a photon
 2030 arising from the decays of hadrons) The fraction is determined separately for the pass and fail
 2031 region and for each bin in cone- p_T and η of the lepton. The effect of this correction is to reduce
 2032 the FF for electrons by 10-20%.

2033 The FF for electrons and muons, obtained from the fit, are shown in Figs. 88 and 89.

Table 49: List of 2016 MC samples used to obtain the shape templates for multijet production for the measurement of lepton misidentification rates.

Sample name	Cross section [pb]
/QCD_Pt-15to20_MuEnrichedPt5_TuneCUETP8M1-13TeV-pythia8/1	2.81×10^6 [57]
/QCD_Pt-20to30_MuEnrichedPt5_TuneCUETP8M1-13TeV-pythia8/1	2.53×10^6 [57]
/QCD_Pt-30to50_MuEnrichedPt5_TuneCUETP8M1-13TeV-pythia8/1	1.37×10^6 [57]
/QCD_Pt-50to80_MuEnrichedPt5_TuneCUETP8M1-13TeV-pythia8/1	3.78×10^5 [57]
/QCD_Pt-80to120_MuEnrichedPt5_TuneCUETP8M1-13TeV-pythia8/1,2	8.86×10^4 [57]
/QCD_Pt-120to170_MuEnrichedPt5_TuneCUETP8M1-13TeV-pythia8/1,3	2.12×10^4 [57]
/QCD_Pt-170to300_MuEnrichedPt5_TuneCUETP8M1-13TeV-pythia8/2,3,4	7.02×10^3 [57]
/QCD_Pt-300to470_MuEnrichedPt5_TuneCUETP8M1-13TeV-pythia8/1,5,6	6.20×10^2 [57]
/QCD_Pt-470to600_MuEnrichedPt5_TuneCUETP8M1-13TeV-pythia8/1,2,6	5.91×10^1 [57]
/QCD_Pt-600to800_MuEnrichedPt5_TuneCUETP8M1-13TeV-pythia8/1,2,3	1.82×10^1 [57]
/QCD_Pt-800to1000_MuEnrichedPt5_TuneCUETP8M1-13TeV-pythia8/1,2,6	3.28 [57]
/QCD_Pt-1000toInf_MuEnrichedPt5_TuneCUETP8M1-13TeV-pythia8/1,2	1.08 [57]
/QCD_Pt-20to30_EMEnriched_TuneCUETP8M1-13TeV-pythia8/1	4.91×10^6 [57]
/QCD_Pt-30to50_EMEnriched_TuneCUETP8M1-13TeV-pythia8/1,2	6.42×10^6 [57]
/QCD_Pt-50to80_EMEnriched_TuneCUETP8M1-13TeV-pythia8/1,2	1.99×10^6 [57]
/QCD_Pt-80to120_EMEnriched_TuneCUETP8M1-13TeV-pythia8/1,2	3.67×10^5 [57]
/QCD_Pt-120to170_EMEnriched_TuneCUETP8M1-13TeV-pythia8/1,2	6.65×10^4 [57]
/QCD_Pt-170to300_EMEnriched_TuneCUETP8M1-13TeV-pythia8/1	1.66×10^4 [57]
/QCD_Pt-300toInf_EMEnriched_TuneCUETP8M1-13TeV-pythia8/1	1.10×10^3 [57]
/QCD_Pt-15to20_bctoE_TuneCUETP8M1-13TeV-pythia8/1	1.87×10^5 [57]
/QCD_Pt-20to30_bctoE_TuneCUETP8M1-13TeV-pythia8/1	3.05×10^5 [57]
/QCD_Pt-30to80_bctoE_TuneCUETP8M1-13TeV-pythia8/1	3.61×10^5 [57]
/QCD_Pt-80to170_bctoE_TuneCUETP8M1-13TeV-pythia8/3	3.38×10^4 [57]
/QCD_Pt-170to250_bctoE_TuneCUETP8M1-13TeV-pythia8/1	2.13×10^3 [57]
/QCD_Pt-250toInf_bctoE_TuneCUETP8M1-13TeV-pythia8/1	5.63×10^2 [57]

¹ RunII Summer16 MiniAODv3-PUMoriond17_94X_mcRun2_asymptotic_v3-v2/MINIAODSIM

² RunII Summer16 MiniAODv3-PUMoriond17_94X_mcRun2_asymptotic_v3_ext1-v2/MINIAODSIM

³ RunII Summer16 MiniAODv3-PUMoriond17_backup-94X_mcRun2_asymptotic_v3-v2/MINIAODSIM

⁴ RunII Summer16 MiniAODv3-PUMoriond17_94X_mcRun2_asymptotic_v3-v1/MINIAODSIM

⁵ RunII Summer16 MiniAODv3-PUMoriond17_94X_mcRun2_asymptotic_v3_ext1-v1/MINIAODSIM

⁶ RunII Summer16 MiniAODv3-PUMoriond17_94X_mcRun2_asymptotic_v3_ext2-v2/MINIAODSIM

Table 50: List of 2017 MC samples used to obtain the shape templates for multijet production for the measurement of lepton misidentification rates.

Sample name	Cross section [pb]
/QCD_Pt-15to20_MuEnrichedPt5_TuneCP5_13TeV-pythia8/1	2.81×10^6 [57]
/QCD_Pt-20to30_MuEnrichedPt5_TuneCP5_13TeV-pythia8/1	2.53×10^6 [57]
/QCD_Pt-30to50_MuEnrichedPt5_TuneCP5_13TeV-pythia8/1	1.37×10^6 [57]
/QCD_Pt-50to80_MuEnrichedPt5_TuneCP5_13TeV-pythia8/1	3.78×10^5 [57]
/QCD_Pt-80to120_MuEnrichedPt5_TuneCP5_13TeV-pythia8/1	8.86×10^4 [57]
/QCD_Pt-120to170_MuEnrichedPt5_TuneCP5_13TeV-pythia8/1	2.12×10^4 [57]
/QCD_Pt-170to300_MuEnrichedPt5_TuneCP5_13TeV-pythia8/1	7.02×10^3 [57]
/QCD_Pt-300to470_MuEnrichedPt5_TuneCP5_13TeV-pythia8/1	6.20×10^2 [57]
/QCD_Pt-470to600_MuEnrichedPt5_TuneCP5_13TeV-pythia8/1	5.91×10^1 [57]
/QCD_Pt-600to800_MuEnrichedPt5_TuneCP5_13TeV-pythia8/1	1.82×10^1 [57]
/QCD_Pt-800to1000_MuEnrichedPt5_TuneCP5_13TeV-pythia8/1	3.28 [57]
/QCD_Pt-1000toInf_MuEnrichedPt5_TuneCP5_13TeV-pythia8/1	1.08 [57]
/QCD_Pt-15to20_EMEnriched_TuneCP5_13Tev-pythia8/1	1.32×10^6 [57]
/QCD_Pt-20to30_EMEnriched_TuneCP5_13Tev-pythia8/1	4.91×10^6 [57]
/QCD_Pt-30to50_EMEnriched_TuneCP5_13Tev-pythia8/1	6.42×10^6 [57]
/QCD_Pt-50to80_EMEnriched_TuneCP5_13Tev-pythia8/1	1.99×10^6 [57]
/QCD_Pt-80to120_EMEnriched_TuneCP5_13Tev-pythia8/1	3.67×10^5 [57]
/QCD_Pt-120to170_EMEnriched_TuneCP5_13Tev-pythia8/1	6.65×10^4 [57]
/QCD_Pt-300toInf_EMEnriched_TuneCP5_13Tev-pythia8/1	1.10×10^3 [57]
/QCD_Pt-20to30_bctoE_TuneCP5_13TeV-pythia8/3	3.05×10^5 [57]
/QCD_Pt-30to80_bctoE_TuneCP5_13TeV-pythia8/1	3.61×10^5 [57]
/QCD_Pt-80to170_bctoE_TuneCP5_13TeV-pythia8/1	3.38×10^4 [57]
/QCD_Pt-170to250_bctoE_TuneCP5_13TeV-pythia8/1	2.13×10^3 [57]
/QCD_Pt-250toInf_bctoE_TuneCP5_13TeV-pythia8/1	5.63×10^2 [57]

¹ RunIIFall17MiniaODv2–PU2017-12Apr2018-94X_mc2017_realistic-v14-v1/MINIAODSIM

² RunIIFall17MiniaODv2–PU2017-12Apr2018-94X_mc2017_realistic-v14-v2/MINIAODSIM

³ RunIIFall17MiniaODv2–PU2017-12Apr2018_new_pmx_94X_mc2017_realistic-v14-v1/MINIAODSIM

Table 51: List of 2018 MC samples used to obtain the shape templates for multijet production for the measurement of lepton misidentification rates.

Sample name	Cross section [pb]
/QCD_Pt-15to20_MuEnrichedPt5_TuneCP5_1.3TeV-pythia8/1	2.81×10^6 [57]
/QCD_Pt-20to30_MuEnrichedPt5_TuneCP5_1.3TeV-pythia8/2	2.53×10^6 [57]
/QCD_Pt-30to50_MuEnrichedPt5_TuneCP5_1.3TeV-pythia8/1	1.37×10^6 [57]
/QCD_Pt-50to80_MuEnrichedPt5_TuneCP5_1.3TeV-pythia8/1	3.78×10^5 [57]
/QCD_Pt-80to120_MuEnrichedPt5_TuneCP5_1.3TeV-pythia8/3 ⁴	8.86×10^4 [57]
/QCD_Pt-120to170_MuEnrichedPt5_TuneCP5_1.3TeV-pythia8/3 ⁴	2.12×10^4 [57]
/QCD_Pt-170to300_MuEnrichedPt5_TuneCP5_1.3TeV-pythia8/1	7.02×10^3 [57]
/QCD_Pt-300to470_MuEnrichedPt5_TuneCP5_1.3TeV-pythia8/1 ⁵	6.20×10^2 [57]
/QCD_Pt-470to600_MuEnrichedPt5_TuneCP5_1.3TeV-pythia8/3 ⁴	5.91×10^1 [57]
/QCD_Pt-600to800_MuEnrichedPt5_TuneCP5_1.3TeV-pythia8/3 ⁴	1.82×10^1 [57]
/QCD_Pt-800to1000_MuEnrichedPt5_TuneCP5_1.3TeV-pythia8/6 ⁶	3.28 [57]
/QCD_Pt-1000toInf_MuEnrichedPt5_TuneCP5_1.3TeV-pythia8/3 ⁷	1.08 [57]
/QCD_Pt-15to20_EMEnriched_TuneCP5_1.3TeV-pythia8/4	1.32×10^6 [57]
/QCD_Pt-20to30_EMEnriched_TuneCP5_1.3TeV-pythia8/3	4.91×10^6 [57]
/QCD_Pt-30to50_EMEnriched_TuneCP5_1.3TeV-pythia8/4	6.42×10^6 [57]
/QCD_Pt-50to80_EMEnriched_TuneCP5_1.3TeV-pythia8/3	1.99×10^6 [57]
/QCD_Pt-80to120_EMEnriched_TuneCP5_1.3TeV-pythia8/3	3.67×10^5 [57]
/QCD_Pt-120to170_EMEnriched_TuneCP5_1.3TeV-pythia8/3	6.65×10^4 [57]
/QCD_Pt-170to300_EMEnriched_TuneCP5_1.3TeV-pythia8/3	1.66×10^4 [57]
/QCD_Pt-300toInf_EMEnriched_TuneCP5_1.3TeV-pythia8/3	1.10×10^3 [57]
/QCD_Pt-15to20_bctoE-TuneCP5_1.3TeV-pythia8/ ⁷	1.87×10^5 [57]
/QCD_Pt-20to30_bctoE-TuneCP5_1.3TeV-pythia8/ ⁷	3.05×10^5 [57]
/QCD_Pt-30to80_bctoE_TuneCP5_1.3TeV_pythia8/ ³	3.61×10^5 [57]
/QCD_Pt-80to170_bctoE_TuneCP5_1.3TeV_pythia8/ ³	3.38×10^4 [57]
/QCD_Pt-170to250_bctoE_TuneCP5_1.3TeV_pythia8/ ³	2.13×10^3 [57]
/QCD_Pt-250toInf_bctoE_TuneCP5_1.3TeV_pythia8/ ³	5.63×10^2 [57]

¹ RunIIIAutumn18MiniAOD-102X_upgrade2018_realistic_v15-v3/MINIAODSIM

² RunIIIAutumn18MiniAOD-102X_upgrade2018_realistic_v15-v4/MINIAODSIM

³ RunIIIAutumn18MiniAOD-102X_upgrade2018_realistic_v15-v1/MINIAODSIM

⁴ RunIIIAutumn18MiniAOD-102X_upgrade2018_realistic_v15_ext1-v2/MINIAODSIM

⁵ RunIIIAutumn18MiniAOD-102X_upgrade2018_realistic_v15_ext3-v1/MINIAODSIM

⁶ RunIIIAutumn18MiniAOD-102X_upgrade2018_realistic_v15_ext3-v2/MINIAODSIM

⁷ RunIIIAutumn18MiniAOD-102X_upgrade2018_realistic_v15-v2/MINIAODSIM

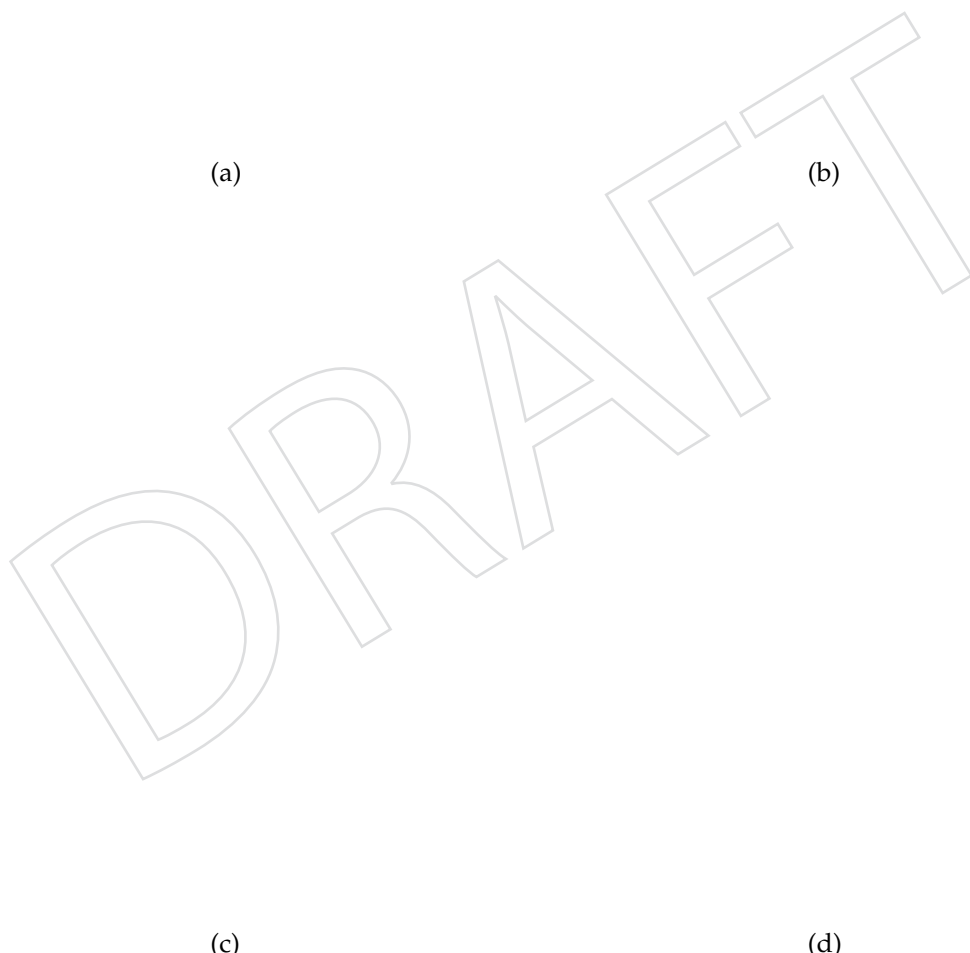


Figure 87: Distributions in the observable m_T^{fix} in the pass (a, c) and fail (b, d) regions. for two example bins in η and cone- p_T of the lepton: for electrons of $25 < \text{cone-}p_T < 35$ GeV and $|\eta| < 1.479$ (a, b) and for muons of $15 < \text{cone-}p_T < 20$ GeV and $|\eta| > 1.2$ (b, d).

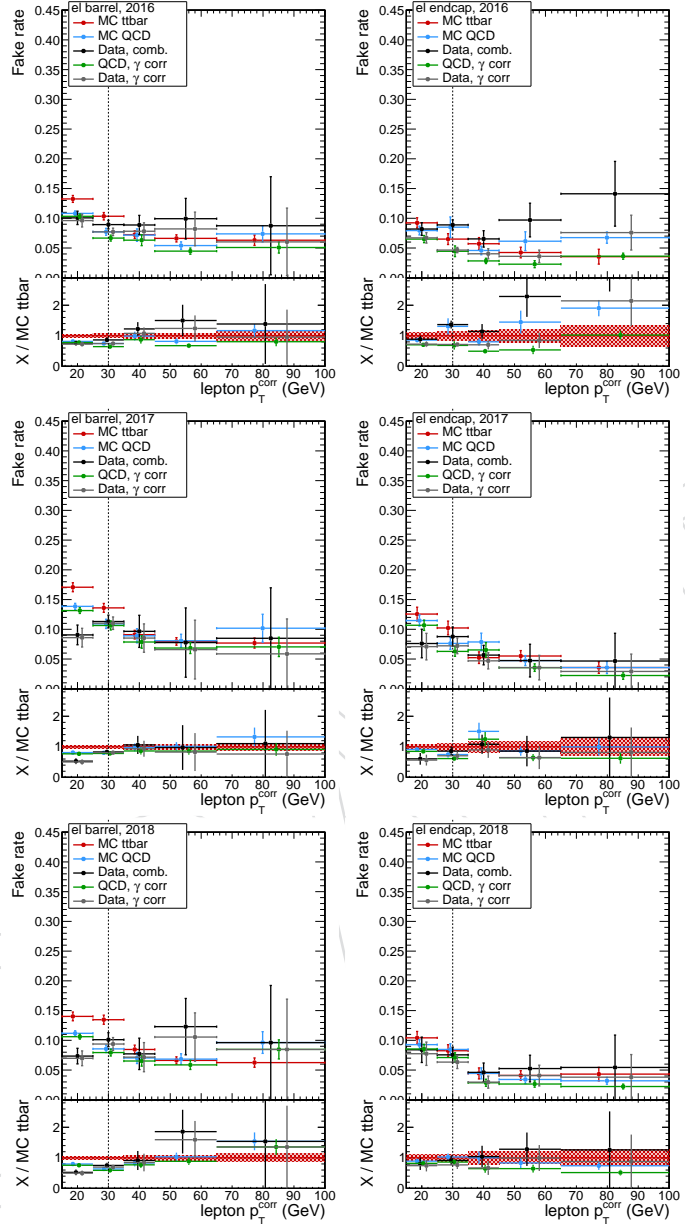


Figure 88: Probabilities f for non-prompt leptons and hadrons, which pass the fakeable lepton selection criteria, to pass the tight electron selection criteria, measured as function of cone- p_T of the lepton in multijet events, for electrons of $|\eta| < 1.479$ (left) and $|\eta| > 1.479$ (right), for 2016 (top), 2017 (middle) and 2018 data (bottom). The FF in simulated multijet and top quark pair production events are shown for comparison. In case of simulated top quark pair production events, only those reconstructed fakeable leptons, which are not matched to prompt leptons on generator level, are considered in the FF computation.

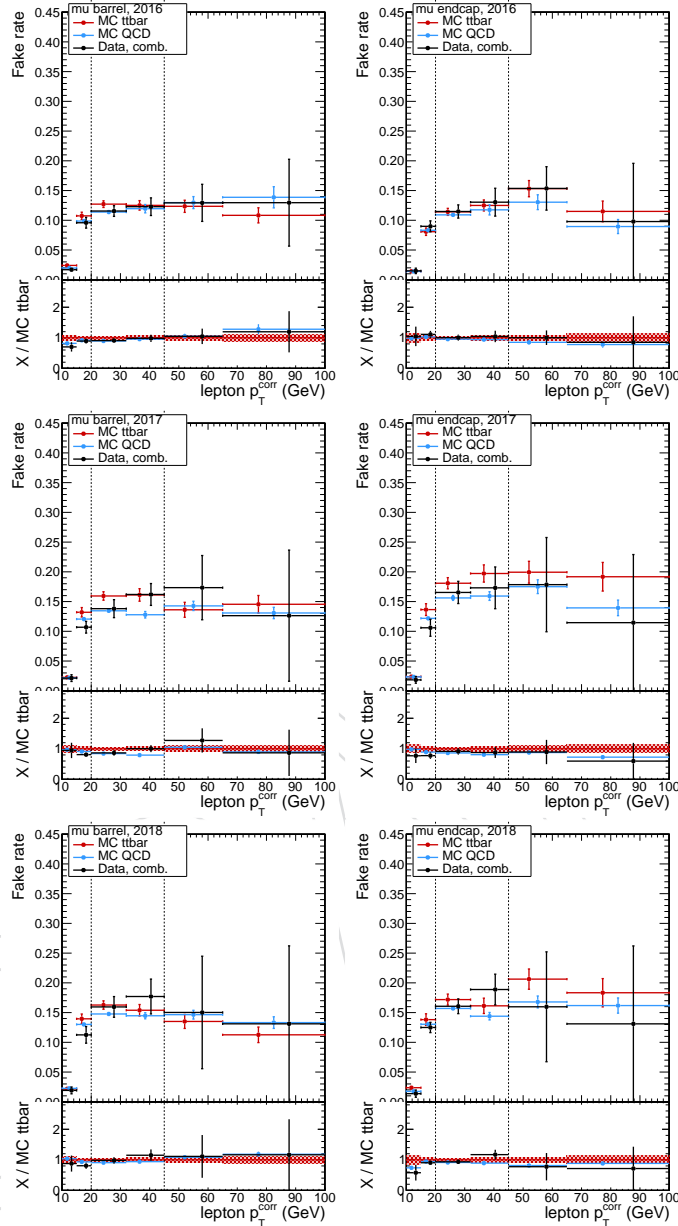


Figure 89: Probabilities f for non-prompt leptons and hadrons, which pass the fakeable lepton selection criteria, to pass the tight muon selection criteria, measured as function of cone- p_T of the lepton in multijet events, for muons of $|\eta| < 1.2$ (left) and $|\eta| > 1.2$ (right), for 2016 (top), 2017 (middle) and 2018 data (bottom). The FF in simulated multijet and top quark pair production events are shown for comparison. In case of simulated top quark pair production events, only those reconstructed fakeable leptons, which are not matched to prompt leptons on generator level, are considered in the FF computation.

2034 Small differences between the FF in simulated multijet and top quark pair production events
2035 can be seen in Figs. 88 and 89. The differences in the FF reflect differences in the fractions of
2036 non-prompt leptons and hadrons between multijet and top quark pair production events, with
2037 multijet events containing a higher fraction of fake leptons from light quark and gluon jets,
2038 and top quark pair production events containing a higher fraction of non-prompt leptons from
2039 decays of heavy (*c* and *b*) quarks. The differences between the FF have been reduced by tuning
2040 the fakeable lepton selection criteria, in particular by adjusting the cut on the CSVv2 *b*-tagging
2041 discriminant that is applied in the selection of fakeable electrons and muons. The small residual
2042 differences are not corrected for, but considered as systematic uncertainties (*cf.* Section 8).

2043 An alternative procedure to measure the FF, which does not rely on the MC simulation to
2044 obtain the shape templates for multijet production, is used as a cross-check. In the alternative
2045 procedure, the event yield N_{fail} of multijet production is determined by subtracting the MC
2046 expectation for $W+jets$, $Z+jets$, diboson, and top quark pair production from the data in the
2047 fail region. The distribution in m_T^{fix} observed in the fail region, corrected by subtracting the
2048 expected contributions of $W+jets$, $Z+jets$, diboson, and top quark pair production, is then used
2049 as shape template for multijet production when performing the ML fit in the pass region. The
2050 event yield N_{pass} of multijet production in the pass region is determined by an ML fit as before.
2051 The results of this cross-check agree with the nominal values of the FF within 10-20% [134]. The
2052 difference is within the systematic uncertainties associated to the FF method.

2053 I.1 Closure test

2054 In order to check the validity of the method, a closure test is performed in simulated events
2055 passing the requirements of the signal region. This ensures that the method is not introducing
2056 any bias due to the different flavor composition of the measurement region with respect to the
2057 application region, as well as due to the kinematic of the signal region. The validity of the
2058 method is checked depending on the lepton kinematics, the jet and *b* tagged jet multiplicity,
2059 and the response of the DNN discriminants used in the signal extraction of the analysis.

2060 The closure test is shown in Figs. 92-93 for electrons and Figs. 90-91 for muons for the $2\ell ss + 0\tau_h$
2061 signal region. The estimation of the semileptonic $t\bar{t}$ yields in the signal region given by the
2062 Monte Carlo simulations is compared to the estimation given by the tight-to-loose method
2063 applied to the same simulations. Two values of the fake-rate are considered for this estimation:
2064 the one obtained in QCD simulations and in $t\bar{t}$ simulation.

2065 The comparison between the fake-rates obtained in QCD and $t\bar{t}$ simulations show the effect
2066 of the residual flavor composition and kinematics between the non-prompt leptons produced
2067 in multijet events and those produced in $t\bar{t}$ events. The comparison between the $t\bar{t}$ simulation
2068 and the $t\bar{t}$ fake-rate aims to check whether there is a dependence of the fake-rate with respect
2069 to the variables and selections used in the signal extraction.

2070 The closures observed in simulations are of the order of 10% in non-prompt muons and 30 to
2071 40% for non-prompt lepton, depending on the data-taking era and the kinematic regime.

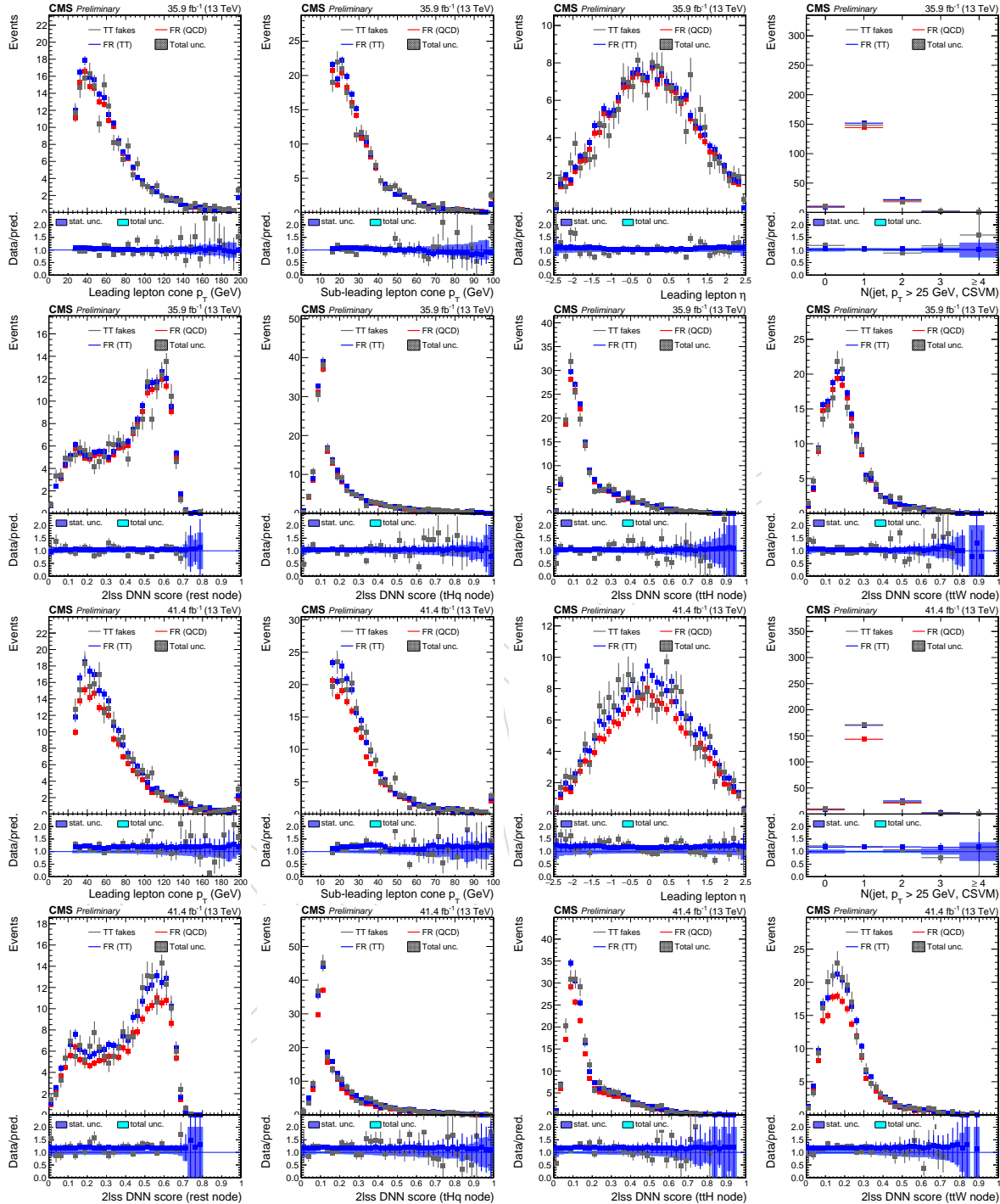


Figure 90: Closure test for muons in 2016 (first and second row), and 2017 data (third and fourth row). Non-prompt MC yield in the signal region (gray) is compared with the tight-to-loose estimation applied to the same simulation using fake-rate obtained in $t\bar{t}$ (blue) and QCD (red) simulations.

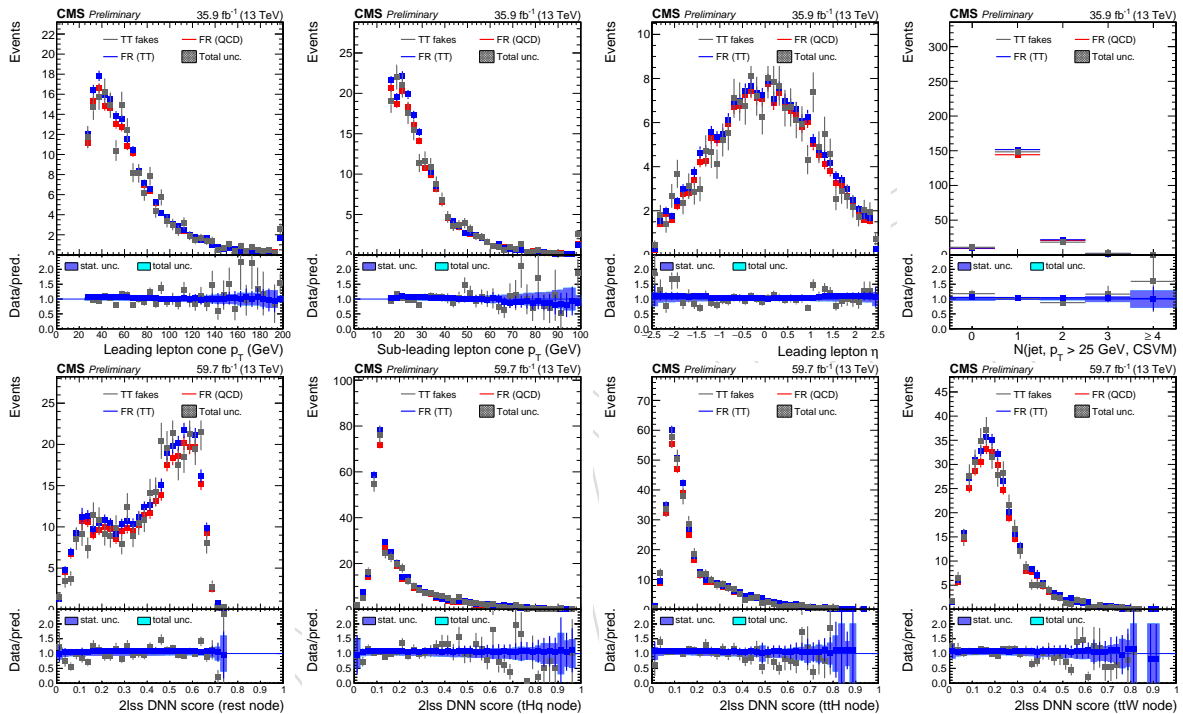


Figure 91: Closure test for muons in 2018 data. Non-prompt MC yield in the signal region (gray) is compared with the tight-to-loose estimation applied to the same simulation using fake-rate obtained in $t\bar{t}$ (blue) and QCD (red) simulations.

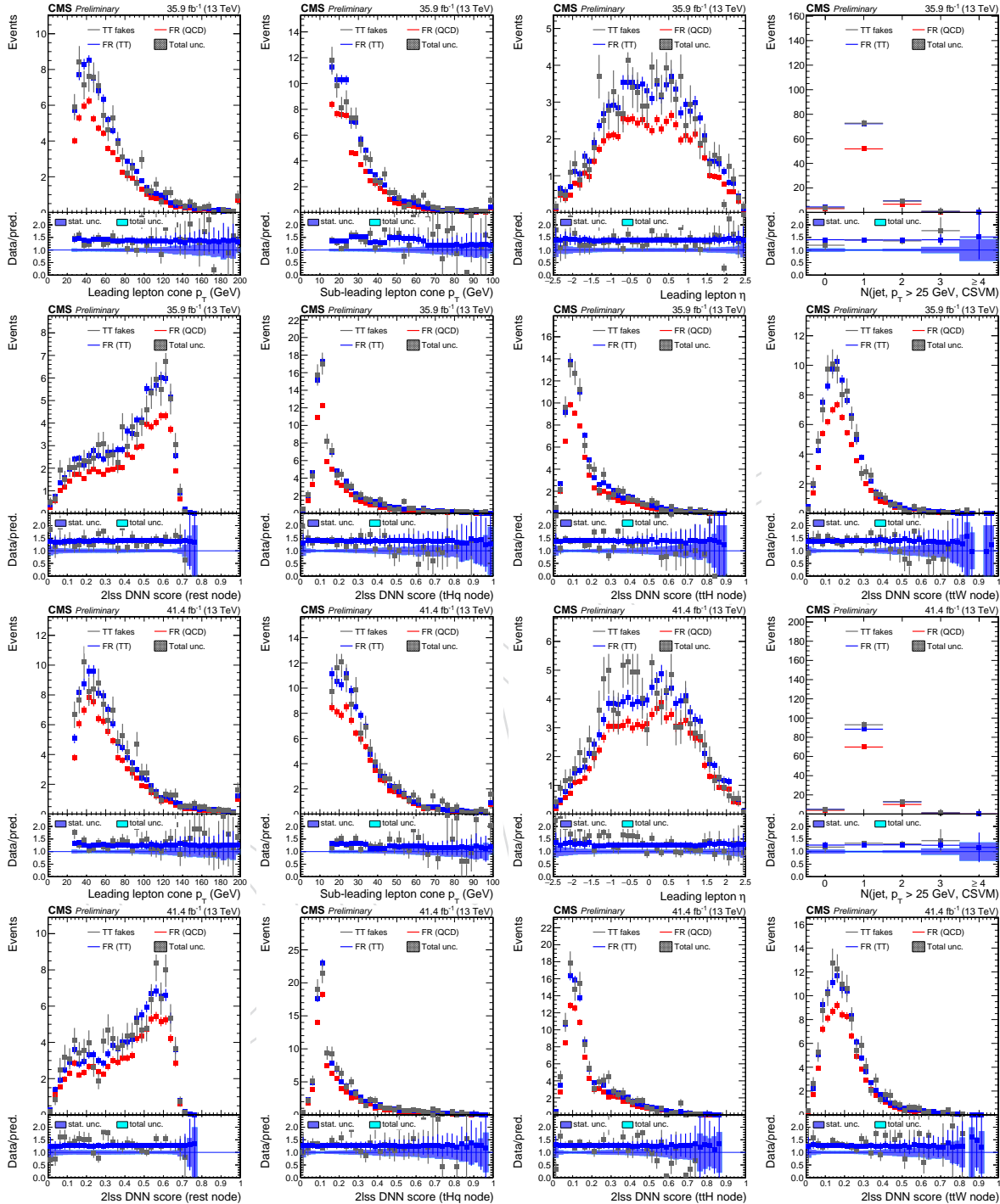


Figure 92: Closure test for electrons in 2016 (first and second row), and 2017 data (third and fourth row). Non-prompt MC yield in the signal region (gray) is compared with the tight-to-loose estimation applied to the same simulation using fake-rate obtained in $t\bar{t}$ (blue) and QCD (red) simulations.

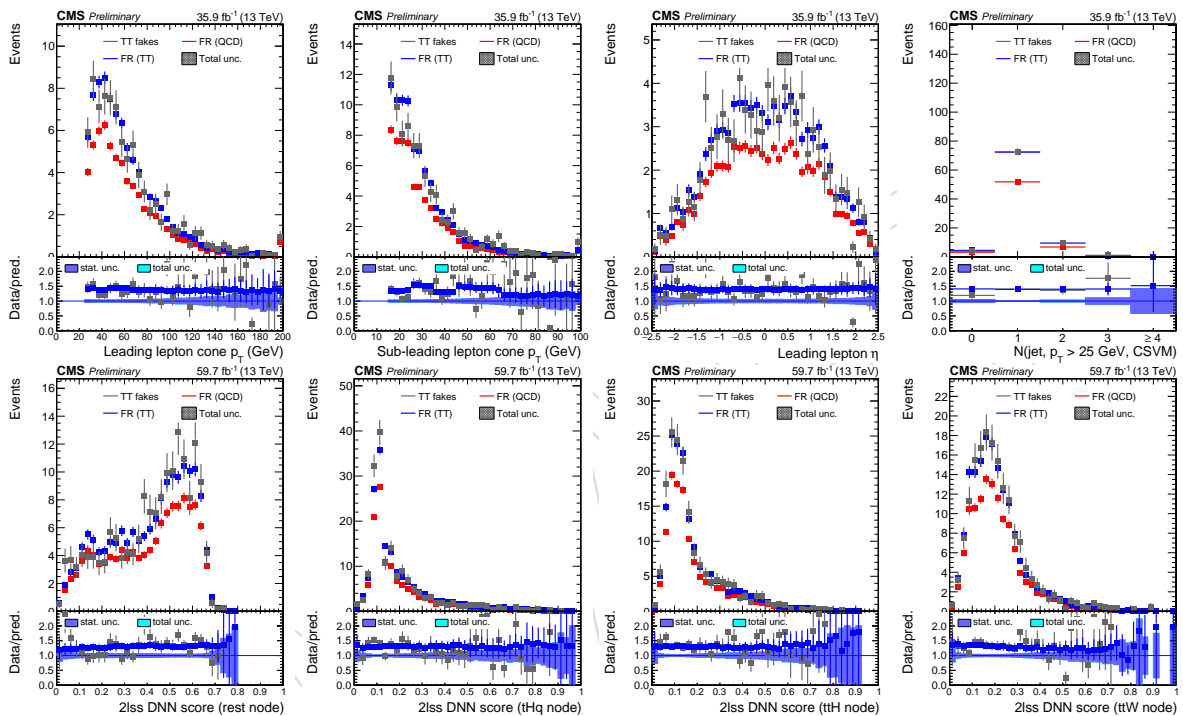


Figure 93: Closure test for electrons in 2018 data. Non-prompt MC yield in the signal region (gray) is compared with the tight-to-loose estimation applied to the same simulation using fake-rate obtained in $t\bar{t}$ (blue) and QCD (red) simulations.

2072 J Measurement of τ_h misidentification rate

2073 The rate with which quark and gluon jets passing the fakeable τ_h selection criteria pass the
 2074 tight τ_h selection (*cf.* Table 22) is measured using $t\bar{t}$ +jets events in which the two W bosons
 2075 produced in the top quark decays decay to an electron plus muon pair. Electron and muon are
 2076 required to pass the tight selection criteria defined in Tables 20 and 21, respectively, and to be
 2077 of opposite charge. The “leading” lepton (lepton of higher p_T) is required to have $p_T > 25$ GeV,
 2078 while the “subleading” lepton (lepton of lower p_T) is required to have $p_T > 15$ GeV. Selected
 2079 events are further required to contain at least one τ_h candidate passing the fakeable τ_h selection
 2080 and ≥ 2 jets of $p_T > 25$ GeV and $|\eta| < 2.4$, of which either ≥ 2 pass the loose WP of the
 2081 DeepCSV b-tagging discriminant (*cf.* Section 3.3), or ≥ 1 passes the medium WP. The jets are
 2082 required not to overlap, within $\Delta R = 0.3$, with the electron, the muon, and any τ_h candidate
 2083 that passes the fakeable τ_h selection. The contribution of backgrounds with lepton pairs of low
 2084 mass, which are not well modelled by the MC samples used in the analysis, are removed by
 2085 requiring the mass of the electron plus muon pair to satisfy the condition $m_{e\mu} > 12$ GeV. The
 2086 purity of the $t\bar{t}$ +jets sample is enhanced by requiring the linear discriminant based on E_T^{miss}
 2087 and H_T^{miss} , defined by Eq. (3), to satisfy the condition $E_T^{miss}LD > 0.2$. Events selected in data
 2088 are required to pass either the triggers based on the presence of an electron plus muon pair, the
 2089 single muon, or the single electron triggers (*cf.* Table 25).

2090 Residual contributions of background processes in which the reconstructed τ_h are due to a
 2091 genuine τ_h , an electron, or a muon are subtracted based on the MC simulation.

2092 The measured probabilities for jets passing the fakeable τ_h selection to pass the very-loose WP
 2093 of the τ_h identification discriminant applied in the $3\ell + 1\tau_h$ channel, the loose WP applied in
 2094 the $0\ell + 2\tau_h$ channel, and the medium WP applied in the $1\ell + 1\tau_h$, $1\ell + 2\tau_h$, $2\ell ss + 1\tau_h$ and
 2095 $2\ell + 2\tau_h$ are compared to the MC expectation in Figs. 94, 95, and 96 for the 2016, 2017, and
 2096 2018 data-taking periods, respectively. The probabilities, denoted by f , are determined in bins
 2097 of τ_h candidate p_T and separately for τ_h candidates reconstructed in the central ($|\eta| < 1.479$)
 2098 and in the forward ($|\eta| > 1.479$) region of the detector.

2099 In order to reduce statistical fluctuations when using the measured probabilities for the purpose
 2100 of obtaining a data-driven estimate of the fake τ_h background as described in Section 7, we do
 2101 not directly use the probabilities measured in data, but instead use the MC expectation for
 2102 these probabilities times a linear function of the form $c_0 + c_1 \cdot p_T$, obtained by fitting the data-
 2103 to-MC ratio of these probabilities. In case the statistical uncertainty of f amounts to less than
 2104 2% the statistical uncertainty is set to 2%, in order to avoid that bins at low p_T , with high event
 2105 statistics, dominate the fit.

2106 The uncertainty on the parameters of the fit is considered as systematic uncertainty on the fake
 2107 τ background estimate (*cf.* Section 8). Possible correlations between the parameters c_0 and c_1
 2108 are accounted for by determining the Eigenvectors, v_i , and Eigenvalues, λ_i , of the covariance
 2109 matrix $cov(c_0, c_1)$ returned by the fit. The Eigenvectors yield transformed parameters, $k_i =$
 2110 $v_{i0} \cdot c_0 + v_{i1} \cdot c_1$ ($k = 0, 1$), which are uncorrelated; the Eigenvalues represent the uncertainties on
 2111 the transformed parameters. The systematic uncertainties on the fake τ background estimate
 2112 are then obtained by using the functions $(1 + \lambda_i v_{i0}) c_0 + (1 + \lambda_i v_{i1}) c_1 \cdot p_T$ and $(1 - \lambda_i v_{i0}) c_0 +$
 2113 $(1 - \lambda_i v_{i1}) c_1 \cdot p_T$ as well as the function $c_0 + c_1 \cdot p_T$ as input to the background estimation
 2114 procedure described in Section 7 and taking the difference.

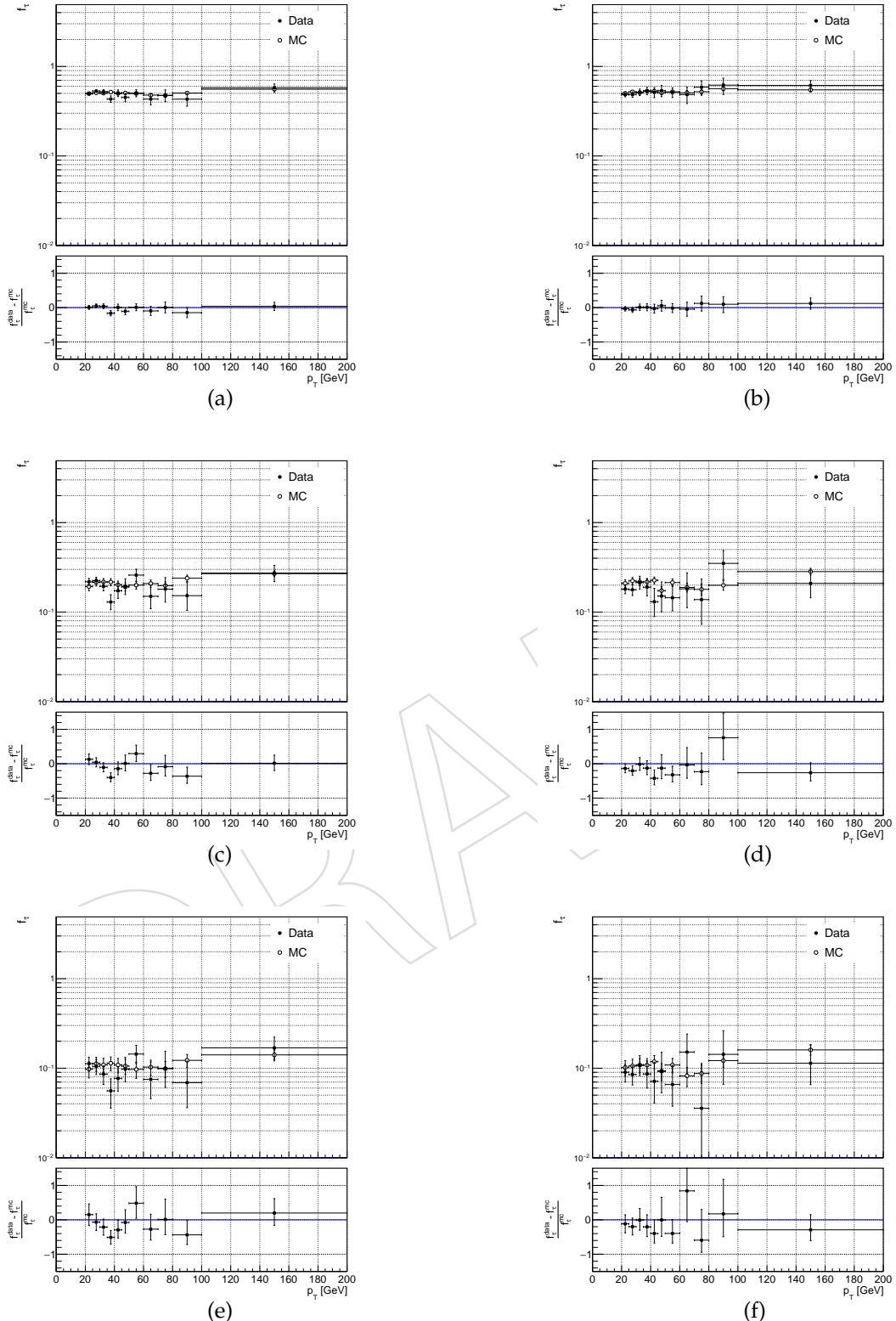


Figure 94: Probabilities f for jets passing the fakeable τ_h selection to pass the (a, b) very- loose, (c, d) loose, and (e, f) medium WP of the τ_h identification discriminant, separately for τ_h candidates reconstructed in the regions $|\eta| < 1.479$ (a, c, e) and $|\eta| > 1.479$ (b, d, f) for the 2016 data-taking period.

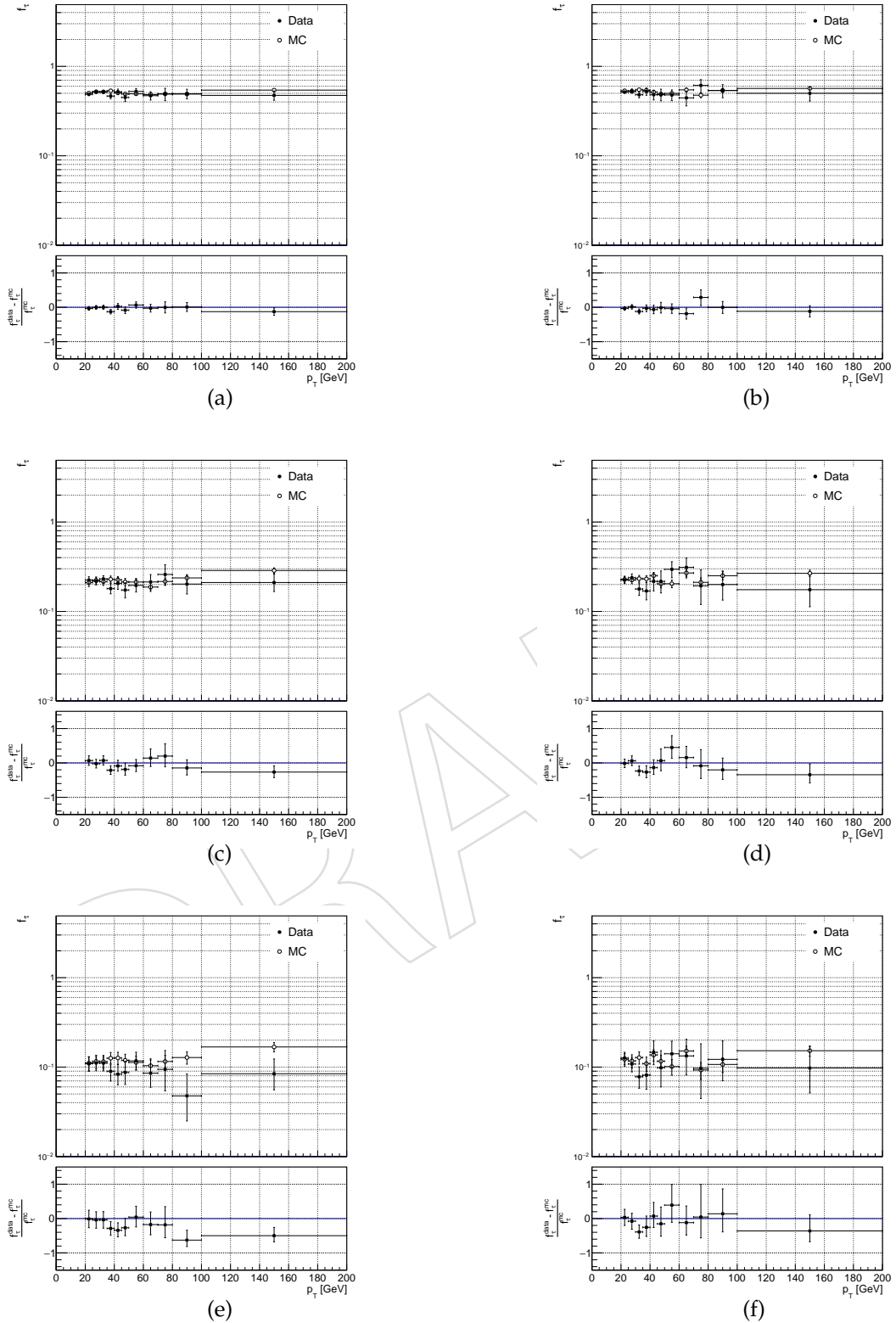


Figure 95: Probabilities f for jets passing the fakeable τ_h selection to pass the (a, b) very-loose, (c, d) loose, and (e, f) medium WP of the τ_h identification discriminant, separately for τ_h candidates reconstructed in the regions $|\eta| < 1.479$ (a, c, e) and $|\eta| > 1.479$ (b, d, f) for the 2017 data-taking period.

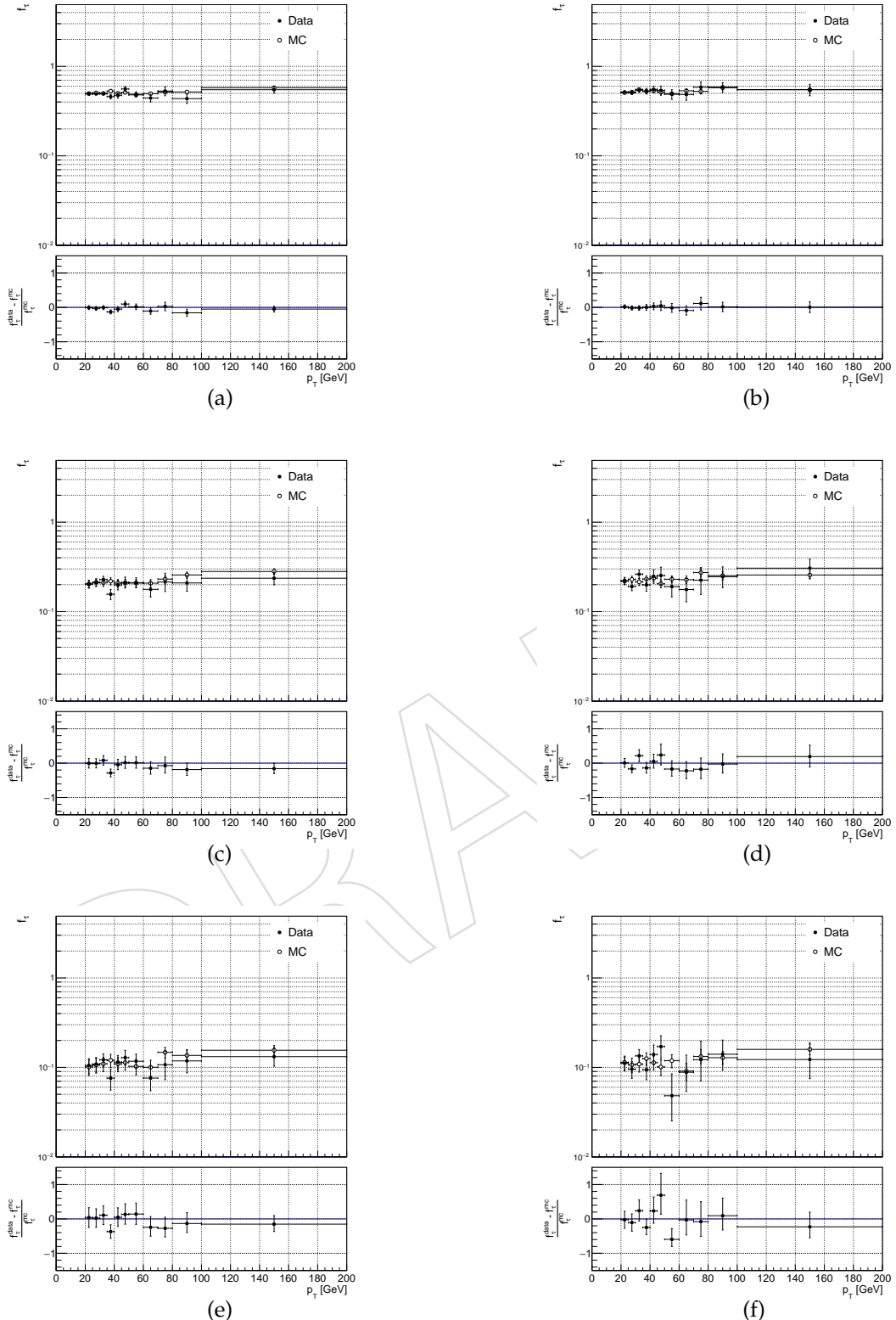


Figure 96: Probabilities f for jets passing the fakeable τ_h selection to pass the (a, b) very-tight, (c, d) loose, and (e, f) medium WP of the τ_h identification discriminant, separately for τ_h candidates reconstructed in the regions $|\eta| < 1.479$ (a, c, e) and $|\eta| > 1.479$ (b, d, f) for the 2018 data-taking period.

2115 K Measurement of the lepton charge misidentification rate

2116 NOTE: TEXT, PLOTS, AND TABLES STILL NEED TO BE UPDATED!!

2117 The measurement of the lepton charge misidentification rate is important to estimate the charge
 2118 “flip” background in the $2\ell ss$ and $2\ell ss + 1\tau_h$ categories, which originates from events with two
 2119 prompt leptons of opposite charge, in which the charge of one of the two leptons is mismeasured.
 2120

2121 The charge misidentification probability for electrons (muons) is determined from data, by
 2122 measuring the ratio of $Z/\gamma^* \rightarrow ee$ ($Z/\gamma^* \rightarrow \mu\mu$) events with two leptons of the same charge
 2123 (SS) leptons to $Z/\gamma^* \rightarrow ee$ ($Z/\gamma^* \rightarrow \mu\mu$) events with two leptons of opposite charge (OS).
 2124 The measurement utilizes the fact that $Z/\gamma^* \rightarrow ee$ events exhibit a narrow peak at $m_Z =$
 2125 91.2 GeV [92], even in case the charge of an electron is mismeasured, which allows to separate
 2126 $Z/\gamma^* \rightarrow ee$ events from backgrounds by means of performing a maximum likelihood fit of the
 2127 distribution in mass of the electron pair. The measurement is performed in bins of p_T and η of
 2128 the leptons.

2129 Events selected in the control region used to measure the charge misidentification rate are re-
 2130 quired to contain two leptons passing the “tight” lepton selection described in Section 3.1.4.
 2131 Lepton pairs of SS and of OS charge are selected in separate control regions.

2132 Samples of simulated events are used to obtain the shape templates for the maximum likeli-
 2133 hood fit, as well as a prediction for the rate of $Z/\gamma^* \rightarrow \ell\ell$ ($\ell = e, \mu$) signal events and for the
 2134 rate of background events in the SS and OS regions. The list of samples utilized in the measure-
 2135 ment of the lepton charge misidentification rate is given in Tables 4-6. The $Z/\gamma^* \rightarrow \ell\ell$ events
 2136 are considered as “signal” in case both reconstructed leptons are matched to leptons of the
 2137 same flavor (but possibly different charge) on generator level. The contribution of $Z/\gamma^* \rightarrow \ell\ell$
 2138 events in which one or both of the leptons are not matched to generator-level leptons and of
 2139 the other processes given in Tables 4-6 are considered as background.

2140 K.1 Electrons

2141 The electron charge misidentification rates are measured in 6 bins in p_T and η , given in Table 52.
 2142 A complication arises from the fact that events selected in the SS region contain two electrons,
 2143 in general of different p_T and η , and we do not know the charge of which of the two electrons
 2144 is mismeasured. Thus, the measurement is performed in event categories that are based on p_T
 2145 and η of both electrons. The categories are given in Table 53. We denote by e_1 the electron of
 2146 higher p_T and by e_2 the electron of lower p_T . For example, the category that contains events
 2147 in which e_1 is in the endcap and has a high p_T (**EH**), while e_2 is in the barrel and has medium
 2148 p_T (**BM**) is denoted **EH_BM**. Making the assumption that the charge misidentification rates
 2149 for both electrons are independent allows to combine the categories **EH_BM** and **BM_EH** into
 2150 a single category. Performing such a combination for all categories reduces the number of
 2151 categories from $6^2 = 36$ to 21.

$p_T / \eta $	$ \eta \leq 1.479$	$1.479 < \eta < 2.5$
$10 < p_T < 25$ GeV	BL	EL
$25 < p_T < 50$ GeV	BM	EM
$p_T > 50$ GeV	BH	EH

Table 52: Bins in p_T and η in which the electron charge misidentification rate is measured.

2152 The measured ratios, $r = \frac{N_{SS}}{N_{SS} + N_{OS}}$, of $Z/\gamma^* \rightarrow ee$ events in the SS and OS regions of the 21
 2153 events categories are related to the charge misidentification rates p in the 6 bins of electron p_T

$e_1 \ e_2$	EH	BH	EM	BM	EL	BL
EH	EH_EH	EH_BH	EH_EM	EH_BM	EH_EL	EH_BL
BH	-	BH_BH	BH_EM	BH_BM	BH_EL	BH_BL
EM	-	-	EM_EM	EM_BM	EM_EL	EM_BL
BM	-	-	-	BM_BM	BM_EL	BM_BL
EL	-	-	-	-	EL_EL	EL_BL
BL	-	-	-	-	-	BL_BL

Table 53: Event categories, based on p_T and η of e_1 and e_2 , used for the measurement of the electron charge misidentification rate.

and η by the set of expressions given by Eq. (18). The expressions assume that the probabilities for electron charge misidentification are small, i.e. $p \cdot p \ll p$.

$$\begin{aligned}
r_{BL_BL} &= 2p_{BL} & r_{BH_EH} &= p_{BH} + p_{EH} \\
r_{BM_BL} &= p_{BM} + p_{BL} & r_{BL_EL} &= p_{BL} + p_{EL} \\
r_{BM_BM} &= 2p_{BM} & r_{BM_EL} &= p_{BM} + p_{EL} \\
r_{BH_BL} &= p_{BH} + p_{BL} & r_{EM_BL} &= p_{EM} + p_{BL} \\
r_{BH_BM} &= p_{BH} + p_{BM} & r_{BM_EM} &= p_{BM} + p_{EM} \\
r_{BH_BH} &= 2p_{BH} & r_{BH_EL} &= p_{BH} + p_{EL} \\
r_{EL_EL} &= 2p_{EL} & r_{EH_BL} &= p_{EH} + p_{BL} \\
r_{EM_EL} &= p_{EM} + p_{EL} & r_{BH_EM} &= p_{BH} + p_{EM} \\
r_{EM_EM} &= 2p_{EM} & r_{EH_BM} &= p_{EH} + p_{BM} \\
r_{EH_EL} &= p_{EH} + p_{EL} & r_{BH_EH} &= p_{BH} + p_{EH} \\
r_{EH_EM} &= p_{EH} + p_{EM}
\end{aligned} \tag{18}$$

The electron charge misidentification rates p in the 6 bins of p_T and η , and the corresponding uncertainties, are obtained from the ratios r measured in the 21 event categories by using matrix algebra [135] to solve the overconstrained system of linear equations given by Eq. (18).

The ratios r on the left-hand-side of Eq. (18) are determined by maximum likelihood fits of the distributions in mass, m_{ee} , if the electron pairs within the range $60 < m_{ee} < 120$ GeV. The mass distributions for different event categories are fitted independently. In each category, the SS and OS regions are fitted simultaneously. Systematic uncertainties are represented by nuisance parameters, which are correlated between the SS (low statistics) and OS (high statistics) regions. Three different approaches were tried to perform the fit.

The first approach uses analytic functions to model the $Z/\gamma^* \rightarrow ee$ signal and to model the backgrounds in the SS and OS regions, following Refs. [77, 103, 116]. The $Z/\gamma^* \rightarrow ee$ signal is modeled by a convolution of a crystal-ball and a Breit-Wigner function. The CMSShape function is used to model the background. It consists of an exponential tail at high mass and a sigmoid function, to model threshold effects, at low mass. The advantage of the analytic approach is that it does not require high statistics MC samples. Its disadvantage is that it relies on the assumption that the signal and background distributions in each of the 21 event categories are well modeled by the chosen analytic functions.

It turns-out, however, that the analytic functions do not model well the high and low mass tails of the m_{ee} distribution for signal and background, causing the fit to be biased. To mitigate the issue, a “hybrid” approach of analytic and simulation based modeling was attempted, in which

Category	r	Category	r
BL_BL	0.047 ± 0.022	EH_EH	0.337 ± 0.037
BM_BL	0.037 ± 0.004	BL_EL	0.028 ± 0.017
BM_BM	0.016 ± 0.001	BM_EL	0.042 ± 0.006
BH_BL	0.016 ± 0.009	EM_BL	0.069 ± 0.007
BH_BM	0.020 ± 0.001	BM_EM	0.078 ± 0.003
BH_BH	0.026 ± 0.014	BH_EL	0.046 ± 0.012
EL_EL	0.000 ± 0.000	EH_BL	0.198 ± 0.018
EM_EL	0.000 ± 0.000	BH_EM	0.088 ± 0.007
EM_EM	0.181 ± 0.008	EH_BM	0.119 ± 0.007
EH_EL	0.340 ± 0.070	BH_EH	0.204 ± 0.022
EH_EM	0.191 ± 0.009		

Table 54: Ratios r measured in the 21 event categories with the fit approach based on template histograms obtained from the MC simulation.

an analytic function was used to model the background in the SS region, which suffers the most from insufficient MC statistics, while template histograms obtained from the simulation were used to model the $Z/\gamma^* \rightarrow ee$ signal and the background in the OS region. Comparing data to the sum of fitted signal plus background shapes, we still find a bias for some of the 21 event categories, however.

We find that the best performing approach, with the least bias, is to use template histograms obtained from the simulation to model the signal and background shapes in the SS and OS regions, even though the MC statistics in some of the 21 event categories is severely limited. Systematic uncertainties on the electron energy scale (eES) and resolution (eER) are represented by nuisance parameters in the fit. The eES uncertainty amounts to 1% for electrons in the barrel and to 2.5% for electrons in the endcap. The eER is allowed to vary from 0.75 to 1.25 times the nominal eER, obtained from the simulation. Statistical uncertainties are taken into account by the technique described in Refs. [136, 137]. The fits are performed using the `combine` tool [138] developed by the Higgs combination group.

The electron charge misidentification rates measured with different approaches differ by up to 30% with respect to each other and with respect to the MC truth in a closure test that we performed. We take the differences into account as systematic uncertainty when applying the measured charge misidentification rates to estimate the charge “flip” background in the $2\ell_{\text{SS}}$ and $2\ell_{\text{SS}} + 1\tau_h$ categories (*cf.* Sections 7.2 and 8).

The ratios r measured in the 21 categories with the template histogram approach are given in Table 54.

For illustration, the m_{ee} distributions observed in data are compared to the results of the fit for the SS and OS regions of the **BM_BM**, **EM_BM**, and **EM_EM** categories in Fig. 97.

The electron charge misidentification rates measured in the 6 bins of p_T and η , obtained by solving Eq. (18) for the numbers shown in Table 54, are given in Table 55.

K.2 Muons

The muon charge misidentification rates have been measured in data recorded in 2016 and found to be negligible [139].



Figure 97: (b,d,f) regions of the **BM_BM** (a,b), **EM_BM** (c,d), and Distributions in m_{ee} observed in the SS (a,c,e) and OS **EM_EM** (e,f) category, compared to the sum of $Z/\gamma^* \rightarrow ee$ signal and background processes. The distributions expected for signal and backgrounds are shown for the values of nuisance parameters obtained from the ML fit. The fit approach based on templates histograms obtained from the MC simulation is used.

		$15 \leq p_T < 25 \text{ GeV}$	$25 \leq p_T < 50 \text{ GeV}$	$p_T \geq 50 \text{ GeV}$
MC truth	$ \eta < 1.479$	0.0081 ± 0.0015	0.0053 ± 0.0003	0.0071 ± 0.0009
	$1.479 \leq \eta < 2.5$	0.0579 ± 0.0068	0.0507 ± 0.0016	0.0915 ± 0.0061
Pseudodata	$ \eta < 1.479$	0.0009 ± 0.0024	0.0096 ± 0.0027	0.0132 ± 0.0019
	$1.479 \leq \eta < 2.5$	0.0095 ± 0.0045	0.0507 ± 0.0028	0.0907 ± 0.0067
Data	$ \eta < 1.479$	0.0134 ± 0.0041	0.0224 ± 0.0041	0.0228 ± 0.0053
	$1.479 \leq \eta < 2.5$	0.0199 ± 0.0070	0.0560 ± 0.0041	0.1387 ± 0.0087

Table 55: Charge misidentification rates (in units of percent) for electrons of different p_T and η , measured with the fit approach based on template histograms obtained from the MC simulation. The difference between MC truth and pseudodata quantifies the bias of the fit model. The m_{ee} distribution that is used as input in the pseudodata case is constructed by setting the “data” in each bin to a random variable, drawn from a Poisson distribution the average of which is given by the sum of $Z/\gamma^* \rightarrow ee$ signal plus background expected in that bin.

2204 L Measurement of the phase space extrapolation uncertainty

2205 L.1 Introduction

2206 It is crucial to have a precise estimation of the lepton selection efficiencies, as they will affect
2207 the yield estimation of both signal and background contributions in the measurement regions.
2208 This is particularly important given that small discrepancies between data and the Monte Carlo
2209 (MC) models are observed, therefore the models must be corrected by the efficiency measure-
2210 ments in data. The measurement of lepton efficiencies from the loose to the tight $t\bar{t}H$ selection
2211 on both data and MC is performed using the tag-and-probe method using Z events, results
2212 shown in Section 6.3. Scale factors are derived as the ratio of the efficiency measured in data
2213 over the efficiency measured in MC simulations.

2214 Uncertainties due to lepton selection efficiency determination uncertainty constitute one of the
2215 main sources of uncertainty in many analyses. These uncertainties can be further studied and
2216 factorized in two groups: those due to the measurement of the efficiency in Z events in data,
2217 and another one by the potential topology differences between the events used as reference, Z
2218 events, and signal events, $t\bar{t}$ events in this case. The first source of uncertainty applies for all
2219 analyses and is properly assessed within the POGs and will not be described here, while the
2220 method to estimate the potential bias that is introduced by the phase space extrapolation from
2221 Z events to $t\bar{t}$ events is presented in this section.

2222 L.2 Phase space extrapolation uncertainty

2223 Identification variables are robust enough to be independent of the topology of the event. How-
2224 ever, other variables can yield to a bias due to the application of the scale factor in a different
2225 region to what has been measured. This bias can also appear when requirements are applied in
2226 variables dependent on the topology of the event, such as on the presence of close-by objects.
2227 We denote this as *phase extrapolation bias*.

2228 Phase space extrapolation uncertainty can affect analyses in different manners. This must be
2229 therefore assessed in a analysis-by-analysis or topology-by-topology basis.

2230 A method is proposed to determine the magnitude of a potential bias introduced by the phase
2231 space extrapolation in this analysis. The method consists on a in-situ efficiency measurement of
2232 leptons produced in a dilepton region. When measuring lepton efficiencies in a process that is
2233 not a resonance, the problem arises of how to subtract the contribution of background leptons
2234 (in this case, non-prompt leptons, i.e., those not produced in W or Z decays). This method
2235 tackles this problem using a data-driven background estimation method.

2236 The method allows to measure efficiencies of a given selection criterion, denoted as tight, in
2237 leptons passing looser selection criteria, denoted as loose. Events are selected with a recon-
2238 structed $e\mu$ pair with an opposite sign in the final state. Additionally, further event selection
2239 criteria should be applied in order to measure the efficiency on the relevant phase space. For
2240 instance, in order to measure the extrapolation bias in $t\bar{t}$ events, two jets and a b jet can be
2241 required.

2242 We denote the lepton whose efficiency is to be measured as the probe, and the remaining one,
2243 as the tag. Both tag and probe leptons must pass the loose criterion, and the tag is also required
2244 to have passed the tight criterion. This is done in order to remove the contamination from
2245 background leptons.

2246 Efficiency can be then determined by counting the amount of events with a probe passing the
2247 tight criteria, over the total number of events

$$\epsilon = \frac{N_{\text{passing}}}{N_{\text{total}}}. \quad (19)$$

2248 However, equation (19) only holds when all the selected probes are signal leptons. This may
 2249 not be the case when performing this measurement in data, therefore non-prompt leptons must
 2250 be subtracted in the numerator and the denominator:

$$\epsilon = \frac{N_{\text{passing}}^{\text{data}} - N_{\text{passing}}^{\text{non-prompt}}}{N_{\text{total}}^{\text{data}} - N_{\text{total}}^{\text{non-prompt}}}. \quad (20)$$

2251 With a suitable non-prompt lepton estimation method, expression (20) allows us to measure
 2252 the efficiency of leptons in events in a $t\bar{t}$ -control region in data.

2253 The non-prompt lepton estimation method employed exploits the fact that not many processes
 2254 in the Standard Model yield to events with a same-sign pair. Therefore, a non-prompt lepton
 2255 enriched region can be defined by considering a sideband region with a same-sign $e\mu$ pair.
 2256 Subtracting the contribution from prompt leptons in this region, the estimation of the amount
 2257 of non-prompt leptons in the opposite-sign can be obtained

$$N_{\text{OS}}^{\text{non-prompt}} = \left(N_{\text{SS}}^{\text{data}} - N_{\text{SS}}^{\text{prompt}} \right) \times R_{\text{SS}}^{\text{OS}}, \quad (21)$$

2258 where $R_{\text{SS}}^{\text{OS}}$ is defined as the ratio between opposite-sign and same-sign events of processes
 2259 with prompt-leptons. This quantity as well as the prompt lepton subtraction is estimated from
 2260 Monte Carlo simulations. When measuring the efficiency as a function of a given quantity all
 2261 the inputs in equations (20) and (21) are evaluated as a function of that variable.

2262 L.3 Application to $t\bar{t}$ -enriched analyses

2263 In this section, the method developed in section L.2 is applied to the events in order to evaluate
 2264 the efficiency of the loose to the tight $t\bar{t}H$ selection cuts. Events are required to pass a set of
 2265 single lepton trigger paths and to contain an $e\mu$ pair in the final state, with the tag lepton been
 2266 always tight. Additionally, only events with at least two jets with $p_T > 25$ GeV, out of which
 2267 one passes the medium working point of the Deep Jet discriminant, are taken into account.

2268 The efficiency measured in data is done using the method developed in section L.2, while the
 2269 efficiency in MC is determined using the $t\bar{t}$ simulation and corrected by the appropriate scale
 2270 factors. For the loose selection the pileup, b-tagging and trigger scale factors are applied. For
 2271 the tight selection an additional lepton scale factor determined using the tag-and-probe method
 2272 in Drell-Yan events (as mentioned above) in order to correct the loose to tight $t\bar{t}H$ selection is
 2273 also applied. Given that the efficiencies are estimated to exactly evaluate this effect, the scale
 2274 factors are expected to be very close to 1. Differences between the two methods can both be due
 2275 to a bias introduced by the model choice or by the phase space extrapolation bias. Therefore
 2276 these differences can be taken as the upper limit for the phase space extrapolation bias.

2277 The data and $t\bar{t}$ MC efficiencies and the scale factors are shown from figures to 98 to 103 for
 2278 muon and electron probes for the 2016, 2017 and 2018 datasets as a function of lepton p_T (left)
 2279 and lepton $|\eta|$ (right).

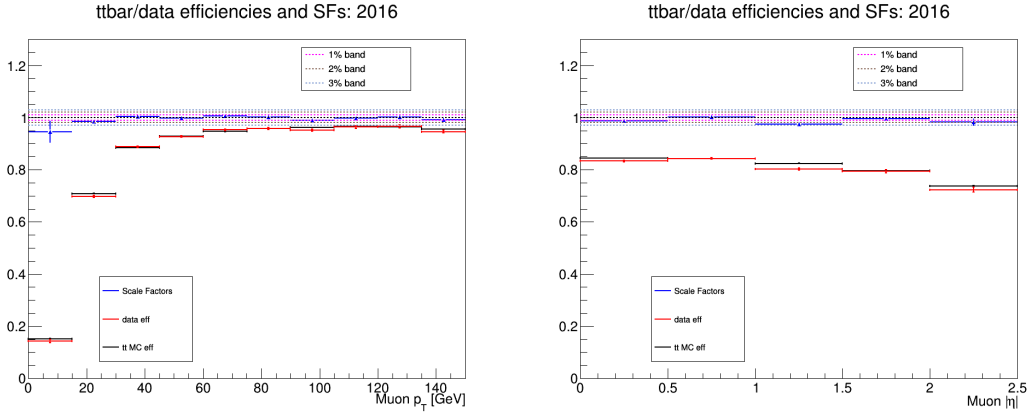


Figure 98: Data and $t\bar{t}$ efficiencies and the scale factor as a function of the muon (probe) p_T (left) and $|\eta|$ (right) for the 2016 dataset.

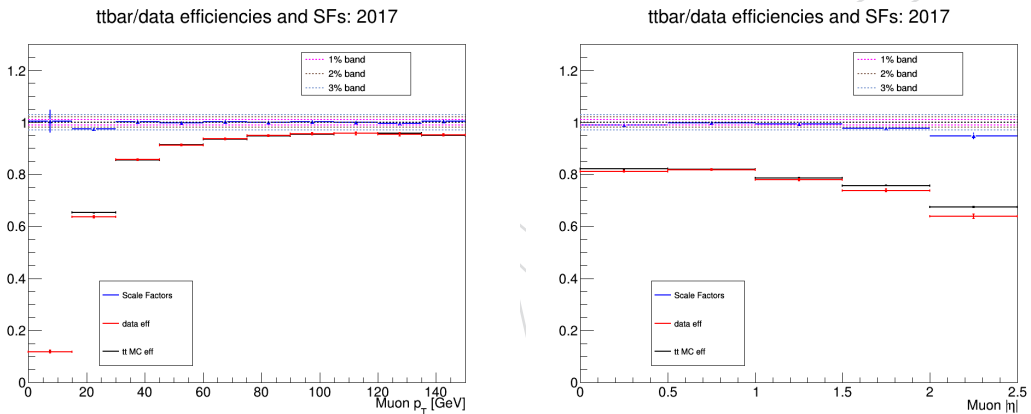


Figure 99: Data and $t\bar{t}$ efficiencies and the scale factor as a function of the muon (probe) p_T (left) and $|\eta|$ (right) for the 2017 dataset.

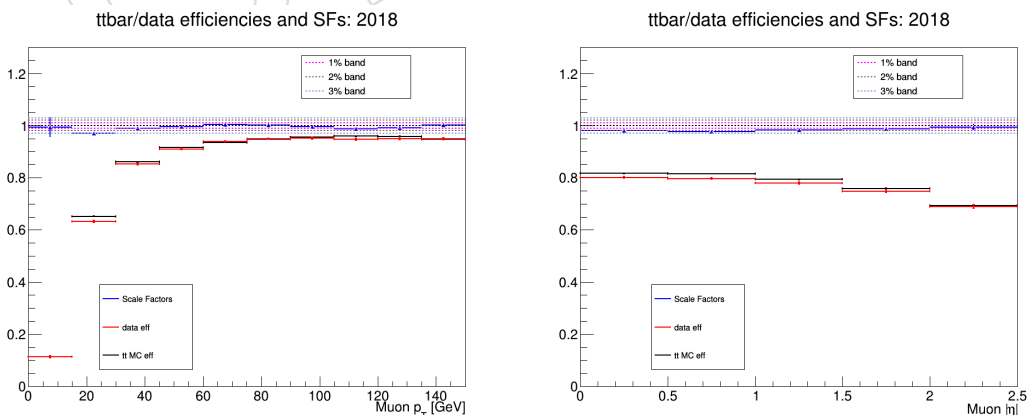


Figure 100: Data and $t\bar{t}$ efficiencies and the scale factor as a function of the muon (probe) p_T (left) and $|\eta|$ (right) for the 2018 dataset.

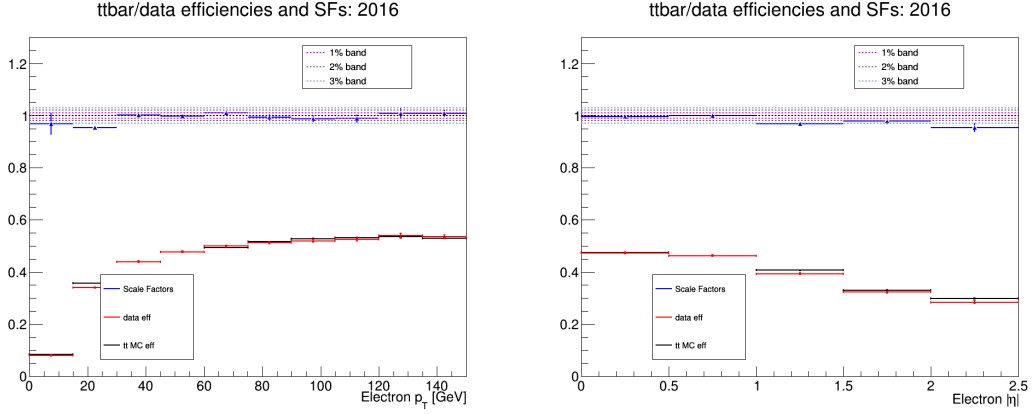


Figure 101: Data and $t\bar{t}$ efficiencies and the scale factor as a function of the electron (probe) p_T (left) and $|\eta|$ (right) for the 2016 dataset.

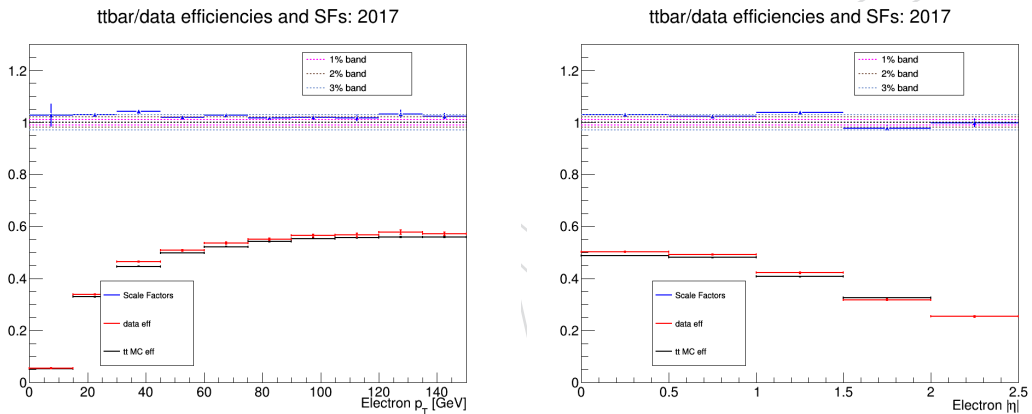


Figure 102: Data and $t\bar{t}$ efficiencies and the scale factor as a function of the electron (probe) p_T (left) and $|\eta|$ (right) for the 2017 dataset.

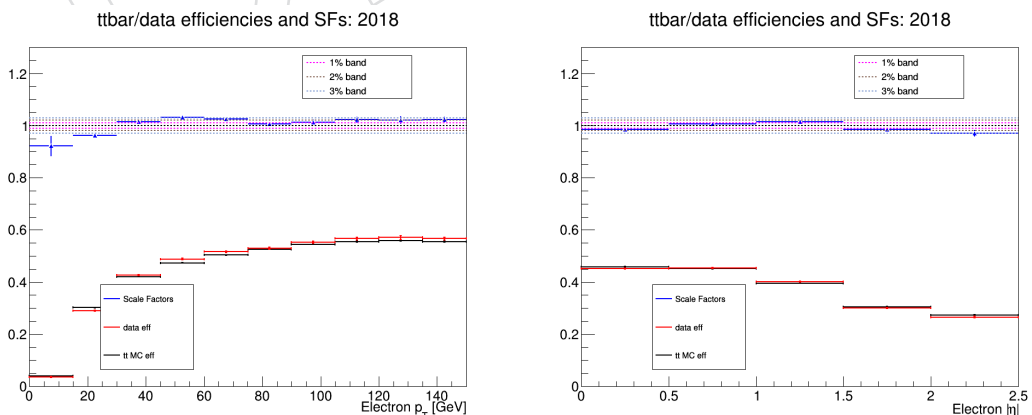


Figure 103: Data and $t\bar{t}$ efficiencies and the scale factor as a function of the electron (probe) p_T (left) and $|\eta|$ (right) for the 2018 dataset.

2280 **L.4 Conclusions**

2281 A method is proposed to determine the potential bias that is introduced by the phase space
2282 extrapolation from Z events to dileptonic $t\bar{t}$ events, and is applied to the lepton $t\bar{t}H$ selection.
2283 The results show that this effect is around 1% for muons and 1-3% for electrons. The plan is
2284 to provide the scale factors uncertainties estimated with this method to replace the current DY
2285 scale factor uncertainties.

DRAFT

2286 M Prefiring

2287 Gradual timing shift of ECAL was not propagated to L1 trigger primitives in 2016 and 2017, due
 2288 to this mistiming and trigger rules, events with a significant amount of ECAL energy deposits
 2289 in the region of $2.0 < |\eta| < 3.0$ can be preferentially lost. The impact of this issue in the
 2290 analysis is checked. Inefficiency maps to be applied to simulation are taken from [140]. Maps
 2291 for photons and jets are separated as significant differences in prefiring rate between photons
 2292 and jets were found. For each event, we consider all jets and photons that pick up a non-zero
 2293 scale factor from the inefficiency map, parametrized by p_T and η and obtain a multiplicative
 2294 scale factor (< 1), that is a prefiring probability and it can be applied to MC. The tool used is
 2295 detailed in [112].

2296 This allows to obtain the central value but also upward and downward values of the event
 2297 weight, obtained by shifting all prefiring probabilities plus or minus their uncertainties. The
 2298 uncertainty is taken as the quadratic sum of 20 percent of the object prefiring probability and
 2299 the statistical uncertainty associated to the considered bin in the prefiring map. That 20% is
 2300 estimated by the difference of measurement between datasets and jet flavours, extrapolation to
 2301 very high p_T and closure in validation regions.

2302 Those weights are applied to all samples in the analysis, here $t\bar{t}H$ and $t\bar{t}Z$ MC samples are used
 2303 in order to check the impact of the L1 prefiring issue in the measurement. First, the variations
 2304 in the analysis categories for the $2\ell ss$ signal region are shown in Fig. 104. Discrepancies are
 2305 shown and it can be seen that applying the weights to the $t\bar{t}H$ samples leads into a 2.9% (2.2%)
 2306 variation in the yields for 2017 (2016). For $t\bar{t}Z$ samples variations in the yields are a 3.8% (2.2%)
 2307 in 2017 (2016).

2308 Besides, variables used in the signal extraction are also checked showing similar discrepancies.
 2309 The effect is uniform in most of the variables except in the number of forward jets and in the
 2310 max lep η distributions, where a clear trend is shown, as is depicted in Fig. 105. That figure
 2311 shows MC samples with the 2017 conditions, as the impact of the L1 prefiring issue is bigger in
 2312 that year, however, that trend is also visible in 2016.

Figure 104: $2\ell ss$ signal categories using $t\bar{t}H$ and $t\bar{t}Z$ MC samples for 2016 (upper row) and 2017 (lower row). Dashed lines show the MC after applying prefiring weights.

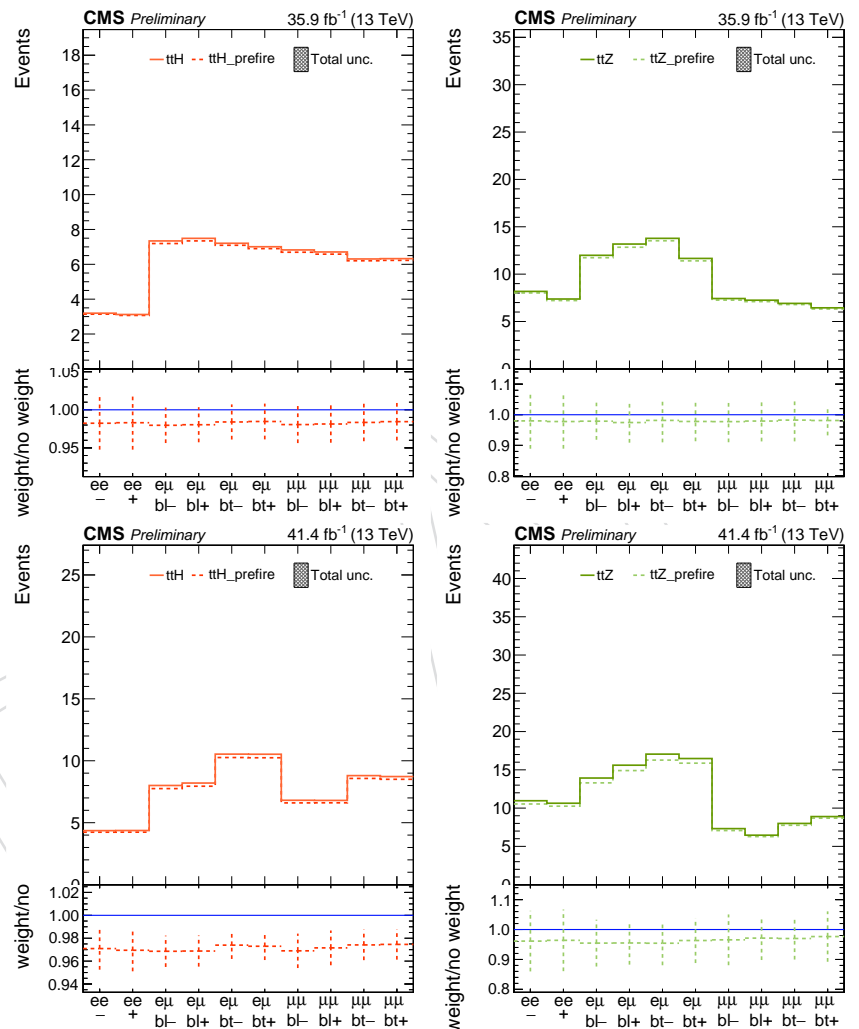
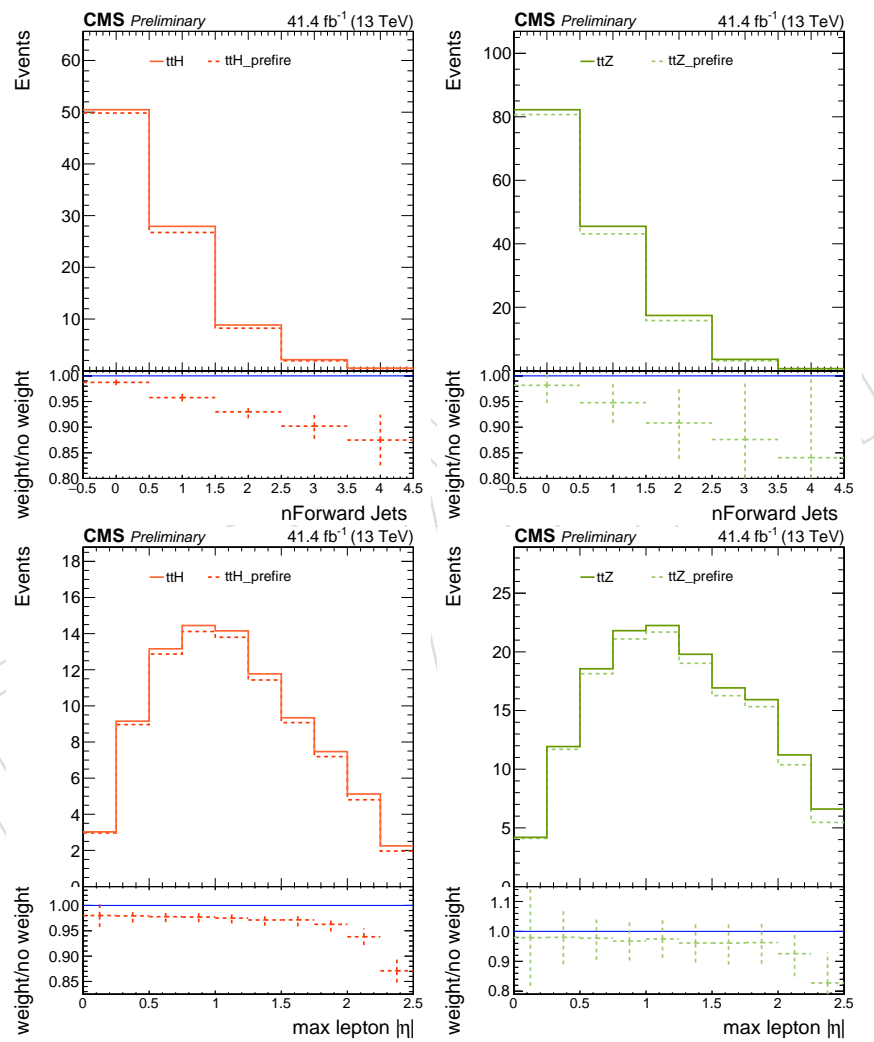


Figure 105: 2ℓ ss number of forward jets (upper row) and max lepton η (lower row) distributions inclusive in number of jets and number of b-jets using $t\bar{t}H$ and $t\bar{t}Z$ MC samples for 2017. Dashed lines show the MC after applying prefiring the weight.



2313 **N Tables with event yields, prefit/postfitplots, ML fit diagnostics,
2314 etc**

2315 [PLACE ALL RESULTS HERE]

DRAFT

²³¹⁶ **O Results separated by year**

²³¹⁷ [Tables with event yields, prefit/postfitplots, ML fit diagnostics, etc]

DRAFT

Table 56: The selected number of events in the $2\ell ss + 0\tau_h$ for the regions enriched with $t\bar{t}H$ and tH signal (upper part) and for the regions that are BKG enriched (bottom part). Only for the dominant Higgs process ($t\bar{t}H$) we show the separation of the branching ratios.

Region	$t\bar{t}H$ – region			tH – region		
	Leptons	ee	$e\mu$	$\mu\mu$	ee	$e\mu$
$t\bar{t}H, H \rightarrow ZZ$	X.X \pm X.X	X.X \pm X.X	X.X \pm X.X	X.X \pm X.X	X.X \pm X.X	X.X \pm X.X
$t\bar{t}H, H \rightarrow WW$	\pm					
$t\bar{t}H, H \rightarrow \tau\tau$	\pm					
$t\bar{t}H, H \rightarrow \mu\mu$	\pm					
$t\bar{t}H, H \rightarrow Z\gamma$	\pm					
$t\bar{t}H$ (sum)	\pm					
tH	\pm					
WH	\pm					
ZH	\pm					
ggH (sum)	\pm					
$VBFH$ (sum)	\pm					
$t\bar{t}W$	\pm					
$t\bar{t}WW$	\pm					
$t\bar{t}W + ttWW$	\pm					
ZZ	\pm					
WZ	\pm					
$t\bar{t}Z$	\pm					
Misidentified Conversions	\pm					
signal flip	\pm					
Other	\pm					
SM expectation	\pm					
Observed data	\pm					

Region	$t\bar{t}W$ – region			BKG – region		
	Leptons	ee	$e\mu$	$\mu\mu$	ee	$e\mu$
$t\bar{t}H, H \rightarrow ZZ$	X.X \pm X.X	X.X \pm X.X	X.X \pm X.X	X.X \pm X.X	X.X \pm X.X	X.X \pm X.X
$t\bar{t}H, H \rightarrow WW$	\pm					
$t\bar{t}H, H \rightarrow \tau\tau$	\pm					
$t\bar{t}H, H \rightarrow \mu\mu$	\pm					
$t\bar{t}H, H \rightarrow Z\gamma$	\pm					
$t\bar{t}H$ (sum)	\pm					
tH	\pm					
WH	\pm					
ZH	\pm					
ggH (sum)	\pm					
$VBFH$ (sum)	\pm					
$t\bar{t}W$	\pm					
$t\bar{t}WW$	\pm					
$t\bar{t}W + ttWW$	\pm					
ZZ	\pm					
WZ	\pm					
$t\bar{t}Z$	\pm					
Misidentified Conversions	\pm					
signal flip	\pm					
Other	\pm					
SM expectation	\pm					
Observed data	\pm					

Table 57: The selected number of events in the $3\ell + 0\tau_h$ category. The rates are obtained from the ML fit (post-fit). Uncertainties smaller than 0.05 are denoted by “ < 0.05 ”.

Region	ttH – region		tH – region		BKG – region	
	bl	bt	bl	bt	bl	bt
ttH, H $\rightarrow ZZ$	X.X \pm X.X					
ttH, H $\rightarrow WW$	\pm					
ttH, H $\rightarrow \tau\tau$	\pm					
ttH, H $\rightarrow \mu\mu$	\pm					
ttH, H $\rightarrow Z\gamma$	\pm					
ttH (sum)	\pm					
tH	\pm					
WH	\pm					
ZH	\pm					
ggH (sum)	\pm					
VBFH (sum)	\pm					
ttW	\pm					
ttWW	\pm					
ttW + ttWW	\pm					
ZZ	\pm					
WZ	\pm					
ttZ	\pm					
Misidentified	\pm					
Conversions	\pm					
signal flip	\pm					
Other	\pm					
SM expectation	\pm					
Observed data	\pm					

Table 58: The selected number of events in the $2\ell ss + 1\tau_h$. The rates are obtained from the ML fit (post-fit). Uncertainties smaller than 0.05 are denoted by “ < 0.05 ”.

Region	ttH – region		tH – region		BKG – region	
	bl	bt	bl	bt	bl	bt
ttH, H $\rightarrow ZZ$	X.X \pm X.X					
ttH, H $\rightarrow WW$	\pm					
ttH, H $\rightarrow \tau\tau$	\pm					
ttH, H $\rightarrow \mu\mu$	\pm					
ttH, H $\rightarrow Z\gamma$	\pm					
ttH (sum)	\pm					
tH	\pm					
WH	\pm					
ZH	\pm					
ggH (sum)	\pm					
VBFH (sum)	\pm					
ttW	\pm					
ttWW	\pm					
ttW + ttWW	\pm					
ZZ	\pm					
WZ	\pm					
WZ + ZZ	\pm					
ttZ	\pm					
Misidentified	\pm					
Conversions	\pm					
signal flip	\pm					
Other	\pm					
SM expectation	\pm					
Observed data	\pm					

Figure 106: Distributions in the discriminating observables used for the signal extraction in the $2\ell ss + 0\tau_h$ category for the 2016 luminosity (a) the $t\bar{t}H$ – region, (b) the $t\bar{t}Z$ – region, (c) the BKG – region, and (d) the $t\bar{t}W$ – region. The post-fit rates and uncertainties are used. [PLACEHOLDER - PREFIT, BLINDED - THERE IS A BUG IN THE IMPLEMENTATION OF THE DNN WEIGHTS]

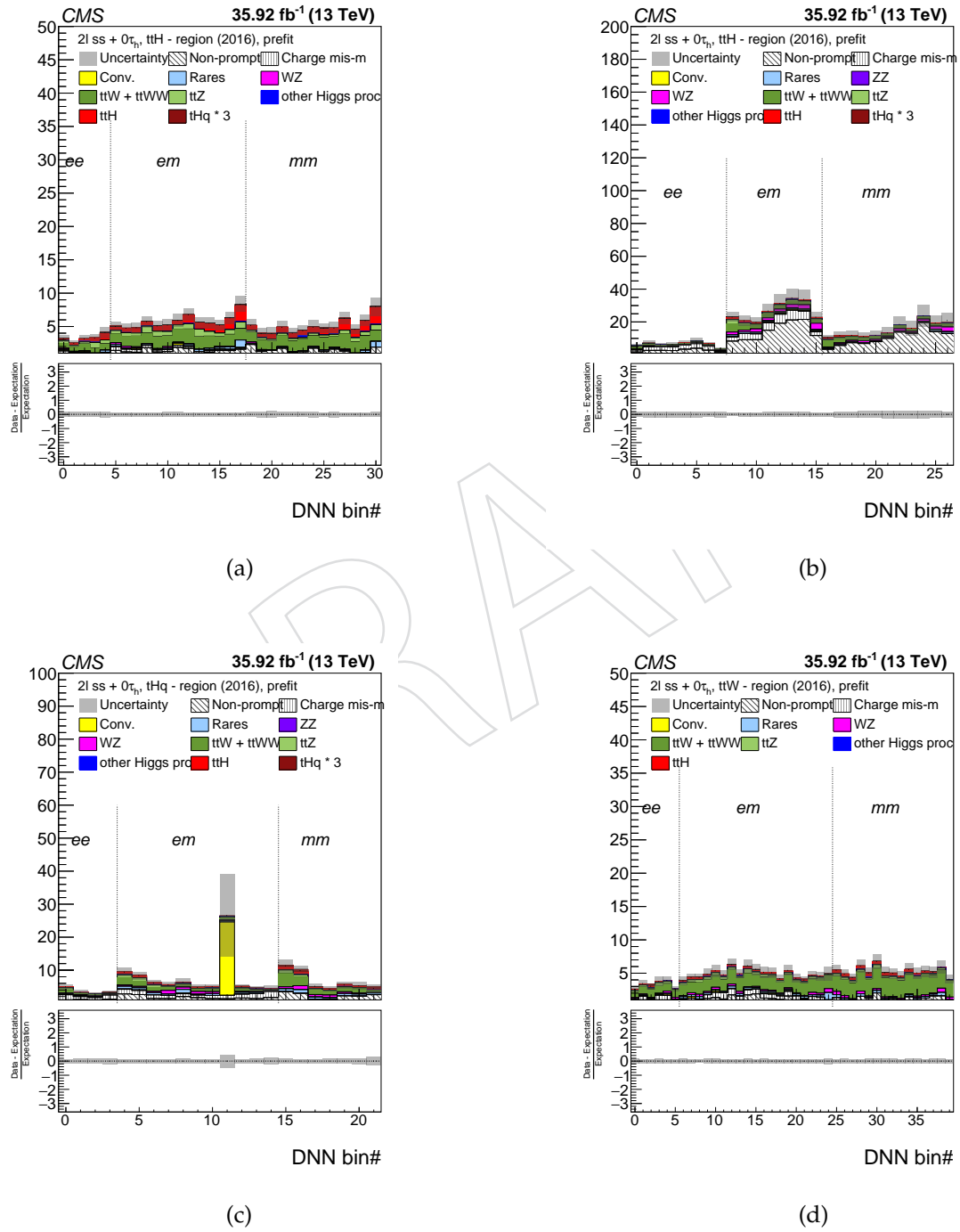


Figure 107: Distributions in the discriminating observables used for the signal extraction in the $2\ell ss + 0\tau_h$ category for the 2017 luminosity (a) the $t\bar{t}H$ – region, (b) the $t\bar{t}Z$ – region, (c) the BKG – region, and (d) the $t\bar{t}W$ – region. The post-fit rates and uncertainties are used. [PLACEHOLDER - PREFIT, BLINDED - THERE IS A BUG IN THE IMPLEMENTATION OF THE DNN WEIGHTS]

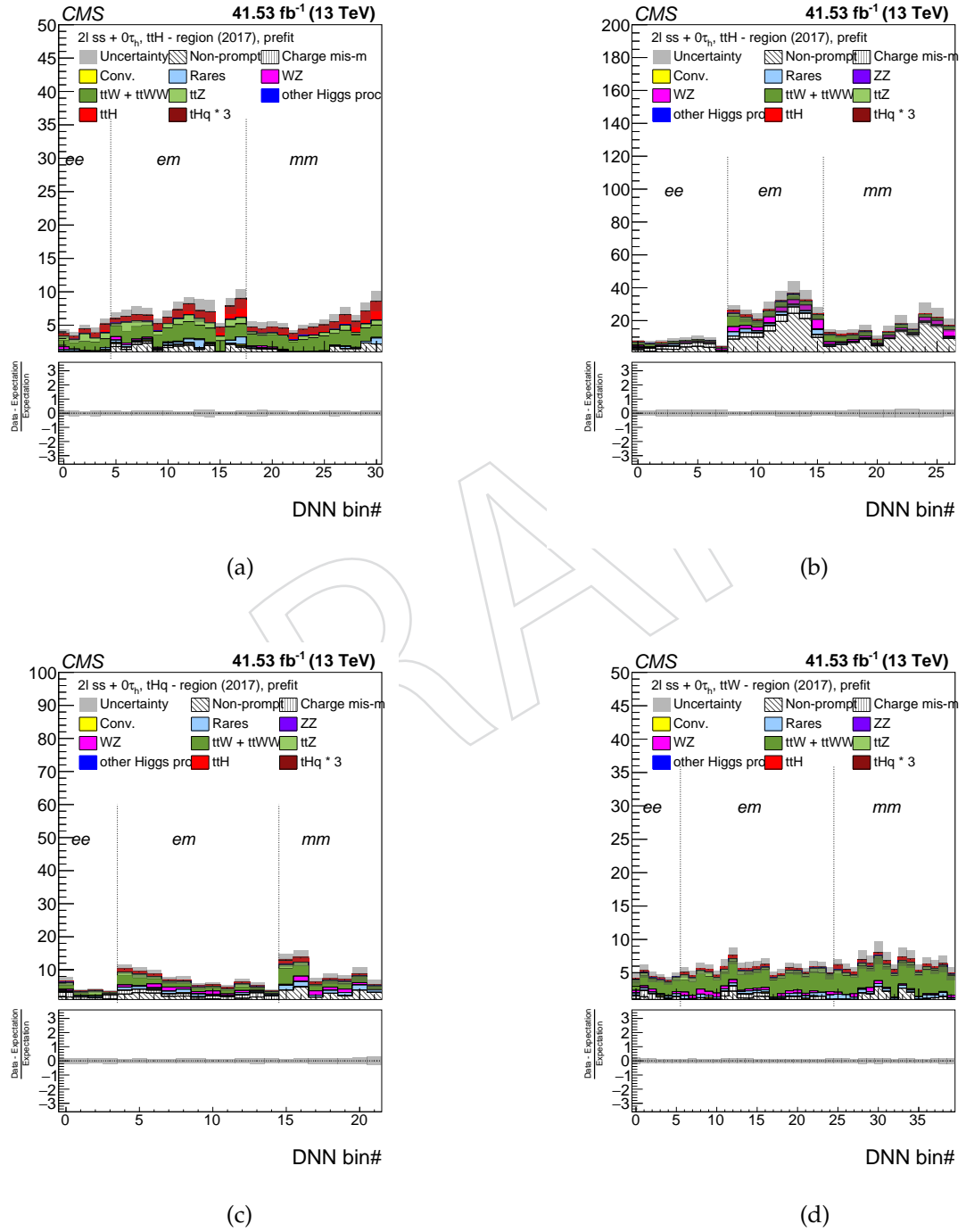


Figure 108: Distributions in the discriminating observables used for the signal extraction in the $2\ell ss + 0\tau_h$ category for the 2018 luminosity (a) the $t\bar{t}H$ – region, (b) the $t\bar{t}Z$ – region, (c) the BKG – region, and (d) the $t\bar{t}W$ – region. The post-fit rates and uncertainties are used. [PLACEHOLDER - PREFIT, BLINDED - THERE IS A BUG IN THE IMPLEMENTATION OF THE DNN WEIGHTS, MOSTLY AFFECTING THE THQ-NODE]

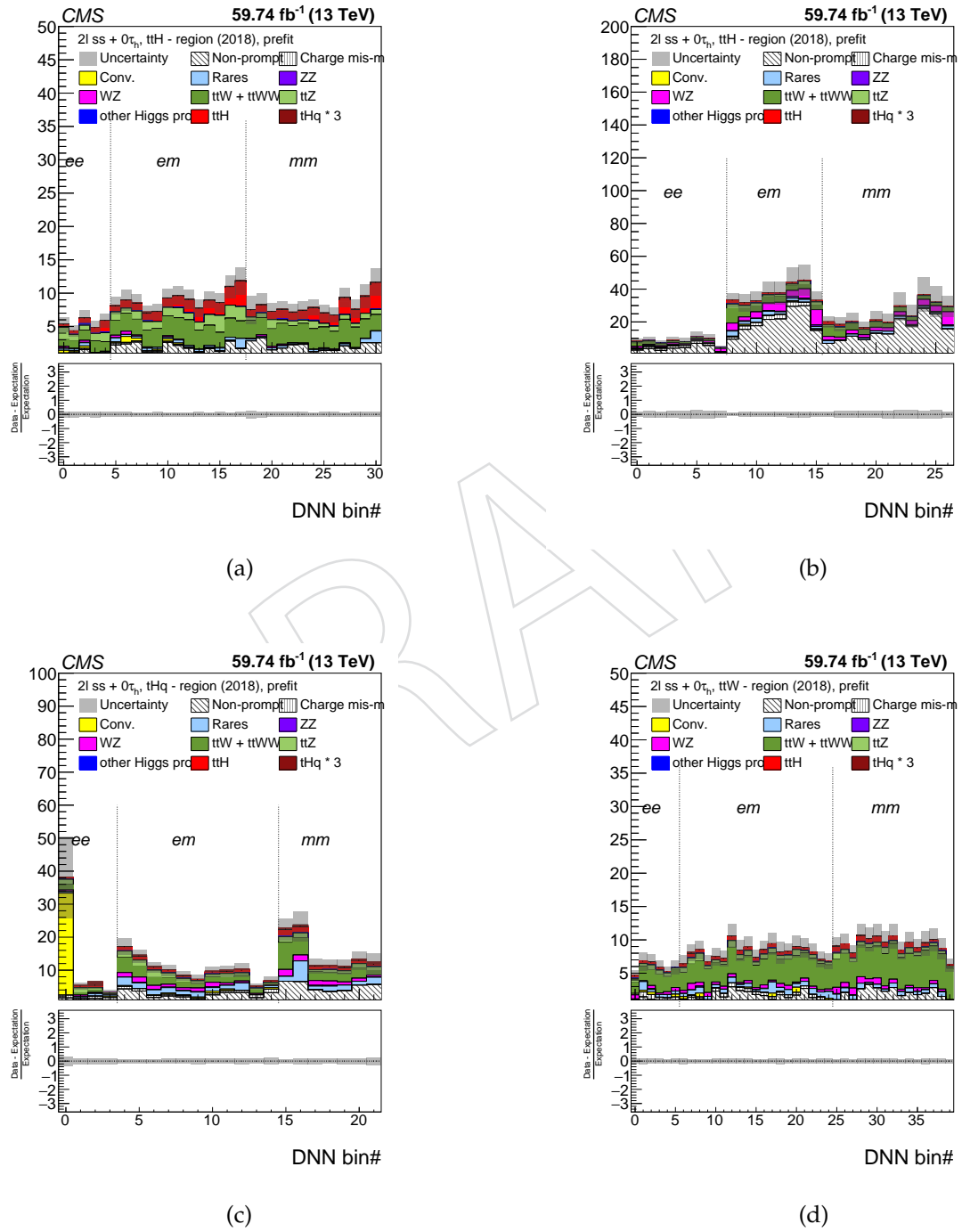


Table 59: The selected number of events in the signal regions extracted from BDT. The rates are obtained from the ML fit (post-fit). Uncertainties smaller than 0.05 are denoted by “ < 0.05 ”.

Category	$1\ell + 2\tau_h$	$2\ell os + 1\tau_h$	$1\ell + 1\tau_h$	$0\ell + 2\tau_h$	$3\ell + 1\tau_h$	$2\ell + 2\tau_h$	$4\ell + 0\tau_h$
$t\bar{t}H, H \rightarrow ZZ$	$X.X \pm X.X$	$X.X \pm X.X$	$X.X \pm X.X$	$X.X \pm X.X$	$X.X \pm X.X$	$X.X \pm X.X$	$X.X \pm X.X$
$t\bar{t}H, H \rightarrow WW$	\pm	\pm	\pm	\pm	\pm	\pm	\pm
$t\bar{t}H, H \rightarrow \tau\tau$	\pm	\pm	\pm	\pm	\pm	\pm	\pm
$t\bar{t}H, H \rightarrow \mu\mu$	\pm	\pm	\pm	\pm	\pm	\pm	\pm
$t\bar{t}H, H \rightarrow Z\gamma$	\pm	\pm	\pm	\pm	\pm	\pm	\pm
$t\bar{t}H$ (sum)	\pm						
tH	\pm						
WH	\pm						
ZH	\pm						
ggH (sum)	\pm						
$VBFH$ (sum)	\pm						
$t\bar{t}W$	\pm						
$t\bar{t}WW$	\pm						
$t\bar{t}W + ttWW$	\pm						
ZZ	\pm						
WZ	\pm						
DY	\pm						
$t\bar{t}Z$	\pm						
Misidentified	\pm						
Conversions	\pm						
signal flip	\pm						
Other	\pm						
SM expectation	\pm						
Observed data	\pm						

Figure 109: Distributions in the discriminating observables used for the signal extraction in the $3\ell + 0\tau_h$ category for the 2016 luminosity for (a) the $t\bar{t}H$ – region and (b) the $t\bar{t}H$ – region and (c) the BKG – region. The post-fit rates and uncertainties are used. [PLACEHOLDER - PREFIT, BLINDED - THE DNN WEIGHTS ARE GOING TO BE UPDATED]

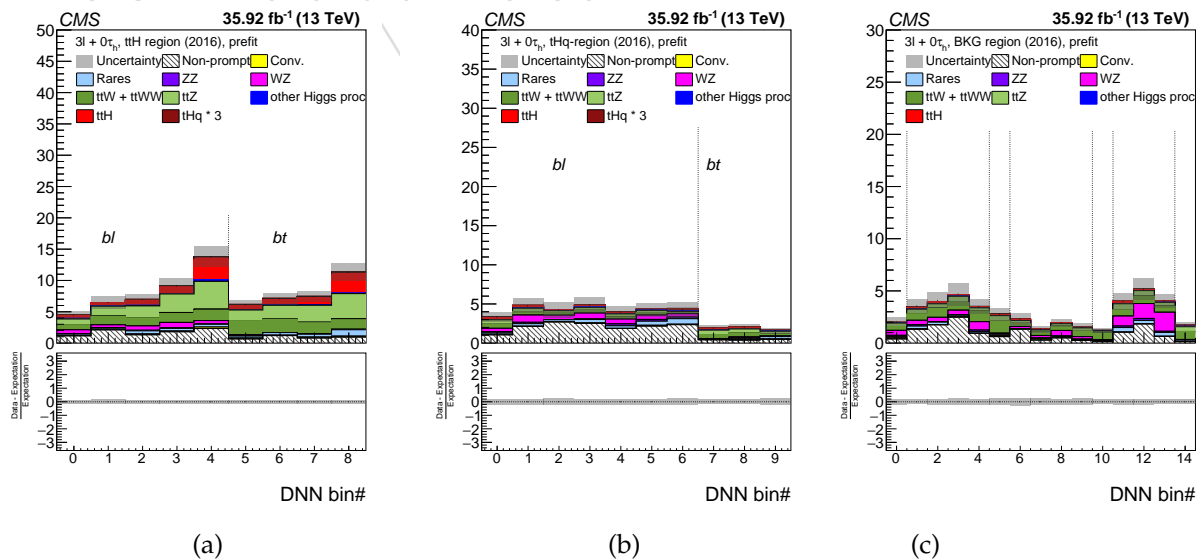


Figure 110: Distributions in the discriminating observables used for the signal extraction in the $3\ell + 0\tau_h$ category for the 2017 luminosity (a) the $t\bar{t}H$ – region and (b) the $t\bar{t}H$ – region and (c) the BKG – region. The post-fit rates and uncertainties are used. [PLACEHOLDER - PREFIT, BLINDED - THE DNN WEIGHTS ARE GOING TO BE UPDATED]

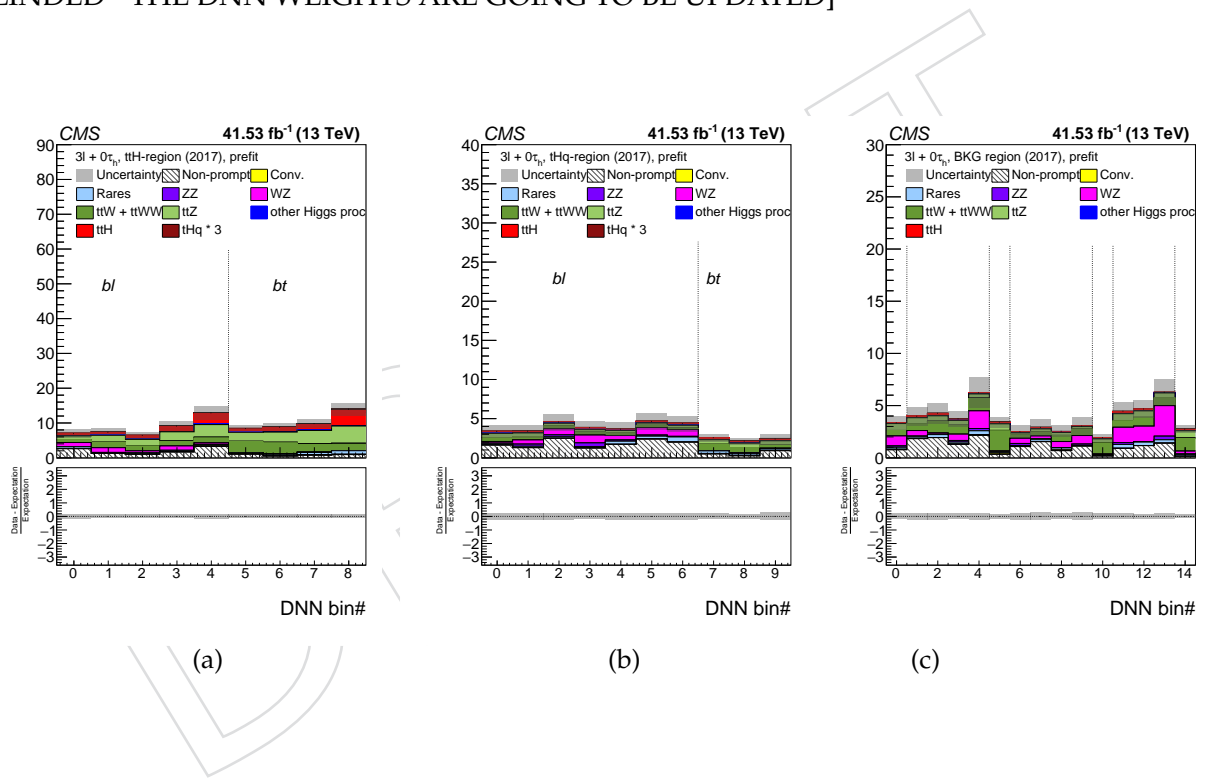


Figure 111: Distributions in the discriminating observables used for the signal extraction in the $3\ell + 0\tau_h$ category for the 2018 luminosity for (a) the $t\bar{t}H$ – region and (b) the $t\bar{t}H$ – region and (c) the BKG – region. The post-fit rates and uncertainties are used. [PLACEHOLDER - PREFIT, BLINDED - THE DNN WEIGHTS ARE GOING TO BE UPDATED]

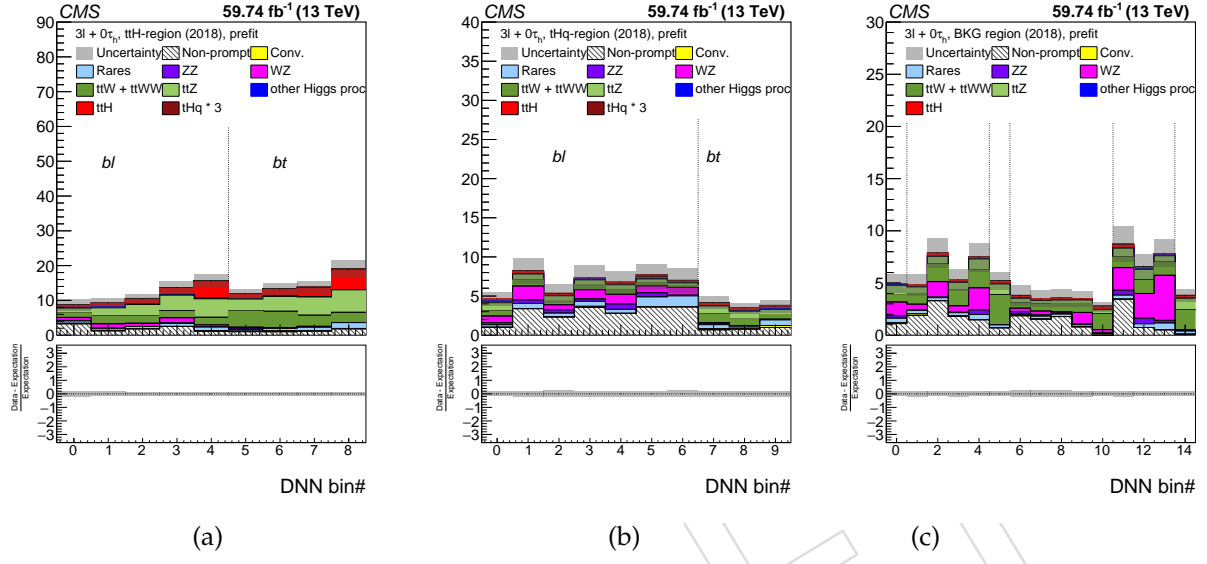


Figure 112: Distributions in the discriminating observables used for the signal extraction in the $2\ell ss + 1\tau_h$ category for the luminosity of 2016 era (a), 2017 era (b) and 2018 era (c). The post-fit rates and uncertainties are used. [PLACEHOLDER - PREFIT, BLINDED - THE DNN WEIGHTS ARE GOING TO BE UPDATED]

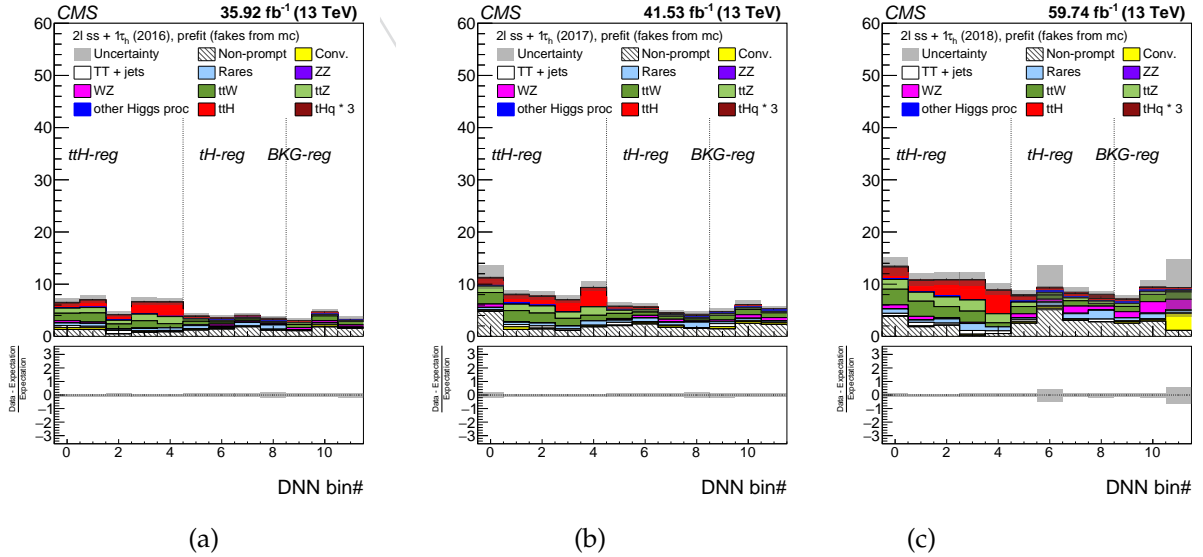


Figure 113: Distributions in the discriminating observables used for the signal extraction in the $0\ell + 2\tau_h$ category for the luminosity of 2016 era (a), 2017 era (b) and 2018 era (c). The post-fit rates and uncertainties are used. [PLACEHOLDER - PREFIT, BLINDED - CALCULATE IT WITH DATA DRIVEN FAKES ESTIMATION - REVISIT 0L_2TAU BINNING (EMPTY DY BINS IN SOME ERAS)]

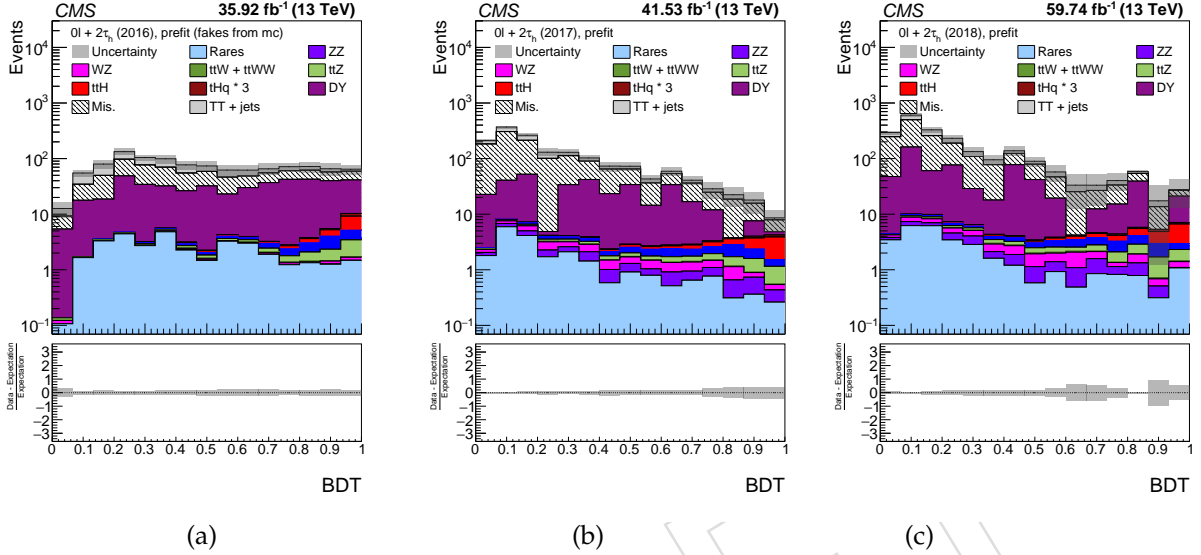


Figure 114: Distributions in the discriminating observables used for the signal extraction in the $1\ell + 2\tau_h$ category for the luminosity of 2016 era (a), 2017 era (b) and 2018 era (c). The post-fit rates and uncertainties are used. [PLACEHOLDER - PREFIT, BLINDED - CALCULATE IT WITH DATA DRIVEN FAKES ESTIMATION]

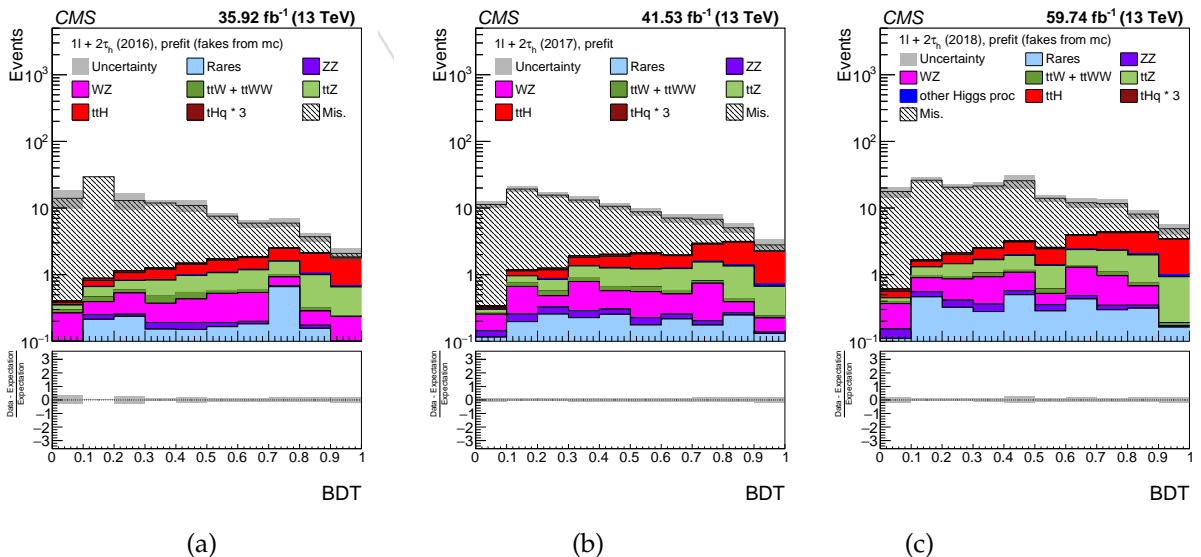


Figure 115: Distributions in the discriminating observables used for the signal extraction in the $1\ell + 1\tau_h$ category for the luminosity of 2016 era (a), 2017 era (b) and 2018 era (c). The post-fit rates and uncertainties are used. [PLACEHOLDER - PREFIT, BLINDED - CALCULATE IT WITH DATA DRIVEN FAKES ESTIMATION]

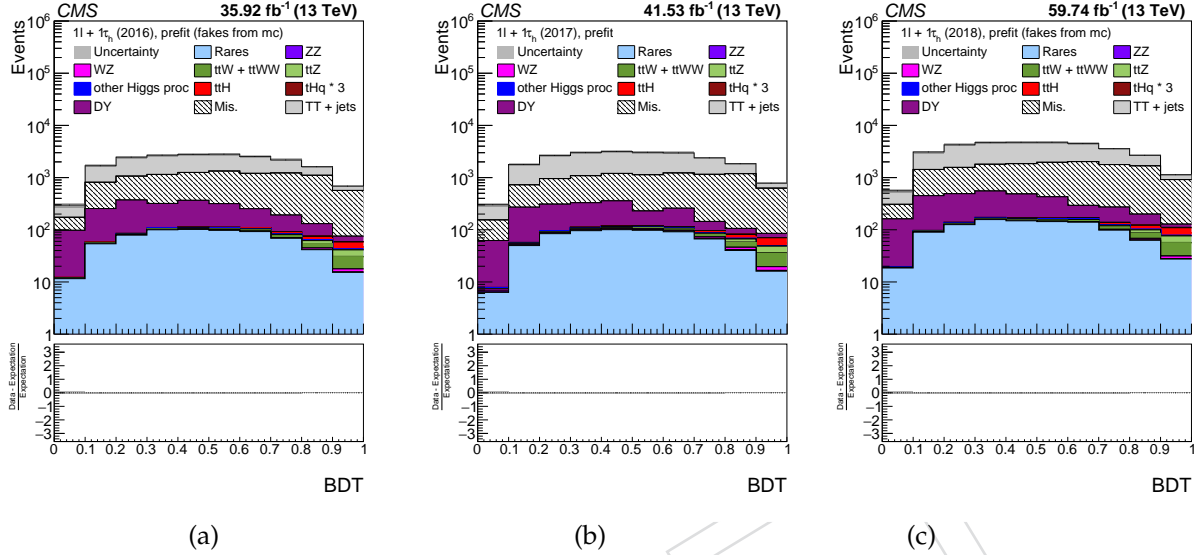


Figure 116: Distributions in the discriminating observables used for the signal extraction in the $2\ell_{\text{os}} + 1\tau_h$ category for the luminosity of 2016 era (a), 2017 era (b) and 2018 era (c). The post-fit rates and uncertainties are used. [PLACEHOLDER - PREFIT, BLINDED - CALCULATE IT WITH DATA DRIVEN FAKES ESTIMATION]

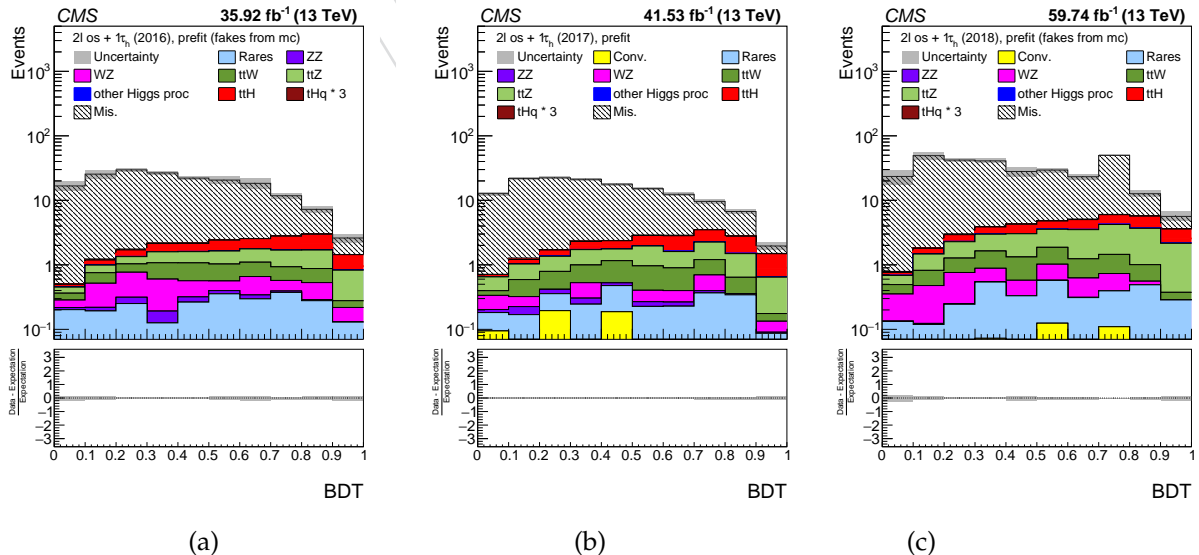


Figure 117: Distributions in the discriminating observables used for the signal extraction in the $2\ell + 2\tau_h$ category for the luminosity of 2016 era (a), 2017 era (b) and 2018 era (c).. The post-fit rates and uncertainties are used. [PLACEHOLDER - PREFIT, BLINDED - INCORPORATE TT+JETS TO THE TTZ COMPONENT]

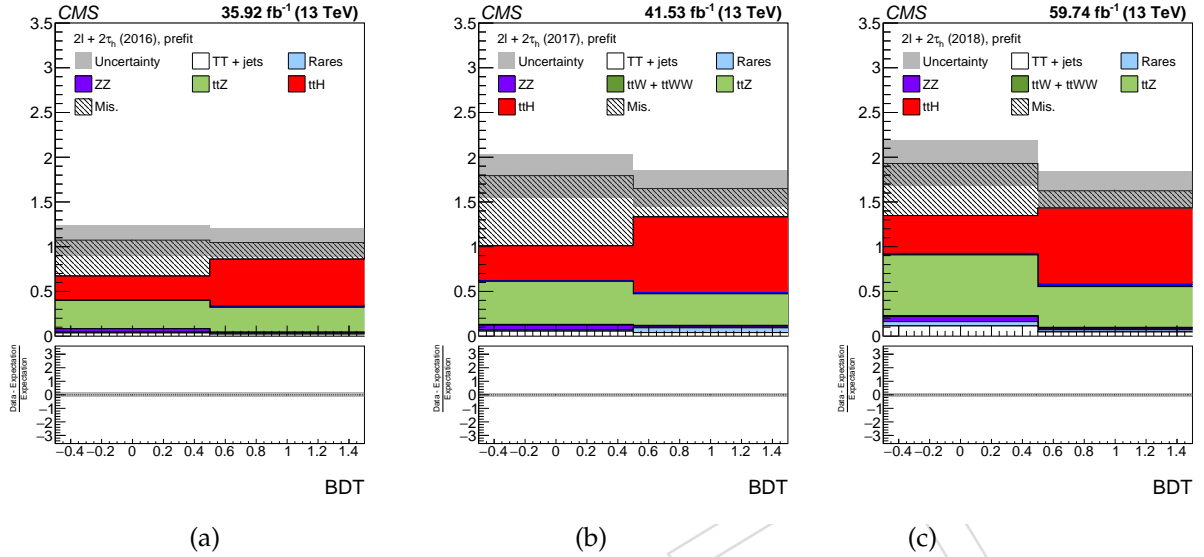


Figure 118: Distributions in the discriminating observables used for the signal extraction in the $3\ell + 1\tau_h$ category for the luminosity of 2016 era (a), 2017 era (b) and 2018 era (c).. The post-fit rates and uncertainties are used. [PLACEHOLDER - PREFIT, BLINDED - INCORPORATE TT+JETS TO THE TTZ COMPONENT]

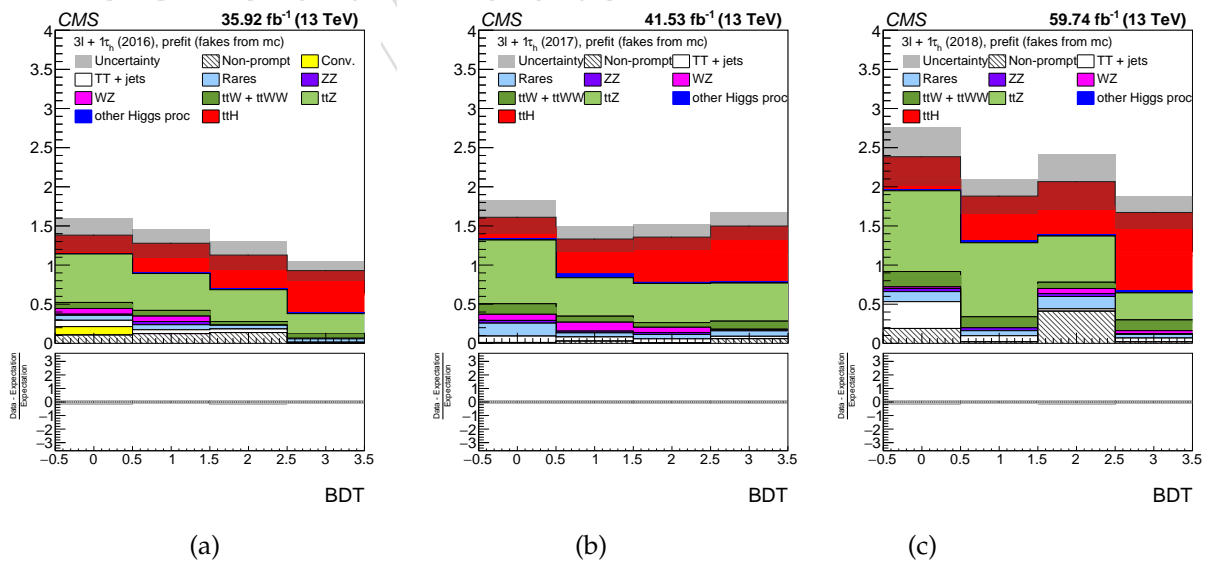


Figure 119: Distributions in the discriminating observables used for the signal extraction in the $4\ell + 0\tau_h$ category for the luminosity of 2016 era (a), 2017 era (b) and 2018 era (c). The post-fit rates and uncertainties are used. [PLACEHOLDER - PREFIT, BLINDED - INCORPORATE TT+JETS TO THE TTZ COMPONENT]

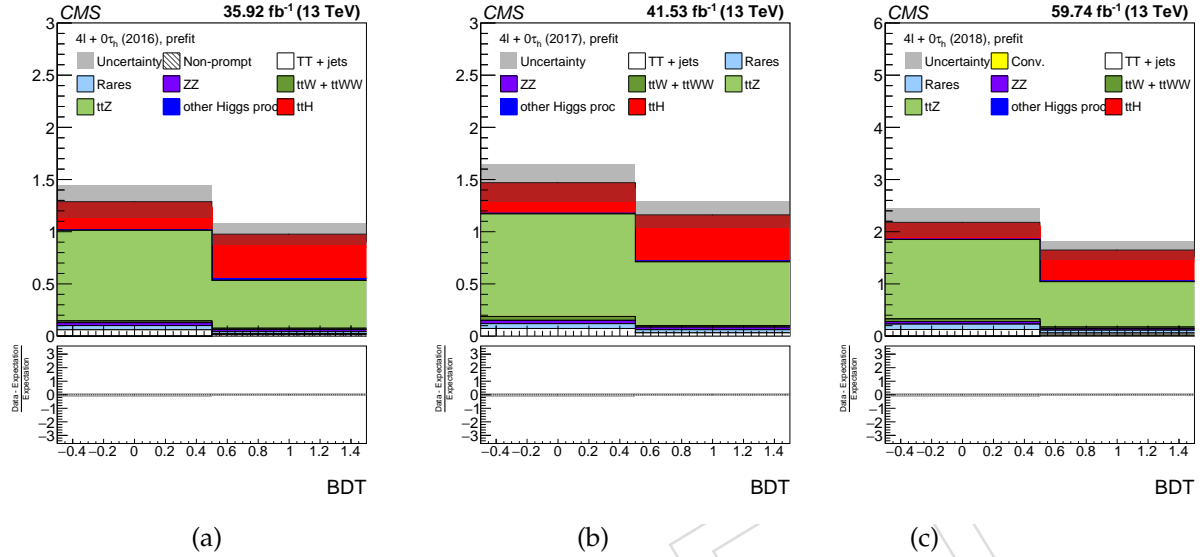


Figure 120: Distributions in the discriminating observables used for the signal extraction in the control regions 3ℓ -CR for the luminosity of 2016 era (a), 2017 era (b) and 2018 era (c).. The post-fit rates and uncertainties are used.

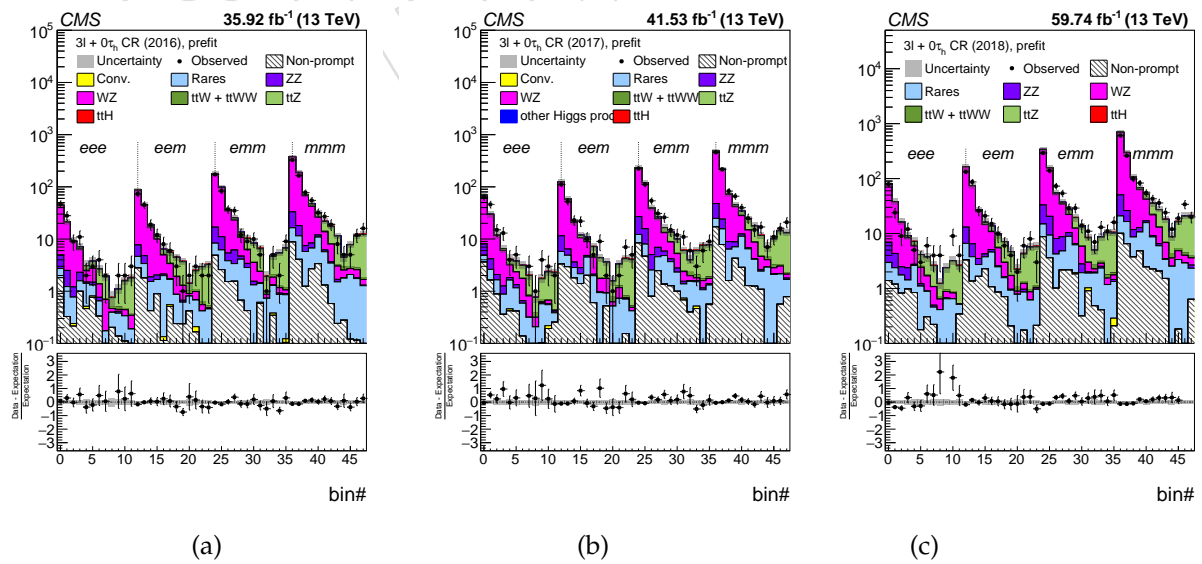
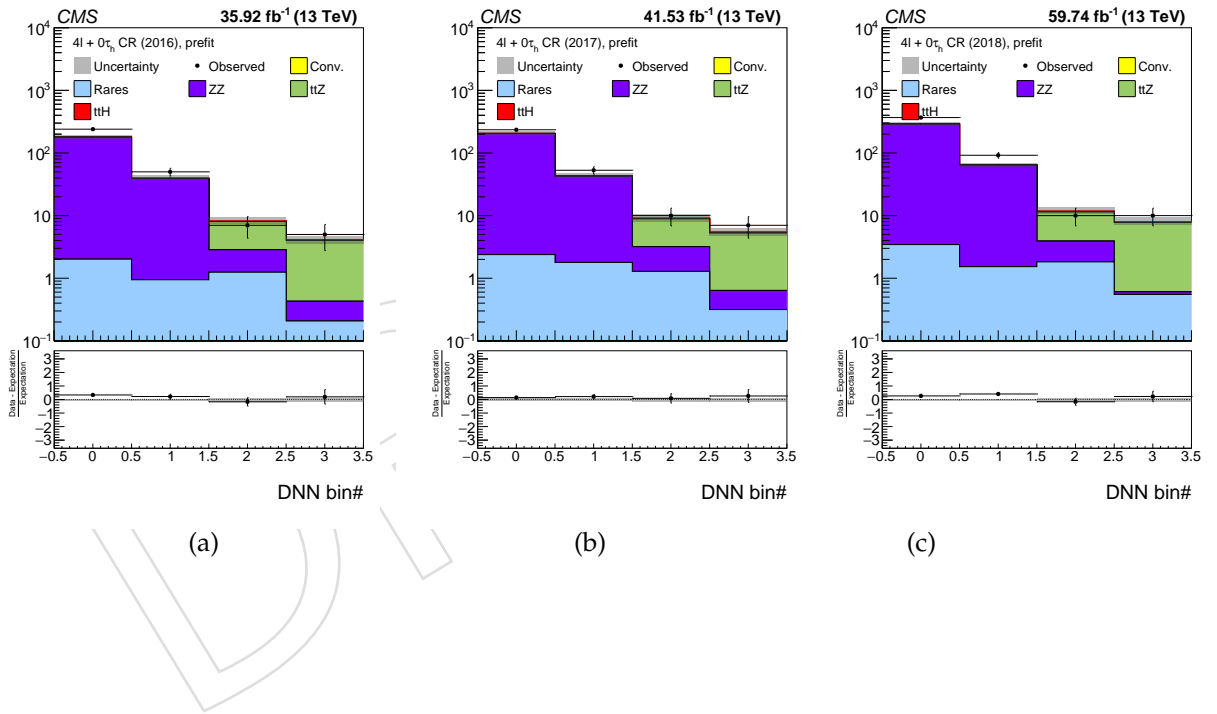


Figure 121: Distributions in the discriminating observables used for the signal extraction in the control regions 4ℓ -CR for the luminosity of 2016 era (a), 2017 era (b) and 2018 era (c).. The post-fit rates and uncertainties are used.



References

- [1] ATLAS Collaboration, "Observation of a new particle in the search for the Standard Model Higgs boson with the ATLAS detector at the LHC", *Phys. Lett.* **B 716** (2012) 1, doi:10.1016/j.physletb.2012.08.020, arXiv:1207.7214.
- [2] CMS Collaboration, "Observation of a new boson at a mass of 125 GeV with the CMS experiment at the LHC", *Phys. Lett.* **B 716** (2012) 30, doi:10.1016/j.physletb.2012.08.021, arXiv:1207.7235.
- [3] ATLAS, CMS Collaboration, "Combined measurement of the Higgs boson mass in pp collisions at $\sqrt{s} = 7$ and 8 TeV with the ATLAS and CMS experiments", *Phys. Rev. Lett.* **114** (2015) 191803, doi:10.1103/PhysRevLett.114.191803, arXiv:1503.07589.
- [4] CMS Collaboration, "Precise determination of the mass of the Higgs boson and tests of compatibility of its couplings with the standard model predictions using proton collisions at 7 and 8 TeV", *Eur. Phys. J.* **C75** (2015), no. 5, 212, doi:10.1140/epjc/s10052-015-3351-7, arXiv:1412.8662.
- [5] ATLAS, CDF, CMS, D0 Collaboration, "First combination of Tevatron and LHC measurements of the top-quark mass", arXiv:1403.4427.
- [6] B. A. Dobrescu and C. T. Hill, "Electroweak symmetry breaking via top condensation seesaw", *Phys. Rev. Lett.* **81** (1998) 2634–2637, doi:10.1103/PhysRevLett.81.2634, arXiv:hep-ph/9712319.
- [7] R. S. Chivukula, B. A. Dobrescu, H. Georgi, and C. T. Hill, "Top Quark Seesaw Theory of Electroweak Symmetry Breaking", *Phys. Rev.* **D59** (1999) 075003, doi:10.1103/PhysRevD.59.075003, arXiv:hep-ph/9809470.
- [8] D. Delepine, J. M. Gerard, and R. Gonzalez Felipe, "Is the standard Higgs scalar elementary?", *Phys. Lett.* **B372** (1996) 271–274, doi:10.1016/0370-2693(96)00048-2, arXiv:hep-ph/9512339.
- [9] LHC Higgs Cross Section Working Group Collaboration, "Handbook of LHC Higgs Cross Sections: 4. Deciphering the Nature of the Higgs Sector", doi:10.23731/CYRM-2017-002, arXiv:1610.07922.
- [10] F. Maltoni, G. Ridolfi, and M. Ubiali, "b-initiated processes at the LHC: a reappraisal", *JHEP* **07** (2012) 022, doi:10.1007/JHEP04(2013)095, 10.1007/JHEP07(2012)022, arXiv:1203.6393. [Erratum: JHEP04,095(2013)].
- [11] S. Biswas, E. Gabrielli, F. Margaroli, and B. Mele, "Direct constraints on the top-Higgs coupling from the 8 TeV LHC data", *JHEP* **07** (2013) 073, doi:10.1007/JHEP07(2013)073, arXiv:1304.1822.
- [12] B. Hespel, F. Maltoni, and E. Vryonidou, "Higgs and Z boson associated production via gluon fusion in the SM and the 2HDM", *JHEP* **06** (2015) 065, doi:10.1007/JHEP06(2015)065, arXiv:1503.01656.
- [13] CMS Collaboration, "Search for the associated production of the Higgs boson with a top-quark pair", *JHEP* **09** (2014) 087, doi:10.1007/JHEP09(2014)087, 10.1007/JHEP10(2014)106, arXiv:1408.1682. [Erratum: JHEP10,106(2014)].

- [14] ATLAS Collaboration, "Search for the Standard Model Higgs boson produced in association with top quarks and decaying into $b\bar{b}$ in pp collisions at $\sqrt{s} = 8$ TeV with the ATLAS detector", *Eur. Phys. J. C* **75** (2015), no. 7, 349, doi:10.1140/epjc/s10052-015-3543-1, arXiv:1503.05066.
- [15] ATLAS Collaboration, "Search for the Standard Model Higgs boson decaying into $b\bar{b}$ produced in association with top quarks decaying hadronically in pp collisions at $\sqrt{s} = 8$ TeV with the ATLAS detector", *JHEP* **05** (2016) 160, doi:10.1007/JHEP05(2016)160, arXiv:1604.03812.
- [16] ATLAS Collaboration, "Search for the associated production of the Higgs boson with a top quark pair in multilepton final states with the ATLAS detector", *Phys. Lett. B* **749** (2015) 519, doi:10.1016/j.physletb.2015.07.079, arXiv:1506.05988.
- [17] ATLAS Collaboration, "Search for $H \rightarrow \gamma\gamma$ produced in association with top quarks and constraints on the Yukawa coupling between the top quark and the Higgs boson using data taken at 7 TeV and 8 TeV with the ATLAS detector", *Phys. Lett. B* **740** (2015) 222, doi:10.1016/j.physletb.2014.11.049, arXiv:1409.3122.
- [18] CMS Collaboration, "Measurements of properties of the Higgs boson decaying into the four-lepton final state in pp collisions at $\sqrt{s} = 13$ TeV", *JHEP* **11** (2017) 047, doi:10.1007/JHEP11(2017)047, arXiv:1706.09936.
- [19] ATLAS Collaboration, "Evidence for the associated production of the Higgs boson and a top quark pair with the ATLAS detector", *Phys. Rev. D* **97** (2018), no. 7, 072003, doi:10.1103/PhysRevD.97.072003, arXiv:1712.08891.
- [20] ATLAS Collaboration, "Search for the standard model Higgs boson produced in association with top quarks and decaying into a $b\bar{b}$ pair in pp collisions at $\sqrt{s} = 13$ TeV with the ATLAS detector", *Phys. Rev. D* **97** (2018), no. 7, 072016, doi:10.1103/PhysRevD.97.072016, arXiv:1712.08895.
- [21] CMS Collaboration, "Evidence for associated production of a Higgs boson with a top quark pair in final states with electrons, muons, and hadronically decaying τ leptons at $\sqrt{s} = 13$ TeV", *JHEP* **08** (2018) 066, doi:10.1007/JHEP08(2018)066, arXiv:1803.05485.
- [22] CMS Collaboration, "Search for $t\bar{t}H$ production in the all-jet final state in proton-proton collisions at $\sqrt{s} = 13$ TeV", *JHEP* **06** (2018) 101, doi:10.1007/JHEP06(2018)101, arXiv:1803.06986.
- [23] CMS Collaboration, "Measurements of Higgs boson properties in the diphoton decay channel in proton-proton collisions at $\sqrt{s} = 13$ TeV", *JHEP* **11** (2018) 185, doi:10.1007/JHEP11(2018)185, arXiv:1804.02716.
- [24] CMS Collaboration, "Search for $t\bar{t}H$ production in the $H \rightarrow b\bar{b}$ decay channel with leptonic $t\bar{t}$ decays in proton-proton collisions at $\sqrt{s} = 13$ TeV", *JHEP* **03** (2019) 026, doi:10.1007/JHEP03(2019)026, arXiv:1804.03682.
- [25] CMS Collaboration, "Observation of $t\bar{t}H$ production", *Phys. Rev. Lett.* **120** (2018), no. 23, 231801, doi:10.1103/PhysRevLett.120.231801, arXiv:1804.02610.
- [26] ATLAS Collaboration, "Observation of Higgs boson production in association with a top quark pair at the LHC with the ATLAS detector", *Phys. Lett. B* **784** (2018) 173–191, doi:10.1016/j.physletb.2018.07.035, arXiv:1806.00425.

- [2403] [27] CMS Collaboration, "Search for the associated production of a Higgs boson with a
 2404 single top quark in proton-proton collisions at $\sqrt{s} = 8$ TeV", *JHEP* **06** (2016) 177,
 2405 doi:10.1007/JHEP06(2016)177, arXiv:1509.08159.
- [2406] [28] CMS Collaboration, "Search for associated production of a Higgs boson and a single top
 2407 quark in proton-proton collisions at $\sqrt{s} = 13$ TeV", *Phys. Rev.* **D99** (2019), no. 9, 092005,
 2408 doi:10.1103/PhysRevD.99.092005, arXiv:1811.09696.
- [2409] [29] A. Hocker et al., "TMVA - toolkit for multivariate data analysis", *PoS ACAT* (2007) 040,
 2410 arXiv:physics/0703039.
- [2411] [30] T. Chen and C. Guestrin, "XGBoost: A scalable tree boosting system", *CoRR*
 2412 **abs/1603.02754** (2016) arXiv:1603.02754.
- [2413] [31] F. Pedregosa et al., "Scikit-learn: Machine learning in python", *Journal of Machine*
 2414 *Learning Research* **12** (2011) 2825.
- [2415] [32] K. Kondo, "Dynamical likelihood method for reconstruction of events with missing
 2416 momentum. 1: method and toy models", *J. Phys. Soc. Jap.* **57** (1988) 4126–4140,
 2417 doi:10.1143/JPSJ.57.4126.
- [2418] [33] K. Kondo, "Dynamical likelihood method for reconstruction of events with missing
 2419 momentum. 2: mass spectra for $2 \rightarrow 2$ processes", *J. Phys. Soc. Jap.* **60** (1991) 836–844,
 2420 doi:10.1143/JPSJ.60.836.
- [2421] [34] Software guide PhysicsTools Collaboration.
 2422 <https://twiki.cern.ch/twiki/bin/view/CMSPublic/SWGuideGoodLumiSectionsJSONFile>.
- [2423] [35] J. Alwall et al., "The automated computation of tree-level and next-to-leading order
 2424 differential cross sections, and their matching to parton shower simulations", *JHEP* **07**
 2425 (2014) 079, doi:10.1007/JHEP07(2014)079, arXiv:1405.0301.
- [2426] [36] P. Nason, "A new method for combining NLO QCD with shower Monte Carlo
 2427 algorithms", *JHEP* **11** (2004) 040, doi:10.1088/1126-6708/2004/11/040,
 2428 arXiv:hep-ph/0409146.
- [2429] [37] S. Frixione, P. Nason, and C. Oleari, "Matching NLO QCD computations with parton
 2430 shower simulations: the POWHEG method", *JHEP* **11** (2007) 070,
 2431 doi:10.1088/1126-6708/2007/11/070, arXiv:0709.2092.
- [2432] [38] S. Alioli, P. Nason, C. Oleari, and E. Re, "A general framework for implementing NLO
 2433 calculations in shower Monte Carlo programs: the POWHEG BOX", *JHEP* **06** (2010)
 2434 043, doi:10.1007/JHEP06(2010)043, arXiv:1002.2581.
- [2435] [39] CMS Collaboration, "Event generator tunes obtained from underlying event and
 2436 multiparton scattering measurements", arXiv:1512.00815.
- [2437] [40] C. Diez and M. Seidel, "Powheg+Pythia8 $t\bar{t}$: tuning α_S^{ISR} and h_{damp} ".
 2438 https://indico.cern.ch/event/567994/contributions/2299854/attachments/1336057/2009649/tt_tuning
- [2439] [41] CMS Collaboration, "Extraction and validation of a new set of CMS PYTHIA8 tunes
 2440 from underlying event measurements", *CMS Analysis Note* **2017/001** (2019).
- [2441] [42] P. Skands, S. Carrazza, and J. Rojo, "Tuning PYTHIA 8.1: the Monash 2013 tune",
 2442 *Eur. Phys. J.* **C 74** (2014), no. 8, 3024, doi:10.1140/epjc/s10052-014-3024-y,
 2443 arXiv:1404.5630.

- [43] NNPDF Collaboration, "Parton distributions with QED corrections", *Nucl. Phys.* **B** **877** (2013) 290, doi:10.1016/j.nuclphysb.2013.10.010, arXiv:1308.0598.
- [44] NNPDF Collaboration, "Parton distributions for the LHC Run II", *JHEP* **04** (2015) 040, doi:10.1007/JHEP04(2015)040, arXiv:1410.8849.
- [45] NNPDF Collaboration, "Parton distributions from high-precision collider data", *Eur. Phys. J.* **C77** (2017), no. 10, 663, doi:10.1140/epjc/s10052-017-5199-5, arXiv:1706.00428.
- [46] K. Melnikov and F. Petriello, "Electroweak gauge boson production at hadron colliders through $O(\alpha_s^2)$ ", *Phys. Rev.* **D** **74** (2006) 114017, doi:10.1103/PhysRevD.74.114017, arXiv:hep-ph/0609070.
- [47] M. Czakon and A. Mitov, "Top++: A program for the calculation of the top-pair cross section at hadron colliders", *Comput. Phys. Commun.* **185** (2014) 2930, doi:10.1016/j.cpc.2014.06.021, arXiv:1112.5675.
- [48] CMS Collaboration.
https://indico.cern.ch/event/746829/contributions/3138541/attachments/1717905/2772129/Drell-Yan_jets_crosssection.pdf.
- [49] T. Seva et al., "Measurement of the differential cross section of Z bosons produced in association with jets in pp collisions at $\sqrt{s} = 8$ TeV", *CMS Analysis Note* **2013/049** (2013).
- [50] Kant, P. and Kind, O. M. and Kintscher, T. and Lohse, T. and Martini, T. and Mölbitz, S. and Rieck, P. and Uwer, P., "HATHOR for single top-quark production: Updated predictions and uncertainty estimates for single top-quark production in hadronic collisions", *Comput. Phys. Commun.* **191** (2015) 74, doi:10.1016/j.cpc.2015.02.001, arXiv:1406.4403.
- [51] M. Aliev et al., "HATHOR: HAdronic Top and Heavy quarks crOss section calculatoR", *Comput. Phys. Commun.* **182** (2011) 1034–1046, doi:10.1016/j.cpc.2010.12.040, arXiv:1007.1327.
- [52] N. Kidonakis, "Two-loop soft anomalous dimensions for single top quark associated production with a W^- or H^- ", *Phys. Rev.* **D** **82** (2010) 054018, doi:10.1103/PhysRevD.82.054018, arXiv:1005.4451.
- [53] CMS Collaboration.
<https://twiki.cern.ch/twiki/bin/view/LHCPhysics/CERNYellowReportPageBR>.
- [54] CMS Collaboration.
<https://twiki.cern.ch/twiki/bin/view/LHCPhysics/CERNYellowReportPageAt13TeV>.
- [55] CMS Collaboration.
<https://twiki.cern.ch/twiki/bin/view/CMS/SummaryTable1G25ns>.
- [56] CMS Collaboration.
<https://twiki.cern.ch/twiki/bin/view/LHCPhysics/SingleTopRefXsec>.
- [57] CMS Collaboration.
<https://twiki.cern.ch/twiki/bin/view/CMS/HowToGenXSecAnalyzer>.

- [2483] [58] PDG Collaboration.
 2484 <http://pdglive.lbl.gov/BranchingRatio.action?design=8&parCode=S043>.
- [2485] [59] CMS Collaboration.
 2486 https://indico.cern.ch/event/448517/contributions/1943045/attachments/1164999/1679225/Long_G
- [2487] [60] CMS Collaboration.
 2488 <https://twiki.cern.ch/twiki/bin/view/LHCPhysics/LHCHXSWGHH?rev=48>.
- [2489] [61] CMS Collaboration. <https://twiki.cern.ch/twiki/bin/view/LHCPhysics/TtbarNNLO>.
- [2490] [62] CMS Collaboration.
 2491 <https://indico.cern.ch/event/841566/contributions/3565385/attachments/1914850/3185933/Drell->
 2492 Yan_jets_crossection_September2019_update.pdf.
- [2493] [63] GEANT4 Collaboration, “GEANT4—a simulation toolkit”, *Nucl. Instrum. Meth. A* **506**
 2494 (2003) 250, doi:10.1016/S0168-9002(03)01368-8.
- [2495] [64] CMS Collaboration, “Particle-flow event reconstruction in CMS and performance for
 2496 jets, taus, and E_T^{miss} ”, CMS Physics Analysis Summary CMS-PAS-PFT-09-001, 2009.
- [2497] [65] CMS Collaboration, “Commissioning of the particle-flow event reconstruction with the
 2498 first LHC collisions recorded in the CMS detector”, CMS Physics Analysis Summary
 2499 CMS-PAS-PFT-10-001, 2010.
- [2500] [66] CMS Collaboration, “Commissioning of the particle-flow reconstruction in
 2501 minimum-bias and jet events from pp collisions at 7 TeV”, CMS Physics Analysis
 2502 Summary CMS-PAS-PFT-10-002, 2010.
- [2503] [67] CMS Collaboration, “Particle-flow commissioning with muons and electrons from
 2504 $J/\psi(1S)$ and W events at 7 TeV”, CMS Physics Analysis Summary
 2505 CMS-PAS-PFT-10-003, 2010.
- [2506] [68] CMS Collaboration, “Particle-flow reconstruction and global event description with the
 2507 CMS detector”, *JINST* **12** (2017), no. 10, P10003,
 2508 doi:10.1088/1748-0221/12/10/P10003, arXiv:1706.04965.
- [2509] [69] CMS Collaboration, “Performance of electron reconstruction and selection with the
 2510 CMS detector in pp collisions at $\sqrt{s} = 8$ TeV”, *JINST* **10** (2015) P06005,
 2511 doi:10.1088/1748-0221/10/06/P06005, arXiv:1502.02701.
- [2512] [70] EGamma POG Collaboration.
 2513 <https://twiki.cern.ch/twiki/bin/view/CMS/MultivariateElectronIdentificationRun2#Recommended>.
- [2514] [71] CMS Collaboration, “Performance of CMS muon reconstruction in pp collision events at
 2515 $\sqrt{s} = 7$ TeV”, *JINST* **7** (2012) P10002, doi:10.1088/1748-0221/7/10/P10002,
 2516 arXiv:1206.4071.
- [2517] [72] Muon POG Collaboration.
 2518 https://twiki.cern.ch/twiki/bin/view/CMS/SWGuideMuonIdRun2#Medium_Muon.
- [2519] [73] M. Cacciari, G. P. Salam, and G. Soyez, “The catchment area of jets”, *JHEP* **04** (2008)
 2520 005, doi:10.1088/1126-6708/2008/04/005, arXiv:0802.1188.
- [2521] [74] M. Cacciari and G. P. Salam, “Pileup subtraction using jet areas”, *Phys. Lett. B* **659**
 2522 (2008) 119, doi:10.1016/j.physletb.2007.09.077, arXiv:0707.1378.

- 2523 [75] CMS Collaboration, "Search for $t\bar{t}H$ production in multilepton final states at
2524 $\sqrt{s} = 13$ TeV", CMS Physics Analysis Summary CMS-PAS-HIG-15-008, 2015.
- 2525 [76] CMS Collaboration, "Search for associated production of Higgs bosons and top quarks
2526 in multilepton final states at $\sqrt{s} = 13$ TeV", CMS Physics Analysis Summary
2527 CMS-PAS-HIG-16-022, 2016.
- 2528 [77] C. Mueller et al., "Search for ttH in multilepton final states with 2016 data", CMS
2529 *Analysis Note* **2016/211** (2016).
- 2530 [78] CMS Collaboration, "Reconstruction and identification of τ lepton decays to hadrons
2531 and ν_τ at CMS", *JINST* **11** (2016), no. 01, P01019,
2532 doi:10.1088/1748-0221/11/01/P01019, arXiv:1510.07488.
- 2533 [79] CMS Collaboration, "Performance of reconstruction and identification of τ leptons in
2534 their decays to hadrons and ν_τ in LHC Run 2", CMS Physics Analysis Summary
2535 CMS-PAS-TAU-16-002, 2016.
- 2536 [80] Perez, E. and Steggemann, J. and Takahashi, Y. and Veelken, C., "Improved τ
2537 identification algorithm for LHC Run 2", *CMS Analysis Note* **2015/083** (2015).
- 2538 [81] Tau POG.
2539 <https://twiki.cern.ch/twiki/bin/viewauth/CMS/TauIDRecommendation13TeV>.
- 2540 [82] M. Cacciari, G. P. Salam, and G. Soyez, "The anti- k_T jet clustering algorithm", *JHEP* **04**
2541 (2008) 063, doi:10.1088/1126-6708/2008/04/063, arXiv:0802.1189.
- 2542 [83] JetMET POG. <https://twiki.cern.ch/twiki/bin/view/CMS/JetID13TeVRun2017>.
- 2543 [84] CMS Collaboration, "Determination of jet energy calibration and transverse momentum
2544 resolution in CMS", *JINST* **6** (2011) P11002,
2545 doi:10.1088/1748-0221/6/11/P11002, arXiv:1107.4277.
- 2546 [85] CMS Collaboration, "Identification of b quark jets with the CMS experiment", *JINST* **8**
2547 (2013) P04013, doi:10.1088/1748-0221/8/04/P04013, arXiv:1211.4462.
- 2548 [86] CMS Collaboration, "Identification of heavy-flavour jets with the CMS detector in pp
2549 collisions at 13 TeV", *Submitted to JINST* (2017) arXiv:1712.07158.
- 2550 [87] BTV POG Collaboration.
2551 <https://twiki.cern.ch/twiki/bin/viewauth/CMS/BtagRecommendation94X>.
- 2552 [88] CMS Collaboration, "Performance of the CMS missing transverse momentum
2553 reconstruction in pp data at $\sqrt{s} = 8$ TeV", *JINST* **10** (2015), no. 02, P02006,
2554 doi:10.1088/1748-0221/10/02/P02006, arXiv:1411.0511.
- 2555 [89] JetMET POG Collaboration.
2556 https://twiki.cern.ch/twiki/bin/view/CMSPublic/SWGuidePATTools#MET_Systematics_Tools.
- 2557 [90] JetMET POG.
2558 https://twiki.cern.ch/twiki/bin/view/CMS/MissingETOptionalFiltersRun2#MET_Filter_Recommenda
- 2559 [91] A. Tiko.
2560 <https://indico.cern.ch/event/606232/contributions/2444209/attachments/1398539/2133074/chargef>

- [92] Particle Data Group, "Review of particle physics", *Chin. Phys. C* **40** (2016) 100001,
doi:10.1088/1674-1137/40/10/100001.
- [93] CMS Collaboration, "Measurements of properties of the Higgs boson decaying into the four-lepton final state in pp collisions at $\sqrt{s} = 13$ TeV", *JHEP* **11** (2017) 047,
doi:10.1007/JHEP11(2017)047, arXiv:1706.09936.
- [94] M. Hildreth.
https://twiki.cern.ch/twiki/bin/viewauth/CMS/PdmVPileUpDescription#Reweighting_Method.
- [95] P. Group. <https://twiki.cern.ch/twiki/bin/view/CMS/PileupJSONFileforData>.
- [96] C. Palmer.
<https://hypernews.cern.ch/HyperNews/CMS/get/luminosity/613/2/1/1/1.html>.
- [97] T. Boccali et al.
<https://indico.cern.ch/event/695872/contributions/2877123/attachments/1593469/2522749/pileup.pdf>
- [98] A. Raspereza and V. Botta. <https://github.com/CMS-HTT/LeptonEfficiencies>.
- [99] J. Berryhill, V. Halyo, A. Hunt, and K. Mishra, "Generic Tag and Probe tool for measuring efficiency at CMS with early data", *CMS Analysis Note* **2009/111** (2009).
- [100] L. Wezenbeek.
<https://indico.cern.ch/event/824099/contributions/3446487/attachments/1855016/3046461/2016Leg.pdf>
- [101] T. Ruggles and H. Sert.
<https://indico.cern.ch/event/799374/contributions/3323191/attachments/1797874/2931826/TauTrig.pdf>
- [102] K. Androsov and H. Sert.
<https://indico.cern.ch/event/820066/contributions/3430600/attachments/1843348/3023303/TauTrig.pdf>
- [103] Bloch, D. and others, "Search for $t\bar{t}H$ in multilepton final states with the full 2016 dataset", *CMS Analysis Note* **2017/029** (2017).
- [104] J. Bechtel et al., "Tau reconstruction and performance using the 2016 dataset", *CMS Analysis Note* **2017/094** (2017).
- [105] Y. Takahashi, I. Neutelings, and C. Galloni.
https://indico.cern.ch/event/763206/contributions/3170631/attachments/1730040/2795667/Izaak_Tau.pdf
- [106] Y. Takahashi, I. Neutelings, and C. Galloni.
https://indico.cern.ch/event/806425/contributions/3360023/attachments/1813804/2963629/Izaak_Tau.pdf
- [107] BTV POG Collaboration.
<https://twiki.cern.ch/twiki/bin/view/CMS/BTagSFMethods>.
- [108] BTV POG Collaboration.
<https://twiki.cern.ch/twiki/bin/view/CMS/BtagRecommendation>.
- [109] M. Marionneau and C. Veelken, "Study of E_T^{miss} performance in events containing one Z boson decaying into two muons in 2012 data", *CMS Analysis Note* **2012/333** (2012).
- [110] CMS Collaboration, "Performance of missing energy reconstruction in 13 TeV pp collision data using the CMS detector", CMS Physics Analysis Summary CMS-PAS-JME-16-004, 2016.

- 2599 [111] Petyt, D. A. and Zghiche, A. Collaboration.
2600 <https://indico.cern.ch/event/726510/contributions/3012698/attachments/1654740/2648394/ecaltp.pdf>
- 2601 [112] Thomas, L. Collaboration.
2602 <https://twiki.cern.ch/twiki/bin/viewauth/CMS/L1ECALPrefiringWeightRecipe>.
- 2603 [113] Thomas, L. Collaboration.
2604 <https://indico.cern.ch/event/764279/contributions/3175800/attachments/1734412/2811545/prefiring.pdf>
- 2605 [114] CMS TOP POG Collaboration.
2606 <https://twiki.cern.ch/twiki/bin/viewauth/CMS/TopPtReweighting>.
- 2607 [115] A. Brinkerhoff et al., "Search for the standard model Higgs boson produced in
2608 association with top quarks and decaying to leptons", *CMS Analysis Note* **2013/159**
2609 (2013).
- 2610 [116] B. Stieger et al., "Search for ttH in multilepton final states at 13 TeV", *CMS Analysis Note*
2611 **2015/321** (2016).
- 2612 [117] Conway, J. and Friis, E. K. and Veelken, C., "Estimation of background contributions to
2613 τ analyses via fake-rate technique", *CMS Analysis Note* **2010/074** (2010).
- 2614 [118] JetMET POG.
2615 <https://twiki.cern.ch/twiki/bin/view/CMSPublic/WorkBookJetEnergyCorrections>.
- 2616 [119] LHC Higgs Cross Section Working Group Collaboration, "Handbook of LHC Higgs
2617 Cross Sections: 3. Higgs Properties: Report of the LHC Higgs Cross Section Working
2618 Group", Technical Report arXiv:1307.1347. CERN-2013-004, Geneva, 2013. Comments:
2619 404 pages, 139 figures, to be submitted to CERN Report. Working Group web page:
2620 <https://twiki.cern.ch/twiki/bin/view/LHCPhysics/CrossSections>.
- 2621 [120] CMS Collaboration, "CMS luminosity measurement for the 2017 data-taking period at
2622 $\sqrt{s} = 13$ TeV", CMS Physics Analysis Summary CMS-PAS-LUM-17-004, 2017.
- 2623 [121] CMS Collaboration, "Evidence for the 125 GeV Higgs boson decaying to a pair of τ
2624 leptons", *JHEP* **05** (2014) 104, doi:10.1007/JHEP05(2014)104,
2625 arXiv:1401.5041.
- 2626 [122] F. Maltoni, D. Pagani, A. Shivaji, and X. Zhao, "Trilinear Higgs coupling determination
2627 via single-Higgs differential measurements at the LHC", *Eur. Phys. J.* **C77** (2017), no. 12,
2628 887, doi:10.1140/epjc/s10052-017-5410-8, arXiv:1709.08649.
- 2629 [123] LHC Higgs Cross Section Working Group Collaboration, "Handbook of LHC Higgs
2630 Cross Sections: 3. Higgs Properties", doi:10.5170/CERN-2013-004,
2631 arXiv:1307.1347.
- 2632 [124] P. Artoisenet et al., "A framework for Higgs characterisation", *JHEP* **11** (2013) 043,
2633 doi:10.1007/JHEP11(2013)043, arXiv:1306.6464.
- 2634 [125] ATLAS, CMS Collaboration, "Measurements of the Higgs boson production and decay
2635 rates and constraints on its couplings from a combined ATLAS and CMS analysis of the
2636 LHC pp collision data at $\sqrt{s} = 7$ and 8 TeV", *JHEP* **08** (2016) 045,
2637 doi:10.1007/JHEP08(2016)045, arXiv:1606.02266.

- 2638 [126] Carvalho, A.
2639 https://indico.cern.ch/event/718591/contributions/3022720/attachments/1658083/2655364/BDT_20
- 2640 [127] CMS Collaboration, "Jet algorithms performance in 13 TeV data", CMS Physics
2641 Analysis Summary CMS-PAS-JME-16-003, 2016.
- 2642 [128] CMS Collaboration, "Evidence for associated production of a Higgs boson with a top
2643 quark pair in final states with electrons, muons, and hadronically decaying τ leptons at
2644 $\sqrt{s} = 13$ TeV", arXiv:1803.05485.
- 2645 [129] F. Maltoni, E. Vryonidou, and C. Zhang, "Higgs production in association with a
2646 top-antitop pair in the Standard Model Effective Field Theory at NLO in QCD", *JHEP*
2647 **10** (2016) 123, doi:10.1007/JHEP10(2016)123, arXiv:1607.05330.
- 2648 [130] B. A. Betchart, R. Demina, and A. Harel, "Analytic solutions for neutrino momenta in
2649 decay of top quarks", *Nucl. Instrum. Meth.* **A736** (2014) 169–178,
2650 doi:10.1016/j.nima.2013.10.039, arXiv:1305.1878.
- 2651 [131] F. Chollet et al., "Keras", 2015. <https://keras.io>.
- 2652 [132] M. Abadi et al., "TensorFlow: large-scale machine learning on heterogeneous systems",
2653 2015. <https://www.tensorflow.org>.
- 2654 [133] Vischia, P. Collaboration.
2655 http://vischia.web.cern.ch/vischia/tth_regression/2019-11-08.
- 2656 [134] R. K. Dewanjee.
2657 https://indico.cern.ch/event/718591/contributions/3022719/attachments/1657989/2654969/ttH_mee
- 2658 [135] Wikipedia Collaboration.
2659 [https://en.wikipedia.org/wiki/Linear_least_squares_\(mathematics\)#Weighted_linear_least_squares](https://en.wikipedia.org/wiki/Linear_least_squares_(mathematics)#Weighted_linear_least_squares).
- 2660 [136] R. Barlow and C. Beeston, "Fitting using finite Monte Carlo samples",
2661 *Comput. Phys. Commun.* **77** (1993) 219.
- 2662 [137] J. S. Conway, "Incorporating nuisance parameters in likelihoods for multisource
2663 spectra", (2011). arXiv:1103.0354.
- 2664 [138] Higgs PAG.
2665 <https://twiki.cern.ch/twiki/bin/viewauth/CMS/SWGuideHiggsAnalysisCombinedLimit>.
- 2666 [139] A. Tiko.
2667 <https://indico.cern.ch/event/606232/contributions/2444209/attachments/1398539/2133074/chargef>
- 2668 [140] Thomas, L. Collaboration.
2669 https://lathomas.web.cern.ch/lathomas/TSGStuff/L1Prefiring/PrefiringMaps_2016and2017/.